Frustrated magnetism on the anisotropic kagome lattice : a local probe study of Y-kapellasite compounds

Dipranjan Chatterjee

université PARIS-SACLAY

Frustrated magnetism on the anisotropic kagome lattice: a local probe study of Y-kapellasite compounds

Magnétisme frustré sur le réseau kagome anisotrope : une étude par sondes locales dans les composés Y-kapellasite

Thèse de doctorat de l'université Paris-Saclay

École doctorale n° 564, Physique en Île-de-France (PIF)

Spécialité de doctorat: Physique

Graduate School: Physique

Référent : Faculté des sciences d'Orsay

Thèse préparée au **Laboratoire de Physique des Solides** (Université Paris-Saclay, CNRS), sous la direction de **Fabrice BERT**, Professeur, la co-direction de **Philippe MENDELS**, Professeur émérite, et le co-encadrement d'**Edwin KERMARREC**, Maître de conférence

Thèse soutenue à Paris-Saclay, le 9 November 2023, par

Dipranjan CHATTERJEE

Composition du jury

Membres du jury avec voix délibérative

Anuradha JAGANNATHAN	Présidente
Professeur, Université Paris-Saclay	
Sophie DE BRION	Rapporteure & Examinatrice
Professeur, Université Grenoble Alpes	
Martin KLANJSEK	Rapporteur & Examinateur
Professeur assistant (équiv. HDR), Jozef Stefan Institute	
Johannes REUTHER	Examinateur
Professeur, Freie Universität Berlin	
Stephen BLUNDELL	Examinateur
Professeur, University of Oxford	

THESE DE DOCTORAT

NNT : 2023UPASP148

université PARIS-SACLAY | ÉCOLE DOCTORALE Physique en Île-de-France (PIF)

Titre: Magnétisme frustré sur le réseau kagome anisotrope : une étude par sondes locales dans les composés Y-kapellasite.

Mots clés: Frustration magnétique, RMN, Liquide de spins, Techniques spectroscopiques locales

Résumé: Le réseau kagome, avec son arrangement bidimensionnel de triangles à sommets partagés, est un exemple classique où la frustration joue un rôle central dans l'émergence de phases magnétiques originales. En particulier, le hamiltonien antiferromagnétique de Heisenberg pour des spins S=1/2 sur un réseau kagome parfait conduit à la stabilisation d'états quantiques exotiques, y compris les très recherchés liquides de spin, qui ne présentent aucune brisure de symétrie même au zero absolu (T = 0 K). La quête de matériaux capables de réaliser de tels états quantiques a récemment conduit à la découverte d'une nouvelle famille de composés kagome. Ces composés résultent de la substitution des ions Zn^{2+} par Y^{3+} dans le candidat liquide de spin archétype herbertsmithite $ZnCu_3(OH)_6Cl_2$. Le but initial était de doper en charge un liquide quantique de spin sans gap. Bien que le dopage ne fonctionne pas, les nouveaux matériaux isolants obtenus, $YCu_3(OH)_{6+x}X_{3-x}$ (X = Cl, Br et $x = 0$ ou 1/3), souvent appelés Y-kapellasite, sont des composés frustrés intéressants avec des couches kagome bien isolées et aucune dilution significative du réseau magnétique. Dans ce travail expérimental, nous présentons une étude détaillée des composés $x = 1/3$, chlorés ($Y_3Cu_9(OH)_{19}Cl_8$) et bromés ($Y_3Cu_9(OH)_{19}Br_8$). Ils matérialisent un réseau kagome anisotrope original avec trois interactions premier-voisins différentes. Le modèle théorique correspondant présente un diagramme de phase classique riche englobant une phase liquide de spin exotique et des ordres à longue portée. Après une introduction générale à la physique de la frustration magnétique et aux techniques que nous avons utilisées, cette thèse comprend deux parties expérimentales. La première partie porte sur l'étude de monocristaux purs de $Y_3Cu_9(OH)_{19}Cl_8$, obtenus par une méthode de croissance hydrothermale à gradient externe, par des techniques locales μSR et RMN, ainsi que des mesures thermodynamiques et de diffusion de neutrons. Contrairement aux études précédentes sur des échantillons en poudre, cette étude de monocristaux donne des preuves d'instabilités structurales subtiles à 33 K et 13 K qui préservent la symétrie globale du système, donc le modèle magnétique, et que nous avons attribuées à la localisation de l'un des hydrogènes. De plus, nos résultats mettent en évidence une transition magnétique à 2.1 K en bon accord avec la prédiction théorique d'un ordre à longue portée (1/3,1/3). Cependant, notre analyse des excitations d'ondes de spin donne des interactions magnétiques qui situe le composé très près de la phase liquide classique. Probablement en raison de fortes fluctuations quantiques à cette limite, le moment ordonné des Cu^{2+} est fortement réduit, non détecté par diffraction de neutrons, mais révélé par μSR et RMN. Dans la deuxième partie, nous nous intéressons à la variante au brome (Br) du système, introduisant ainsi une pression chimique en substituant un atome plus grand dans le but d'explorer le diagramme de phase magnétique. En utilisant, comme pour le cas du chlore, des techniques thermodynamiques et locales sur une collection de petits monocristaux alignés selon l'axe c, nous avons identifié une transition structurale à environ 15 K tandis qu'une transition magnétique autour de 9 K a été attribuée à une phase d'impureté. Le système présente un gel de spin inhomogène surprenant, correspondant à un état fondamental partiellement ordonné en dessous de 2.5 K. Le gel partiel rappelle l'absence d'ordre magnétique dans les échantillons en poudre de la variante au chlore, contrairement aux monocristaux, et met en évidence la fragilité de l'état fondamental vis à vis désordre probablement en raison de sa proximité avec une phase de liquide de spin.

université PARIS-SACLAY

ÉCOLE DOCTORALE
Physique en Île-de-France (PIF)

Title: Frustrated magnetism on the anisotropic kagome lattice: a local probe study of Y-kapellasite compounds.

Keywords: Magnetic frustration, NMR, Spin liquids, Local spectroscopic techniques

Abstract: The kagome lattice, with its two dimensional arrangement of corner-sharing triangles is a classic example where frustration plays a central role in the emergence of intriguing magnetic phases. Noticeably, the S = 1/2 Heisenberg antiferromagnetic Hamiltonian on a perfect kagome lattice is known to lead to the stabilization of exotic quantum states, including the long sought spin liquids, which do not exhibit any symmetry breaking even at absolute zero temperature (T = 0 K). The quest for materials that can realize such quantum states has recently led to the discovery of a new family of kagome compounds. These compounds are the result of substituting Zn^{2+} with Y^{3+} in the well-known spin liquid candidate herbertsmithite $ZnCu_3(OH)_6Cl_2$ with the initial goal to charge-dope a gapless quantum spin liquid. Although charge doping could not be achieved, the new insulating materials, denoted as $YCu_3(OH)_{6+x}X_{3-x}$ (X =Cl, Br and $x = 0$ or 1/3), often referred to as Y-kapellasite, are interesting frustrated magnets with well isolated kagome layers and no significant dilution of the magnetic lattice. In this experimental work, we present a detailed study of the $x = 1/3$ counterparts, with chlorine ($Y_3Cu_9(OH)_{19}Cl_8$) and bromine ($Y_3Cu_9(OH)_{19}Br_8$) variants. They materialize an original anisotropic kagome lattice with three different nearest neighbor interactions. The corresponding theoretical model hosts a rich classical phase diagram encompassing an exotic spin liquid phase and long-range orders.
After a general introduction to the physics of magnetic frustration and to the techniques we used, this dissertation comprises two experimental parts. The first part reports the study of large phase-pure single crystals of $Y_3Cu_9(OH)_19Cl_8$, obtained via an external gradient hydrothermal growth method, by local μSR and NMR techniques as well as complementary thermodynamic and neutron scattering measurements. In contrast with previous powder sample studies, this single crystal investigation gives evidence for subtle structural instabilities at 33 K and 13 K which preserve the global symmetry of the system, thus the magnetic model, and which we ascribed to the localization of one of the hydrogen. Further, our results provide clear evidence for a magnetic transition at 2.1 K from complementary experimental methods, which is in line with the theoretical prediction of a (1/3,1/3) long range ordering. However, our analysis of the spin wave excitations yields magnetic interactions which locate the compound closer to the phase boundary of the classical liquid phase. Likely due to large quantum fluctuations at this boundary, the ordered moment of Cu^{2+} is strongly reduced, undetected with neutron diffraction, but revealed with µSR and NMR. In the second part, we delved into the Bromine (Br) variant of the system, introducing chemical pressure by incorporating a larger atom with the aim to further explore the magnetic phase diagram. Employing similar thermodynamic and local techniques on a collection of small single crystals co-aligned along their c-axis, we identified a structural transition at approximately 15 K while a magnetic transition around 9 K was ascribed to an impurity phase. Notably, the system exhibited an intriguing inhomogeneous spin freezing, resulting in a partially ordered ground state below 2.5 K. The partial freezing is reminiscent of the absence of magnetic order in powder samples of the Cl-variant, unlike in the single crystals, and emphasizes the fragility of the ground state to disorder likely as a result of its proximity to a spin liquid phase.

Dedicated to,

Mithu Chatterjee

Surath Sankar Chatterjee

Soumen Banerjee

The Gratitude Gallery

My odyssey to becoming a physicist has been a captivating journey, intricate and without a one-size-fits-all solution. There were no grand epiphanies, no secret formulas – just dedication and the timely guidance of remarkable individuals who illuminated the way. Joining LPS (Laboratoire de physique des solides) and pursuing a PhD at the Université Paris-Saclay has not only been a prestigious opportunity but also an immensely worthwhile one, for which I am truly grateful.

First and foremost, I'd like to give a big shoutout to my thesis director, Fabrice BERT. Your guidance and support throughout these three years have been absolutely fantastic, even when my 'eureka' moments were tinged with a touch of clumsiness. Whether it was the NMR experiments in LPS (and in LNCMI) or the μSR experiments in PSI, I genuinely enjoyed every experiment we tackled. They not only deepened my understanding of the subject and related physics but also made this journey incredibly enriching. A heartfelt thanks to Philippe MENDELS for engaging in numerous important discussions, ranging from experiments and results to the formulation of my thesis. These conversations were not limited to just the academic realm but extended to providing guidance even before other interviews took place (for jobs and post docs). I'm deeply grateful for his invaluable contributions and support. I'd like to extend my gratitude to Edwin KERMARREC for imparting me with invaluable neutron skills. From sharing a well-deserved beer after my first diffraction experiment in ILL to our collaborative work on specific heat experiments in LPS, his contributions have been nothing short of impeccable. I wish to express my heartfelt gratitude once more to my dedicated supervisors for their invaluable guidance in constructing this thesis. Your support has been instrumental in shaping the work, and I am truly appreciative of your assistance.

Next, I would like to express my gratitude to the jury members for dedicating their time to evaluate my thesis and for posing significant and thought-provoking questions during the defense. Special thanks to Sophie DE BRION and Martin KLANJSEK for serving as the rapporteurs and examining my thesis. Your detailed report has been incredibly encouraging. I am also thankful to Anuradha JAGANNATHAN, Johannes REUTHER, and Stephen BLUNDELL for agreeing to be examiners and for generously contributing their time and energy to this endeavor.

When it comes to my group, no words can adequately portray the amount of help I received from Irek MUKHAMEDSHIN (although I strongly disagree that football and cricket are boring games!). As for Veronique BROUET, there

are things to mention throughout the three years. From coffee discussions to my first conference with her in Ax-les-Thermes, many memories stand out, including the ice cream treat in Toulouse. To complete the group's contributions, I extend my heartfelt thanks to the 'founding father' of the SQM group, Henri ALLOUL. A special thank you to Henry for being present on the most important day.

And now, onto my buddies from the SQM. A huge thanks to Brendan LE PENNEC for being a teacher and an unmentioned supervisor at the start of my thesis. Thanks to Suvam BHATTACHARYA, Quentin BARTHÉLEMY, and Paul FOULQUIER for their consistent support and assistance throughout my PhD. Guillaume BERNARD, ex-master's student in the group—playing with the superconducting train and exploring the vanadium NMR line was incredibly enjoyable. I have to mention the beautiful Italy trip, from Capri to Venice, was an unforgettable experience. Emma DAVID, the other master's student, made my time in the group enjoyable, and even after their departure, the group's coffee sessions and conversations continued seamlessly with new students and researchers, making the entire PhD journey pleasant.

Now, onto my brother Antoine FAVIER—thank you for turning office 310 into a homely space during my last year, tolerating my music choices, and making life bearable with your cooking skills, basketball coaching, anime, and movie suggestions, especially during the stressful thesis writing and interviews. Moving along the timeline, the next significant mention is Hafsa ZEROUAL! From our coffee times on the rooftop, discussions about LPS and Paris experiences, to the NMR knight shifts and talks on spin liquids, I truly value your enthusiasm, high-spirited nature, and dedication to work. Keep it up throughout your upcoming PhD, and hopefully, we'll collaborate again soon! My passion for skyrmions, although unrelated to my work, finds expression through my friendship with Greis CIPI. Thanks, Greis, for all the wonderful memories and your incredible stories. Keep contributing to increasing entropy in LPS and work as an infinite source of happy energy. Regarding her supervisor during her master's, Dr. Sujit PANIGRAHY (the soul of the soul of skyrmion), the gratitude gallery isn't enough to encapsulate your contributions over the past three years. At the end, amidst the multitude of names within LPS and the countless memories—be it the non-permanent weekends, cookies clubs, or the lively Paris bars—I extend my heartfelt appreciation to each individual. Your presence contributed significantly to the tapestry of my PhD life, making it an interesting and fulfilling journey. Thank you all for being a part of these wonderful experiences and I wish everyone of them good luck with their future endeavours.

I'd like to extend my heartfelt thanks to the visitors of my group over the past three years, Bruce GAULIN, Rena ZIEVE, and Jeffrey QUILLIAM. Our engaging discussions during lunches, coffee sessions, and important physics conversations have significantly enriched my knowledge. I am especially grateful to Bruce GAULIN for involving me in the triple-axis neutron experiment at ILL and the muSR experiment at PSI. I sincerely hope for future opportunities to collaborate and work together.

My heartfelt thanks to Pascal PUPHAL for providing the exquisite crystals of Yttrium kapellasites. Their invaluable contribution made this PhD work possible. Without these crystals, this research endeavor would not have been

achievable. I extend my heartfelt thanks to all the local contacts and instrument scientists at PSI and ILL. Your invaluable assistance and guidance during my experiments with neutron and muon have been pivotal to my thesis. Your support has been instrumental in shaping and enriching my research.

I also extend my sincere gratitude to my scientific tutor, Anuradha JAGANNATHAN, and my mentor, Richard DEBLOCK, for their pivotal roles in my thesis monitoring committee. The pleasant exchanges and valuable guidance I've had with them have been truly invaluable to my academic journey.

I extend my sincere gratitude to the technical and administrative support teams for their invaluable contribution to facilitating my thesis work under the best possible conditions. On the experimental front, I want to give a special thank you to Pascale SENZIER, Jean-Pierre DALAC, Gilles GUILLIER, Stéphane CABARET, and Sambath SARANGA. On the administrative side, my heartfelt thanks go to Pouneh MILANIAN, Sophie TOURLET, Véronique THIEULART, Marie-France MARIOTTO, Sandrine ERMISSE, and Sabine HOARAU.

Lastly, and most importantly, I want to express my deepest gratitude to my family for their unwavering support throughout this journey, and for continuing to stand by me. Additionally, I am immensely grateful to my friends for their encouragement and their presence on the most crucial day. Their support has meant the world to me and has been an invaluable source of strength.

Résumé

Dans le cadre de ma thèse de doctorat, j'ai exploré de nouveaux types de matériaux appelés "kagome" anisotropes, intéressants pour leurs propriétés issues de la géométrie originale de leur réseau magnétique. Au long de ce manuscrit, je vous emmènerai dans un voyage pour découvrir ces matériaux, incluant leur structure complexe et leurs propriétés magnétiques. Nous étudierons également les changements subtils qu'ils présentent lors de transitions de phase et tenterons de comprendre leur physique fondamentale. J'insisterai sur l'importance de combiner ce que nous observons dans les expériences avec notre compréhension théorique pour mieux appréhender ces matériaux fascinants. Dans cette étude, nous avons utilisé diverses méthodes expérimentales pour caractériser en détail les propriétés électroniques des matériaux kagome quantiques. Cette exploration exhaustive couvre un éventail d'approches: l'analyse des susceptibilités macroscopiques en utilisant des mesures SQUID, la caractérisation de la chaleur spécifique par des mesures PPMS (Physical Property Measurement System), l'examen des structures cristallines et magnétiques en utilisant la diffraction des neutrons, et surtout l'étude des phénomènes magnétiques statiques et dynamiques à l'échelle locale, à quelques angströms du noyau ou de la sonde muonique par résonance magnétique nucléaire pulsée (RMN) ou par rotation et relaxation du spin muonique (μSR). Ces techniques sont des outils essentiels pour étudier le comportement intrinsèque des composés kagome déformés, nous permettant de mieux comprendre leurs états fondamentaux et leurs excitations.

Commençons notre discussion en introduisant le réseau kagome, caractérisé par son agencement bidimensionnel de triangles partageant leurs sommets. Il constitue un exemple classique où la frustration joue un rôle central, donnant lieu à des phases magnétiques intrigantes. Notamment, l'Hamiltonien antiferromagnétique de Heisenberg $S = 1/2$ sur un réseau kagome parfait est connu pour stabiliser des états quantiques exotiques, y compris les liquides de spins très recherchés tels que l'état RVB (Valence Bond Résonant) Anderson 1973. Ces états ne présentent aucune rupture de symétrie, même au zéro absolu ($T = 0$ K).

Du côté expérimental, il existe désormais quelques bonnes réalisations du modèle kagome. Le plus étudié est l'herbertsmithite $ZnCu_3(OH)_6Cl_2$ [Philippe Mendels et al. 2007, T.-H. Han et al. 2012, M. Fu et al. 2015, Norman 2016, Khuntia et al. 2020], qui présente une absence d'ordre magnétique même à des températures extrêmement basses devant l'énergie d'interaction, suggérant que l'état fondamental est un liquide de spin.

Suivant la proposition initiale d'Anderson [Anderson 1987], l'idée qu'un état liquide de spins pourrait être l'état

précurseur conduisant à l'émergence d'un état supraconducteur par dopage, a attiré l'attention des chercheurs, suscitant de nombreuses études. Indépendamment de la supraconductivité, le dopage d'un système kagome ouvrirait des possibilités passionnantes pour découvrir des états originaux. Malheureusement, le dopage en charge s'est révélé inefficace jusqu'à présent, ces systèmes restant isolants. La cause de ce comportement peut probablement être attribuée à la chimie spécifique des matériaux kagome étudiés, en particulier les hydroxydes de cuivre halogénés [Qihang Liu et al. 2018], qui empêcherait la délocalisation de la charge en excès, par formation de polarons piégés. Malgré les défis posés par le dopage, les composés synthétisés restent d'un intérêt scientifique significatif en tant que modèles magnétiques proches de la structure kagome parfaite très étudiée de l'herbertsmithite. Poursuivre les études de ces systèmes peut offrir un point de vue précieux sur les effets des perturbations et aider à comprendre les propriétés intrinsèques du modèle quantique antiferromagnétique de Heisenberg sur le réseau kagome.

Dans cette démarche, des avancées significatives ont émergé des efforts visant à introduire des ions yttrium (Y^{3+}) dans l'herbertsmithite en les substituant aux ions de zinc. Ceci a conduit à la découverte de deux nouveaux composés: $YCu_3(OH)_6Cl_3$ et $Y_3Cu_9(OH)_{19}Cl_8$. Ces composés, collectivement appelés Y-kapellasites, peuvent être représentés de manière générique par la formule $YCu_3(OH)_{6+x}Cl_{3-x}$, avec x valant 0 ou 1/3. Ils ont été initialement synthétisés respectivement en 2016 [Wei Sun et al. 2016] et 2017 [Puphal, Bolte, et al. 2017].

La variante $x = 0$ présente une structure kagome parfaite avec une symétrie $P\bar{3}m1$. Cette variante présente une transition vers un ordre magnétique à environ 15 K. Cette transition a été attribuée à une contribution substantielle de l'interaction de Dzyaloshinskii-Moriya (DMI) avec $D/J \sim 0.25$ dans le système.

Inversement, la variante pour $x = 1/3$ présente une structure kagome déformée avec trois longueurs de liaison distinctes, matérialisant le modèle kagome anisotrope étudié théoriquement dans [Hering et al. 2022]. Le réseau adopte une structure $R\bar{3}$ [1(a)], donnant un réseau kagome particulier avec trois interactions d'échange proches voisins distinctes ($J_{\hexagon} \ll J, J'$) [1(b)]. Le diagramme de phase classique correspondant à ce modèle kagome déformé anisotrope [1(c)] a été établi dans Hering et al. 2022 par des calculs analytiques et des méthodes numériques. Cette étude révèle un diagramme de phase classique riche et encore largement inexploré pour ce modèle.

En particulier, le diagramme présente une phase ordonnée assez étendue correspondant à un état de spins coplanaires avec un vecteur d'onde magnétique commensurable $\vec{Q} = (\frac{1}{3}, \frac{1}{3})$, étendant la maille magnétique à 27 atomes, soit un triplement de la maille cristallographique. De plus, une partie substantielle du diagramme de phase, incluant le cas du réseau kagome non déformé, correspond à une phase complexe "liquide de spin classique". Cette phase, dénommée "phase de liquide de spin bloqué", comprend des états fondamentaux discrètement dégénérés, caractérisés par des configurations de spin non coplanaires. Enfin, lorsque $J_{\hexagon} \ll J, J'$, le système sort de son état frustré pour passer à une configuration colinéaire simple avec $\vec{Q} = 0$.

Concernant le cas spécifique de notre composé, des études antérieures ont présenté des résultats contradic-

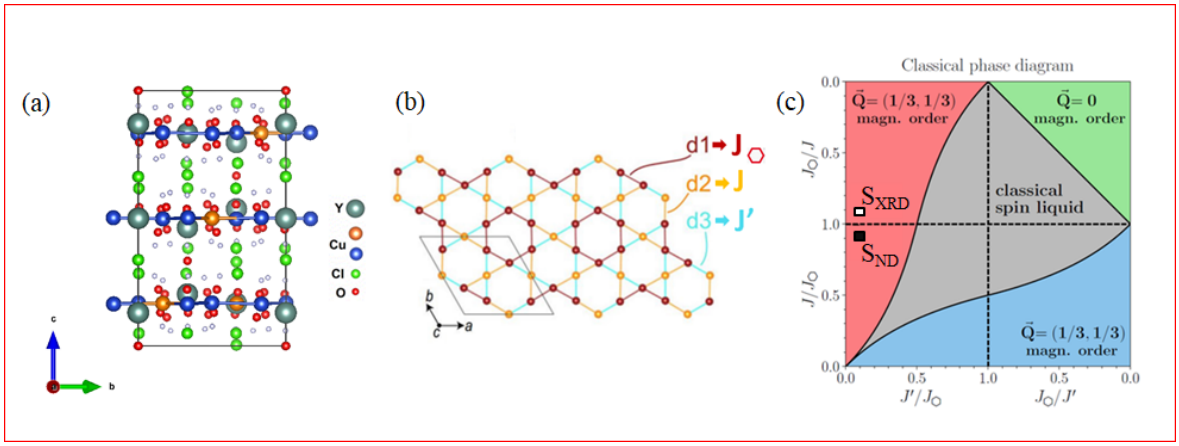

Figure 1: (a) La structure de $Y_3Cu_9(OH)_{19}Cl_8$, observée le long de l'axe a grâce à des mesures de diffraction de neutrons de monocristaux à 40 K. b) le réseau kagome anisotrope qui présente trois liaisons Cu-Cu proches voisins différentes et trois interactions magnétiques associées. (c) Diagramme de phase classique issu de [Hering et al. 2022] pour le réseau kagome déformé sans désordre. Le carré noir (basé sur les données de diffraction X de [Puphal, Bolte, et al. 2017]) et le carré blanc (issu des données de diffraction neutronique de [Barthélemy, Puphal, et al. 2019]) indiquent la position obtenue à partir des calculs de DFT.

toires. Certaines indiquent un état fondamental de type liquide de spin, tandis que d'autres suggèrent un ordre magnétique. Nos efforts de recherche visent à comprendre ces disparités et à découvrir le véritable état fondamental. Théoriquement, il a été proposé Hering et al. 2022, que la variante $x = 1/3$ devrait présenter un ordre magnétique avec $\vec{Q} = (\frac{1}{3}, \frac{1}{3})$.

Nos études expérimentales ont commencé par la caractérisation de monocristaux de $Y_3Cu_9(OH)_{19}Cl_8$, synthétisés par Pascal Puphal de l'Institut Max Planck à Stuttgart. Ces cristaux ont été préparés par une méthode de croissance cristalline optimisée par gradient externe de température dans une ampoule horizontale de quartz à paroi épaisse. Cette méthode, utilisée aussi pour la synthèse d'herbertsmithite, est détaillée dans la [T. Han et al. 2011]. Les cristaux de $Y_3Cu_9(OH)_{19}Cl_8$ varient en taille, allant de $3 \times 3 \times 1$ mm^3 à $3 \times 3 \times 3$ mm^3, et ont été produits avec succès, sans présence de phases parasites indésirables. La taille et la pureté des cristaux obtenus constituent un avantage significatif par rapport à la méthode de synthèse conventionnelle décrite dans [Puphal, Bolte, et al. 2017].

Avec ces gros monocristaux de phase pure à notre disposition, mes collaborateurs et moi-même avons entrepris des mesures macroscopiques, visant à caractériser le comportement du composé $Y_3Cu_9(OH)_{19}Cl_8$. Comme mentionné précédemment, nous avons effectué des mesures de susceptibilité, de capacité calorifique, de dilatation, et de diffraction neutronique. Les résultats ont révélé une série de transitions structurales et magnétiques intrigantes se produisant à des températures inférieures à 33 K. Notamment, la transition à 33K, absente dans les échantillons en poudre et non rapportée dans les monocristaux précédemment étudiés, a attiré notre attention. L'absence de changements brusques dans la susceptibilité magnétique (χmag) implique que ce pic à environ 33 K provient probablement d'une transformation structurale. Des expériences supplémentaires de dilatation thermique le long de l'axe c ont confirmé la présence d'anomalies à la fois à 33 K et une autre à 15 K. Les études par diffraction neutronique

sur un échantillon deutéré montrent aussi une transition à $\sim$ 33 K, révélée par un changement de l'intensité des pics de diffraction. On interprète cette transition comme le gel d'un des atomes de deutérium, D1, mobile à haute température, conduisant à une probable réduction de symétrie en P1. Il faut noter que malgré le déplacement de la position D1, le réseau kagome moyen est resté globablement inchangé, avec des altérations minimes des angles de superéchange.

Les mesures de susceptibilité montrent un comportement Curie-Weiss antiferromagnétique, avec une température Curie-Weiss (θ) d'environ 100 K. Bien en dessous de cette échelle d'énergie, un pic marqué à 2,1 K dans les données de capacité calorifique suggère une transition vers un ordre magnétique à longue portée. Il s'accompagne d'un maximum dans la susceptibilité magnétique refroidie sans champ (χ). Néanmoins, il est à noter qu'aucun pic de Bragg magnétique supplémentaire n'a pu être détecté à 65 mK à l'aide de mesures de diffraction neutronique.

Pour révéler la nature de l'état fondamental, nous avons entrepris l'étude par μSR des propriétés magnétiques de l'Y-kapellasite ($Y_3Cu_9(OH)_{19}Cl_8$) [2 (a)-(c)]. Grâce à cette étude μSR sur des monocristaux, nous avons identifié une transition magnétique se produisant à environ 2,1 K, vers un état magnétique fondamental entièrement ordonné. Nous avons observé une distribution assez large des champs magnétiques locaux, avec une valeur moyenne faible de 8,6 mT. Notre analyse conduit à un moment magnétique des Cu^{2+} fortement réduit, d'environ 1/30 μ_B. Ceci suggére une phase magnétique fragile et probablement affectée par des fluctuations quantiques fortes, liée à la proximité d'une transition de phase quantique vers la phase liquide de spin. Les études antérieures sur des échantillons polycristallins (poudre) montraient au contraire un état fondamental dynamique. Cette différence suggère une forte sensibilité de l'état ordonné à la cristallinité de l'échantillon et aux propriétés structurales en général, impliquant la présence d'un désordre supplémentaire ou de variations dans les interactions dans les échantillons polycristallins. Ces facteurs semblent suffisant pour perturber l'état ordonné fragile observé dans les gros monocristaux.

Une partie importante du travail de thèse a été l'étude par RMN du ^{35}Cl de cristaux $Y_3Cu_9(OH)_{19}Cl_8$, orientés pour avoir l'axe *c* parallèle au champ appliqué. Dans cette configuration, il y a deux sites de chlore distincts, à savoir hexagonal et triangulaire. Notre but était de révéler les évolutions structurales et magnétiques complexes en fonction de la température, grâce à une sonde locale. Les spectres acquis à différentes températures, montrent des modifications nettes vers 33 K et 15 K. Ces études ont non seulement mis en évidence des phénomènes de brisure de symétrie, qui n'étaient pas évidents dans les données de diffraction des neutrons, mais ont également confirmé la nature structurale des transitions observées.

A plus basse température, l'identification de la transition magnétique à environ 2,1 K représente un développement significatif [2 (d)-(e)]. N'ayant pas pu mesurer toutes les composantes du tenseur hyperfin, nous avons proposé de manière provisoire un modèle d'interaction magnétique purement dipolaire. Sous cette hypothèse, le spectre mesuré à la plus basse température, lorsque le paramètre d'ordre est développé dans la phase ordonnée, correspond remarquablement bien aux prédictions théoriques d'une texture de spin caractérisée par un vecteur de

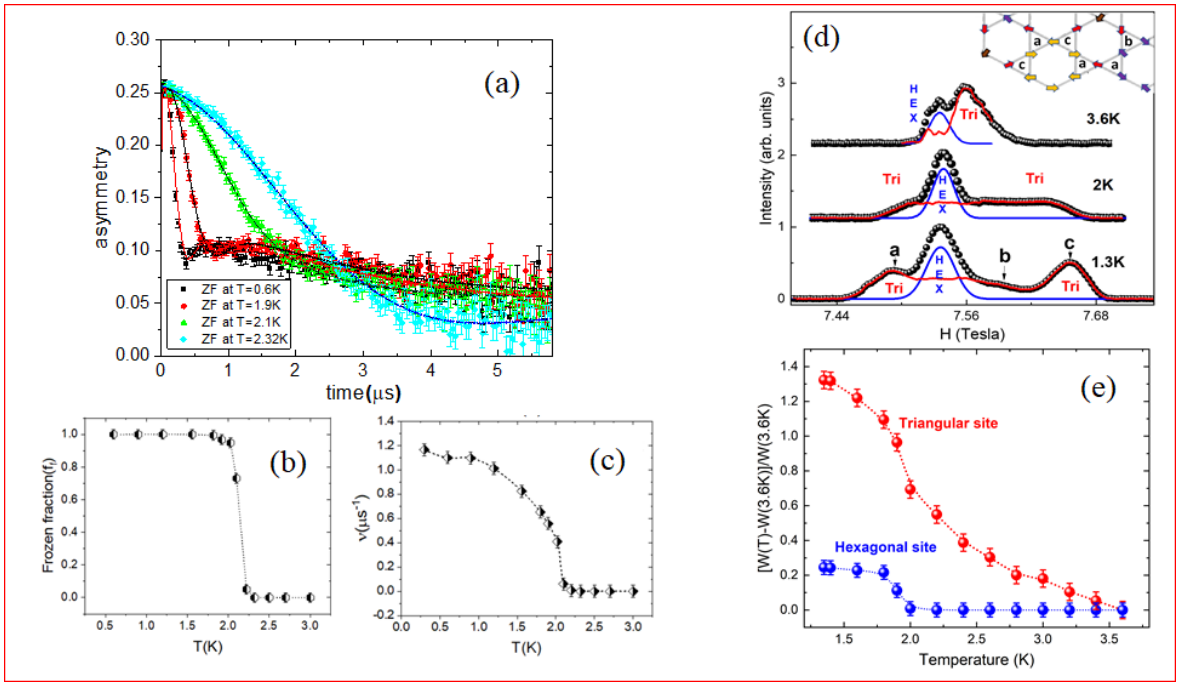

Figure 2: (a) Évolution temporelle de l'asymétrie de désintégration du muon en champ nul (ZF) à 2,32 K, 2,1 K, 1,9 K, 0,6 K dans des échantillons monocristallin. Évolution en température des paramètres : (b) fraction gelée des spins indiquant une phase ordonnée et une transition en volume en dessous de 2,1 K et (c) fréquence ν_f reflétant le développement d'un champ interne en dessous de 2,1 K indiquant la transition magnétique. (d) Spectres RMN de la raie centrale à 1,3 K, 2 K, 3,6 K et vue partielle de la texture de spin de l'état fondamental proposée dans [Hering et al. 2022] dans le coin supérieur droit. Les spectres sont décalés verticalement pour plus de clarté. La ligne bleue est un ajustement gaussien de la raie centrale hexagonale. Cette contribution est soustraite du spectre expérimental pour exposer la raie du site triangulaire, montrée comme une ligne rouge. Les configurations **a**, **b** et **c** donnent trois champs internes différents au site Cl triangulaire en raison des spins non compensés. Les configurations **a** et **c** donnent des champs presque égaux mais opposés, tandis que la configuration **b** a presque un champ nul le long de l'axe z, c'est-à-dire la direction du champ appliqué. (e) Évolution en température de la largeur de raie W(T) pour les sites triangulaire (points rouges) et hexagonal (points bleus) indiquant une transition à $\sim$ 2,1 K.

propagation de (1/3,1/3) [1 (d)]. Cependant, la détermination précise des valeurs du moment magnétique en phase ordonnée reste complexe, en raison des incertitudes sur les couplages hyperfins et aussi de la manière dont se développe l'ordre magnétique dans la direction de l'axe c. De plus, la contribution du champ magnétique externe à l'aimantation globale en phase ordonnée pourrait jouer un rôle.

Les données de relaxation obtenues montrent trois transitions distinctes. Un pic très fin à environ 33 K et un pic beaucoup plus large autour de 15 K indiquent des transitions structurales. Le pic observé à des températures plus basses correspond au point de transition magnétique à environ 2,1 K. Cette transition à 2,1 K est également mentionnée dans la référence-[Jierong Wang et al. 2022], où la RMN du proton a été spécifiquement mise en œuvre à basses températures. Ces points de transition s'alignent parfaitement avec l'évolution des formes et largeurs de raies RMN, ainsi qu'avec les mesures de conductivité thermique et de chaleur spécifique réalisées sur ce monocristal.

Dans les données de diffusion inélastique des neutrons à 1,5 K, une contribution magnétique est présente et

identifiée à des ondes de spin. Des calculs linéaires d'ondes de spin ont été effectués à l'aide du package SPINW, basé sur le modèle d'Heisenberg proches voisins. Cette approche a permis de déterminer trois valeurs d'interaction d'échange différentes : $J_{\bigcirc} = J = 140(10)$ K et $J' = [56, 70]$ K. La valeur de J' obtenue est significativement plus grande que la valeur calculée théoriquement, qui était d'environ $J' \sim 10$ K, par les calculs ab initio. De plus, il s'est avéré nécessaire d'inclure une distribution des valeurs de J' pour rendre compte de la distribution observée de l'intensité, suggérant un désordre local dans le système.

Les interactions déterminées expérimentalement placent l'Y-kapellasite dans le diagramme de phase classique près de la frontière qui sépare la phase ordonnée à longue portée (1/3, 1/3) de la phase liquide de spin. Bien que l'effet des fluctuations quantiques à proximité de la séparation de phase n'ait pas été exploré, il est concevable que ces fluctuations jouent un rôle important en réduisant la valeur des moments Cu^{2+} à moins de 0.1 µB.

Dans le but d'explorer plus avant le diagramme de phase du modèle de kagome anisotrope, nous avons étudié la version bromée de l'Y-kapellasite. La substitution de Cl par les ions Br plus grands augmente les paramètres de la maille sans changer le groupe d'espace $R\overline{3}$, créant ainsi une "pression chimique". Par conséquent, les longueurs des arêtes des triangles de Cu et les angles de super-échange magnétique correspondants sont modifiés, semblant mener à un modèle plus anisotrope.

Contrairement aux rapports récents dans la littérature J. Liu et al. 2022, X.-H. Chen et al. 2020, Zeng et al. 2022] concernant la variante Br qui concluent tous à l'absence d'ordre magnétique dans le système, même à des températures extrêmement basses, nos petits monocristaux ne présentent pas de mélange notable Br/OH et montrent un comportement à basse température assez différent avec plusieurs transitions non signalées jusqu'à présent. Des mesures de chaleur spécifique ont été réalisées jusqu'à 1.8 K, avec des champs magnétiques appliqués jusqu'à 9 Tesla. Par comparaison entre $Y_3Cu_9OH_{19}Br_8$ et $Y_3Cu_9OH_{19}Cl_8$, le pic à 33 K est absent dans la variante bromée mais un nouveau pic non magnétique à environ $\sim$ 15,5 K émerge, suggérant des différences structurales. De plus, des mesures de chaleur spécifique dépendantes du champ fournissent des preuves de pics magnétiques à 9 K et 2.3 K dans $Y_3Cu_9OH_{19}Br_8$. Des mesures d'aimantation SQUID ont été effectuées sur des monocristaux alignés. Au-dessus de 60 K, un comportement Curie-Weiss est observé, d'où on extrait une interaction AF significative mais plus faible que dans le cas du Cl, avec $\theta_c = 74(2)$ K. Une petite bosse à 9 K dans la susceptibilité se retrouve dans la chaleur spécifique, que nous avons attribué à une impureté magnétique. Contrairement à $Y_3Cu_9OH_{19}Cl_8$, nous n'observons pas de pic ou d'hystérésis qui pourraient signaler une transition magnétique autour de 2 K.

Enfin, nous avons étudié une collection de petits monocristaux de $Y_3Cu_9(OH)_{19}Br_8$ en utilisant les techniques locales de μSR et de RMN. Les résultats de μSR ont mis en évidence un gel magnétique partiel, affectant 40% de l'échantillon et se produisant en dessous de 2.2 K. De manière intéressante, ce gel partiel n'est pas clairement visible dans les mesures de susceptibilité mais entraîne une augmentation notable de la capacité calorifique. Pour les mesures de RMN, nous avons utilisé un échantillon en poudre, orienté avec un champ magnétique appliqué le long de l'axe c, suivant une approche similaire à notre étude précédente de la variante au chlore. Nos observations

ont révélé la présence de deux sites Br distincts, conformément à nos attentes.

Les raies de RMN pour cet échantillon sont significativement plus étroites que celles rapportées dans [F. Lu et al. 2022] pour des échantillons avec un désordre Br/OH, mais sont un peu plus larges que dans le cas du chlore. À une température de 15.5 K, nous avons détecté une transition claire marquée par un élargissement net des raies RMN et leur dédoublement. Cette transition est cohérente avec un changement structural, suggérant une réduction de la symétrie cristalline, similaire au comportement de la variante au chlore autour de 33 K. De plus, nous avons observé une transition magnétique à 2,2 K, indiquée par un changement notable dans les spectres de RMN. Cependant, en raison de la fusion des raies et d'un manque de contraste de T_1 clair, nous n'avons pas pu aboutir à une interprétation fine de ce spectre. Notamment, contrairement au cas du chlore, nos mesures de relaxation n'ont montré aucun ralentissement critique, probablement en raison de la nature partielle du gel et du caractère dynamique prédominant de l'état fondamental.

Les différents résultats obtenus au cours de cette thèse nous motivent à poursuivre l'étude de ces matériaux kagome anisotropes en utilisant d'autres perturbations telles que l'application d'une pression, d'une contrainte uniaxiale, le désordre ou encore les champs magnétiques élevés, influençant potentiellement les couplages d'échange dans le réseau de kagome anisotrope et/ou l'état fondamental. Bien que certaines voies aient déjà été explorées, des projets en cours, y compris les nôtres, visent à approfondir ces aspects. En particulier, des recherches récentes publiées dans [Jierong Wang et al. 2022] explorent l'impact d'une contrainte uniaxiale sur la modification des interactions de superéchange et les caractéristiques de l'état fondamental. Par des mesures RMN de temps de relaxation du proton, les auteurs de cette étude montrent que la transition magnétique à environ 2,2 K sous contrainte nulle augmente significativement sous contrainte. L'application d'une contrainte semble ainsi atténuer la frustration et stabiliser l'état fondamental ordonné. De nôtre côté, nous souhaitons étudier l'impact de la pression hydrostatique jusqu'à 25 kbar, par μSR, sur la ligne GPD au PSI. L'application de la pression pourrait conduire le système vers un état fondamental de liquide de spin ou renforcer la phase ordonnée [Hering et al. 2022]. De plus, l'introduction d'atomes plus gros comme le brome a donné $Y_3Cu_9(OH)_{19}Br_8$, largement discuté dans cette thèse. Les études [F. Lu et al. 2022, Zeng et al. 2022, J. Liu et al. 2022] lient l'état de liquide de spin observé dans $Y_3Cu_9(OH)_{19}Br_8$ aux effets du désordre résultant du mélange des sites Br-OH, perturbant l'ordre magnétique. Le même effet de désordre pourrait expliquer l'absence d'ordre dans l'échantillon en poudre de la variante au chlore [Barthélemy, Puphal, et al. 2019].

L'influence d'un champ magnétique externe, comme décrit dans [Biesner et al. 2022], s'avère aussi très intéressant. Au-dessus de 5 K, l'aimantation est presque linéaire avec le champ magnétique, jusqu'à 50 T. En dessous de T_N=2,2 K, un plateau d'aimantation émerge autour de 20 T, observé à la fois dans les mesures dans le plan et hors plan. De plus, un changement subtil de pente suggère l'existence potentielle d'un autre plateau autour de 40 à 45 T. Pour mieux comprendre ces plateaux magnétiques, nous avons réalisé des mesures de RMN à haut champ au LNCMI-Grenoble. La présence d'un plateau d'aimantation est évidente dans les données de relaxation spin-

réseau entre 16 T et 26 T. Des études supplémentaires sont nécessaires pour comprendre l'évolution des spectres de RMN en fonction de l'amplitude du champ magnétique et de la température. Ces études devraient conduire à une compréhension fine de la nature de ce premier plateau magnétique, de sa structure magnétique et de ses excitations. Ainsi, les composés Y-kapellasite dont nous avons initié l'étude dans cette thèse, offrent un éventail de possibilités futures et restent un sujet d'intérêt scientifique captivant.

AT A GLANCE!

Recent studies are dedicated to discovering materials capable of hosting exotic quantum states, including spin liquids, characterized by their persistence of disorder down to absolute zero temperature ($T = 0$ K), macroscopic entanglement, and the presence of fractionalized excitations. Kagome systems serve as ideal structures for realizing these phenomena. This pursuit has led to the remarkable discovery of a family of kagome compounds.

In this study, we delve into the unique properties of $YCu_3(OH)_{6+x}X_{3-x}$ (X= Cl, Br) materials, with a specific focus on the $x = 1/3$ variant, known as $Y_3Cu_9(OH)_{19}Cl_8$ and $Y_3Cu_9(OH)_{19}Br_8$, collectively referred to as Y-kapellasite. These compounds originate from the substitution of Zn^{2+} ions with Y^{3+} ions within the renowned herbertsmithite structure, $ZnCu_3(OH)_6Cl_2$. Notably, Y-kapellasite introduces a distorted kagome lattice, giving rise to a novel and intriguing magnetic model characterized by a diverse and complex magnetic phase diagram [Hering et al. 2022]. The thesis is organized as follows:

Chapter [1] introduces the concept of frustration in the kagome lattice and presents the classical phase diagram for the anisotropic kagome case. Chapter [2] describes the fundamental principles of local techniques, particularly NMR and μSR. To comprehensively investigate this class of materials, we employed large, phase-pure single crystals of $Y_3Cu_9(OH)_{19}Cl_8$, prepared by Pascal Puphal from MPI Stuttgart, studied in Part-A of this thesis [Chatterjee et al. 2023]. Chapter [3] provides an introduction to the structural and magnetic model of $Y_3Cu_9(OH)_{19}Cl_8$. Chapter [4] involves the characterization of the $Y_3Cu_9(OH)_{19}Cl_8$ crystals through bulk thermodynamic measurements. Chapter [5] unveils the ground state of Y-kapellasite through μSR investigations. Chapter [6] delves into NMR measurements for the study of structural and magnetic properties and transitions and finally concluding with inelastic neutron scattering and discussions related to the phase diagram in Chapter-[7].

Part-B comprises two chapters. Chapter [8] emphasizes the significance of the Br variant of Y-kapellasite, $Y_3Cu_9(OH)_{19}Br_8$, along with its thermodynamic properties. Chapter [9] focuses on the local study with μSR and NMR to assess the ground state of small single crystals of $Y_3Cu_9(OH)_{19}Br_8$. Finally, Chapter [10] serves as the conclusion of the entire thesis, providing future perspectives for these rich kagome compounds.

Contents

Chapter 1

Introduction to frustrated Kagome Physics:

In this doctoral dissertation, I indulge into the intriguing geometrically frustrated materials known as anisotropic "kagome." Throughout my Ph.D. journey, I will lead you through a detailed exploration of these materials, unraveling their intricate structural and magnetic properties. We'll investigate the enigmatic phase transitions they undergo and decipher the complex nature of their ground state physics. Alongside this experimental investigation, I will emphasize the importance of aligning experimental findings with theoretical insights to enhance our understanding of these remarkable materials. In this chapter, I will lay the groundwork by elucidating the fundamental physics principles that underpin my subsequent research in the following chapters.

We will describe two competing states within two-dimensional frustrated networks. Firstly, we will discuss the 'classic' Néel state. Secondly, we will explore the state characterized by resonant valence bonds, which serves as an archetype for the exotic ground state of spin liquids. In addition, I will delve into the broader concept of frustration, both in general and within the specific context of the kagome structure. I'll also explore the recently studied anisotropic kagome model, which will provide valuable insights for interpreting the results of our experiments. Furthermore, it's essential to explore the origins of the compounds we'll be investigating in the following chapters.

1.1 Classic Néel ordering

In insulating materials with localized magnetic moments, the interactions between spins are typically described by the following Heisenberg Hamiltonian:

$$H = \frac{1}{2}\sum_{i,j} J_{i,j}\mathbf{S}_i \cdot \mathbf{S}_j \tag{1.1}$$

The coupling constant $J_{i,j}$ represents the interaction strength between different nearest neighbor spins (i and j). In the case of antiferromagnetic coupling, we have $J_{i,j} > 0$. In such a system, the spins on a cubic three-dimensional lattice tend to order by anti-aligning, starting from a certain finite temperature. The coupling energy per bond, when there's only one coupling constant (i.e, $J_{i,j} = J$), can be expressed as $E_{NA} = \frac{-J}{4}$ for spins with a value of $\frac{1}{2}$ in a model where the spins are not paired, often referred to as the "classic" case. Consequently, the energy per site is given by $E_{NA} = \frac{-zJ}{8}$, where z represents the coordination of the lattice network. The described state exhibits a finite-temperature transition at T_N, that scales proportionally with the coordination number and the coupling constant (J). Within the ordered state, collective excitations, known as spin waves or magnons, manifest. These excitations are characterized as bosons with an integer spin ($S = 1$) and can be detected through inelastic neutron measurements. Their presence is often indicated by a quasiparticle peak whose dispersion depends on the magnitude and sign of the coupling constants. In the long wavelength approximation, in cases of antiferromagnetic interactions, the energy of the magnon scales linearly with its wave vector $\vec{q}$, whereas for ferromagnetic interactions, it scales with the square of the wave vector ($\vec{q}^2$). [Ashcroft and Mermin 1976].

1.2 The resonating valence bond state

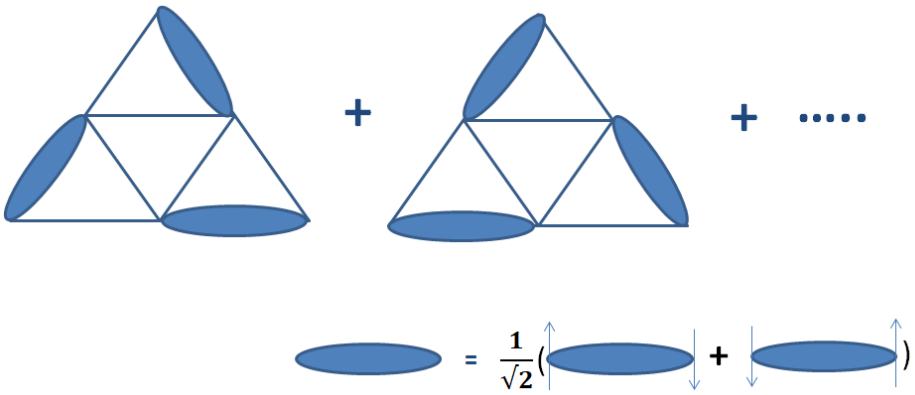

Figure 1.1: The representation of the Resonating Valence Bond (RVB) state on the triangular lattice is created through the superposition of all conceivable coverings of the lattice by singlets.

The state of resonating valence bonds shown in figure-1.1, RVB for Resonating Valence Bond, was first proposed as the fundamental state of a triangular lattice of antiferromagnetic 1/2 spins [Anderson 1973]. In this exotic state, the building blocks of magnetism are no longer isolated moments (spins) but quantum pairings of them, i.e., singlets in the ground state. The magnetization of such a system is zero, and the nearest neighbor spins pair up in the form of singlets:

$$|\phi_{i,j}\rangle = \frac{1}{\sqrt{2}}(\uparrow_i\downarrow_j - \downarrow_i\uparrow_j) \tag{1.2}$$

In the case of an infinite chain of spins where pairings occur between nearest neighbor spins, two states, $|+\rangle = \sum_i \frac{1}{\sqrt{2}}(\uparrow_{2i}\downarrow_{2i+1} - \downarrow_{2i}\uparrow_{2i+1})$ and $|-\rangle = \sum_i \frac{1}{\sqrt{2}}(\uparrow_{2i-1}\downarrow_{2i} - \downarrow_{2i-1}\uparrow_{2i})$, have the same energy. In this particular case, the ground state is a resonating state that is the superposition of $|+\rangle$ and $|-\rangle$. Likewise in the general case, the ground state is thought to be a resonating state that is the superposition of the different possible covering by singlets of the lattice. The ground state described here is a fully quantum state with no 'classical' analogue, characterized by strong entanglement of spins in the form of singlets, and these singlets resonate across the lattice in a macroscopic manner. This state does not exhibit any spontaneous symmetry breaking even down to absolute zero temperature ($T = 0\,$K). Consequently, we are dealing with an exotic fundamental state that demonstrates macroscopic quantum coherence, similar to the high critical-temperature superconductors. These superconducting states are observed near a metal- magnetic insulator transition, and P.W. Anderson, proposed the Resonating Valence Bond (RVB) state as the fundamental state for undoped cuprate compounds, [Anderson 1987].

For a pair of spins forming a singlet, the energy is $E_A = -\frac{3}{8}J$. This energy remains the same for one configuration of singlet covering, regardless of the lattice's coordination number and geometry. It's worth noting that in the case of a system with a cubic three-dimensional lattice ($z = 6$), the Neel state with energy per site $E_{NA} = -\frac{6J}{8}$, is a robust configuaration and is indeed observed experimentally. Therefore, destabilizing this Neel state seems to be a crucial step in promoting more exotic states, such as the RVB state.

1.3 Destabilisation of Néel State

To destabilize the Neel state, one approach is to begin by reducing the dimension of the lattice, thereby disrupting the long-range ordering of the spins. However, in dimensions greater than 1, this alone is insufficient, and it becomes necessary to introduce frustration.

1.3.1 Antiferromagnetic spins in dimension D=1

According to the Mermin-Wagner theorem [Mermin and Wagner 1966], it is impossible to have long-range order in dimensions less than or equal to 2 at finite temperatures. Numerous studies have been conducted in the context of antiferromagnetic spin chains, including neutron scattering studies on systems like $KCuF_3$ [Lake, Tennant, and Nagler 2000], $CuSO_4 \cdot 5D_2O$ [Mourigal et al. 2013], and $LiCuVO_4$ [Enderle et al. 2010]. Theoretically, this system is one of the rare ones that can be exactly solved thanks to the Bethe Ansatz [Bethe 1931].The ground state energy per site is given by:

$$E_{1D} = -[4ln(2) - 1]\frac{J}{4} < -J/4 \tag{1.3}$$

The ground state energy calculated using the [Bethe 1931] is lower than that of the Neel state ($-J/4$) or that of a given covering by singlets ($-3J/8$), suggesting the presence of a more intricate ground state beyond simple

alignment of antiferromagnetic spins. Additionally, the Bethe Ansatz has provided insights into the nature of excitations within such systems, revealing the existence of spinons (S=$1/2$) rather than magnons. It is anticipated that in higher-dimensional lattices, the excitations within the RVB state may share similarities with 1D spinons.

1.3.2 Spin liquid state in dimension $D = 2$ and concept of frustration

In two dimensions, long-range order tends to stabilize more easily compared to one dimension. For instance, antiferromagnetic spins on a square lattice will anti-align to reach an ordered Neel state at $T = 0$ K. In this case, we have a coordination number, $z = 4$, lower than in the three-dimensional case ($z = 6$) but higher than in the one-dimensional case ($z = 2$). Therefore, we must introduce a new ingredient to destabilize the ordered state, which is 'frustration', a term first introduced by G. Toulouse [Toulouse, Vannimenus, and Maillard 1977].

Let's begin by delving into a fundamental concept in frustration known as degeneracy. In such scenarios, the interactions within a system don't converge to a single ground state; instead, they give rise to a multitude of similar low-energy states which share the characteristics of energy minimization within the classical framework. This phenomenon has played a pivotal role in unraveling new magnetic states across various two-dimensional and three-dimensional materials. These states possess distinctive characteristics, including persistent fluctuations even at temperatures approaching absolute zero. They are commonly labeled as "spin liquids" and can also give rise to captivating phenomena such as "spin ice" [Harris et al. 1997], [Bramwell and Gingras 2001], [Castelnovo, Moessner, and Sondhi 2008]. A frustrated system is characterized by its inability to simultaneously minimize all individual interaction energies. In magnetic systems, as illustrated with Ising spins in Figure-1.2, there are three primary forms of frustration:

(a) Disorder-Induced Frustration:

This type of frustration occurs due to the presence of randomly distributed ferromagnetic (FM) or antiferromagnetic (AFM) interactions within the spin network, as illustrated in Figure -1.2(a). Extensive research has delved into this form of frustration, particularly in the realm of spin glasses. In spin glasses, interaction disorder can arise from various sources, such as the random placement of magnetic impurities (e.g., CuMn, AuFe, AgMn) and oscillating or variable spin-spin couplings that change in sign over distance.

(b) Geometric Frustration:

Geometric frustration, in contrast, arises solely from the structure of the magnetic network. A straightforward example is a triangular lattice where a spin resides on each vertex, and antiferromagnetic (AFM) interactions exist between adjacent neighbors [as depicted in Figure 1.2(b)]. Unlike spin glasses, these systems do not display interaction disorder. The absence of long-range order on this type of lattice for Ising spins was first demonstrated in

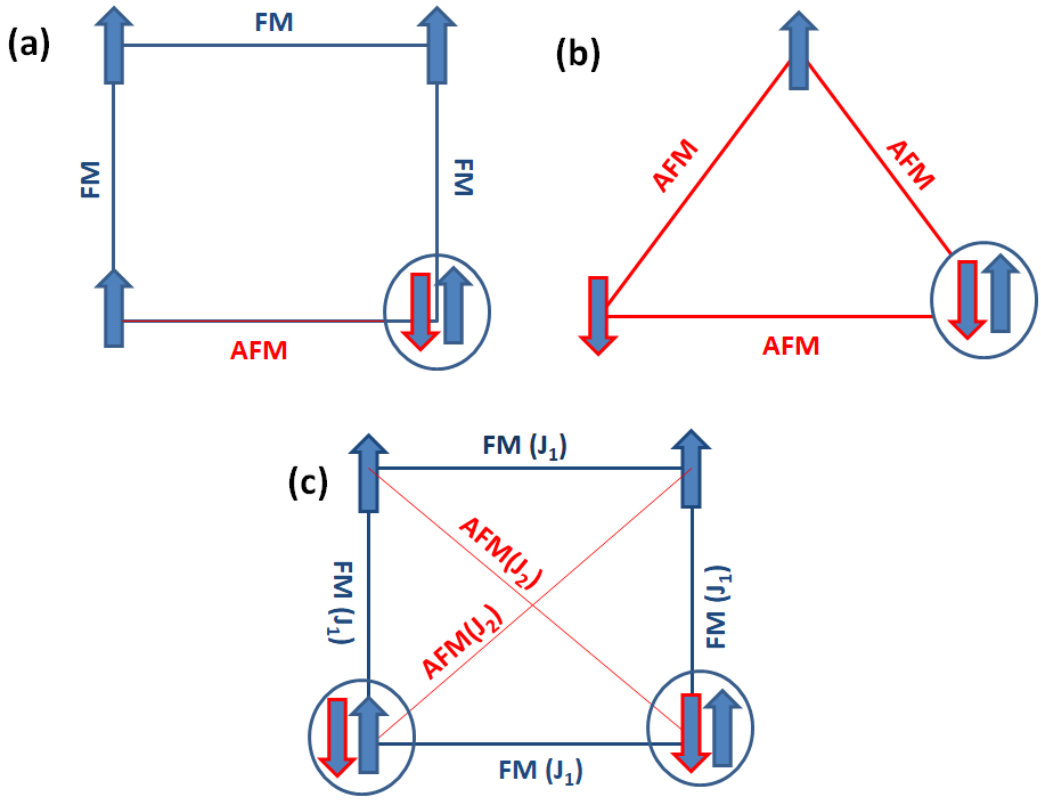

Figure 1.2: Examples of spin frustration can be observed in two different scenarios: (a) one generated by the disorder of interactions on a square lattice, and (b) the other arising from geometric constraints on a triangular lattice . (c) This case arises due to competition between the interactions within the spins demonstrated on a square lattice.

[Wannier 1950].

(c) Frustration due to competition between interactions:

This type of frustration emerges from the competition between interactions within the spin system even though the lattice is not frustrated at all. To illustrate, imagine a square lattice where nearest neighbor interactions are ferromagnetic, denoted as J_1. In contrast, the next-nearest neighbor spins, situated diagonally, are primarily influenced by antiferromagnetic interactions, represented as J_2. In this scenario, the competition between J_1 and J_2 plays a crucial role in determining the ground state [Richter et al. 2010], [Godoy, Schmidt, and Zimmer 2020].

Frustration arising from geometric considerations, which is the fundamental concept of this thesis, will be explored in greater detail here. In the context of geometric frustration, the absence of disorder results in remarkably distinct and theoretically intriguing fundamental states. As depicted in Figure 1.2, for the geometry of a two-dimensional triangular lattice decorated by Heisenberg spins, frustration results in a compromise regarding the alignment of spins in the classical state. Considering the hamiltonian for equilateral the triangular lattice (shown in

figure-1.2 with $J_{i,j}$ = J),

$$H = \frac{1}{2}\sum_{\Delta} J(\vec{S_1} + \vec{S_2} + \vec{S_3})^2 - (S_1^2 + S_2^2 + S_3^2) \tag{1.4}$$

The lowest energy state is achieved when spins are oriented at 120-degree angles to each other, leading to an energy per site of $E_{NA} = -zJ/16$. Notably, in the case of a triangular lattice with a coordination number of $z = 6$, we have a unique scenario where $E_{NA} = -3J/8 = E_A$ (this is equal to the spin-singlet energy) . It was on this triangular lattice that P. W. Anderson initially proposed the RVB state (figure-1.1) as the ground state [Anderson 1973]. Subsequent theoretical investigations, employing exact diagonalization, indicated that this system exhibits a tendency towards an ordered state at absolute zero temperature [Lecheminant et al. 1995]. It is crucial to emphasize that the stability of the Neel state can be compromised by a reduction in the coordination number. To illustrate, consider a triangular lattice with shared vertices and a coordination number of $z = 4$, resulting in $E_{NA} = -J/4 > E_A$. A prominent example of such a lattice is the kagome lattice, characterized by a pattern resembling David's star, as depicted in Figure-[1.3] which has degenerate ground states. Given that the kagome lattice serves as the central focus of this thesis, we will delve into a more in-depth exploration of its theoretical behavior.

1.4 Ground state of the ideal antiferromagnetic Heisenberg kagome lattice

The degeneracy of the ground state alone is not enough to guarantee a fluctuating magnetic ground state, like a spin liquid, at low temperatures. For example, the ground state of spin glasses is also degenerate, but the cooling process tends to select local energy minima, leading to magnetic freezing. However, in the case of frustrated systems with unique geometries, magnetic fluctuations are induced even at absolute zero temperature (T = 0 K). In networks with low coordination and shared vertices, such as the kagome lattice in the Heisenberg model, there exists another interesting property. It's possible to continuously change the orientation of a finite number of spins without affecting the system's total energy, regardless of temperature, thus exploring the degenerate classical ground states at no cost in energy.

For instance, in coplanar states on the kagome lattice, soft modes can be obtained by selecting a loop where two types of spins alternate and rotating them around the axis defined by the third spin (as illustrated in Figure 1.4) [Huse and Rutenberg 1992], [Ritchey, Chandra, and Coleman 1993]. More generally, numerical simulations conducted by Keren [Keren 1995] reveal that the density of zero-energy magnetic excitations continuously increases as the temperature decreases and doesn't exhibit a transition for $T > 10^{-3}J$. In contrast, a maximum in this density is observed for $T \sim 10^{-1}J$ in the square lattice [Keren 1994]. The pyrochlore lattice, made of tetrahedrons with common vertices also remains disordered and fluctuating at all temperatures [Moessner and Chalker 1998]. In

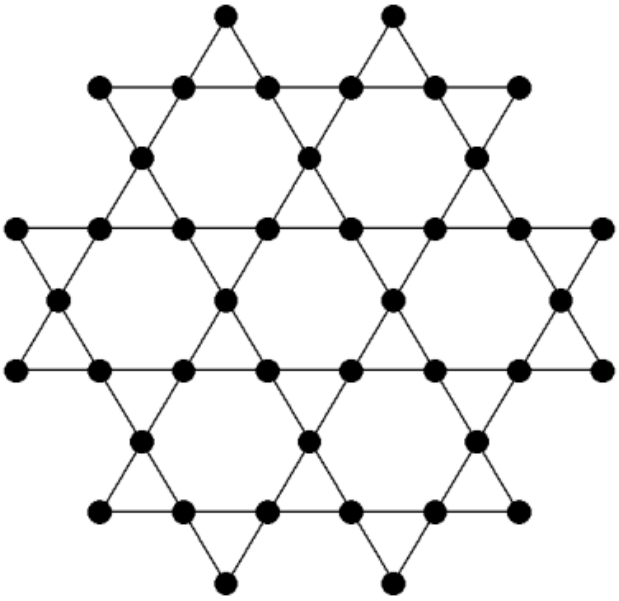

Figure 1.3: The Kagome lattice exhibits several key characteristics that collectively contribute to the destabilization of the Neel state in favor of more exotic phases. These factors include its two-dimensionality, low coordination number, the presence of a triangular motif, and the involvement of spins with a magnitude of 1/2. Consequently, the Kagome lattice is considered a model lattice for facilitating the stabilization of a two-dimensional spin liquid state.

classical Heisenberg spin systems, the existence of these soft modes are responsible for the absence of magnetic order.

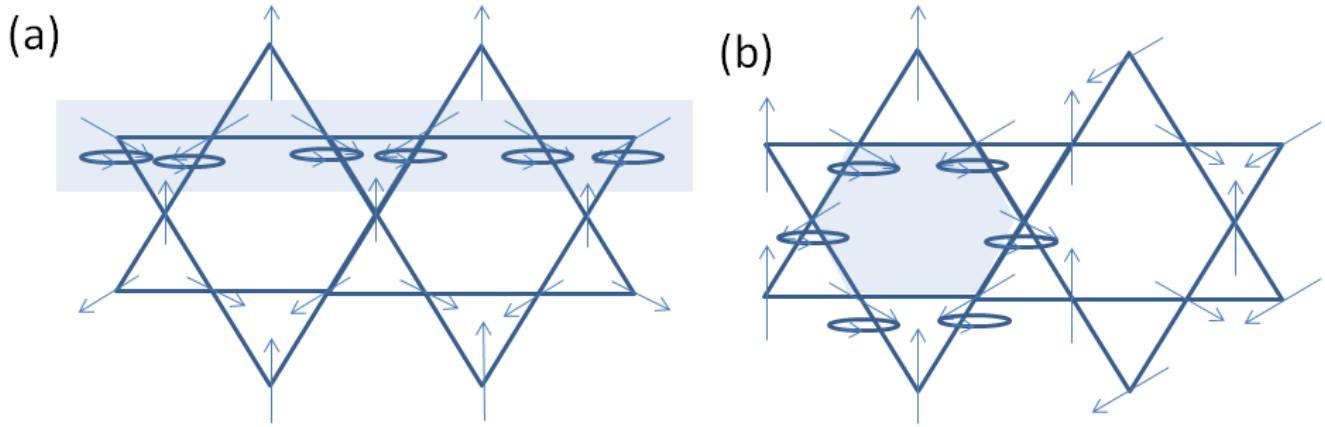

Figure 1.4: The system exhibits two configurations: $q = 0$, which possesses crystallographic unit cell periodicity, and $\sqrt{3} \times \sqrt{3}$ (3 $\times$ unit cell periodicity). The spins participating in a soft mode are located within the shaded regions of these configurations.

The quantum problem of spins interacting on the kagome network has attracted significant attention in various theoretical studies for instance [Läuchli, Sudan, and Sørensen 2011], [Nakano and Sakai 2011], [Lecheminant et al. 1995], [Depenbrock, McCulloch, and Schollwöck 2012],[Nishimoto, Shibata, and Hotta 2013] [Henley 2009]; with different outcomes regarding the ground state. Amidst all these discussions, it is crucial to underscore the

significance of taking into account two pivotal parameters: the energy of the ground state level and the nature of the excitation spectrum. Regrettably, despite continuous research endeavors, a conclusive comprehension of these facets continues to elude us.

Experiments exploring spin liquids in dimensions higher than 1, have been relatively recent compared to the theoretical development, primarily due to the scarcity of suitable frustrated and quantum model compounds. The resurgence of interest in spin liquids over the past decade can be largely attributed to the synthesis of the first perfect kagome compound featuring S = 1/2 spins, known as herbertsmithite, named in honor of the mineralogist G. F. Herbert Smith (1872-1953). This compound was initially synthesized at MIT [Shores et al. 2005] and boasts an ideal kagome structure built on Cu^{2+} ions with S = 1/2 spins. Remarkably, herbertsmithite exhibits an absence of magnetic ordering even at extremely low temperatures, making it a subject of continuous investigation since its synthesis [Philippe Mendels et al. 2007], [T.-H. Han et al. 2012], [M. Fu et al. 2015], [Norman 2016], [Khuntia et al. 2020] which suggest the ground state is a spin liquid (gapped or gapless). It serves as the prototypical experimental specimen for ideal kagome compounds and indeed, the majority of research on kagome lattices has concentrated on herbertsmithite or related minerals searching for ideal undistorted structure like in Zn- barlowite [Tustain et al. 2020],[Y. Fu et al. 2021],[Jiaming Wang et al. 2022], kapellasite [Fåk et al. 2012] [Kermarrec, Zorko, et al. 2014] and many more.

1.5 Deviations from the Heisenberg model of spins 1/2

1.5.1 Exchange anisotropy

However, it's important to note that in real materials, the ground state is not defined by the geometry of the lattice alone. In the case of kagome systems, several deviations from the ideal model of S = 1/2 Heisenberg spins have been identified through various experimental characterizations. Herbertsmithite exhibits substitution disorder with Cu^{2+} ions in interplanar positions at approximately 10-30%, and their magnetic response can mask the intrinsic behavior of the spin physics within the macroscopic measurements. More fundamentally, they may also locally affect the underlying kagome plane and modify the magnetic model. Beyond disorder, another deviation to consider is the presence of anisotropic exchange in the Hamiltonian,

$$H = \sum_{\langle i,j \rangle} J_{i,j} \mathbf{S}_i \cdot \mathbf{S}_j + \mathbf{D}_{i,j} \cdot (\mathbf{S}_i \times \mathbf{S}_j) + \mathbf{S}_i \cdot \overline{\mathbf{A}}_{i,j} \mathbf{S}_j \tag{1.5}$$

where the sum concerns pairs of nearest neighbor spins. The first term is the isotropic exchange of the Heisenberg model. The second term is the antisymmetric anisotropic exchange, called the Dzyaloshinsky-Moriya (DM) interaction which also plays an important role in alteration of the ground state. It arises from spin-orbit coupling [Moriya 1960], and its order of magnitude is given by $D \sim (\Delta g/g)^2 J$, where Δg is the anisotropy of the Landé g-factor.

Therefore, it is of first order with the amplitude of the spin-orbit coupling. Finally, the third term represents the symmetric anisotropic exchange with the second order $A \sim (\Delta g/g)^2 J$. The DM interaction is allowed by symmetry when there is no inversion center between two spins as seen in the case of the kagome lattice [Elhajal et al. 2005]. By symmetry, the vector $\mathbf{D}_{ij}$ must belong to the median plane separating two copper atoms from the plane. There are thus three related $\mathbf{D}_{ij}$ vectors corresponding to the three sides of the triangle, with identical magnitude, having a component in the $\mathbf{D}_{ij}$ plane, D_c, and a perpendicular component D_z. Through a mean-field approach and classical Monte Carlo calculations, [Elhajal et al. 2005] have indeed shown that the disordered phase of the ideal kagome ground state becomes unstable in the presence of the DM interaction. The phase diagram obtained in the classical case reveals that the disordered liquid phase disappears as soon as a nonzero DM interaction is considered. The quantum case has been thoroughly explored through exact diagonalization [Cepas et al. 2008] and more recently by tensor network analysis [Ferrari et al. 2023]. These investigations have revealed that quantum fluctuations indeed facilitate the existence of a liquid phase even when Dzyaloshinskii-Moriya (DM) interactions ($D \neq 0$) are present. Pioneering, exact diagonalization calculations have indicated the absence of order for values of D_z/J lesser than the critical value $D_c/J \approx 0.1$. [Cepas et al. 2008] while more recent studies suggest a much lower critical value [Ferrari et al. 2023]. In one variant of Y kapellasite, $YCu_3(OH)_6Cl_3$, a DMI value of D/J $\sim$ 0.25 has been evaluated. This suggests that DMI is one of the physical properties that can be important in our materials.

1.5.2 From the ideal kagome to the distorted one

The bulk of intense research efforts in the field I have discussed so far, has primarily concentrated on the undistorted and ideal kagome lattice structure. In stark contrast, investigations into distorted versions of this lattice have received considerably less attention, despite the fact that such distortions are observed in many magnetic compounds. Remarkably, the physical phenomena arising from these distorted kagome lattices, such as volborthite [H. Yoshida et al. 2012], [Janson et al. 2016],[Ishikawa et al. 2015],[Watanabe et al. 2016], which exhibits rich field induced physics, and the family of $(Cs,Rb)_2Cu3(Ti,Sn,Zr,Hf)F12$ [Matan et al. 2010], [Markus Müller and B. G. Müller 1995], [Grbić et al. 2013], [Downie et al. 2015], which displays a variety ranging from a pinwheel valence bond solid ground state to order-disorder transitions, could potentially be as intricate and diverse as those observed in the standard kagome lattice. To the particular context of this thesis, it is important to discuss the anisotropic kagome model which is relevant for Y- kapellasite.

1.5.3 Anisotropic kagome model

Motivated by the discovery of the Y-kapellasite compounds that we study in this thesis, an unexplored anisotropic kagome model has been investigated theoretically, consisting of three distinct symmetry-inequivalent nearest-neighbor antiferromagnetic Heisenberg couplings, denoted as J, J', and $J_{\hexagon}$ [Hering et al. 2022]. They correspond

to the 3 inequivalent distances in the distorted kagome network, shown in 1.5 (a). If all exchange couplings satisfy the condition $J = J' = J_{\hexagon}$ [Hering et al. 2022], it indeed brings us back to the standard undistorted nearest-neighbor kagome model, which we've discussed previously. All the couplings are considered to be antiferromagnetic hence positive, in accordance with the Heisenberg hamiltonian shown in equation-1.1. The distortion introduces a break in translational symmetry, resulting in a periodic structure that can be described as a triangular lattice. This lattice unit cell consists of nine sites, as depicted in Figure-1.5(a). In this figure, one can see the presence of two distinct sublattices, labeled as A and B, within the unit cell. These sublattices, A and B, are not connected by point group symmetries, making them unique and separate from each other. Sublattice A encompasses the six sites linked by $J_{\hexagon}$, coinciding with the vertices of the red hexagons. In contrast, sublattice B consists of the remaining sites. It's noteworthy that the exchange couplings J and J' can be interchanged through reflection across the $\vec{a}_1$ axis.

Through the analysis of the associated Heisenberg model and the variation of its two coupling ratios, the study reported in [Hering et al. 2022] employs both analytical arguments and numerical techniques to investigate the phase diagram of the ground state. At the classical level, the model displays a rich phase diagram, offering intriguing possibilities for the exploration of unique magnetic phenomena. Significantly, within the phase diagram, large regions are characterized by a coplanar spin state with a commensurate magnetic wave vector $\vec{Q} = \left(\frac{1}{3}, \frac{1}{3}\right)$. In this ordered state, the magnetic unit cell expands beyond the crystallographic unit cell, encompassing 27 atoms. Furthermore, an extensive region around the standard undistorted kagome lattice exhibits a complex classical spin liquid phase. The classical ground-state phase diagram for the distorted kagome lattice, governed by the Heisenberg model, established by exploring the ratios $\frac{J}{J_{\hexagon}}$ and $\frac{J'}{J_{\hexagon}}$, is constructed using a iterative minimization techniques and classical Monte Carlo simulations [Hering et al. 2022]. Although discussing the methodology is beyond the scope of this dissertation, I would like to discuss the evaluation of the phase boundaries from the arguments mentioned in [Hering et al. 2022] and also in [Bilitewski, Zhitomirsky, and Moessner 2017], where a related bond disorder model was investigated. The Heisenberg hamiltonian modified by considering the parameters $\gamma_{i\Delta} = \sqrt{\frac{J_{ij}J_{ik}}{J_{jk}}}$, where i, j and k are spins in the triangle Δ , is rewritten as,

$$H = \frac{1}{2}\sum_{\Delta} \vec{L}_{\Delta}^2 + constant \tag{1.6}$$

where $\vec{L}_{\Delta}$= $\sum_{i\in\alpha} \gamma_{i\Delta}\vec{S}_i$, which generates a bond dependent interaction model with exchange couplings J_{ij} = $\gamma_{i\Delta}$ $\gamma_{j\Delta}$ between two spins of the same triangle Δ. In the context of the anisotropic kagome lattice illustrated in Figure 1.5, where the Heisenberg exchange interactions are denoted as J, J', and $J_{\hexagon}$, the local constraint L_{Δ} is expressed as follows:

$$\vec{L}_{\Delta} = \sqrt{\frac{J'J}{J_{\hexagon}}}\vec{S}_i + \sqrt{\frac{JJ_{\hexagon}}{J'}}\vec{S}_j + \sqrt{\frac{J'J_{\hexagon}}{J}}\vec{S}_k \tag{1.7}$$

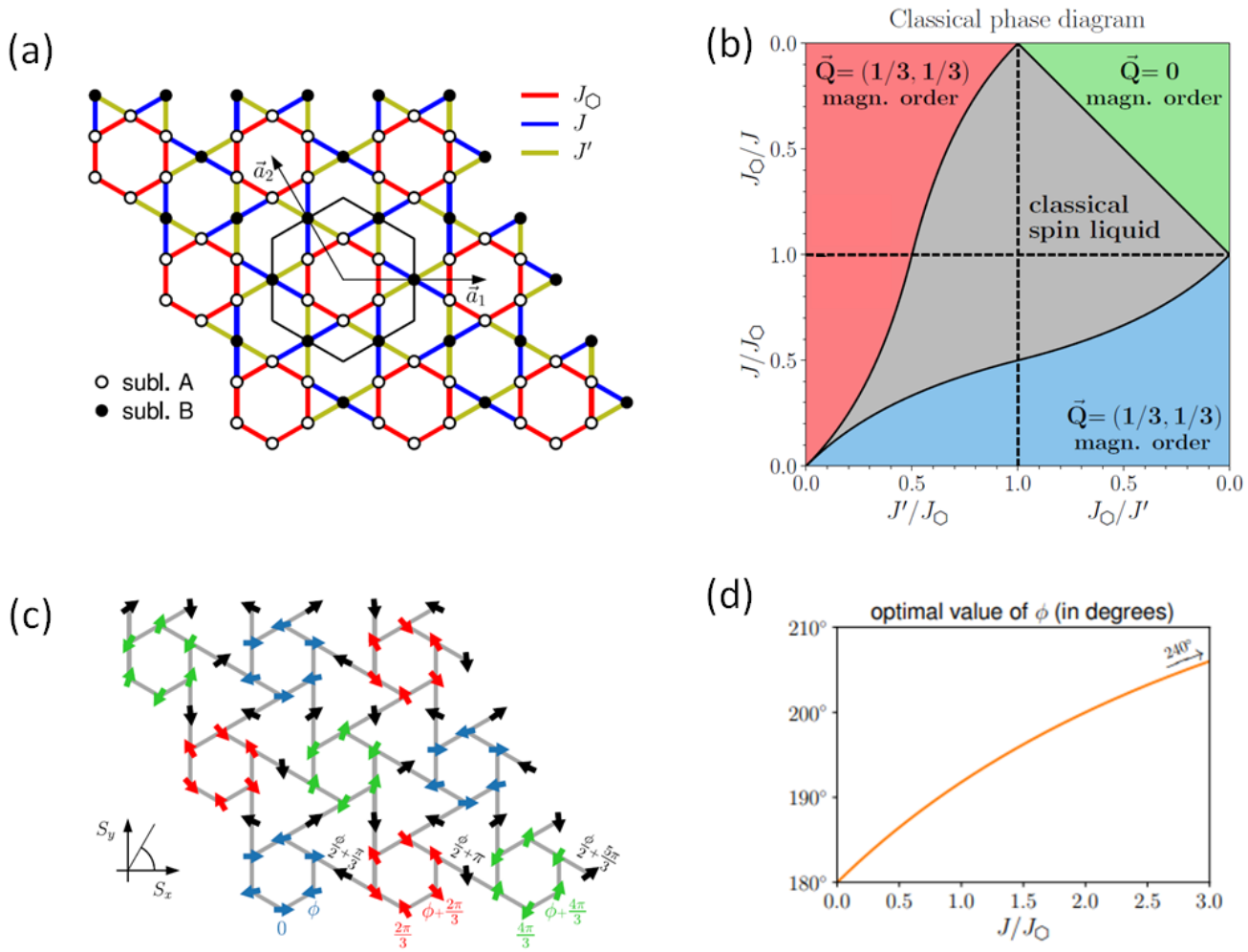

Figure 1.5: (a) A schematic illustration of the three exchange couplings characterizing the effective Heisenberg Hamiltonian for an anisotropic kagome lattice, denoted as J, J', and $J_\bigcirc$ adapted from [Hering et al. 2022]. The Hamiltonian of the system exhibits periodicity under translations along the Bravais vectors $\vec{a}_1$ and $\vec{a}_2$. The sites within the unit cell are divided into two sublattices: sublattice A (hollow symbols) and sublattice B (solid symbols). (b) The classical phase diagram of the distorted kagome model exhibits symmetry under the exchange of the axes (i.e., J $\leftrightarrow$ J') due to the Hamiltonian's inherent symmetry. The magnetic order with $\vec{Q} = \left(\frac{1}{3}, \frac{1}{3}\right)$ is observed in the red region and is related to the $\vec{Q} = \left(\frac{1}{3}, \frac{1}{3}\right)$ order observed in the blue region through a mirror reflection with respect to $\mathbf{a_1}$. Within the gray area of the phase diagram, the system features a classical spin-liquid phase with degenerate non-coplanar ground states. The $\vec{Q} = \mathbf{0}$ magnetic order can be visualized as parallel spins on the same sublattice, whereas spins on different sublattices are anti-aligned. (c) Spin texture for the classical $\vec{Q} = \left(\frac{1}{3}, \frac{1}{3}\right)$ order for $J > J'$. The spin orientations are determined by the angle ϕ between neighboring spins in the perfect hexagon. In this figure ϕ is taken for the case $J' = 0$ and $J_\bigcirc = J$). The spins are arranged in the xy-plane, and their orientation is represented by the angle with respect to the S_x axis. (d) Optimal value of the angle ϕ for the $\vec{Q} = \left(\frac{1}{3}, \frac{1}{3}\right)$ magnetic order as a function of the $J/J_\bigcirc$ ratio (in the considered limit of $J' = 0$).

Equation (1.6) provides a crucial insight: any spin configuration that satisfies the condition $\vec{L_\Delta} = 0$ for all the triangles Δ qualifies as a ground state of the system. Nevertheless, the specific values of the couplings J, J', and $J_\bigcirc$ can lead to a scenario where, for certain triangles, one term on the right-hand side of Equation (1.7) becomes overwhelmingly dominant, making it impossible to compensate with the other two terms. When considering an

isolated triangle, $\vec{L_\Delta} = 0$ is only possible if

$$\frac{J}{J_\hexagon} \leq \frac{J'}{J' - J_\hexagon}, \quad J' \leq \min(J, J_\hexagon) \tag{1.8}$$

$$\frac{J}{J_\hexagon} \geq \frac{J'}{J' + J_\hexagon}, \quad J \leq \min(J', J_\hexagon) \tag{1.9}$$

$$\frac{J}{J_\hexagon} \geq \frac{J'}{J_\hexagon - J'}, \quad J_\hexagon \leq \min(J', J) \tag{1.10}$$

These conditions serve as the defining criteria for the phase boundaries as illustrated in Figure-1.5(b). In regions where an isolated triangle can meet the conditions described by equations (1.8), (1.9), and (1.10), a classical spin-liquid phase emerges (grey area in the phase diagram). However, it's important to note that while satisfying $\vec{L}_\Delta = 0$ in an isolated triangle is possible, achieving $\vec{L}_\Delta = 0$ in each individual triangle of the entire system is not necessarily straightforward. The study conducted by [Bilitewski, Zhitomirsky, and Moessner 2017] examined this thoroughly and demonstrated that $\vec{L}_\Delta = 0$ can indeed be satisfied for all triangles in bond-disordered systems, a result reaffirmed by [Hering et al. 2022] for the disorder-free model. Moreover, they revealed the existence of global ground states where each triangle can adopt up to two potential spin configurations that satisfy the local condition of $\vec{L}_\Delta = 0$. In general cases, this results in an extensive phase that is distinct from the isotropic kagome and boundary cases. This phase consists of discretely degenerate classical ground states characterized by non-coplanar spin configurations. These states are not connected by soft modes and are referred to as a "jammed spin liquid phase".

Conversely, in regions where an isolated triangle cannot satisfy the condition $\vec{L_\Delta} = 0$ due to large disparity between bond lengths, the system adopts one of the coplanar phases, either with $\vec{Q} = (\frac{1}{3}, \frac{1}{3})$ order, or the colinear $\vec{Q} = 0$ order. However, even in cases where $\vec{L_\Delta} = 0$ is violated, the Hamiltonian (equation- 1.7) still implies with the condition of $(\vec{L_\Delta})^2$ should be minimized. Following [Hering et al. 2022], we consider the simple case $J' = 0$ where $\vec{Q} = \left(\frac{1}{3}, \frac{1}{3}\right)$ long range order is realised. In this limit the model is characterized by a lattice composed of hexagons, which are formed by sublattice A sites. The hexagonal units are interconnected via J-trimers, which involve sublattice B sites, as illustrated in Figure-1.5(c). The central spin within each trimer is constrained to align in the direction opposite to the cumulative orientation of the edge spins. This configuration leads to the magnetic order observed along the $J' = 0$ line, as schematically depicted in Figure-[1.5(c)]. Within a single unit cell, the spins on sublattice A exhibit an alternating pattern around the symmetric $J_\hexagon$-hexagons. The spins on even and odd sites in this sublattice align ferromagnetically in two distinct directions, each rotated by an angle ϕ. In contrast, the spins on sublattice B, which are two-coordinated, are uniquely determined by the angle ϕ. Consequently, in the $J' = 0$ limit, we can express the classical energy per site for the $\vec{Q} = \left(\frac{1}{3}, \frac{1}{3}\right)$ ordered state as a function of ϕ, as shown by:

$$E/N = \frac{2}{3}[J_{\hexagon}\cos(\phi) + J\cos(\frac{\phi}{2} + \frac{\pi}{3})] \tag{1.11}$$

The optimal angle ϕ obtained from minimization changes weakly with the strength of the hexagon interactions (shown in figure-1.5): In the strong hexagon limit, where $J \ll J_{\hexagon}$, the optimal angle ϕ is π, whereas in the trimer limit, where $J \gg J_{\hexagon}$, the optimal angle ϕ is $\frac{4\pi}{3}$. Beyond J'=0 case, the $\vec{Q} = \left(\frac{1}{3}, \frac{1}{3}\right)$ order persists within the boundaries of the phase diagram. In this region, numerical minimization of the classical energy confirms that the spin arrangement remains coplanar and similar to what was previously explained for J'=0 and depicted in figure-1.5(c). The orientation of the spin texture in this region continues to be governed by the angle ϕ.

As previously mentioned, it's important to emphasize that the phase diagram remains unchanged when swapping the roles of J and J'. In the vicinity of the $J = 0$ limit, denoted by the blue area in Fig-[1.5](b), we still observe a corresponding $\vec{Q} = \left(\frac{1}{3}, \frac{1}{3}\right)$ order. These two phases, characterized by $\vec{Q} = \left(\frac{1}{3}, \frac{1}{3}\right)$, can be mapped onto each other through a mirror reflection with respect to the $\vec{a}_1$ axis. Finally when $J_{\hexagon} \ll J, J'$, the system transitions out of its frustrated state, as each neighboring A site is connected to a B site and vice versa. This results in the ground state adopting a simple collinear configuration with $\vec{Q} = 0$ (indicated in green on the phase diagram), where the two sublattices have opposite spin orientations.

The primary focus of this thesis revolves around the exploration of the yet unexplored distorted kagome lattice, as exemplified by the recently synthesized variants of herbertsmithite, namely $Y_3Cu_9(OH)_{19}Cl_8$ and $Y_3Cu_9(OH)_{19}Br_8$, which exhibit three distinct bond lengths within the kagome network,it is important to delve briefly into the background and origins of these intriguing compounds.

1.6 Doping attempts of herbertsmithite

In 1987, a significant breakthrough followed the discovery of high critical temperature superconducting cuprates by Bednorz and Müller in 1986 [Bednorz and K. A. Müller 1986]. At that time, Anderson proposed a fascinating connection between his earlier concept of the resonating valence bond (RVB) state, which he had formulated in 1973 [Anderson 1973], and the formation of Cooper pairs in these groundbreaking materials. Anderson's proposition went beyond the conventional BCS theory and became a subject of great interest (Chapter 1). The idea that a liquid state of spins could be the fundamental state, particularly under the influence of doping, leading to the emergence of a superconducting state, has since drawn the attention of researchers, leading to numerous theoretical investigations. Of particular note is the possibility of a spin liquid state, with an excitation spectrum lacking a gap, which may give rise to a "d-wave" superconducting state featuring nodal quasi-particles [P. A. Lee, Nagaosa, and Wen 2006]. For a considerable time, the search for spin liquids in experimental settings yielded no success, making it challenging to validate theoretical predictions. However, recent progress has shed light on the ground state of herbertsmithite,

revealing it to be a spin liquid ground state gapless [Khuntia et al. 2020] or paritally gapped [Jiaming Wang et al. 2021]. This breakthrough has opened up new avenues for investigating the effects of doping in the system through the substitution of monovalent or trivalent ions for zinc ions, as depicted in Figure-10.1.

Doping a kagome system offers the potential to access various exotic states beyond superconductivity. The tight binding approach reveals that the electronic band structure associated with the kagome network exhibits Dirac nodes at filling $n = \frac{4}{3}$ (electron doping) and a flat band at filling $n = \frac{2}{3}$ (hole doping). Through various numerical methods, it has been proposed that materials like $LiCu_3(OH)_6Cl_2$ (Li-herbertsmithite, hole-doped with monovalent lithium ions, $n = \frac{2}{3}$) and $GaCu_3(OH)_6Cl_2$ (Ga-herbertsmithite, electron-doped with trivalent gallium ions, $n = \frac{4}{3}$) may exhibit topological insulator behavior with metallic surface states [Guterding, Valenti, and Jeschke 2016]. Additionally, a slightly under-doped version of $GaCu_3(OH)_6Cl_2$ ($Ga_xZn_{1-x}Cu_3(OH)_6Cl_2$, with x close to 1) has the potential to become an "f-wave" superconductor [Mazin et al. 2014]. These exciting theoretical prospects offer intriguing avenues for exploring exotic phenomena in the context of doping kagome systems.

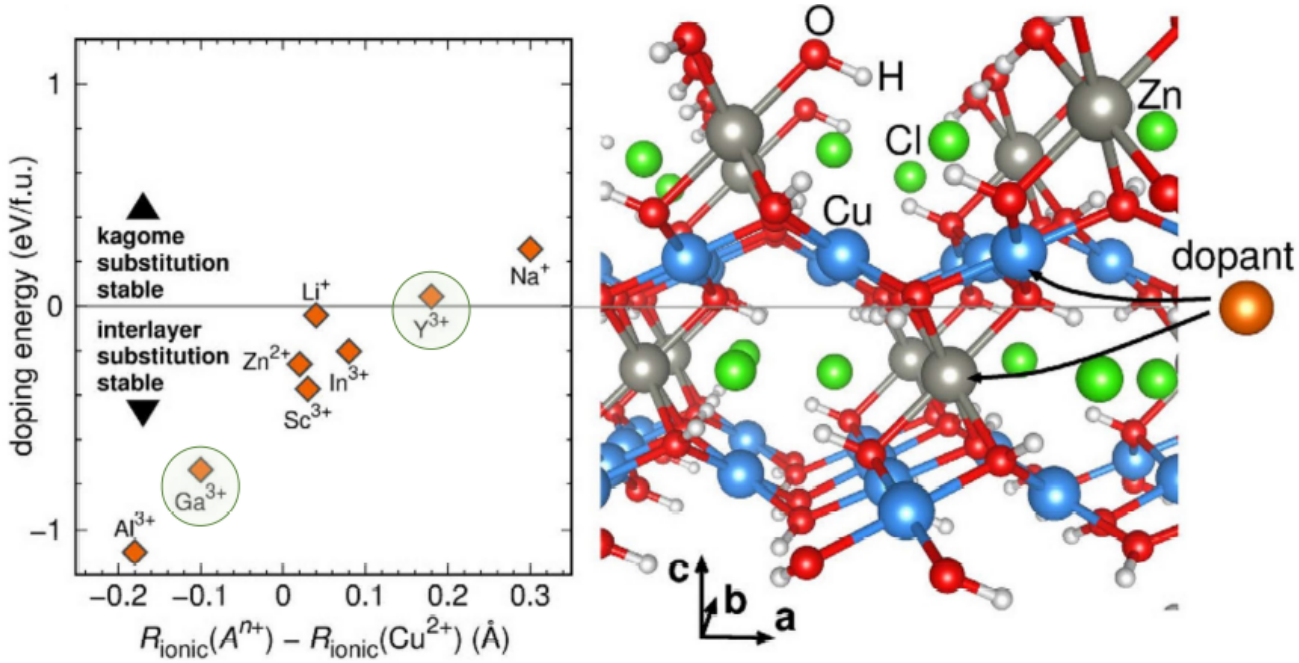

Figure 1.6: Doping Energies for Herbertsmithite: The points above the line, which correspond to zero energy, indicate that the lattice will be distorted under the effect of doping. The dopants of small ionic radius should preferably be located on the interplanar sites of Herbertsmithite. Shown in reference-[Guterding, Valenti, and Jeschke 2016].

Unfortunately, all attempts to introduce doping into herbertsmithite have proved unsuccessful thus far. Initially, the technique of choice was the topochemical intercalation of lithium ions into the structure, resulting in the synthesis of compounds with the formula $ZnLi_xCu_3(OH)_6Cl_2$ ($x \leq 1.8$) (n = 8/5) [Kelly, Gallagher, and McQueen 2016]. More recently, efforts focused on synthesizing compounds with the formula $Ga_xCu_{4-x}(OD)_6Cl_2$ ($x \leq 0.8$) (n = 4/3.2) [Puphal, Ranjith, et al. 2019]. Although these systems are all exhibiting insulating behaviour and this insulating behavior observed in these doped systems can be plausibly attributed to the distinctive chemistry of the investigated

kagome materials, particularly halogenated copper hydroxides [Qihang Liu et al. 2018]. This unique geometry may impede the delocalization of excess charge, leading to the formation of self-trapped polarons. Despite the challenges posed by these dopants, the synthesized compounds remain of significant scientific interest, as they serve as magnetic models closely resembling herbertsmithite. Further investigations of these systems in a more generalized manner can provide valuable insights into the effects of specific disturbances and help elucidate intrinsic properties relevant to the $HAQK$ model. In this experimental study, we investigate compounds obtained through attempts to introduce yttrium ions (Y^{3+}) into herbertsmithite by substituting them for zinc ions. These compounds also remain insulating but with different structures. They follow the generic formula $YCu_3(OH)_{6+x}X_{3-x}$, where X can be either chlorine ($Y_3Cu_9(OH)_{19}Cl_8$) or bromine ($Y_3Cu_9(OH)_{19}Br_8$). Detailed introductions to these materials will be provided in the opening sections of both Part-A and Part-B of the thesis.

Chapter 2

Principles of Local Techniques: NMR and μSR Spectroscopies

In this study, we have employed a diverse set of experimental methodologies to thoroughly investigate the electronic properties of quantum kagome materials. This comprehensive exploration covers a spectrum of approaches, including the analysis of macroscopic susceptibilities using SQUID measurements, the characterization of specific heat through PPMS (Physical Property Measurement System) measurements, the examination of structural and magnetic lattice structures using neutron diffraction, and most extensively the investigation of the interplay between static and dynamic magnetic phenomena at a local scale, within mere angstroms of the nucleus or muon probe which has been facilitated by the application of pulsed nuclear magnetic resonance (NMR) and muon spin rotation and relaxation (μSR) techniques. In the upcoming sections, a detailed exploration of NMR and μSR techniques will be provided. These techniques serve as critical tools for the intrinsic evaluation of distorted kagome compounds, enabling us to gain a comprehensive understanding of their underlying kagome ground states.

2.1 Pulsed Nuclear Magnetic Resonance (NMR)

Since its discovery in 1946 by Bloch and Purcell [Bloch 1946,Edward M Purcell, Torrey, and Pound 1946], Nuclear Magnetic Resonance (NMR) has evolved into a versatile investigative tool, stretching its influence beyond the confines of physics to various domains such as chemistry and medicine. Notably, NMR has gained recognition for its pivotal roles in both organic chemistry analysis and medical imaging (MRI). Operating as a spectroscopic technique, it delves into the immediate atomic surroundings by scrutinizing nuclear spins. In the realm of solid-state physics, NMR's efficacy lies in its capability to evaluate the influence of the local magnetic environment on nuclear spins, offering valuable insights into magnetism at the angstrom scale. When a population of nuclear spins encounters

a static magnetic field and periodic excitation, it responds most strongly at a distinct field-dependent excitation frequency, a phenomenon known as Nuclear Magnetic Resonance (NMR). The resonance conditions linked to specific nuclei undergo adjustments based on the magnetic environment encompassing them.

In the arena of condensed matter, NMR investigates local electronic magnetism within a range roughly on the order of a few angstrom around the probed nucleus. This exploration relies on hyperfine interactions between nuclear and electronic spins. The overarching objective of this section is to provide an introduction to the phenomenon of nuclear magnetic resonance, followed by an exploration of local interactions with electrons and their implications on resonance behavior.

2.2 Zeeman effect and nuclear magnetic resonance phenomenon

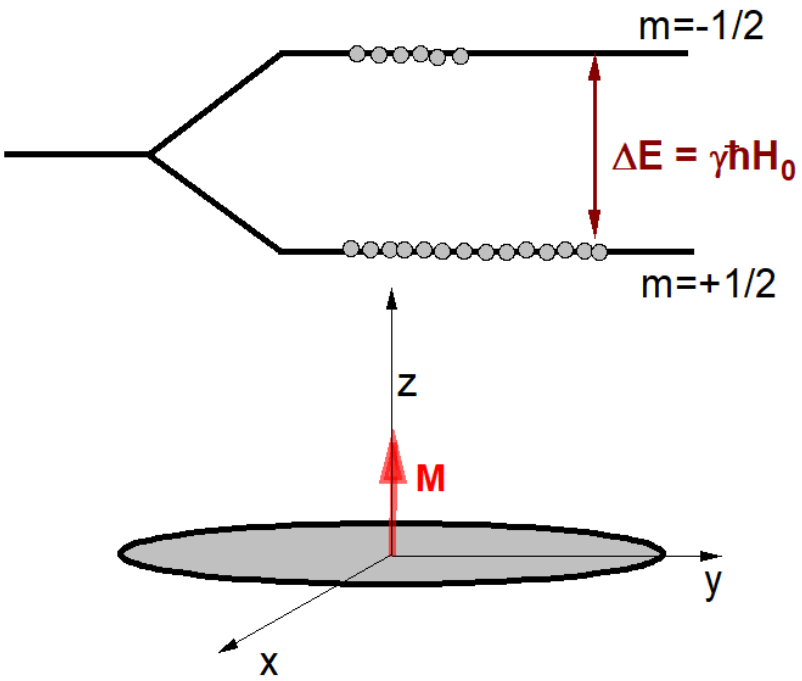

Figure 2.1: When a spin with $I = \frac{1}{2}$ is subjected to an external magnetic field along the z-axis, the occupation of energy levels at equilibrium gives rise to magnetization aligned with the z-axis, hence a finite component of magnetization along the z-axis exists denoted as **M**.

The core principle underpinning the nuclear magnetic resonance (NMR) technique is rooted in the Zeeman effect. Consider a nucleus possessing a nuclear spin vector $\vec{I}$ and an associated magnetic moment $\vec{\mu} = \gamma\vec{I}$, where γ represents the nuclear gyromagnetic ratio. The Zeeman Hamiltonian $\mathcal{H}$, which characterizes the energy of this magnetic moment in the presence of a magnetic field along the z-axis ($\vec{H} = H_0\vec{e}_z$), can be formulated as:

$$\mathcal{H} = -\vec{\mu} \cdot \vec{H} \tag{2.1}$$

$$\text{and} \quad \mathcal{H} = -\gamma\hbar H_0 I_z \tag{2.2}$$

The corresponding 2I+1 energies corresponding to this Hamiltonian are:

$$E_m = -\gamma\hbar H_0 m \quad \text{with} \quad m = -I, -I+1, \ldots, I-1, I \tag{2.3}$$

The introduction of a magnetic field serves to break the degeneracy among these energy levels, revealing their equally spaced energy intervals. The energy difference between consecutive levels defines the resonance energy $E = \gamma\hbar H_0$, thus establishing the nuclear resonance frequency $\nu_0 = \gamma H_0/(2\pi)$. By exciting the system at this specific frequency, transitions between energy levels are induced. Consequently, NMR functions as a resonant spectroscopic technique, enabling the determination of energy gaps between nuclear levels by subjecting nuclei to electromagnetic frequencies ν. During an NMR experiment, one can opt to keep either the magnetic field $H = H_0$ or the frequency $\nu = \nu_0$ constant, and then progressively vary the irradiating frequency or the magnetic field until the resonance condition is fulfilled. Both approaches were employed across various temperature ranges,in this thesis.

When dealing with a macroscopic sample, the population of the various Zeeman energy levels conforms to the Boltzmann distribution.

In the absence of an external magnetic field, the macroscopic nuclear magnetization remains null in the paramagnetic state. Yet, upon introducing a magnetic field H_0 aligned with the z-axis, the nuclear magnetization develops along the field direction, (refer to Figure 2.1). The magnetization M_z can be presented as, following the Curie's law:

$$M_z = \frac{N_0(\gamma\hbar)^2 I(I+1)}{3k_B T} H_0 \tag{2.4}$$

It's worth noting that different atomic nuclei exhibit specific gyromagnetic ratios, which reflect their response to external magnetic fields. The hydrogen nucleus stands out with the highest nuclear gyromagnetic ratios ($\frac{\gamma_H}{2\pi} = 42.57$ MHz/T), while the gold nucleus exhibits one of the lowest values ($\frac{\gamma_{\mathbf{Au}}}{2\pi} = 0.729$ MHz/T). It's noteworthy that these nuclear gyromagnetic ratios are significantly weaker in comparison to the gyromagnetic ratio of the electron, denoted as γ_e. For instance, in the context of a proton, the quantity $(\gamma_\mu/\gamma_e)^2 \sim 10^{-6}$, highlighting that nuclear magnetization is roughly a million times weaker than electronic magnetization. This stark contrast underscores the need for highly sensitive electronics in detecting NMR signals, as NMR experiments often contend with a relatively low signal-to-noise ratio. This signal is directly proportional to the nuclear magnetization M, implying that its amplitude becomes increasingly substantial with higher magnetic field strengths and lower temperatures as indicated in Equation 2.4.

2.3 Local interactions

The purpose of this section is to lay the groundwork for understanding the measurements carried out using NMR, which will be applied to experimental systems discussed in subsequent chapters of this manuscript. The initial part of this section delves into the theoretical description of interactions involving nuclear spins and their surrounding environment. This theoretical foundation is then connected to practical experimental measurements, explaining NMR resonance spectra and relaxation, in typical scenarios. For a more comprehensive understanding, readers can refer to sources such as [Abragam 1961], [Slichter 2013], and [Cohen and Reif 1957] for detailed insights into NMR principles.

Nuclear spin interaction with an electron

These interactions can be broadly categorized into two primary types. The first type is magnetic, associated to the interaction with the spin of the adjacent electrons, which holds significance for both NMR and μSR investigations. The second type arises from electrostatic effects resulting from the gradient of the local electric field for nuclei I $> 1/2$, a factor particularly pertinent to NMR studies. The comprehensive description of these interactions is encapsulated within the nuclear Hamiltonian denoted as $\mathcal{H}$:

$$\mathcal{H} = \mathcal{H}_m + \mathcal{H}_q \tag{2.5}$$

where, the magnetic hyperfine Hamiltonian is denoted as $\mathcal{H}_m$, while the quadrupole Hamiltonian is represented by $\mathcal{H}_q$.

Magnetic Hyperfine Hamiltonian

Let's consider a particle, whether it's a nucleus or a muon, possessing a spin vector $\mathbf{I}$ with a gyromagnetic ratio γ. This particle interacts with an electron, described by its spin vector $\mathbf{S}$, orbital moment vector $\mathbf{L}$, gyromagnetic ratio γ_e, and positioned at $\mathbf{r}$. The first-order Hamiltonian H_m, as deduced from calculations [Abragam 1961], is formulated as follows:

$$H_m = -\hbar^2\gamma\gamma_e \left[\frac{3(\vec{I}\cdot\vec{r})\cdot(\vec{I}\cdot\vec{r}) - \vec{I}\cdot\vec{S}r^2}{r^5} + \frac{\vec{I}\cdot\vec{L}}{r^3} + \frac{8\pi}{3}\vec{I}\cdot\vec{S}\delta(\vec{r}) \right] \tag{2.6}$$

The comprehensive Hamiltonian equation-2.6 encompasses a range of contributions originating from diverse sources, as outlined below:

(a) Dipole Hamiltonian: The first term describes the dipole field produced by the surrounding electron located in the orbital of the same atom as the nucleus on further away in the structure. This interaction is characterized by

its anisotropic nature and its relatively weak strength.

(b) Orbital Hamiltonian: The following term corresponds to the magnetic field arising from orbital motion, generated as electrons orbit around their respective nuclei. This term accounts for both the orbital contribution of unpaired electrons, which can often be neglected in initial approximations for ions of the 3d shell with quenched orbital moments, and the impact of paired electrons, which arises due to the distortion of electron shells induced by an externally applied magnetic field. This coupling remains weak, anisotropic, and temperature-independent.

(c) Contact Hamiltonian: Finally, the concluding term arises from the contact interaction, which results from the overlap of electron orbitals with the nuclear spin. This phenomenon is characterized by the presence of the Dirac delta distribution $\delta(\vec{r})$. In the context of NMR, this aspect primarily concerns s-electron orbitals with non-zero density at the nucleus site. Notably, this term can persist even when these orbitals are fully occupied, particularly in cases involving polarization transfer from other electron orbitals (referred to as core polarization). This interaction, if present, is generally dominant and isotropic. Although the Hamiltonian terms match between the two techniques μSR and NMR, the distinct characteristics of muons and nuclei introduce a nuanced perspective. In the context of NMR, a more localized viewpoint prevails, given the prevailing coupling terms arising from orbital overlaps.
To sum up, these combined terms effectively characterize the local magnetic field $\vec{H}_{\text{loc}}$, generated by the surrounding environment and interrogated by the nucleus via its magnetic moment $\vec{\mu}$. When an external magnetic field, referred to as the Zeeman field $\vec{H}_0$, is introduced, the magnetic Hamiltonian can be expressed as:

$$\mathcal{H}_m = -\vec{\mu} \cdot (\vec{H}_0 + \vec{H}_{\text{loc}}) \tag{2.7}$$

In situations where the thermodynamic limit applies, it is commonly assumed that the fluctuations of the local field occur at a much faster rate compared to the characteristic observation time. In such cases, the mean-field theory is often employed. It consists in neglecting the fluctuations and enable simplifications. This is exemplified by:

$$\vec{H}_{\text{loc}} = \langle \vec{H}_{\text{loc}} \rangle + (\vec{H}_{\text{loc}} - \langle \vec{H}_{\text{loc}} \rangle) \approx \langle \vec{H}_{\text{loc}} \rangle \tag{2.8}$$

Thus, in this approximation, the local field is treated as time-independent, aligning with the framework of 'static' measurements, i.e measurements of the spectra. However, the fluctuations can be experimentally observed and will be the focus of the dynamic investigations presented later.
This average local field, as it is responsible for shifting the resonance value relative to the anticipated value for the applied magnetic field. In a paramagnetic regime, this shift is precisely quantified by the hyperfine displacement tensor $\overline{K}$, defined by the equation

$$\vec{H}_{\text{loc}} = (\overline{K} + \overline{\sigma})\vec{H}_0 \tag{2.9}$$

This tensor $\overline{K}$ corresponds the temperature-dependent local spin susceptibility. The tensor $\bar{\sigma}$ characterizes the temperature independent chemical shift attributed to the orbital contribution from full layers. When examining a particular direction α of the applied field, the aforementioned equation is simplified into a scalar form, where the change in displacement K_α is directly connected to the variation in local susceptibility χ_{local} assumed here to be isotropic for simplicity which arises solely from the surrounding electrons through the relationship:

$$K_\alpha = \frac{A_{\text{hf}}^\alpha}{N_A \mu_B} \chi_{\text{local}} \tag{2.10}$$

This equation involves the hyperfine temperature independent tensor component A_{hf}^α. expressed in T/μ_B and which encloses the various hyperfine mechanism discussed previously. These hyperfine constants can be determined experimentally if the local susceptibility matches the macroscopic susceptibility measured by SQUID within a certain temperature range i.e., if there is a linear relation between *K* and χ_{SQUID}. The significance of this equation lies in its implication that, even for the same nuclear site, an inhomogeneous magnetic environment and hyperfine couplings of varying magnitudes can substantially modify the line shape. In this context, NMR serves as an excellent technique for probing such inhomogeneous magnetic environments, offering insights that differ from macroscopic measurements that aggregate the responses of all magnetic contributions.

Quadrupolar Hamiltonian

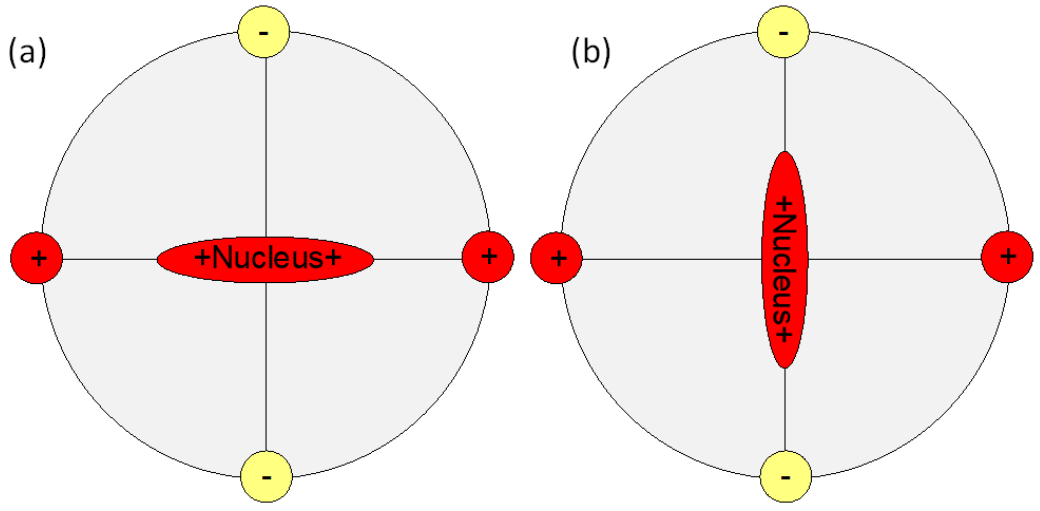

Figure 2.2: An ellipsoidal-shaped nucleus with a positive charge is situated amid two positive charges and two negative charges. Energetically, configuration (a) is less favorable compared to configuration (b) This phenomenon is absent when the nucleus assumes a spherical shape.

The next interaction to consider is the electrostatic interaction between the charges present in the surrounding environment, carried by neighboring atoms, and the charge of the nucleus itself. To illustrate this interaction, let's

consider an example of a nucleus with a non-isotropic positive charge density that is surrounded by four point charges $\pm q$ (as depicted in Fig-2.2). In this scenario, configuration (b), where the charge density extends along the axis formed by the two negative charges, is more favorable from an electrostatic standpoint. This example also aids in understanding that this interaction doesn't exhibit a preference for any particular orientation when dealing with an isotropic spherical charge density, a characteristic that holds true for nucleus with a spin of $1/2$.

Now, we will derive the classical expression for the quadrupole Hamiltonian. Let $\rho(\mathbf{r})$ be the electric charge density of the particle and $V(\vec{r})$ be the electric potential generated by the surrounding environment. The energy E_{q} associated with the electrostatic interaction between the nucleus and its surrounding environment can be expressed as:

$$E_{\mathsf{q}} = \int \rho(\vec{r}) V(\vec{r})\, d^3r \tag{2.11}$$

By developing the potential V in a series at the center of charge ($\vec{r} = \vec{0}$), we obtain:

$$E_{\mathsf{q}} = ZeV_0 + \sum_j P_j \left(\frac{\partial V}{\partial x_i}\right)_{\mathbf{0}} + \frac{1}{2}\sum_{i,j} Q_{ji} \left(\frac{\partial^2 V}{\partial x_j \partial x_i}\right)_{\mathbf{0}} + \dots \tag{2.12}$$

where P_j is the electric dipole moment and Q_{ij} is the (i, j) component of the quadrupolar moment tensor.

$$P_j = \int Z\rho(\vec{r}) x_j\, d^3r \quad \text{and} \quad Q_{ji} = \int Z\rho(\vec{r}) x_j x_i\, d^3r \tag{2.13}$$

The constant term is not of primary concern as we are primarily focused on energy shifts, so we will omit this term in our subsequent discussions. In cases of ellipsoidal symmetry where $\rho(\vec{r}) = \rho(-\vec{r})$, the first-order dipole term (P_j) is null, as corroborated by experimental observations for the neutron [Smith, E. Purcell, and Ramsey 1957]. By truncating the expansion at the second order, only the quadrupole interaction persists. This yields the following expression for the quadrupole Hamiltonian:

$$H_{\mathsf{q}} = \frac{1}{2}\sum_{i,j} Q_{ij} V_{ij}, \quad \text{with} \quad V_{ij} = \frac{\partial^2 V}{\partial x_i \partial x_j} \tag{2.14}$$

The electrostatic energy of the system is determined by the components of the quadrupole tensor Q_{ij}, which in turn relies on the geometric arrangement of the nucleus. There are two specific circumstances under which this interaction becomes null:

1. When a spherical charge density $\rho(r)$ is present, resulting in $Q_{ji} = 0$. This condition is characteristic of particles with spin $\frac{1}{2}$, such as the ^{1}H, F or the muon discussed later in this chapter.

2. When the electric field gradient V_{ij} evaluated at the particle's position is zero. This situation is often encountered in cases of cubic symmetry, as seen for instance in the face-centered cubic structure of metallic sodium.

In our subsequent NMR investigations, we primarily focused on ^{35}Cl and ^{81}Br nuclei, possessing a spin $I = 3/2$,

which implies susceptibility to quadrupole effects. In this study, these effects can be treated as perturbations relative to the prevailing Zeeman effect. It can be demonstrated that Equation 2.14 can be reformulated using the principle axis of the tensor $\overline{V}$ [Slichter 2013]:

$$H_{\mathsf{q}} = \frac{eQ}{4I(2I-1)} \left[V_{zz}(3I_z^2 - I^2) + (V_{xx} - V_{yy})(I_x^2 + I_y^2) \right] \tag{2.15}$$

In this equation, $Q = \frac{1}{e} \int \rho(\vec{r})(3z^2 - r^2)\, d^3r$ represents the constant linked with the electric quadrupole moment, serving as a measure of the charge density's departure from spherical symmetry. The components of the tensor $\overline{\mathbf{V}}$ are interconnected through the Poisson equation $\Delta\overline{\mathbf{V}} = \overline{\mathbf{V}}_{xx} + \overline{\mathbf{V}}_{yy} + \overline{\mathbf{V}}_{zz} = 0$, thus necessitating only two components for a complete description. We can then opt for two experimentally ascertainable parameters: the asymmetry parameter η, reflecting the level of asymmetry within the (x, y) plane, and the quadrupole frequency ν_q, signifying the magnitude of quadrupole effects:

$$\eta = \frac{V_{xx} - V_{yy}}{V_{zz}} \tag{2.16}$$

$$\nu_q = \frac{3eQV_{zz}}{2I(2I-1)h} \tag{2.17}$$

In the convention where the principal axes of the electric field gradient tensor $\overline{\mathbf{V}}$ are oriented such that $|V_{zz}| \geq |V_{yy}| \geq |V_{xx}|$, the asymmetry parameter η falls within the range $0 \leq \eta \leq 1$. This parameter provides insight into the shape of the charge distribution around the nucleus and characterizes the degree of asymmetry in the plane defined by the x and y axes.

2.4 Pulsed NMR technique

2.4.1 Excitation and relaxation

In practical terms, gauging the absorption of a spin system during resonance presents a non-trivial challenge. The predominant technique employed by most current NMR spectrometers is the "pulsed" NMR methodology. This technique revolves around the manipulation of nuclear spin magnetization through the utilization of radio-frequency pulses. The following discussion outlines this approach in a semi-classical manner.

To stimulate transitions between nuclear energy levels, an alternating magnetic field denoted as $\vec{H_1}$ is employed, oriented perpendicular to the primary applied field $\vec{H_0}$. To develop an intuitive understanding of the impact of this transverse magnetic field, we can elucidate the classical motion of the nuclear magnetic moment, denoted as $\vec{\mu}$. In the presence of the magnetic field $\vec{H_0}$, a torque is exerted on the nuclear magnetic moment $\vec{\mu}$, leading to a modification in angular momentum:

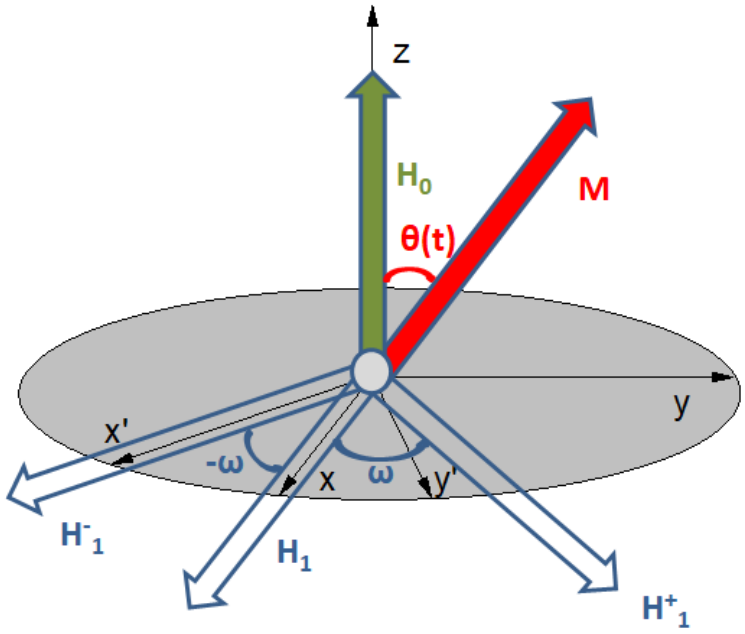

Figure 2.3: Diagram representing the effect of a magnetic field H_1 oscillating at the pulsation ω and perpendicular to H_0. In the rotating frame R', the nuclear magnetization M precesses around H_1^+, forming an angle $\theta(t)$ with the z axis.

$$\frac{d\vec{I}}{dt} = \vec{\mu} \wedge \vec{H}_0 \tag{2.18}$$

Upon multiplying this equation by the nuclear gyromagnetic factor denoted as γ, we derive equation 2.19, which corresponds to the precessional motion of this moment at the Larmor angular frequency $\omega_0 = \gamma H_0$:

$$\frac{d\vec{\mu}}{dt} = \gamma\vec{\mu} \wedge \vec{H}_0 = \vec{\mu} \wedge \vec{\omega_0}, \quad \text{where} \quad \vec{\omega_0} = \omega_0\vec{e_z} \tag{2.19}$$

The oscillating magnetic field $\vec{H}_1$, characterized by an angular frequency ω, generated by a coil aligned along the x-axis, can be deconstructed into two rotating magnetic fields, $\vec{H}_1^+$ and $\vec{H}_1^-$, with opposing angular frequencies ω and $-\omega$, respectively. Since the positively oscillating field is considerably distant from resonance, it is justifiable to disregard its influence in the subsequent discussions. The impact of the $\vec{H}_1^-$ field can be readily comprehended by delving into the rotating reference frame R', characterized by coordinates (x', y', z'). In this frame, the z'-axis aligns with the z-axis of the laboratory frame R, and it involves a rotational vector denoted as $\vec{\Omega} = -\omega\vec{e_z}$. With respect to R', the $\vec{H}_1^-$ field is stationary, with its orientation fixed along the x'-axis. The alteration of $\vec{\mu}$ over time is then articulated within this novel reference frame as follows:

$$\left(\frac{d\vec{\mu}}{dt}\right)_{R'} = \left(\frac{d\vec{\mu}}{dt}\right)_{R} - \vec{\Omega} \wedge \vec{\mu} \tag{2.20}$$

$$\left(\frac{d\vec{\mu}}{dt}\right)_{R'} = \vec{\mu} \wedge [\omega_0 \vec{e_z} + \vec{\omega_1} - \omega \vec{e_z}] \tag{2.21}$$

where,

$$\vec{\omega_1} = \gamma \vec{H_1^-} \tag{2.22}$$

When resonance occurs, i.e., when $\omega = \omega_0$, equation 2.21 simplifies to $\left(\frac{d\vec{\mu}}{dt}\right)_{R'} = \vec{\mu} \wedge \vec{\omega_1}$, signifying that the magnetic moment is solely affected by the perpendicular field $\vec{H_1^-}$. Consequently, the magnetic moment enters into precession around $\vec{H_1^-}$, transpiring within the plane defined by the $\vec{z}$ and $\vec{y'}$ axes.

The equations of motion discussed previously have not taken into consideration the effects of relaxation phenomena. When subjected to an external magnetic field, the nuclear magnetic moment is theoretically expected to sustain its precessing motion indefinitely. However, in reality, various physical processes come into play. Relaxation processes, facilitate the spin system's return to equilibrium. In a classical framework, the evolution of magnetization $\mathbf{M}$ is governed by Bloch's equations:

$$\frac{dM_x(t)}{dt} = \gamma H_0 M_y(t) - \frac{M_x(t)}{T_2} \tag{2.23}$$

$$\frac{dM_y(t)}{dt} = -\gamma H_0 M_x(t) - \frac{M_y(t)}{T_2} \tag{2.24}$$

$$\frac{dM_z(t)}{dt} = -\frac{M_z(t) - M_0}{T_1} \tag{2.25}$$

where $M_0 \vec{e_z}$ represents the equilibrium magnetization (as defined in equation 2.4). These equations reveal the presence of two distinct characteristic times: T_1 and T_2, known respectively as the spin-lattice relaxation time and the spin-spin relaxation time. Longitudinal relaxation, associated with the time T_1, pertains to processes that involve energy transfers with a reservoir, allowing the restoration of magnetization M_z to thermodynamic equilibrium. These processes encompass the transfer of energy into various lattice excitation channels, as magnetic excitations, phonons, and more. Consequently, the populations inhabiting the Zeeman levels gravitate towards populations established by thermodynamic equilibrium. For the sake of simplicity, we posit an energy deposition in the magnetic excitation channels, which we ascribe to electronic origins. As elucidated earlier, the interaction between a nuclear spin and an internal local field $H_{\text{loc}}(t)$, associated with the fluctuating electron spin $S(t)$, transpires through the hyperfine tensor $\overline{A}$. The Fermi Golden Rule enables the expression of the transition rate $W_{m_z \to m_{z\pm1}}$ between consecutive Zeeman levels $|m_z\rangle \to |m_{z\pm1}\rangle$:

$$\frac{1}{T_1} = 2W_{m_z \to m_z \pm 1} = \frac{2}{\hbar^2} \int_{-\infty}^{+\infty} \overline{\langle m_z | - \vec{\mu} \cdot \vec{H}_{\text{loc}}(0) | m_z \pm 1 \rangle \langle m_z \pm 1 | - \vec{\mu} \cdot \vec{H}_{\text{loc}}(t) | m_z \rangle} e^{-2i\pi\nu t} dt; \tag{2.26}$$

where $\overline{\cdots}$ represents the statistical mean and ν is the working frequency. It appears that only the transverse

fluctuations of the internal local field contribute.

$$\frac{1}{T_1} = \frac{\gamma^2}{2} \int_{\infty}^{-\infty} \langle H_{\text{loc.}}^{+}(t) H_{\text{loc.}}^{-}(0) \rangle \exp(-2i\pi\nu t) dt \tag{2.27}$$

$$H_{\text{loc}}^{\pm} = H_{\text{loc}}^{\text{x}} \pm i H_{\text{loc}}^{\text{+y}} \tag{2.28}$$

The internal local field is expressed as a function of the hyperfine tensor:

$$\vec{H}_{\text{loc}} = \frac{1}{\hbar\gamma} \sum_{r} \overline{A(r)} \cdot \vec{S}(r;t) \tag{2.29}$$

Assuming a constant scalar hyperfine coupling, the fluctuation-dissipation theorem allows us to write:

$$\frac{1}{T_1}(T) = \frac{k_B T A^2}{\hbar^2} \sum_{q} \frac{\chi"_{\perp}(q, 2\pi\nu_0)}{2\pi\nu} \tag{2.30}$$

This equation establishes a connection between the relaxation time T_1 and the imaginary part of the susceptibility, $\chi''_{\perp}(q;\nu)$, which can be measured using techniques like inelastic neutron scattering. While inelastic neutron scattering provides a comprehensive view of reciprocal space , NMR, on the other hand, isn't a technique that resolves reciprocal space (summing over q). However, it excels at probing excitation energies of extremely low values, typically in the order of microelectronvolts ($\hbar\omega_0$). By tracking the temperature-dependent evolution of the relaxation time T_1, it becomes possible to discern the presence or absence of an energy gap within the excitation spectrum. In situations where an energy gap exists, there are no available excitations to facilitate the relaxation of nuclear magnetization at temperatures $T << \Delta/k_B$, where Δ is the energy gap. Consequently, the relaxation rate T_1 follows an activation law: $T_1^{-1}(T) = a(T) \exp\left(-\frac{\Delta}{k_B T}\right)$, with $a(T)$ representing a power law term.

On the other hand, transverse relaxation, linked with time T_2, is concerned with processes that maintain the populations of the Zeeman energy levels intact. This phenomenon arises from the stochastic fluctuations in the local magnetic field. These dynamic variations in local fields lead to different precession velocities, inducing a phase shift that causes the attenuation of magnetization components in the M_x and M_y plane. Typically, T_2 is significantly shorter than T_1, denoting $T_2 \ll T_1$. In our magnetic systems, the relaxation times are approximately $T_2 \sim 100\,\mu s$ and $T_1 \sim 10\,ms$.

In conclusion, we have demonstrated that at resonance, applying a weak magnetic field perpendicular to the nuclear magnetization enables manipulation of its rotational direction. Thus, when a transverse magnetic field $\vec{H}_1$ is applied for a duration t, the magnetization $\vec{M}(t)$ undergoes rotation by an angle $\theta(t) = \gamma H_1 t$. In the realm of NMR techniques employing pulsed sequences, specific pulse durations, typically on the order of microseconds (μs), are employed to achieve desired angle rotations. These are referred to as $\pi/2$ or π pulses, corresponding to

magnetization rotations of $\pi/2$ or π radians, respectively.

2.4.2 Spin echo and NMR spectrum

Measuring an NMR signal might seem simple at first: apply a $\pi/2$ pulse and observe the subsequent free induction decay (FID) i.e the free rotation of the nuclear magnetisation around H_0 and it's relaxation. Yet, practical intricacies come into play. After applying a high-power pulse, the reception electronics saturates, leading to a "dead time" interval, τ_m, lasting around $\tau_m \sim 10\,\mu s$, during which measurements become temporarily unfeasible.

Moreover, within the realm of NMR measurements on solid materials, the primary driver of transverse relaxation is often the presence of internal field inhomogeneities within the sample. Each individual spin experiences a composite magnetic field, $\vec{H}_{\text{tot}} = \vec{H}_0 + \delta\vec{H}_{\text{loc}}$, where $\delta\vec{H}_{\text{loc}}$ denotes the static magnetic field contingent on neighboring atomic moments and their spatial arrangement.

In this intricate landscape, spins precess at slightly differing frequencies, $\omega = \gamma H_{\text{tot}}$, inducing swift signal decay over a timespan T_2^*, which is inversely proportional to $(\langle \delta H_{\text{loc}}^2 \rangle)^{1/2}$. Generally, $T_2^* \ll T_2$, signifying that the effective transverse relaxation time for broad wide line spectra (T_2^*) is notably briefer than the dead time τ_m. These conditions often collaborate to render the FID signal inconspicuous.

However, the underlying decay mechanism stems from a static source and is reversible. After the $\pi/2$ pulse, a subsequent π pulse can be deftly introduced, effectively rephasing the spins and producing to what is termed a "spin echo." This sequence, originally implemented by Carr and Purcell, is illustrated in Figure 2.4.

The detection process unfolds through multiple phases. The initial $\pi/2$ pulse positions the magnetization into the (x', y') plane, coaxing it into alignment along the y' axis. Subsequent to the pulse, all spins engage in the precession within the (x, y) plane, their motion orchestrated by the influence of $\vec{H}_0$ + $\vec{H}_{local}$. It is worth noting that the FID can't be observed because of the dead time.

After an interval of time, τ, the second π pulse redirects the nuclear spins in relation to the (x', z') plane, setting the stage for the revival of lost phase after an additional τ-long pause, visually captured in Figure-2.4 This sequence results in the emergence of a spin echo when all nuclear spins are back in phase, resulting in a detectable signal. The NMR spectrum is acquired by measuring this echo. In practical terms, we measure the electromotive force (emf) generated due to the motion of the transverse magnetization within a coil. It's Fourier transform essentially forms a histogram of the nuclei resonating at a specific frequency within the external field $\vec{H}_0$, thereby constituting the absorption spectrum $\chi''(\nu)$ of the system.

2.4.3 NMR by Fourier transforms and broad lines

The Fourier transform analysis facilitates the comprehensive utilization of pulsed NMR techniques. When a rectangular pulse of finite duration t is applied at the frequency $\Delta\nu_{\text{rf}}$, it doesn't just irradiate the nuclei at the frequency ν_{rf},

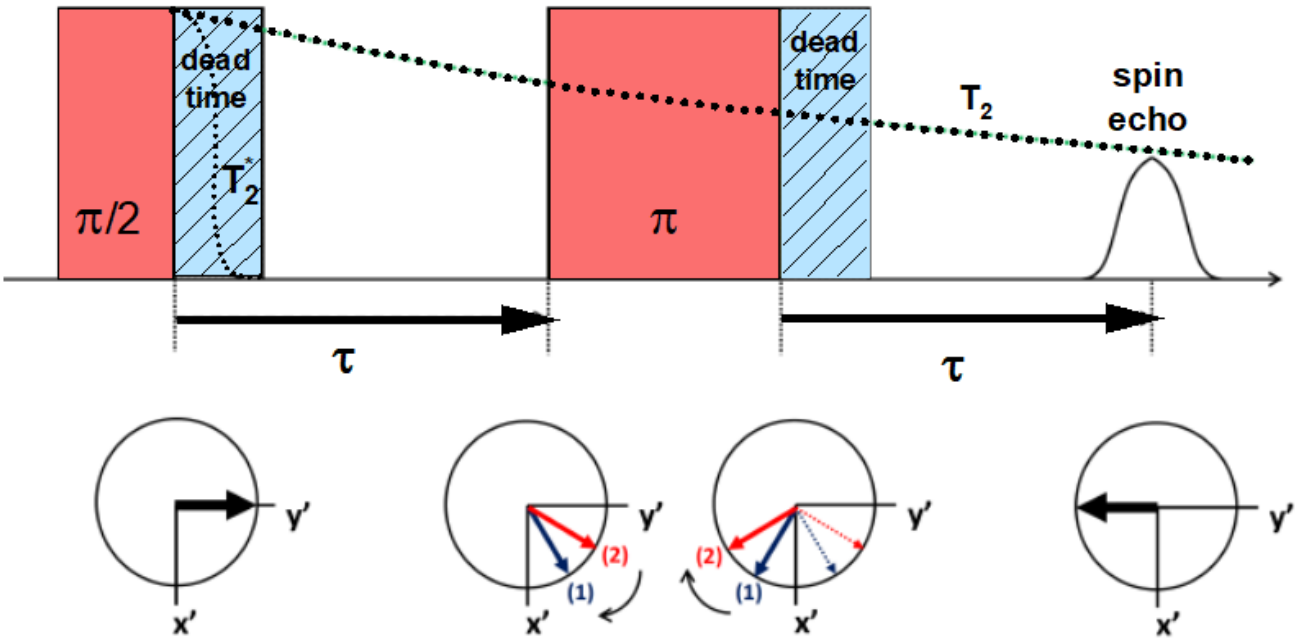

Figure 2.4: Pulse sequence $\frac{\pi}{2} - \tau - \pi$ (top) and the corresponding spin dynamics in the rotating frame (bottom) are illustrated. Spin (1) undergoes precession at a higher rate than spin (2) owing to the impact of a stronger local magnetic field. The shaded region post each pulse denotes the electronic dead time. T_2^* denotes the timeframe beyond which the transverse magnetization becomes unmeasurable, while T_2 signifies the characteristic relaxation time of magnetization within the (x', y') plane.

but across a frequency range dictated by the sinc distribution $[\pi t(\nu - \nu_{\text{rf}})]$. The effective frequency range $\nu \sim 1/t$ that can be accessed is thus constrained by the size of the pulse, and it can also be influenced by the absorption characteristics of the resonant cavity (i.e the resonant circuit used to measure the emf voltage, see next section). This filtering effect, attributed to the pulse and/or cavity, is accommodated by the filter function $f(\nu)$. The recorded transverse magnetization $M_{\text{tr}}(t)$ using ν_{rf} channels, can be expressed as follows:

$$M_{\text{tr}}(t) = M_0 \int_{-\infty}^{\infty} \chi''(\nu) e^{2i\pi\nu t} f(\nu)\, d\nu \tag{2.31}$$

Hence, the NMR spectrum $\chi^{"}(\nu)$ is obtained through the Fourier transform of the spin echo. When dealing with a spectrum fine enough in frequency to disregard the filter effect ($f(\nu) \approx 1$), a single echo measurement yields the complete NMR spectrum. However, in our compounds, where spectra are often broad, the filter effect becomes significant. Consequently, it becomes imperative to gather multiple spectra at varying irradiation frequencies (or applied fields). The complete NMR spectrum can be attained via two approaches. Using the recombination technique [W. Clark et al. 1995], the aggregate spectrum results from summing the Fourier transforms of echoes taken at equidistant frequencies typically 1/2 t. This method is effective in capturing spectra with intricate singularities, such as those observed in high-temperature quadrupole spectra. The alternative method involves calculating the integral

of the signal for each channel. In the case of field scanning measurements, for every applied field value H_0, the spectrum value at the corresponding frequency $\nu_0 = \gamma H_0/(2\pi)$ is determined by:

$$\chi''(\nu_0) = \left[\left(\int_{-\infty}^{\infty} S_A(t)\, dt \right)^2 + \left(\int_{-\infty}^{\infty} S_B(t)\, dt \right)^2 \right]^{\frac{1}{2}} \tag{2.32}$$

The comprehensive NMR spectrum is graphically depicted as the curve generated by the collection of points $(H_0, \chi''(\nu_0))$ within a defined range. This second "point by point" technique can be used for broad lines with no singularities. It eradicates the influence of filters and maintains the electronic setup in a consistent state throughout the measurement, ensuring enhanced stability.

2.4.4 Experimental apparatus

The overall experimental arrangement required to conduct an NMR experiment can be categorized into three primary components (refer to Fig.2.5):

(i) The external magnetic field $\vec{H}_0$;

(ii) The NMR spectrometer, which encompasses an emission chain for transmitting radio frequency pulses, a measurement probe housing the electronic circuitry to quantify the induced electromotive force (e.m.f), and a reception chain for detecting the acquired weak signal;

(iii) The cryogenic equipment, employed for measurements at low temperatures.

External field H_0 and cryogenics:

H_0 NMR measurements require magnetic fields of the order of several Teslas (NMR signals are proportional to square of the external magnetic field) and must be sufficiently homogeneous over the sample volume (around 1-10 ppm/cm³). To achieve such high field values, we employ a setup comprising a superconducting magnet supplied with stabilized direct current and cooled by a cryogenic apparatus utilizing liquid helium (4He). During the course of this thesis, NMR spectra were obtained using various experimental setups.

The first setup involves field scanning ($0 \leq H \leq 7.2$ T) with the magnet immersed in a bath of liquid ^{4}He. The second setup allows for scanning the field over a wider range ($0 \leq H \leq 14$ T), and the magnet is cooled by a helium-free system known as a Cryocooler type [Radebaugh 2009], which operates through expansion-compression cycles. Finally, the third setup is at a fixed field of $B_0 = 7.5$ T, with the magnet submerged in a liquid ^{4}He bath, maintaining the magnet at a superconducting temperature of 4.2 K. This setup provides a particularly stable and homogeneous field ($\sim$ 1 ppm/cm^3).

NMR spectrometer:

(a) Emission chain:

The purpose of the emission chain is to generate sequences of radio frequency pulses designed to manipulate

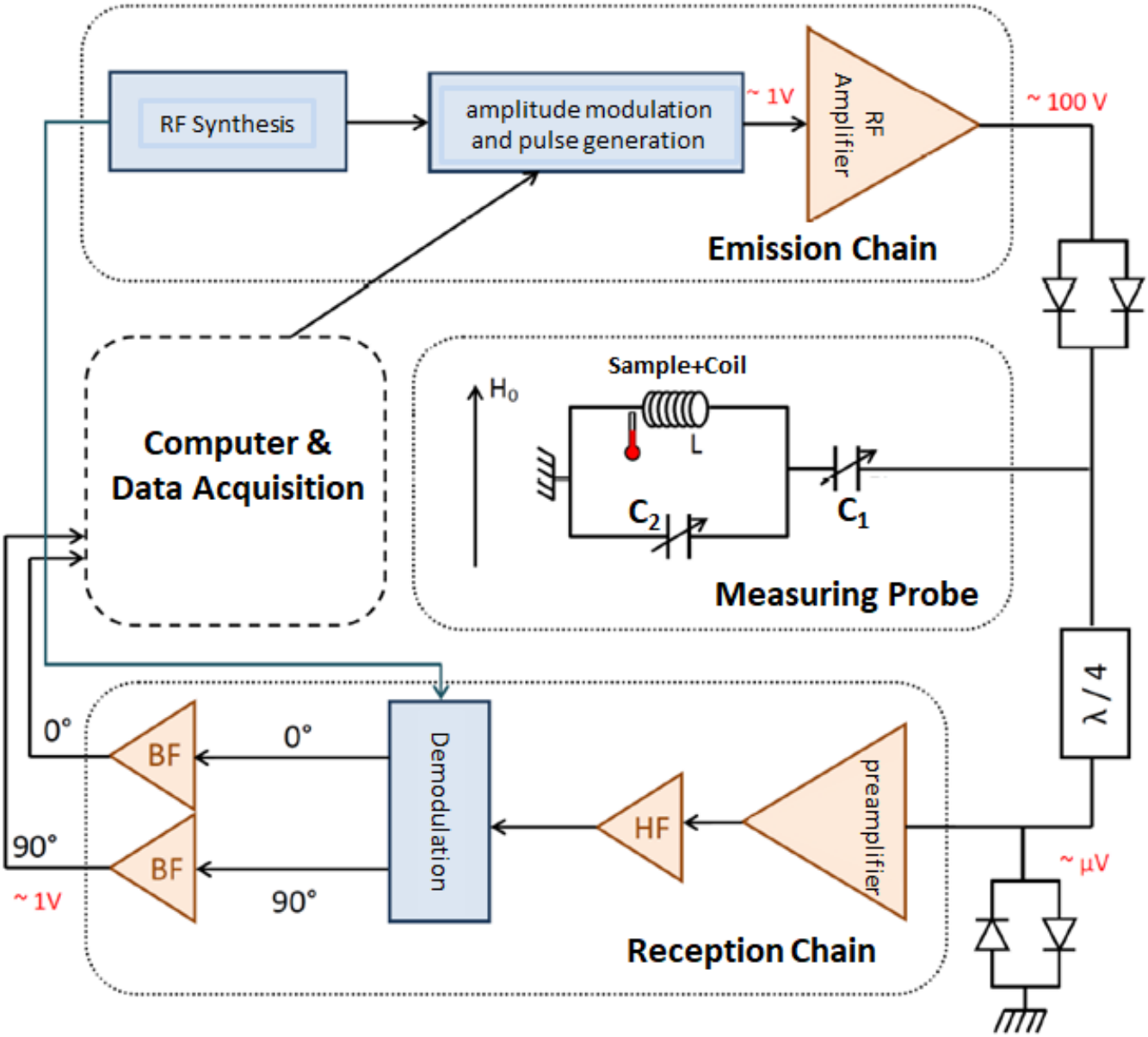

Figure 2.5: Block diagram of an experimental set up for an NMR experiment.

the population of nuclear spins. A high-frequency generator produces a sinusoidal signal at the irradiation frequency, with precision reaching a few tenths of a hertz. This signal is then directed to a sequencer composed of choppers, which convert the signal into rectangular pulses. These pulses exhibit a peak-peak voltage of a predetermined amplitude, duration, and phase. Typically, the duration of pulses and intervals between them span from a few microseconds to several seconds. Subsequently, this sequence is transmitted to a high-power amplifier, effectively elevating the peak-peak voltage to a few hundred volts, before being conveyed to the probe.

(b) Probe: The NMR probe serves a dual role of perturbing the nuclear spin population and detecting the NMR signal. It comprises a resonance cavity structured as a tank circuit (R, L, C_2) in series with a capacitor C1. This compact coil usually consists of multiple windings of copper wire wound around the sample. It is characterized

by its low resistance R and inductance L. Capacitances C_1 and C_2 are adjustable within the range of a few tens of picofarads, and they serve two primary functions: (i) tuning the circuit's resonant frequency at the irradiation frequency (tuning), and (ii) adjusting the circuit's impedance to align with the 50 Ω coaxial cables (matching).

When the radio frequency pulses reach the small coil, they generate a modest perturbing field denoted as $H_1(t)$ (with a maximum strength in the range of a few hundredths of a tesla). This field is oriented along the coil's axis and is perpendicular to the main magnetic field H_0. After each sequence of pulses, the spins within the coil undergo free precession, resulting in the creation of a varying magnetic induction flux denoted as $\Phi(t)$ (as dictated by Lenz's law). The changes in this flux are then detected in the form of a small electromotive force (emf), typically measuring a few microvolts in peak-to-peak amplitude, represented by $e(t) = \frac{d\Phi}{dt}$. This induced flux is directly proportional to the magnitude of the transverse magnetization, which follows a Curie law in a semi-classical approximation, shown in equation-2.4. As a result, a scaling relationship for the NMR signal can be established, showing that the signal's strength is maximized at higher frequencies, fields and lower temperatures.

$$e \propto \nu_{\text{irradiation}} \times \frac{mI(I+1)\gamma^2 H_0}{T} \times Q \propto \frac{mI(I+1)\gamma^3 H_0^2 Q}{T} \tag{2.33}$$

In this context, γ symbolizes the gyromagnetic ratio of nuclear spins with a magnitude of I, while m denotes the sample mass (along with the number of nuclear spins). We have introduced the quality factor of the resonant cavity $Q = \frac{\omega L}{R}$, with $L\left(1 + \frac{C_1}{C_2}\right)^{-1}$. H_0 stands for the external magnetic field, operating under the assumption that $\nu_{\text{irradiation}} = \frac{\gamma H_0}{2\pi}$.

A high-quality factor (Q) of the resonant circuit, offers the advantage of boosting the signal-to-noise ratio and concurrently facilitating the reduction of pulse durations. However, it's important to note that a very high-quality factor inherently implies a decrease in bandwidth ω (where $\omega \propto Q^{-1}$) and an extension of the dead time t_m (where $t_m \propto Q$). This situation presents challenges particularly when the transverse relaxation time T_2 is notably brief. In practice, the quality factor is often adjusted by increasing resistance R, achieved through the use of a carefully chosen length of a non-magnetic resistive wire. Within the framework of the research outlined in this manuscript, a Q value of approximately 50-100 strikes a balance between these considerations.

(c) Reception chain:

The reception chain is utilized to amplify the faint NMR signal (typically a few microvolts in peak-to-peak amplitude) originating from the measuring probe. It comprises a low-noise preamplifier strategically positioned as closely as feasible to the NMR probe. This preamplifier sets the signal-to-noise ratio. Subsequently, a sequence of amplifiers or attenuators is employed to produce a signal of the order of a few 100 mV to a volt. It is often necessary to accumulate a significant number N of acquisitions to render the signal-to-noise ratio relevant, given its variations proportional to $\sqrt{N}$. To ensure sufficient time for the population of nuclear spins to return to equilibrium and optimize

the duration of the experiment, the delay between repetitions of the pulse sequence should be of the order of the longitudinal relaxation time T_1.

The signal emanating from the measuring probe oscillates rapidly, closely aligning with the irradiation frequency (typically in the range of several tens of megahertz). Hence, demodulating the signal before acquisition is advantageous, as the sampling rate of the employed hardware is limited (rarely exceeding ten megahertz). The signal is multiplied by the high-frequency generator signal of the transmission chain, and then filtered to isolate the low-frequency component.

This low-frequency component is of significance, as it corresponds to the absolute value of the shift between the frequency of the NMR signal and the irradiation frequency. This shift arises due to internal local magnetic fields. To obtain not only the absolute value but also the sign of this frequency shift, it is necessary to carry out a detection of a synchronous quadrature .

The transmission chain generates signals with amplitudes ranging in the order of a few hundred peak-to-peak volts which have to be decoupled from the reception chain to protect it and avoid it's saturation. This is achieved effective effectively by the anti-parallel diodes and a $\frac{\lambda}{4}$ cables, as shown in figure-2.5.

Cryogenics:

To conduct measurements at low temperatures, the sample is positioned within a temperature-variable insert connected to a reservoir of liquid ^{4}He. This setup includes a capillary and a needle valve to precisely regulate the flow of helium. This arrangement enables measurements in the temperature range of $1.2 \leq T \leq 80$ K. Beyond 4.2 K, temperature control is achieved by circulating gaseous ^{4}He through a pumping circuit. Within the temperature range $1.2 \leq T \leq 4.2$ K, the sample environment is immersed in liquid ^{4}He, and the desired temperature is achieved by stabilizing the pressure of the helium bath. For higher temperatures ($80 \leq T \leq 300$ K), measurements are conducted within a cryostat using circulating gaseous nitrogen. The use of nitrogen, with a higher breakdown voltage compared to helium, prevents the occurrence of electric arcs caused by high voltage pulses, ensuring interference-free measurements. To maintain temperature control within the cryostat, we use a comercial temperature controller (lakeshore) to regulate the heating of a resistive wire by a calibrated resistive probe (cernox) positioned in close proximity to the sample, providing accurate temperature readings.

2.5 Experimental spectra in NMR

Each element of the Hamiltonian (2.5), whether stemming from magnetic or quadrupole interactions, plays a role in influencing the energy levels of the nucleus, resulting in shifts in the resonance frequency. Let's begin by deducing the resonance frequency shifts that arise from these interactions. Following that, we'll present an illustrative simulation of an NMR spectrum specific to the ^{35}Cl and $^{79/81}$Br nucleus, which is the central point of interest in this particular investigation[2.2].

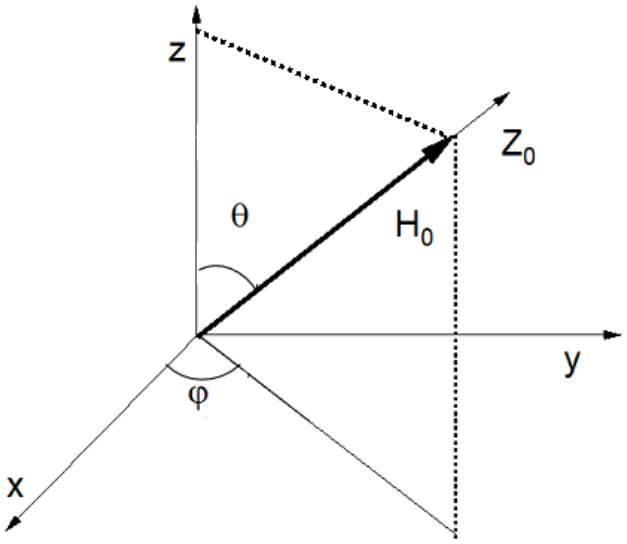

Figure 2.6: Representation of the orientation of the applied field $\vec{H}_0$ in the reference frame of the magnetic displacement tensor $\mathbf{K}$.

2.5.1 Magnetic Contribution

To investigate the magnetic shift, let's proceed with the transformation of the magnetic Hamiltonian (equation-2.6) into the frame where the tensor $\mathbf{K}$ is diagonal. In this frame, the laboratory frame is denoted by (X_0, Y_0, Z_0), and the diagonal frame is (x, y, z). The external magnetic field $\vec{H}_0$ is aligned along the laboratory Z_0 axis. The magnetic Hamiltonian is:

$$\mathcal{H}_{\mathsf{m}} = -\vec{\mu} \cdot \left(\vec{H}_0 + \vec{H}_{\mathsf{loc}}\right) \tag{2.34}$$

$$\mathcal{H}_{\mathsf{m}} = -\gamma\hbar\vec{I}\left(1 + \overline{K}\right)\vec{H}_0 \tag{2.35}$$

When we focus on the diagonal terms I_{Z_0} , the transformed magnetic Hamiltonian can be simplified to:

$$\mathcal{H}_{\mathsf{m}} = -\gamma\hbar H_0 I_{Z_0}\left(\vec{Z}_0 \cdot \vec{Z}_0\right) - \gamma H_0 \hbar I_{Z_0}\left[K_x\left(\vec{x}\cdot\vec{Z}_0\right)^2 + K_y\left(\vec{y}\cdot\vec{Z}_0\right)^2 + K_z\left(\vec{z}\cdot\vec{Z}_0\right)^2\right] \tag{2.36}$$

Moving forward, we can engage in the calculation of the eigenenergy $E_m = \langle m|H_m|m\rangle$ and subsequently deduce the resonant frequency $\nu_m = (E_{m-1} - E_m)/h$ that holds significance in NMR measurements. Adhering to the angle convention introduced by [Narita, Umeda, and Kusumoto 1966], we arrive at the expression:

$$\nu_m = \nu_0 + \nu_0(K_x \sin^2\theta\cos^2\varphi + K_y \sin^2\theta\sin^2\varphi + K_z\cos^2\theta) \tag{2.37}$$

It's important to observe that the magnetic displacement remains unaltered regardless of the specific energy level m under consideration. Consequently, for a given field orientation (θ, φ), there exists only a single resonant frequency in the case of a single crystal. Notably, when $\theta = 0$, the measurement is restricted to assessing the local susceptibility along the z direction:

$$\nu_m = \nu_0(1 + K_z) \tag{2.38}$$

2.5.2 Quadrupolar Contribution

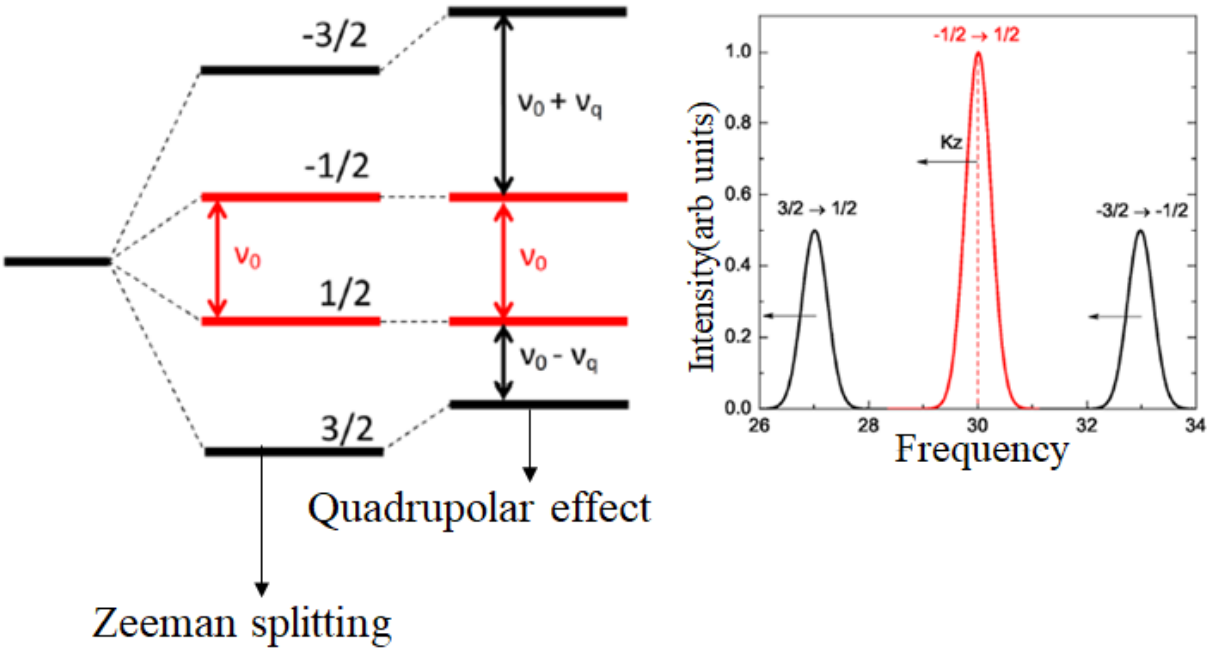

Figure 2.7: **Left:** Elevation of the Zeeman degeneracy in the energy levels m of a nuclear spin $I = \frac{3}{2}$, observed without quadrupole effects and considering them up to the first order. **Right:** The NMR spectrum with quadrupole effects taken into account up to the first order, exhibits three lines: a central line at $\nu_0 = 30\,\text{MHz}$ (highlighted in red) and two satellite lines at $\nu_0 - \nu_q$ and $\nu_0 + \nu_q$, where $\nu_q = 3\,\text{MHz}$. When influenced by a local field, these lines experience a displacement $K_z\nu_0$, located when $\theta' = 0$, leads to a decrease in frequencies when $K_z < 0$.

In our subsequent discussions, it will become evident that the quadrupole effects we observe in our compounds remain significantly weaker than the applied magnetic field, with a ratio $\frac{\nu_q}{\nu_0}$ falling within the range of $\leq 10\%$. Consequently, we treat these effects described by the hamiltonian in 2.15 as perturbations relative to the dominant Zeeman Hamiltonian. While the intricate details of the perturbative calculation won't be presented here, they are thoroughly explored in references [Cohen and Reif 1957], [Abragam 1961].

At the zeroth order, the resonance frequency for the transition between the levels, $m \to m + 1$ corresponds to

the Zeeman energy, denoted as $\nu_m^0 = \nu_0$. Upon considering the first order, the resulting resonance frequency is:

$$\nu_m^{(1)} = -\left(m - \frac{1}{2}\right)\nu_q^2\left(3\cos^2\theta' - 1 - \eta\sin^2\theta'\cos 2\varphi'\right) \tag{2.39}$$

The angles (θ', φ') denote the orientation of the field $\vec{H}_0$ concerning the principal axes of the quadrupolar tensor ($\overline{V}$). Differing from magnetic effects, quadrupole effects lead to the alteration of spacings between distinct energy levels m, as $\nu^{(1)}m$ becomes reliant on m, as depicted in Figure -2.7. Consequently, this generates a set of $2I$ resonance frequencies. For a chlorine or bromine nucleus with $I = \frac{3}{2}$, this predicts the presence of three resonances in the NMR spectrum. It's notable that the intensity of each line is proportional to the transition probability between two levels, given by $[I(I+1)-m(m-1)]$, favoring the central line. Central resonance at the frequency $\nu^{\frac{1}{2}}$, corresponding to the $-\frac{1}{2} \leftrightarrow \frac{1}{2}$ transition, and two satellite transitions $\nu^{\frac{3}{2}}$ and $\nu^{-\frac{1}{2}}$ corresponding, respectively, to the transitions $\frac{1}{2} \leftrightarrow \frac{3}{2}$ and $-\frac{3}{2} \leftrightarrow -\frac{1}{2}$.

Although this first-order calculation doesn't impact the central line's position ($\nu_{\frac{1}{2}}^{(1)} = 0$), the magnitude of the quadrupole interaction in our compounds justifies the inclusion of second-order effects that modify the central line. When $\eta \neq 0$, the second-order expression takes the following form:

$$\Delta\nu_{1/2\leftrightarrow 1/2}^{(2)} = \Delta\nu_{\text{mag}} - \frac{\nu_Q^2}{\nu_0}\left[I(I+1) - \frac{3}{4}\right]\left[A(\eta;\varphi)\cos^4\theta + B(\eta,\varphi)\cos^2\theta + C(\eta,\varphi)\right] \tag{2.40}$$

where,

$$A(\eta,\varphi) = -\frac{27}{8} + \frac{9}{4}\eta\cos(2\varphi) - \frac{3}{8}\eta^2\cos^2(2\varphi); \tag{2.41}$$

$$B(\eta;\varphi) = \frac{30}{8} - 2\eta\cos(2\varphi) + \frac{3}{4}\eta^2\cos^2(2\varphi) - \frac{\eta^2}{2}; \tag{2.42}$$

$$C(\eta;\varphi) = -\frac{3}{8} - \frac{1}{4}\eta\cos(2\varphi) - \frac{3}{8}\eta^2\cos^2(2\varphi) + \frac{\eta^2}{3} \tag{2.43}$$

For simplified case of $\eta = 0$,

$$\nu_m^{(2)} = -\frac{\nu_q^2}{16\nu_0}\left[I(I+1) - \frac{3}{4}\right]\left(1 - \cos^2\theta'\right)\left[9\cos^2\theta' - 1\right] \tag{2.44}$$

Note that in cases where the field is aligned with the principle axis of the EFG ($\theta' = 0$), the frequency shift still does not involve any quadrupole contribution. As a result, the central line's location is entirely governed by the magnetic displacement.

2.5.3 Longitudinal spin-lattice relaxation time T_1 measurement

A significant segment of this manuscript is dedicated to investigating the temperature-dependent changes in the longitudinal relaxation rate, denoted as $T_1^{-1}(T)$, for the nuclear spins of Chlorine (^{35}Cl) and Bromine (^{81}Br) within

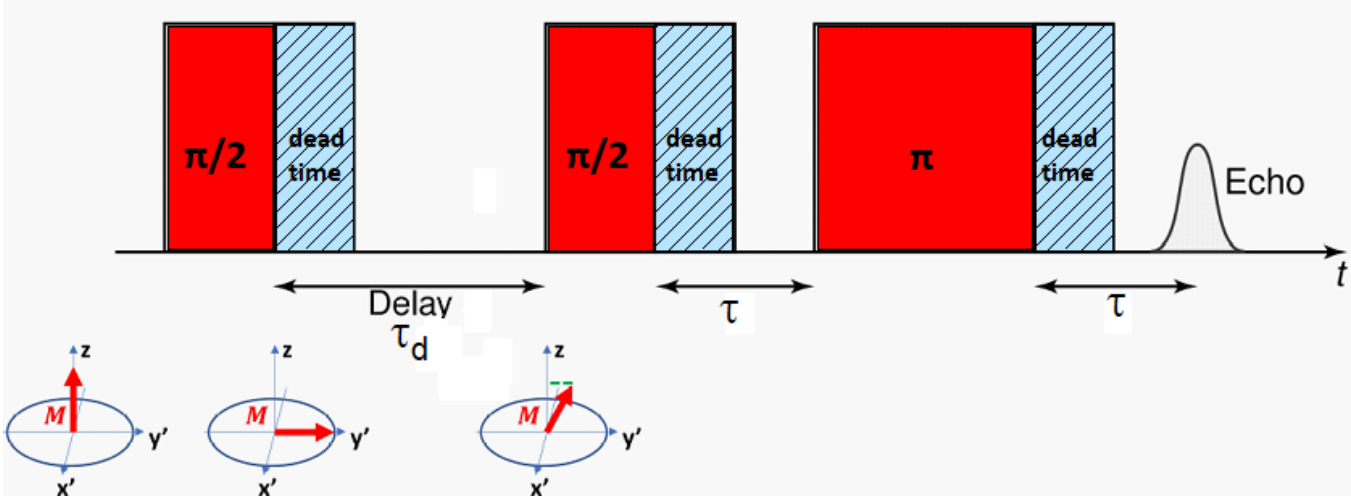

Figure 2.8: Hahn sequence preceded by a preparation sequence $\frac{\pi}{2}$-τ_d, where τ_d is a variable delay, allowing the measurement of a spin echo whose amplitude is affected by the longitudinal relaxation, of characteristic time T_1 (such as $T_1 >> T_2$). We show the evolution of nuclear magnetization in the Bloch sphere before the Hahn sequence. The brown rectangles after the pulses represent the dead time.

the context of kapellasite. The determination of the longitudinal relaxation rate during NMR experiments involves the implementation of a preparation sequence, which frequently includes one or multiple radiofrequency pulses. This sequence perturbs the nuclear magnetization. Following this perturbation, the fraction of spins that reestablish equilibrium is quantified after a time delay τ_d, often through the use of a Hahn echo sequence. The straight forward approach we used involves the utilization of a $\frac{\pi}{2}$ - τ_d - $\frac{\pi}{2} - \tau - \pi$ pulse sequence, as illustrated in Figure 2.8. This sequence entails measuring the intensity of the resulting echo, which is directly proportional to the transverse nuclear magnetization, while adjusting the delay τ_d. When the delay τ_d is short, the intensity is nearly zero, as the magnetization has just switched within the plane. Conversely, at longer delays, the intensity reaches saturation, signifying the restoration of equilibrium magnetization. The interactions between absorption and spontaneous emission events among nuclear energy levels give rise to the magnetization $M(t)$ converging towards an equilibrium value M_{sat} through a multi-exponential decay law. In particular, for a spin $I = \frac{3}{2}$, up to 3 terms can manifest, corresponding to the 3 potential transitions.

$$M(t) = M_{\text{sat}} \left[1 - \sum_{i=1}^{3} a_i \exp\left(-\frac{\lambda_i t}{T_1} \right) \right] \tag{2.45}$$

Here, the coefficients a_i satisfy the condition $\sum_i a_i = 1$, and the values of indiviual a_i are determined based on the specific perturbation conditions, which encompass factors like the initial nuclear magnetization, the irradiated lines (whether they are all irradiated simultaneously, multiple lines, or just a single one) [Andrew and Tunstall 1961], [McDowell 1995], and the characteristics of the fluctuations. The local character of the NMR also makes it possible to measure the dynamics in a specific region of the spectrum. Thus, in the case of a spectrum composed of lines corresponding to different environments for the probe, it is possible to isolate the dynamics of each environment.

2.6 Muon spin relaxation

The acronym μSR stands for "muon spin rotation, relaxation, and resonance simultaneously." It refers to the behavior of muons under the influence of local magnetic fields when they are implanted in a sample ([Cox 1987], [Alex Schenck 2017], [S. Blundell 1999], [S. L. Lee, Cywinski, and Kilcoyne 1999], [Michal, Yaouanc, and Réotier 2010], [Lacroix, Philippe Mendels, and Mila 2011], [Fabrice Bert 2014], [Stephen J Blundell et al. 2022]). Muons, being produced through the weak interaction which violates parity symmetry (symmetry by space inversion), can be implanted with a specific spin polarization [T.-D. Lee and Yang 1956], [Garwin, Lederman, and Weinrich 1957]. The time evolution of this polarization offers unique insights into the characteristics of local magnetic fields (typically around 10^{-5} T), benefiting from the exceptional sensitivity due to the complete polarization of muon beams in spin. Unlike NMR measurements that are constrained by the availability of non-zero spin nuclei and require in most cases external magnetic fields and electromagnetic pulses to extract information about local fields, μSR can provide information on any sample in zero field. At variance with NMR, one issue is the determination of the muon stopping sites within the sample, although muon sites can be identified using Density Functional Theory (DFT) calculations [S. Blundell and Lancaster 2023].

2.6.1 Muon production

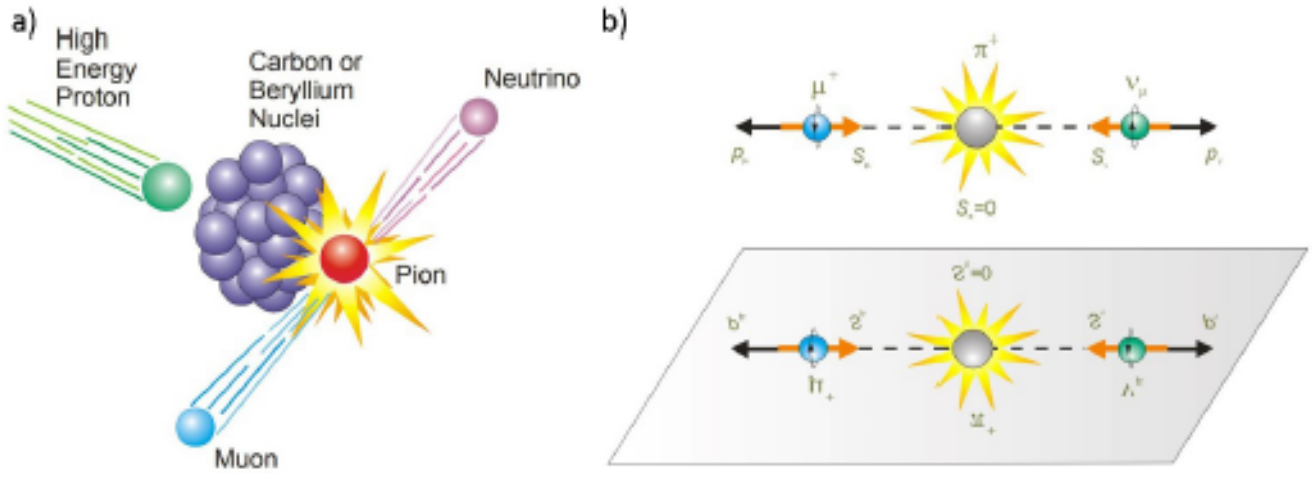

Figure 2.9: (a)Production of muons at the target. b) The decay of the pions under the effect of the weak interaction violates parity symmetry. The spin of the surface muons is opposite to their momentum. [Sonier 2002]

μSR experiments represent a specialized branch of research involving muons. These experiments demand a beam of muons that possess uniform spin polarization. The muon beam needs to be both intense and accurately collimated due to the small sample sizes under investigation. Ensuring a substantial number of muons per square centimeter per minute is crucial, while also controlling their energy to ensure they can come to a stop within the

samples. At present, such muon beams are produced by four major facilities around the world, each equipped with a proton synchrotron: the Paul Scherrer Institute (PSI) in Switzerland, the Rutherford Appleton Laboratory (ISIS & RIKEN) in England, the Tri-University Meson Facility (TRIUMF) in Canada, and the Kō Enerug2̄ Kasokuki Kenkyū Kikō (KEK) also known as J- Parc in Japan. In practice, the production process involves directing a high-energy proton beam (ranging from 600 to 800 MeV) at a precisely designed target made of a light element (typically graphite), as illustrated in Figure-2.9. The interactions between the incoming protons (p) and the target nucleons (p protons and n neutrons) lead to the creation of charged pions through processes that are not highly efficient:

$$p + p \rightarrow \pi^+ + p + n \tag{2.46}$$

The bulk of incident protons (roughly 95%) traverse the target without halting and are utilized for alternate applications, including neutron production. The π^+ and π^- pions undergo decay through the influence of weak interaction, resulting in the creation of two leptons. In 99.98770(4)% of instances, these decays yield either positive (μ^+) or negative (μ^-) muons [Počanić et al. 2004], as illustrated in Figure :2.9

$$\pi^+ \rightarrow \mu^+ + \nu_\mu \tag{2.47}$$

$$\pi^- \rightarrow \mu^- + \bar{\nu}_\mu \tag{2.48}$$

where ν_μ and $\bar{\nu}_\mu$ are the muon neutrinos and antineutrinos. Within the scope of this manuscript's work and in various studies concerning the electronic properties of materials, positive muons take center stage as the primary choice. Conversely, negative muons tend to halt their motion closer to nuclei rather than regions with higher electron density. More specifically, the focus is on "surface" positive muons, derived from positive pions that lacked momentum upon creation. These pions, bearing zero spin, find themselves stationary on the target's surface at the time of their decay. The conservation of angular momentum stipulates that the resulting muons and neutrinos have opposing spins and momenta. In the realm of neutrinos, their intrinsic characteristic involves left-handed helicity, indicating their spin align antiparallel to their momentum. Accordingly, positive surface muons also exhibit left-handed helicity [T.-D. Lee and Yang 1956], [Garwin, Lederman, and Weinrich 1957], as depicted in Figure 2.9. As such, these surface muons, typically possessing energies around 4 MeV, serve as the means to generate an entirely spin-polarized beam.

2.6.2 Muon transport in the system

The beam of polarized muons is directed through vacuum lines using a series of electromagnetic devices that guide it from the production target to the sample area. During this journey, measures are taken to eliminate undesired particles (such as pions, unpolarized muons, positrons, electrons, etc.) to minimize sample irradiation and prevent the detection of false events during measurements. Dipole magnets are employed to manipulate the trajectory of the

muon beam effectively. Given that the Landé g-factor for muons is very close to 2, magnetic fields induce both spin rotation and trajectory bending in muons at an identical rate. This phenomenon arises from the Larmor frequency, represented as ω_L, which can be mathematically expressed as $\omega_L = \frac{qgH}{2m}$, where q is the particle's charge, g is the Landé g-factor, m is the mass, and H is the magnetic field. Additionally, the cyclotron frequency, ω_C, is given by $\omega_C = \frac{qH}{m}$. These fundamental principles dictate the motion of muons in magnetic fields.

We employ the radius of curvature, denoted as $r = \frac{p}{qH}$ (where p represents momentum), to selectively eliminate certain particles while preserving the polarization of muon spins. Placing a slit downstream of a dipole magnet facilitates the sorting of particles based on specific p/q ratios. This arrangement effectively separates negative and neutral particles. For distinguishing muons from other positively charged particles possessing identical momentum, we utilize a separator equipped with crossed fields. This configuration allows for sorting based on velocity, which correlates with mass. Crossed electric and magnetic fields (E and H) are applied perpendicular to the beam's direction. Particles remain undisturbed if their velocity satisfies the condition $V = E/H$.

Prior to reaching the sample area, the beam undergoes focusing through a sequence of quadrupole magnets alternating in polarity. Furthermore, the beam can be split using dipole magnets, providing the capability to direct muons towards different instruments. Within the cryostat, the sample space is isolated from the vacuum line by delicate windows made from light Mylar film, ensuring transparency to muons.

2.6.3 Muon stopping in the sample and local interactions

The penetration capacity of muons increases with their energy. Interestingly, certain cosmic muons can even be detected at depths of 500 meters below sea level. However, to stop surface-positive muons with energies around 4 MeV, a surface density as modest as 100 to 200 mg/cm² of the sample is sufficient. Conversely, for investigating thin layers (approximately 1-10 nm thick), slow muons with energies spanning from 0.5 to 30 keV can be generated [Morenzoni et al. 2001]. The immobilization process of surface muons within a sample entails a series of steps. Upon entering the sample, they rapidly loose energy by ionizing atoms and interacting with electrons, which leads to diffusion. Within 0.1 to 1 ns, their energy diminishes to a few tens of kiloelectronvolts. Subsequently, within roughly a picosecond, they undergo swift capture and release of electrons, forming transient bound states known as muonium (μ^+e^-). This process further reduces their energy to a few tens of electronvolts. After undergoing additional collisions, the muons eventually come to a halt. At this stage, their energy is considerably lower than what is required for substitution within the crystal structure. The muons settle into interstitial positions within the lattice, minimizing electrostatic energy. For instance, in oxides, muons tend to come to rest near oxygen ions. Identifying specific muon sites is typically complex. In cases involving simple crystal structures, Density Functional Theory (DFT) calculations can aid in determining these positions [S. Blundell and Lancaster 2023].

In summary, the muon implantation process occurs swiftly, happening well before their average lifetime of 2.2 μs.

Importantly, this implantation process does not modify the polarization of their spin, as it is primarily influenced by Coulombic interactions. Consequently, prior to muons initiating precession around local magnetic fields ($\gamma_\mu/2\pi \approx 135.539$ MHz/T), which eventually leads to their depolarization, all muon spins maintain the same polarization. The interaction between muon spins and their local environment is mainly governed by dipole interactions, with a smaller contribution from contact interactions. Given that muons possess a spin of $1/2$, there is no necessity to consider quadrupole effects in this context.

2.6.4 Muon decay and measurement principle

Once immobilized within the sample, surface-positive muons undergo decay through the weak interaction after an average time of approximately $2.2, \mu$s. This decay process leads to the generation of a positron, an electron neutrino, and a muon antineutrino:

$$\mu^+ \rightarrow e^+ + \nu_e + \bar{\nu}_\mu \tag{2.49}$$

Similarly to pion decay, the violation of parity symmetry implies that the momentum of each emitted positron is preferentially aligned with the spin direction of the parent muon. Since the decay process yields three particles, the emitted positrons possess energies (E) distributed between $E_m = 26$ and $E_M \approx 53$ MeV, according to a probability density function $P(E)$. The emission angle, defined as the angle between the final spin polarization of the muon and the momentum direction of the positron, is also distributed according to a cardioid probability density function, as illustrated in Figure 2.10:

$$p(\theta, E) \propto 1 + a(E)\cos\theta \tag{2.50}$$

By introducing the normalized energy $\epsilon = \left(\frac{E-E_m}{E_M-E_m}\right)$, the decay asymmetry $a(\epsilon)$ is described by the equation $a(\epsilon) = \frac{2\epsilon-1}{3-2\epsilon}$. For positrons with energy E_M, the asymmetry is 1. The average asymmetry, computed by integrating over all energies with the weight function $f(\epsilon) = 2\,(3-2\epsilon)\,\epsilon^2$, is given by:

$$\bar{a}(\epsilon) = \int_0^1 f(\epsilon)a(\epsilon)\,d\epsilon = \frac{1}{3} \tag{2.51}$$

Consequently, the emission angle is distributed on average as depicted in Figure 2.10:

$$\bar{p}(\theta) \propto 1 + \frac{1}{3}\cos\theta \tag{2.52}$$

This asymmetric distribution enables the investigation of the time evolution of muon spin polarization in response to local fields. By strategically placing detectors around the sample, positron counts can be recorded based on emission angles relative to the initial polarization and time. In practice, two sets of detectors are positioned on opposite sides of the sample along the muon beam axis (perpendicular to the sample's surface): one for forward

and another for backward detection of positron. The normalized numbers of events detected by each detector group at time t, denoted as N_F and N_B, are given by:

$$N_B(t) = N_0 \Omega_B \epsilon_B \exp\left(-\frac{t}{\tau_\mu}\right)[1 + A_B P_z(t)] + B_B \tag{2.53}$$

$$N_F(t) = N_0 \Omega_F \epsilon_F \exp\left(-\frac{t}{\tau_\mu}\right)[1 - A_F P_z(t)] + B_F \tag{2.54}$$

The symbols $\Omega_{F,B}$, $\epsilon_{F,B}$, $A_{F,B}$, and $B_{F,B}$ correspond to the solid angle, average efficiency, average asymmetry, and background noise associated with the respective groups of detectors. The value of $-1 \leq P_z(t) \leq 1$ represents the projection of polarization along the initial polarization axis. It's worth noting that the average asymmetries A_F and A_B deviate slightly from $\frac{1}{3}$ due to the optimized coverage of solid angles by the detector groups, aimed at maximizing the signal flow and their varying effectiveness. Generally, these asymmetries are closer to 0.25. Detectors employed in the measurement consist of scintillators coupled with photomultipliers, such as SiPMs (silicon photomultipliers). The background noise is established during time intervals when no muons are directed to the sample.

To characterize the temporal evolution of events, the quantities $N_F(t)$ and $N_B(t)$ are presented in the form of histograms. The resolution of these histograms is limited by the saturation time of the detectors. The uncertainties associated with these quantities are statistically defined as $\frac{1}{\sqrt{N_F(t)}}$, reflecting smaller uncertainties at shorter times and larger ones at longer times. From these histograms, the temporal asymmetry $A(t)$ between the two detector groups can be constructed:

$$A(t) = \frac{[N_B(t) - B_B] - [N_F(t) - B_F]}{[N_B(t) - B_B] + [N_F(t) - B_F]} \tag{2.55}$$

By entering the parameters $\alpha = \frac{\Omega_F \epsilon_F}{\Omega_B \epsilon_B}$, $\beta = \frac{A_F}{A_B}$, the temporal evolution of the polarization $P_z(t)$ is obtained from the two histograms by calculating the evolution of the asymmetry $a(t)$, corrected for disparities between groups of detectors:

$$a(t) = A_B P_z(t) = \frac{(\alpha - 1) + (\alpha + 1)A(t)}{(\alpha\beta + 1) + (1 - \alpha\beta)A(t)}, \tag{2.56}$$

It is widely acknowledged that $A_F \approx A_B$ for the majority of instruments, or $\beta \approx 1$. In such instances, given that β has been determined, the histograms representing the asymmetry $a(t)$ and the polarization $P_z(t)$ are derived by evaluating:

$$a(t) = A_B P_z(t) \approx \frac{\alpha[N_B(t) - B_B] - [N_F(t) - B_F]}{\alpha[N_B(t) - B_B] + [N_F(t) - B_F]} \tag{2.57}$$

The outcomes of a μSR experiment, represented by these histograms, are usually showcased and adjusted in the time domain. Conversely, the findings of an NMR experiment are commonly presented in the frequency domain (frequency/field/displacement). The time window attainable through a μSR experiment is delimited by the temporal resolution at shorter times and the lifetime of the muons at longer times. Typically, this window spans the range of $[0.01, 10]$ μS at PSI. The μSR technique empowers the examination of magnetic fluctuations across a frequency

spectrum ranging from approximately 10^4 to 10^8 Hz (which also depends on coupling).

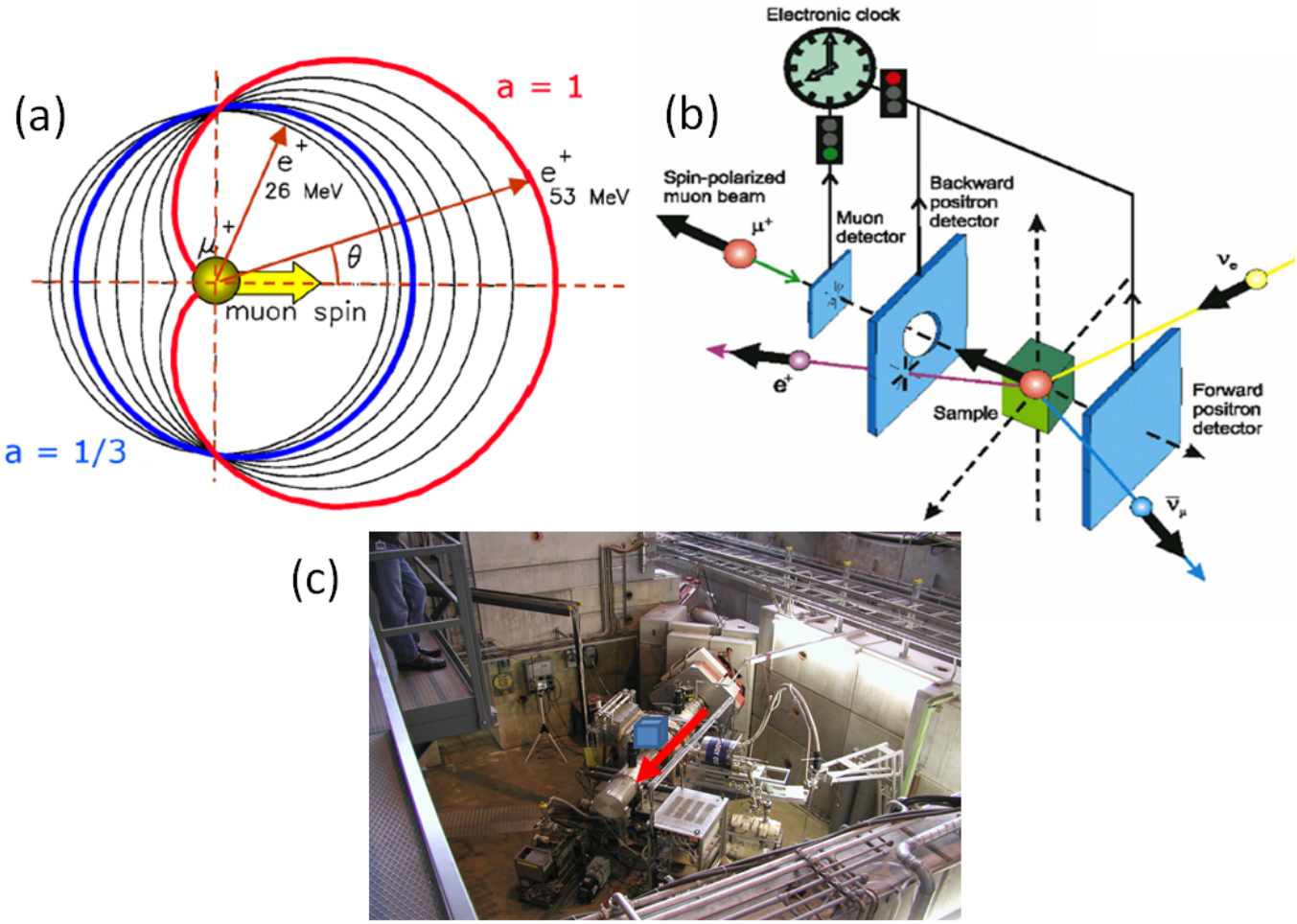

Figure 2.10: (a) Angular probability distribution $P(\theta, \epsilon)$ of emission of the positron e^+ according to the angle θ relative to the spin of the muon. The asymmetry is more pronounced for high-energy positrons ($\epsilon = 1$, $E = 53$ MeV) than in the case of the energy-averaged distribution ($\epsilon = 1/3$).(b) Block diagram of a μSR experiment in zero external field with the groups of forward and backward detectors (in blue) positioned on opposite sides of the sample along the axis of the muon beam. Adapted from [Sonier 2002].(c) Installation of a μSR measuring device on the GPS muon line at Paul Scherrer Institute.Red arrow giving us the muon direction and blue cube identifying the sample space in the beamline set up.

Using a fully polarized muon beam provides access to the evolution of muon spin polarization under the influence of internal local fields, eliminating the necessity for an external magnetic field. Nonetheless, there are instances where the application of an external field can prove advantageous. For example, one can gauge the transverse-field asymmetry $a(t)$ by immersing the sample in a static magnetic field B_{ext} perpendicular to the initial polarization of muon spins (in our case, $H_{\text{ext}} \approx 5$ mT).

In scenarios where muon spins are embedded within a paramagnetic phase, their pulsation precession is straightforward around H_{ext}, and the asymmetry $a(t)$ oscillates at the corresponding frequency $\omega = \gamma_\mu H_{\text{ext}}$. The existence of fluctuations in electronic spins leads to a minor depolarization effect, introducing relaxation modulation to the asymmetry. A measurement conducted under these conditions enables the determination of the coefficient

α, as the asymmetry should oscillate around zero, as depicted in Figure 2.11. In scenarios where muon spins are distributed across a phase containing both frozen and paramagnetic regions, and if the external magnetic field H_{ext} remains significantly weaker compared to the static internal local fields, the oscillating fraction of the asymmetry $a(t)$ at the frequency $\nu = \gamma_\mu H_{\text{ext}}/2\pi$ corresponds to the paramagnetic portion of the sample.

When a strong hyperfine coupling exists between the implanted muon spins and their local surroundings, this allows the measurement of the probed magnetic susceptibility at muon sites, akin to the magnetic frequency shift observed in NMR, a more substantial magnetic field in the range of $H_{\text{ext}} \approx 0.5$ T (and up to 9 T at PSI) can be applied.

Additionally, the asymmetry $a(t)$ can be measured by immersing the sample in a static longitudinal magnetic field H_{ext} aligned with the initial polarization of the muon spins. By modulating the intensity of this longitudinal field, it becomes possible to progressively decouple the muon spins from their static magnetic environment. This approach provides insights into the dynamics of internal local fields.

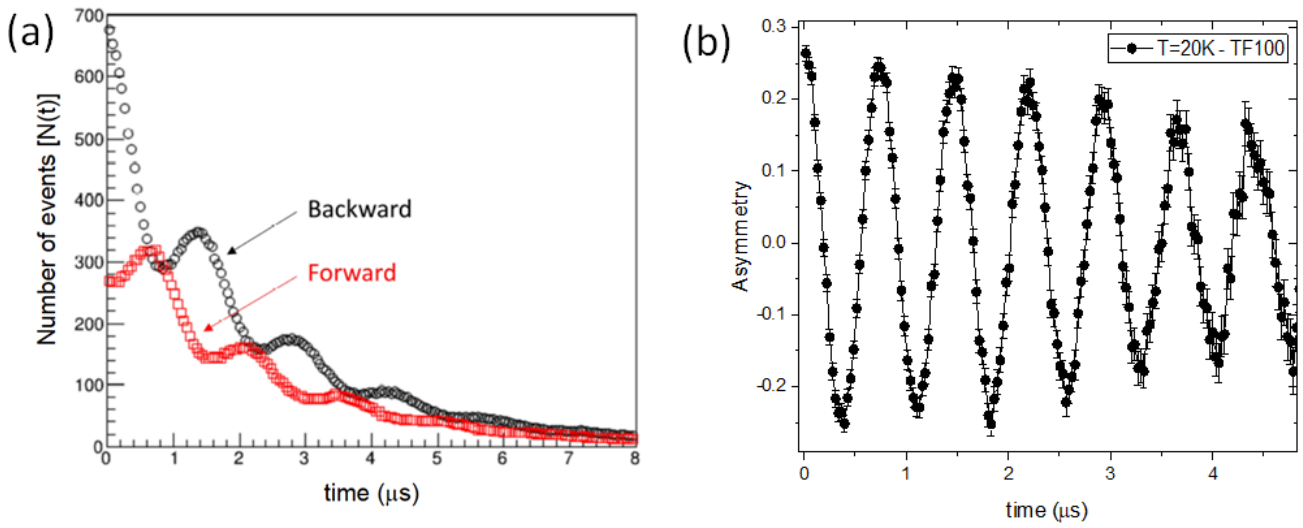

Figure 2.11: (a) Evolution of the number of events as a function of time detected in the counters before (Backward) and after (Forward), during a transverse field experiment. (b) Corresponding asymmetry (eq. 3.23) over time. A characteristic oscillation corresponding to the precession of the spin of the muon in the applied transverse field of 100 G for our single crystal of $Y_3Cu_9(OH)_{19}Cl_8$.

2.6.5 Time evolution of the muon polarization: distribution of static fields

For each implanted muon spin, sensitive to a static field $H = H_{\text{loc}} + H_{\text{ext}}$ (sum of the internal local field and the external field if one decides to apply one) shown in reference-2.13, the evolution time of the polarization is expressed:

$$P_z(H,t) = \cos^2\theta + \sin^2\theta\cos(\omega_L t); \tag{2.58}$$

Here, θ represents the angle between the initial polarization and the magnetic field H, defined as $\cos\theta = \frac{H_z}{H}$ and $\sin\theta = \sqrt{\frac{H_x^2+H_y^2}{H}}$. Additionally, $\omega_L = \gamma H$ signifies the Larmor frequency. Typically, muon spins stopping at the same site exhibit sensitivity to a range of fields, denoted by the probability density function $P(\vec{H})$. As a result, the temporal progression of the average polarization can be described as follows:

$$P_z(H,t) = \int_H P(\vec{H}) \left(\cos^2\theta + \sin^2\theta\cos(\omega_L t)\right)\, d\vec{H} \tag{2.59}$$

When investigating a polycrystalline sample, where the sample is treated as having an infinite number of randomly oriented crystallites, and under the assumption that the distribution solely depends on the magnitude of the fields, the expression is given by:

$$P_z(H;t) = \frac{1}{3} + \frac{8\pi}{3}\int_H \rho(H)\cos(\omega_L t)H^2\, dH \tag{2.60}$$

The first term, independent of time, is referred to as the "one-third tail." When studying a polycrystalline sample, approximately one-third of the muon spin components, on average, possess an initial polarization aligned in the same direction as the local magnetic field $\vec{H}$.

$$\rho(H) = \frac{(\gamma_\mu/\omega_L)^2\delta(H-\omega_L/\gamma_\mu)}{4\pi} \tag{2.61}$$

using the distribution,

$$\rho(H) = \frac{\gamma_\mu}{4\sqrt{2}\pi^{3/2}H^2\Delta}\exp\left[-\frac{2\gamma_\mu^2(H-\omega_L^2/\gamma_\mu^2)}{2\Delta^2}\right] \tag{2.62}$$

where the small Gaussian expansion of width Δ was introduced to describe a small distribution around an average local field of $\omega_L = \gamma_\mu H$, the time evolution of the average polarization is then expressed. (see Figure 2.12):

$$P_z(t;\omega_L;\Delta) = \frac{1}{3} + \frac{2}{3}\cos(\omega_L t)\exp\left(-\frac{\Delta^2 t^2}{2}\right) \tag{2.63}$$

2.6.6 Kubo-Toyabe relaxation and decoupling experiments

If muon spins are influenced by a more complex field distribution, the application of a longitudinal external field enables a deeper exploration of the characteristics of internal local fields in particular whether they are static or dynamical. Deriving an analytical expression for the mean polarization from Equation 2.59 can be challenging. Kubo and Toyabe addressed situations where internal static local fields are randomly oriented, as observed in dense spin glasses or in cases involving quasi-static nuclear magnetization. For a Gaussian probability density of

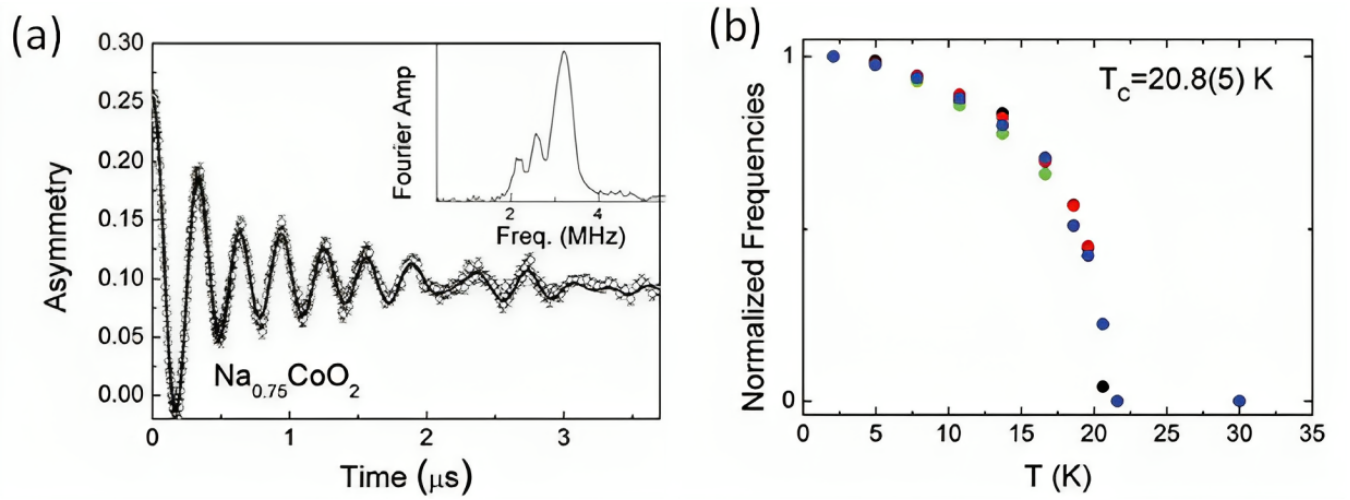

Figure 2.12: Adapted from [Mendels et al. 2005]. (a) Polarization (asymmetry) measured in zero external field at 5 K on a $Na_{0.75}CoO_2$ sample. The Fourier transform is presented as an inset. The oscillations and the "one-third tail" observed at this temperature indicate that muon spins are sensitive to static internal local fields, whose absolute value is little distributed. The frequencies identified thanks to the Fourier transform show the existence of multiple sites of muons. (b) Evolution of the four frequencies (normalized to the maximum values) as a function of the temperature. The magnetic transition to the ordered state at long range is clearly highlighted. The transition is obvious, whatever the muon site.

field components with zero mean value and width Δ [Hayano et al. 1979], [Kubo 1981]:

$$\rho(H^i) = \frac{\gamma_\mu}{\sqrt{2\pi}\Delta} \exp\left[-\frac{-\gamma_\mu^2(H^i_{loc} - -H^i_{\text{ext}})^2}{2\Delta^2}\right] \tag{2.64}$$

Using $\omega_{L,\text{ext}} = \gamma_\mu H_{\text{ext}}$, the average polarization is then formulated, for measurements conducted under a longitudinal field:

$$Pz(t;\omega_{L,\text{ext}};\Delta) = 1 - \frac{2\Delta^2}{\omega^2_{L,\text{ext}}}\left[1 - \exp\left(-\frac{\Delta^2 t^2}{2}\right)\cos(\omega_{L,\text{ext}}t)\right] + \frac{2\Delta^4}{\omega^3_{L,\text{ext}}}\int_0^t \exp\left(-\frac{\Delta^2\tau^2}{2}\right)\sin(\omega_{L,\text{ext}}\tau)d\tau \tag{2.65}$$

In zero field, the average polarization becomes:

$$Pz(t;\omega_{L,\text{ext}} = 0;\Delta) = \frac{1}{3} + \frac{2}{3}\left(1 - \frac{\Delta^2 t^2}{2}\right)\exp\left(-\frac{\Delta^2 t^2}{2}\right) \tag{2.66}$$

As depicted in Figure 2.13, the KT function exhibits Gaussian behavior at short times and reaches a minimum, for $\Delta \approx 3t$, before gradually converging to the "one-third tail" at longer times. Complete decoupling of internal local fields occurs when $\frac{\omega_{L,\text{ext}}}{\Delta} \approx 10$: the external field H_{ext} aligns parallel to the initial polarization, H_{ext} dominates over H_{loc}, and the polarization ceases to evolve over time, as depicted in Figure -2.13(a).

On the other hand in case of purely dynamical relaxation the effect of the external field is much weakened. For fast fluctuation of the local field with acharacteristic frequency ν, the asymmetry follows an exponential relation $e^{-\lambda t}$, where typically $\lambda \propto \frac{\nu}{\sqrt{\nu^2 + H^2_{\text{ext}}}}$.

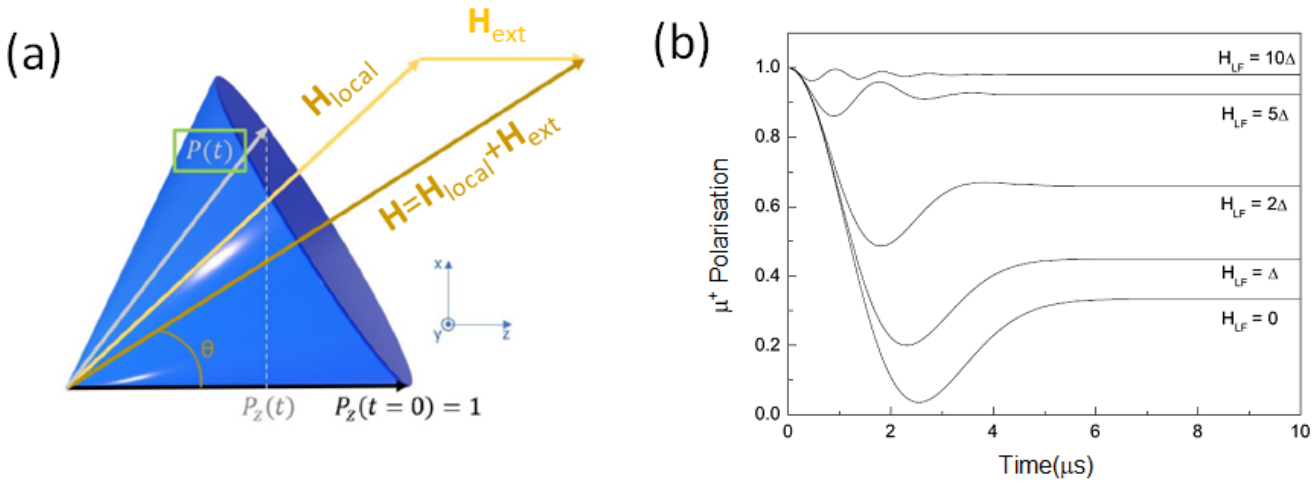

Figure 2.13: (a) Evolution of the polarization (blue cone) during the precession of a spin of a muon around the field $H = H_{\text{loc}} + H_{\text{ext}}$.(b) Static Kubo-Toyabe function with width $\Delta = 8\,\text{G}$ for the distribution of Gaussian fields. The application of a longitudinal field H_{LF} decouples the polarization. When $H_{\text{LF}} = 10\Delta$, the polarization is completely decoupled.

When dealing with the coupling of numerous nuclear spins to each muon spin or under the conditions of weak dipole interactions, it becomes feasible to overlook the coherent precession of individual spins. Instead, it becomes conceivable to treat muon spins as interacting with static internal local fields that are distributed in terms of intensity and orientation. In scenarios involving a Gaussian distribution, this approximation leads to the time evolution of polarization, which follows the Kubo-Toyabe function as described by Equation 2.66. In practical settings, for most crystals devoid of protons or fluorine ions, the polarization observed in the paramagnetic state at elevated temperatures, and in the absence of an external field, aligns with the Kubo-Toyabe function. The internal local fields arising from nuclear interactions typically exhibit quasi-static behavior throughout the muon's lifetime, thereby overshadowing electronic-origin fields that undergo rapid fluctuations in the paramagnetic limit. These electronic-origin fields are often of minor significance due to dynamic narrowing. The usual width of the distribution of internal local fields arising from nuclear interactions is approximately 10^{-4} T. Introducing a longitudinal field around 10^{-3} T is usually enough to decouple these fields.

2.6.7 μ-OH complex: strong dipole coupling with certain nuclear spins

In certain materials, including Y-kapellasite muons come to a stop in close proximity to nuclei with significant dipole magnetic moments, such as protons in OH groups or fluorine nuclei. This leads to the formation of complexes. Notable examples of such complexes are μ-OH, μ-F, and F-μ-F [Alexander Schenck and Crowe 1971; Lord, Cottrell, and Williams 2000]; [Lancaster et al. 2007];[Wilkinson and S. Blundell 2020]. The dipole interaction between the muon spin and the strongly magnetic nuclear spins of the bound proton or fluorine nucleus gives rise to a coherent precession of these spins, causing oscillations in polarization, as illustrated in Figure 2.14. This phenomenon entails

a coherent exchange of polarization between the initially fully polarized muon spin and the initially unpolarized nuclear spins. As an instance, for the scenario involving the creation of μ-OH complexes (encompassing two linked $1/2$ spins)[Lord, Cottrell, and Williams 2000], the expression for the average polarization is:

$$P_z^{OH}(t;\mathsf{OH}) = \frac{1}{6} + \frac{1}{3}\cos\left(\frac{\omega_{OH}t}{2}\right) + \frac{1}{6}\cos(\omega_{OH}t) + \frac{1}{3}\cos\left(\frac{3\omega_{OH}t}{2}\right) \tag{2.67}$$

$$\omega_{OH} = \frac{\hbar\mu_0\gamma_\mu\gamma_H}{4\pi d_{\mu-H}^3} \tag{2.68}$$

The symbol γ_H represents the gyromagnetic ratio of the proton, while d signifies the distance between the muon's position and the proton's position within each complex.

It's essential to acknowledge that even in situations where complexes are established, the nuclear spins existing outside of these complexes, which constitute the neighboring environment, exert an influence on the time evolution of polarization. This phenomenon results in a progressive decline of oscillations, termed polarization relaxation, as demonstrated in Figure 2.14. In situations involving the formation of $\mu - OH$ complexes, the following expression can be used:

$$P_{OH}(t) = p_{OH}(t;\omega_{OH})\exp\left(-\frac{\Delta_{OH}^2 t^2}{2}\right); \tag{2.69}$$

where $\Delta\omega_{OH}$ is the width of the distribution of internal local fields generated by the environment.

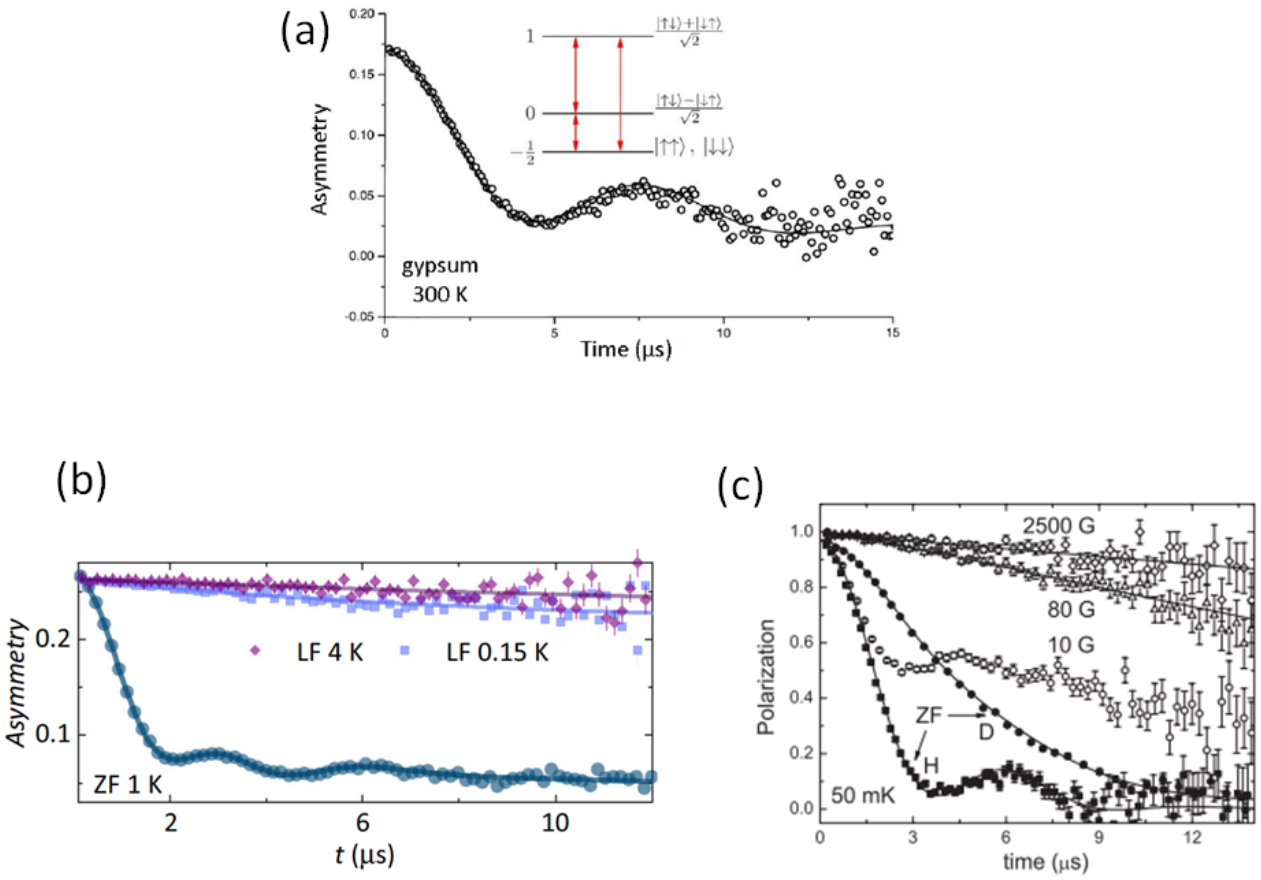

Figure 2.14: When a complex forms, the strong dipole interaction between the muon spin and a small number of nuclear spins leads to coherent precession of these spins. As a result, the polarization's time evolution attributed to muon spins involved in complex formation exhibits oscillations. (a) The polarization (asymmetry) measured in zero external field at 300 K on a $CaSO_4$•$2H_2O$ gypsum sample reveals the presence of μ-OH complexes. The insert depicts energy levels of a μ-OH complex: two spins with 1/2 quantum states interacting through dipolar interactions. The energy levels are given in units of $\hbar\omega_{OH}$. Red arrows indicate quantum interferences. (b)The time-dependent muon asymmetry was measured for $Zn_{0.66(1)}Cu_{3.34}(OH_6)FBr$ in zero-field at 1 K, where the solid line shows a fit using Eq-2.69, and in an applied longitudinal field of 10 mT at 0.15 and 4 K [Tustain et al. 2020]. (c) similar ZF and LF plot adopted from [Philippe Mendels et al. 2007] for Herbertsmithite.

Chapter 3

Yttrium Kapellasite [$YCu_3(OH)_{6+x}Cl_{3-x}$] Chronicles: Introduction to the enigmatic x= $\frac{1}{3}$ Version, $Y_3Cu_9(OH)_{19}Cl_8$

As mentioned in Chapter 1, noteworthy developments emerged from attempts to introduce yttrium ions (Y^{3+}) into herbertsmithite by substituting them for zinc ions, resulting in two compounds: $YCu_3(OH)_6Cl_3$ and $Y_3Cu_9(OH)_{19}Cl_8$. These compounds, collectively referred to as Y-kapellasites, can be represented generically as $YCu_3(OH)_{6+x}Cl_{3-x}$, with x taking values of 0 and 1/3. They were initially synthesized in 2016 [Wei Sun et al. 2016] and 2017 [Puphal, Bolte, et al. 2017], respectively.

Like other doped compounds, the Y-kapellasites exhibit insulating behavior. They appear as another example of the kapellasite-like structure [Fåk et al. 2012]. The $x = 1/3$ variant exhibits a distorted kagome structure with three distinct bond lengths, as depicted in Figure 3.2, resembling the anisotropic kagome model proposed in [Hering et al. 2022], detailed in Chapter 1. In the following sections, I will discuss the structure and magnetic models for both the $x = 0$ and $x = 1/3$ compounds to illustrate the development of these materials and the strong correlations and differences between their ground state physics and phase diagrams, as mentioned in [Hering et al. 2022].

3.1 Comparative Analysis: $YCu_3(OH)_{6+x}Cl_{3-x}$ (x = 0 and x = 1/3) - Exploring Structural and Magnetic Variations

3.1.1 Structural model:

In an endeavor to overcome the challenges arising from the coexistence of magnetic (Cu^{2+}) and diamagnetic divalent ions (Zn^{2+}, Mg^{2+}, etc.) and the subsequent disruption of the ideal Kagome lattices, a pioneering effort was undertaken to synthesize and characterize the compound $YCu_3(OH)_6Cl_3$ [Wei Sun et al. 2016]. This intriguing cuprate was prepared through a non-hydrothermal procedure and stands as an innovative exemplar of the kapellasite ($Cu_3Zn(OH)_6Cl_2$)-type structure [Colman, Ritter, and A. Wills 2008], [Fåk et al. 2012], featuring a trivalent cation Y^{3+}. The strategic placement of diamagnetic Y^{3+} cations at the Zn positions within the lattice, accompanied by the careful arrangement of additional Cl^- anions between the Kagome layers, effectively stabilized the structure by preventing any mingling of magnetic and diamagnetic ions within the kagome lattice. Consequently, the $YCu_3(OH)_6Cl_3$ compound retained the essential kagome lattice features.

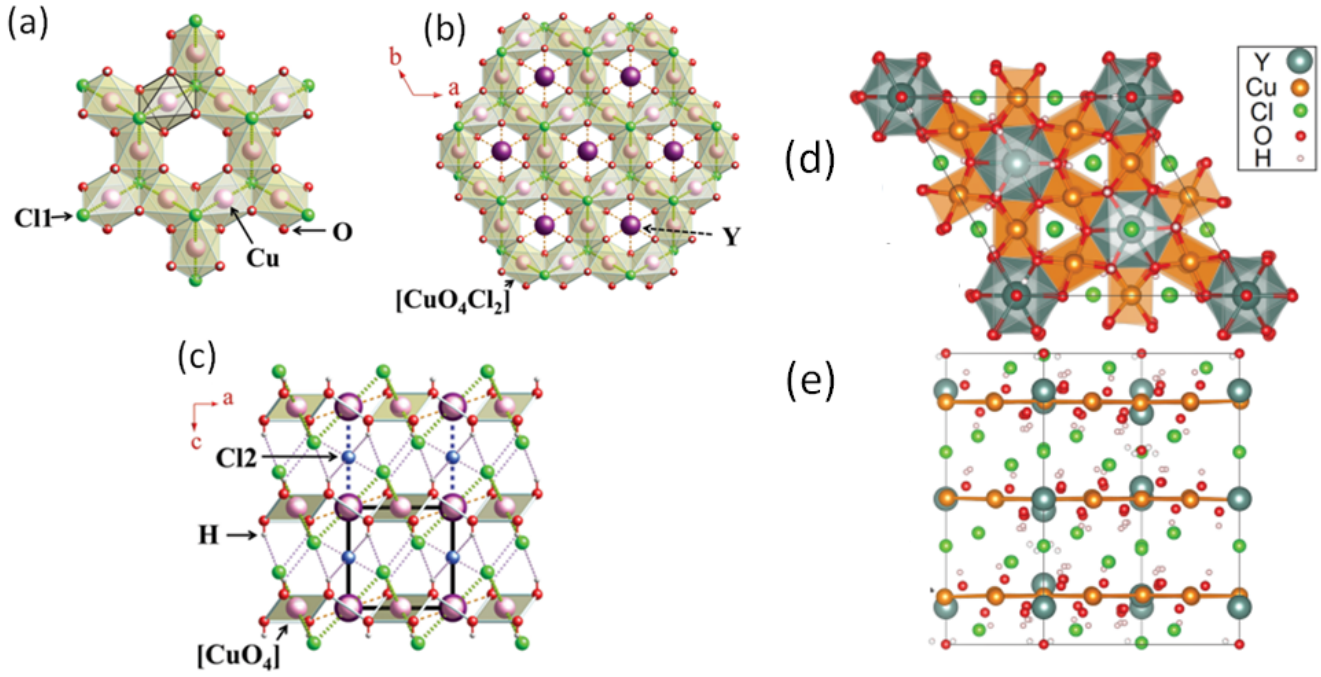

Figure 3.1: (a)–(c) Crystal structure $YCu_3(OH)_6Cl_3$ shown in-Wei Sun et al. 2016. Fig-(a) exhibits the linkage of $[CuO_4Cl_2]$ octahedra . The Y atoms are positioned within the layer, which is composed of $[CuO_4Cl_2]$ octahedra Fig-(b).(d)-(e) Structural model of $Y_3Cu_9(OH)_{19}Cl_8$. Fig-(d) shows a top view of the kagome layer in $Y_3Cu_9(OH)_{19}Cl_8$ crystallizing in the $R\bar{3}$ structure. Fig. (e) presents a side view of the kagome layer in $Y_3Cu_9(OH)_{19}Cl_8$.

The compound $YCu_3(OH)_6Cl_3$ possesses a distinctive crystal structure that exhibits an arrangement of Cu^{+2} atoms which is reminiscent of kapellasite. In each unit, there is a unique copper (Cu) site that interacts with four equatorial oxygen (O) atoms at a distance of $1.9736(10)$ Å, along with two apical chlorine (Cl1 site) atoms at $2.815(2)$

Å. This arrangement results in an intriguingly elongated and inclined octahedral configuration, denoted as [CuO_4Cl_2]. These elongated octahedra are linked to neighboring units by sharing edges composed of oxygen and chlorine atoms.

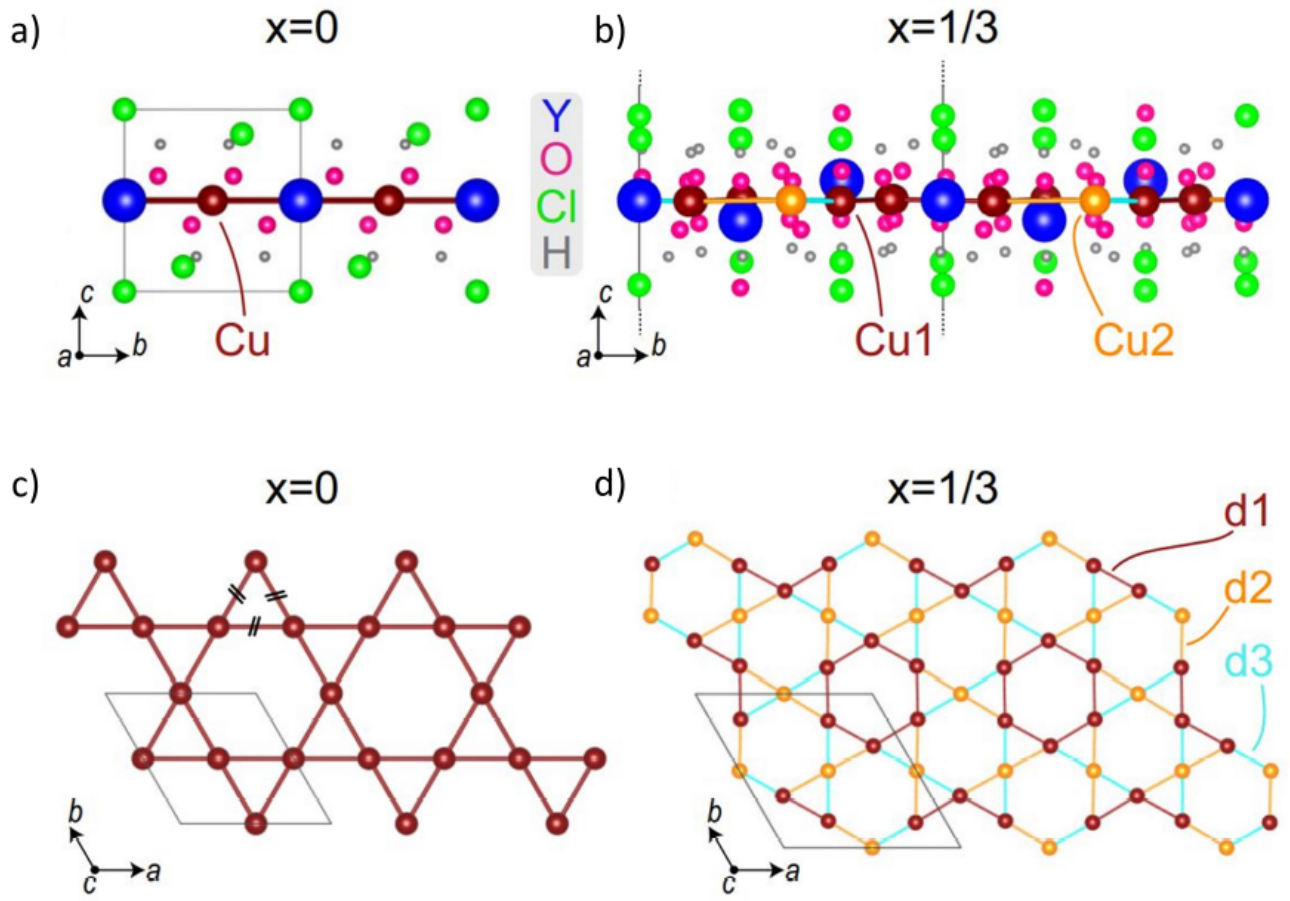

Figure 3.2: This figure is adapted from [Barthélemy, Puphal, et al. 2019]; (a) The crystal structure of $YCu_3(OH)_6Cl_3$ (x = 0 compound) is shown in a projected view along the a-axis. (b) In contrast, an isolated kagome plane in $Y_3Cu_9(OH)_{18}OCl_8$ (x = $\frac{1}{3}$ compound) is illustrated, projected along the a-axis. This view highlights the buckling of the Cu-Y layer. Additionally, the orientation of the a direction with respect to the kagome plane differs between the two compounds. (c) and (d) focus on the magnetic ions Cu^{2+} in the a-b plane for the x = 0 and x = $\frac{1}{3}$ compounds, respectively. The x = 0 compound displays a geometrically perfect kagome lattice. On the other hand, the x = $\frac{1}{3}$ compound features an anisotropic kagome lattice with two distinct copper sites, Cu1 and Cu2, along with three distinct bond lengths, d1, d2, and d3.

These Y atoms coordinate with six oxygen atoms and two additional chlorine atoms (Cl2 site). The crystal packing adopts an octahedral arrangement, where Cu^{2+} cations occupy 3/4 of the octahedral holes, while Y^{3+} cations occupy the remaining 1/4. The unit cell accommodates two distinct positions for chlorine atoms. Cl1 connects to three Cu atoms on one side and three hydrogen (H) atoms via hydrogen bonds on the other side. In contrast, Cl2 forms bonds with six hydrogen atoms in an octahedral configuration through hydrogen bonds. These linkages generate the Kagome layers formed by [CuO_4Cl_2] octahedra with Y^{3+} cations occupying the holes. The kagome layers are interconnected by hydrogen bonds between oxygen and chlorine atoms (O–HCl) and (Y1–Cl2) bonds

with AA stacking characteristic of kapellasite structure. While the structure was initially refined with disorder in the Y-positions [Wei Sun et al. 2016], a further neutron diffraction study reported in [Barthélemy, Puphal, et al. 2019] discarded it and pointed to a non-disordered P$\bar{3}$m1 structure with Y located exactly at the center of the kagome hexagon.

However, the $x = 0$ compound is not stable in water solutions, leading to a substitution of one Cl with OH resulting in the x=$\frac{1}{3}$ variant, $Y_3Cu_9(OH)_{19}Cl_8$, which was studied and documented in references [Puphal, Bolte, et al. 2017], [Barthélemy, Puphal, et al. 2019], [Chatterjee et al. 2023]. The samples for this compound were prepared using a hydrothermal method. This structural arrangement involves the stacking of kagome layers in an AA-type configuration same as x=0 variant but with a space group R$\bar{3}$ (see Figure 3.2(d)).The crystal structure analysis of this variant reveals the presence of two distinct Cu positions, which leads to a slightly distorted kagome layer.

The Y atoms are not located in the interlayer site. Instead, they are situated within the kagome layer itself, leading to a repeating pattern of kagome layers. The interatomic distances between the Cu atoms within the layer were measured to be d1=3.3762 Å, d2=3.3683 Å, and d3=3.2498 Å, while the distances between the layers were determined to be 5.8607 Å [Puphal, Bolte, et al. 2017]. The magnetic layers are observed to undergo a slight buckling, with a maximum ”thickness” along the c-axis of 0.06(1) Å. Moreover, a notable finding is that two-thirds of the yttrium ions (designated as Y1 in Table I) deviate from their ideal positions at the center of the stars. Instead, they are shifted by 0.646(7) Å along the c-axis toward the substitutional oxygen ions. In our study, we have employed a new synthesis method that has allowed us to produce high-quality single crystals devoid of impurities. The detailed analysis of the crystal structure, completed with a verified molecular formula, and an in-depth exploration of the influence of the substituted OH will be thoroughly discussed in Chapter [4], based on our neutron diffraction data, reported in reference-[Chatterjee et al. 2023].

The contrasting kagome arrangements and overall compositions of the two variants, $YCu_3(OH)_6Cl_3$ (x=0) and $Y_3Cu_9(OH)_{18}OCl_8$ (x=$\frac{1}{3}$), highlight the significance of exploring various magnetic models to comprehend the ground state behavior of these kagome systems.

3.1.2 Magnetic model:

The compound $YCu_3(OH)_6Cl_3$ stands out for its stable structure, characterized by the absence of common perturbations found in other materials, such as lattice distortion and intersite ion mixing. Despite these favorable conditions, $YCu_3(OH)_6Cl_3$ exhibits a long-range magnetically ordered state below a critical temperature (T_N) of 15 K [Arh et al. 2020; Zorko, Pregelj, Gomilšek, et al. 2019]. Neutron diffraction experiments reveal that the magnetic structure of $YCu_3(OH)_6Cl_3$ adopts a coplanar 120° state with negative vector spin chirality despite persisting spin dynamics, shown in figure-3.3. The ordered magnetic moments are notably suppressed to 0.42(2)μ_B down to the lowest experimentally accessible temperatures [Zorko, Pregelj, Klanjšek, et al. 2019; Barthélemy, Puphal, et al. 2019]. This

intriguing ordering on the kagome lattice is primarily attributed to Dzyaloshinskii-Moriya (DM) anisotropy (D/J $\sim$ 0.25), as confirmed by a comprehensive study in reference [Arh et al. 2020].

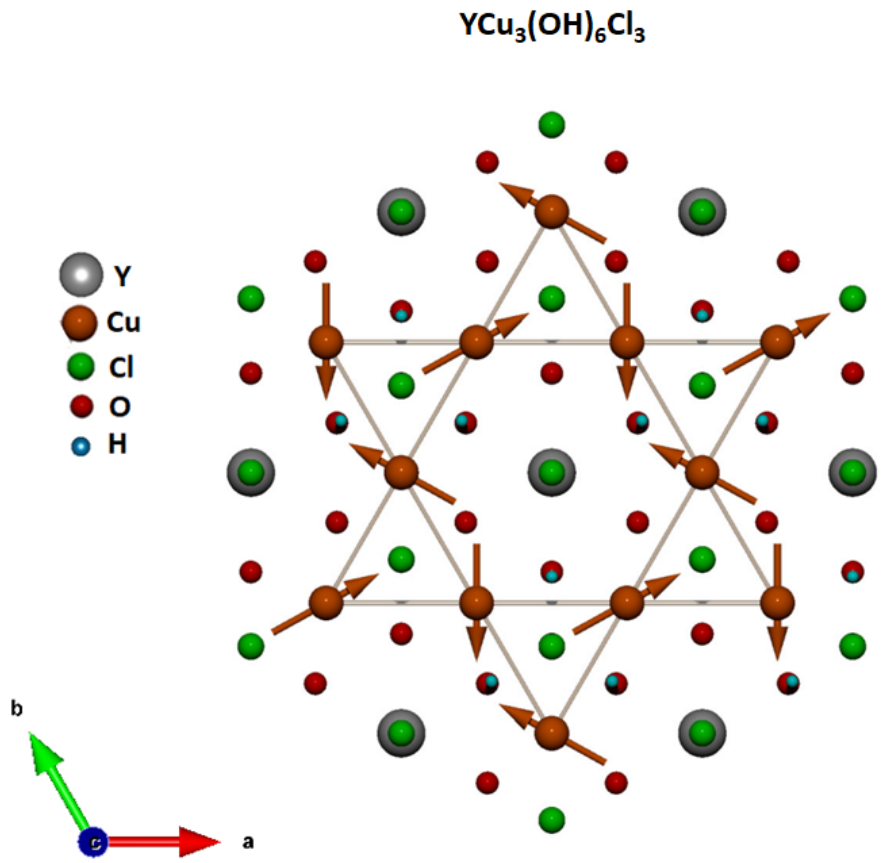

Figure 3.3: (a) Proposed spin texture in ref-[Zorko, Pregelj, Klanjšek, et al. 2019] for $YCu_3(OH)_6Cl_3$ compound, where a perfect kagome lattice of Cu^{2+} spin-1/2 ions (represented in brown) is established in the ab plane and arrows are showing spin texture at ordered state.

In contrast to its sister compound $YCu_3(OH)_6Cl_3$, the variant $Y_3Cu_9(OH)_{19}Cl_8$ has been the subject of divergent findings regarding its magnetic ground state in parallel with the evolution of the synthesis route and sample quality. A μSR study [Barthélemy, Puphal, et al. 2019] reported that powder samples of $Y_3Cu_9(OH)_{19}Cl_8$ exhibits a purely dynamical ground state, indicating the absence of long-range magnetic order down to very low temperatures ($\sim$ 20 mK). However, a separate investigation carried out by [Sun et al. 2021] presented an alternative view, where based on a combination of bulk susceptibility, specific heat, and magnetic torque measurements, the sample undergo magnetic ordering at a Neel temperature of T_N=11 K. It is now clear that the synthesis of this x=$\frac{1}{3}$ variant in [Sun et al. 2021] employed a different method which results in a mixture of $x = 0$ and $\frac{1}{3}$ (which is discussed in details in chapter [5]) rather than the one used in the previous study reported in [Barthélemy, Puphal, et al. 2019].

For our study presented in the following we used phase pure large single crystals which has shown magnetic ordering at 2.1 K. Triggered by the discovery of $Y_3Cu_9(OH)_{19}Cl_8$ and its original distorted kagome structure, Hering

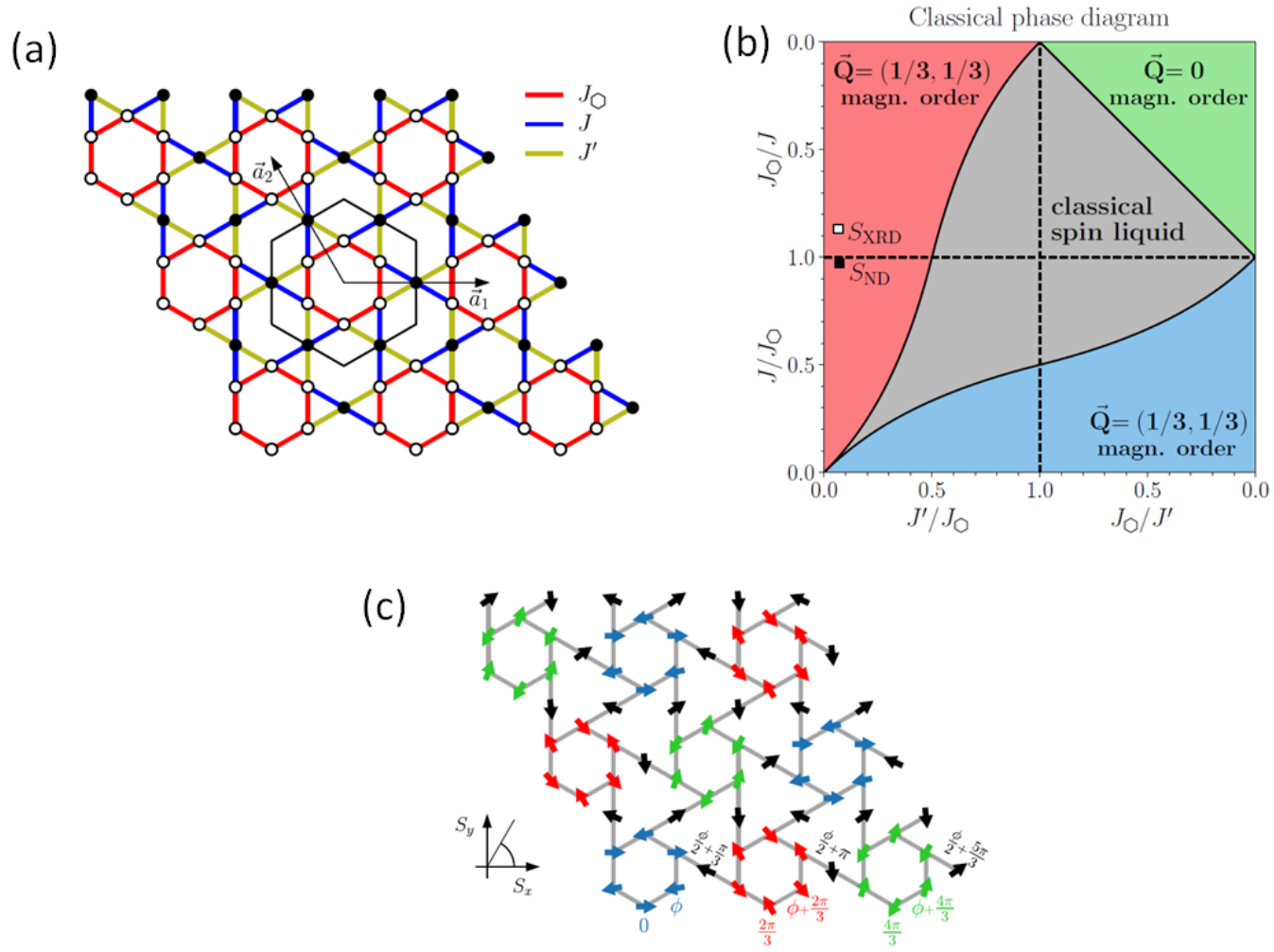

Figure 3.4: (a) A schematic depiction of the three exchange interactions defining the effective Heisenberg Hamiltonian in Y-kapellasite, labeled as J, J', and $J_\bigcirc$, as presented in [Hering et al. 2022], which has been previously discussed in Chapter 1. (b) The classical phase diagram for the distorted kagome model is illustrated. The diagram includes empty and filled squares, denoting two potential sets of couplings corresponding to Y-kapellasite, as determined from X-ray diffraction (referred to as S_{XRD}) and neutron structure analysis (referred to as S_{ND}). (c) Spin texture for classical $\vec{Q} = (\frac{1}{3}, \frac{1}{3})$ for $J > J'$ explained in detail in chapter [1].

et al. investigated the magnetic model discussed in chapter 1, which we reproduce here for convenience in Figure-3.4.

Hering et al. also computed the exchange interactions from first-principle calculations. Their calculations were based on the single crystal structure (S_{XRD}) of $Y_3Cu_9(OH)_{19}Cl_8$, using X-ray data from the reference [Puphal, Bolte, et al. 2017] and powder diffraction data (S_{ND}) from [Barthélemy, Puphal, et al. 2019]. They indicated that the optimal classical ground state in $Y_3Cu_9(OH)_{19}Cl_8$ should correspond to magnetic order with a periodicity characterized by $\vec{Q} = (\frac{1}{3}, \frac{1}{3})$, as shown in Figure-3.4 (b) by white and black squares. They obtained J $\sim$ J$\bigcirc$ $\sim$ 140 K and a much smaller J' $\sim$ 10 K. Their calculations included 24 different exchanges in-plane and interlayer, and they found that the three nearest neighbor exchanges in-plane, J, J', and J$\bigcirc$, are by far the largest ones, confirming the relevance of the magnetic model for $Y_3Cu_9(OH)_{19}Cl_8$.

3.2 Setting the Scene: Motivation and Approach to Investigate the x = $\frac{1}{3}$ Compound, $Y_3Cu_9(OH)_{19}Cl_8$

The presence of contradictory views regarding the ground state and the intriguing structural model of $Y_3Cu_9(OH)_{19}Cl_8$, with its three distinct nearest neighbor exchange interactions had sparked great interest within our research group at LPS (Laboratoire de Physique des Solides).

My PhD work aimed to shed light on the true ground state of $Y_3Cu_9(OH)_{19}Cl_8$, resolving the conflicting findings from previous studies [Puphal, Bolte, et al. 2017],[Barthélemy, Puphal, et al. 2019],[Sun et al. 2021]. By employing state-of-the-art experimental techniques and precise characterization, our collaborators and I sought to unravel the magnetic properties and understand the role of structural variations in this intriguing kagome system. We were fortunate to have access to large phase-pure single crystals of $Y_3Cu_9(OH)_{19}Cl_8$, which were prepared by P. Puphal at the Max Planck Institute in Stuttgart. The availability of high-quality single crystals (each weighs about $\sim$ 15 mg) allowed us to conduct precise local technique measurements and explore the intricate interplay between magnetic interactions, lattice distortions, and ground state behavior. I will discuss the comprehensive study we have done and compare our results with previous literature to develop a basic understanding of the physics concerning the materials.

In Chapter 4, we present a detailed analysis of macroscopic and thermodynamic measurements performed on single crystals. Initial susceptibility measurements and analysis were conducted by Quentin Barthélemy at LPS, and I later joined the group to further analyze the data and unravel the bulk magnetic properties. Collaborators mentioned in the respective sections assisted in conducting the heat capacity and thermal expansion measurements.

Chapter 5 and 6 delve into an extensive investigation using μSR and Cl NMR techniques. These local methods were employed to study and compare the predicted spin behavior in the ground state. The NMR study was a significant part of my PhD project, and I complemented these findings with the analysis of the μSR experiment performed on single crystals of $Y_3Cu_9(OH)_{19}Cl_8$.

In chapter 7, I discuss the spin-wave excitations through inelastic neutron scattering, with a significant contribution from Edwin Kermarrec. This work offers valuable information on the magnetic interactions that extends beyond first-principle calculations.

Summary

In summary, the substitution of Y^{3+} ions for Zn^{2+} ions in herbertsmithite results in the formation of distinct novel compounds exhibiting a kapellasite-like structure, denoted as $YCu_3(OH)_{6+x}Cl_{3-x}$, (x=0,1/3). The x=0 variant gives an almost perfect kagome which shows $P\overline{3}m1$ structure. This variant orders around $\sim$ 15 K and also significant amount of DMI contribution should be noted, D/J$\sim$ 0.25 in the system. On the other hand x=1/3 shows $R\overline{3}$ structure which exhibits a unique kagome lattice with three distinct nearest-neighbor exchange interactions, leading to a complex ground state phase diagram. Previous studies have reported conflicting findings, with some suggesting a spin liquid ground state and others indicating magnetic ordering . Our research aimed to resolve these discrepancies and shed light on the true ground state. A novel magnetic model has been proposed theoretically which suggests that x=1/3 variant shows $\vec{Q} = \left(\frac{1}{3}, \frac{1}{3}\right)$ ordering. Using a phase pure large single crystal through a comprehensive study using various experimental techniques, including thermodynamic measurements, Cl NMR, μSR, and inelastic neutron scattering, we explored the compound's magnetic behavior of the compound.

Chapter 4

Characterization of the single crystals Y-kapellasite: $Y_3Cu_9(OH)_{19}Cl_8$

Let's start our discussion on the experimental studies by characterizing the $Y_3Cu_9(OH)_{19}Cl_8$ single crystals synthesized by Pascal Puphal from the Max Planck Institute in Stuttgart which will be investigated in subsequent chapters. The compound was produced using an improved method of chemical crystal growth by the horizontal external gradient growth method in a thick-walled quartz ampoule, as described in detail for herbertsmithite in Ref. [T. Han et al. 2011]. The $Y_3Cu_9(OH)_{19}Cl_8$ crystals, ranging in size from $3 \times 3 \times 1$ mm^3 to $3 \times 3 \times 3$ mm^3, were successfully synthesized without the presence of any parasitic phases, offering a significant advantage over the conventional synthesis pathway described in [Puphal, Bolte, et al. 2017]. With the availability of these phase-pure large single crystals, I and our collaborators proceeded to conduct macroscopic measurements to characterize the behavior of $Y_3Cu_9(OH)_{19}Cl_8$ compound in detail. Specifically, susceptibility, heat capacity, thermal expansion, and neutron diffraction measurements were performed and are presented in this chapter uncovering a series of intriguing structural and magnetic transitions occurring at temperatures below 33 K.

4.1 Macroscopic susceptibility measurements, Y-kapellasite

The magnetization measurements were conducted by Quentin Barthelemy on the single crystals at LPS (Laboratoire de Physique des Solides). Subsequently, I analyzed the data to extract and illustrate the bulk magnetism characteristics of the samples under study. The magnetic moment measurements were conducted in the DC (Direct Current) measurement mode using a Quantum Design MPMS-XL SQUID (Superconducting Quantum Interference Device) magnetometer. The commercial SQUID utilized in our study exhibited high sensitivity to magnetic moments greater than 10^{-8} emu, allowing us to accurately measure the weak magnetization of our single crystals, which weighed approximately 15 mg. This experimental setup allowed us to measure the magnetic moment of our samples over a temperature range of 1.8 K to 400 K, depending on the applied magnetic field, which varied from -7 T to +7 T. Unlike NMR or μSR techniques, the SQUID magnetization measurements provide a macroscopic view of the sample's magnetic properties. The magnetization measured by SQUID is the cumulative effect of all magnetic contributions, including Van-Vleck paramagnetism, molecular diamagnetism, and the averaged magnetism of the kagome planes, considering contributions from various sites.

This comprehensive perspective offers valuable insights into the overall magnetic behavior of the sample. The magnetic susceptibility ($\chi_{\text{macro}}(T)$) of Y-kapellasite was measured in the temperature range from 1.8 to 300 K, with the applied magnetic field parallel to either the c-axis or the ab plane of the crystal. The variation of magnetic susceptibility with temperature is shown in Figure 4.1(a) for four different applied magnetic field strengths: H = 7 T, 3 T, 1 T, and 100 G. At low temperatures ($T < 20$ K), the magnetic susceptibility exhibits weak dependence on the applied magnetic field, while at high temperatures ($T > 20$ K), it becomes field-independent. In the paramagnetic regime, where the temperature is much larger than the applied magnetic field ($\mu_B H_0 \ll k_B T$), the magnetic susceptibility ($\frac{M}{H_0}$) remains field-independent as expected, indicating the absence of parasitic ferromagnetic phases in the sample.

Approximately above 100 K, the magnetic susceptibility $\chi_{\text{macro}}(T)$ exhibits a Curie-Weiss type dependence, given by:

$$\chi_{\text{macro}}(T) = \frac{C}{T + \theta_{\text{CW}}} \tag{4.1}$$

The antiferromagnetic Curie-Weiss curve shows a Curie-Weiss temperature for field along c axis, $\theta_{\text{cw}} = 102(2)$ K (fitted in the 300-150 K temperature range shown in Fig. 4.1.(c)). The obtained Curie constant (C) is $C_c = 0.547(2)$ cm^3.K/mol Cu and by using the value of C we have obtained Landé g-factor, $g_c = 2.40(2)$ using the formula:

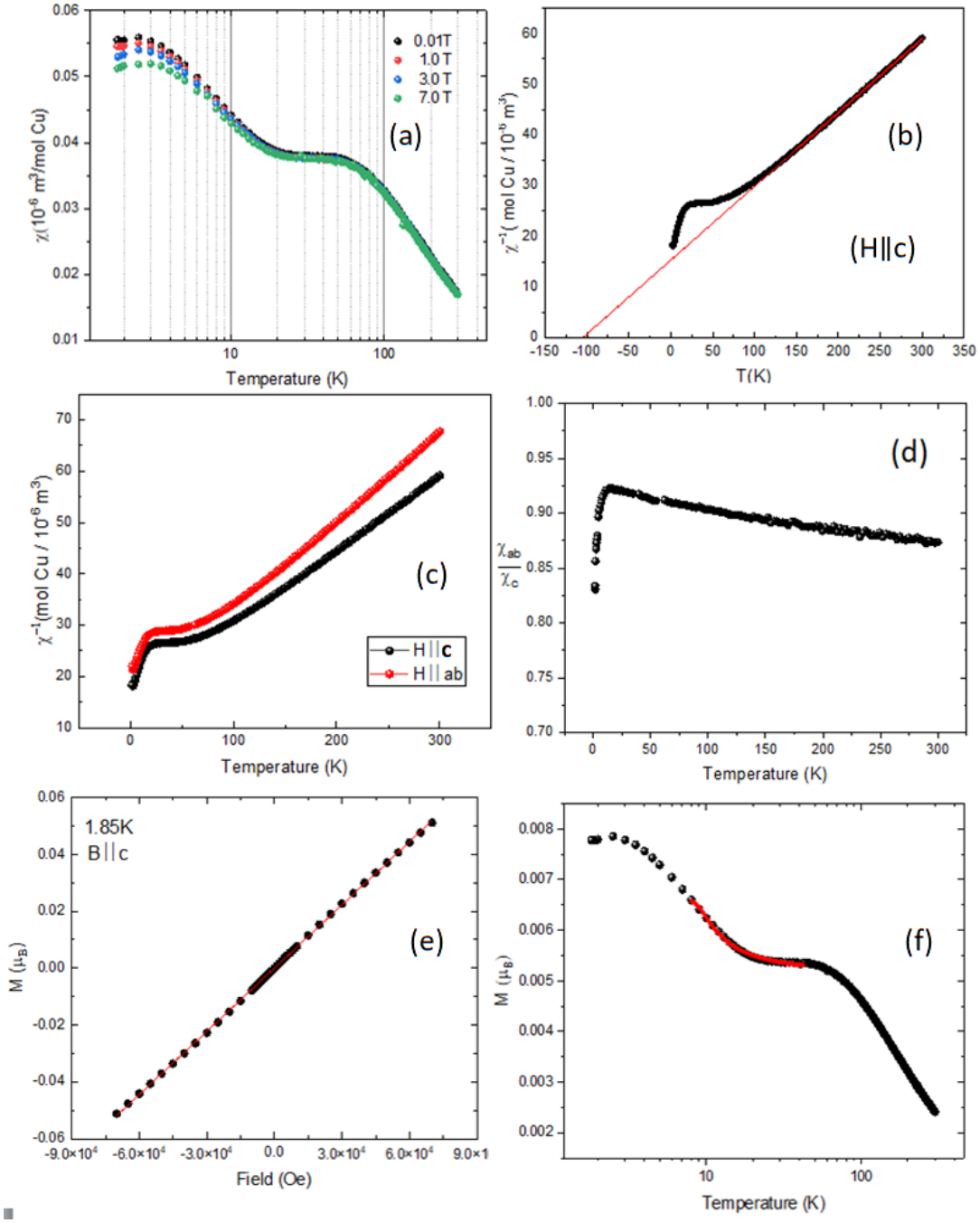

Figure 4.1: (a)Thermal variation of susceptibility with different external fields ($7T$, $3T$, $1T$) for $Y_3Cu_9(OH)_19Cl_8$ (b) Linear Curie-Weiss fitting at high temperature ($150 \leq T \leq 300$ K) in χ^{-1} vs T plot for configuration H$\|$c .(c) Inverse susceptibility measured with a $1T$ field applied along the c axis and in the ab plane. (d) Ratio between susceptibilities along c direction and ab plane.(e) Evolution of the magnetic moment as a function of field at low temperature ($T = 1.8$ K) in the configuration H$\|$c. (f) Fitting Brillouin function mentioned in 4.1 with the magnetic moment vs temperature data for configuration H$\|$c.

$$C = \frac{N_A(g\mu_B)^2 S(S+1)}{3k_B} = \frac{N_A \mu^2_{eff}}{3k_B} \tag{4.2}$$

The comparison of the susceptibilities measured with the applied field of 1 T along c and in the ab plane, shown in figure-4.1(c). Along the ab plane, $\theta_{\text{ab}} \approx 90(2)$ K and the Curie constant $C_{ab} = 0.459$ cm^3·K/mol Cu, with a g-factor of $g_{ab} = 2.20$. The corresponding effective moment is calculated along c axis $\mu_{eff} = 2.07\mu_B/Cu$ and along ab plane $\mu_{eff} = 1.89\mu_B/Cu$. The parameters we obtained in this study are very similar to those initially reported for differently prepared samples in [Sun et al. 2021] using the hydrothermal method. The magnetic field applied along both the c-axis and the ab plane exhibits a similar trend in the development of susceptibility with temperature, although it clearly indicates the c-axis as the easy axis of magnetization. The ratio $\frac{\chi_{ab}}{\chi_c} = \frac{g_{ab}}{g_c} < 1$ remains relatively constant down to approximately 15 K, shown in figure-4.1(d) . However, below this temperature the easy axis anisotropy gets slightly more pronounced.

Below 100 K, the increase in χ_{macro} deviates from the Curie-Weiss behavior, signaling the emergence of correlated effects. The magnetization versus field has been measured and no significant hysteresis cycle is observed down to 1.8 K as shown in 4.1(e). Yet, from figure-4.1(a) a small field dependence of susceptibility has been observed and in the figure 4.1(b) a reappearance of Curie behavior has been detected below $\sim$ 30 K. Such Curie-like behavior is a common issue in many kagome systems. This behavior is often attributed to quasi-free defects, the origin of which remains enigmatic. For example, in herbertsmithite, they are attributed to a 20-30% substitution of Zn^{2+} by Cu^{2+} at the interlayer site. To investigate the possible contribution of free spins in the sample. I analyzed the total magnetization (M) data as a function of temperature (T) and fitted the susceptibility with a Brillouin function under an externally applied magnetic field of 1 Tesla over the temperature change 5 K to 50 K. The employed phenomenological model for the fitting is described below:

$$M = nM_{\text{sat}} \tanh\left(\frac{g_c S\mu_B B}{k_B(T+\theta)}\right) + \chi_{\text{kag}} B \tag{4.3}$$

The hyperbolic term in the model represents the interplane spin response [Philippe Mendels et al. 2007], which is modeled using a function of Brillouin modified by the addition of the term θ to account for the weak coupling of these free spins. The magnetization vs temperature data obtained from the SQUID measurements is fitted to this function, as shown in Figure 4.1(f). The constant parameter $M_{\text{sat}} = N_A g\mu_B S$ represents the saturation magnetization of one mole of spin, where $S = \frac{1}{2}$ and we take $g_c = 2.4$. The parameter n represents the percentage of free spins per mole of the sample, and it is found to be just 0.14% of the total spins, which is a minimal amount. The second T independent part corresponds to the response of the spins of the kagome plane, with a strong interaction value that leads to a magnetization linear in field, resulting in a constant susceptibility of $\chi_{\text{kag}} = 0.033 \times 10^{-6}$m^3/mol Cu.

The magnetic moment exhibits a linear evolution as a function of field at low temperature ($T = 1.8$ K) [shown in Figure 4.1(d)] in the configuration B$\|$c. The susceptibility $\chi_{\text{macro}}(T)$ does not show any divergence up to 6 K, even for a weak applied field of $H = 100$ G [shown in Figure 4.2(a)]. However, an opening between the FC (Field Cooled)

and ZFC (Zero Field Cooled) curves is observed below 6 K, reaching its maximum around $\sim$ 2.5 (5) K. These low field measurements suggest the presence of a magnetic transition at approximately 2.5 (5) K, which will be further investigated in detail using neutron scattering and resonance techniques in the subsequent sections.

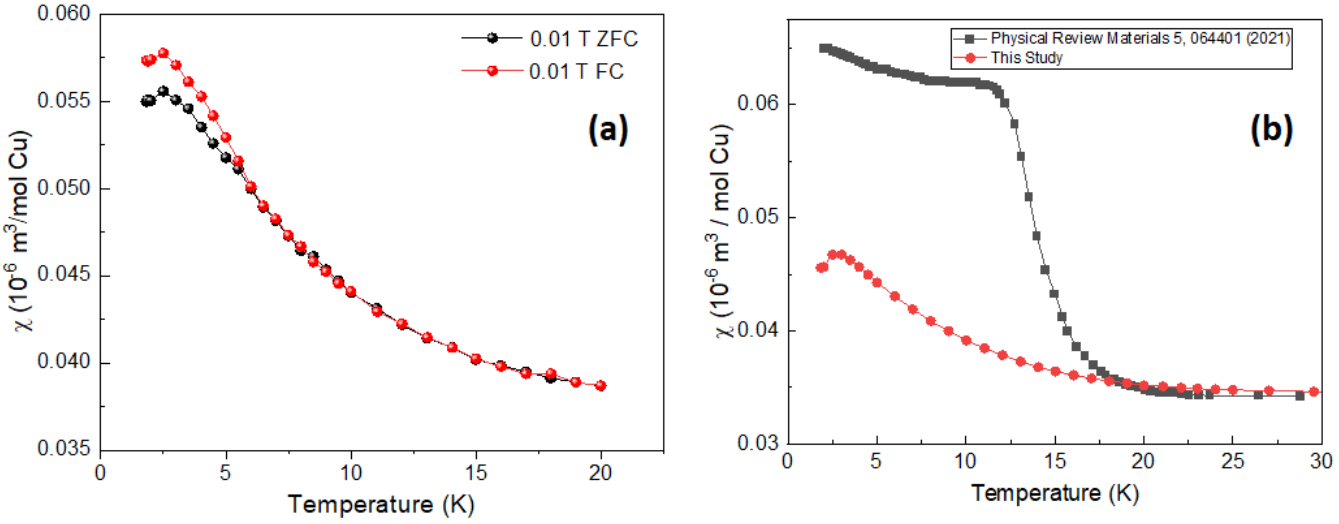

Figure 4.2: (a) Field cooled (FC) and zero-field cooled (ZFC) susceptibility measurements at 0.01 T magnetic field for $Y_3Cu_9(OH)_{19}Cl_8$. (b) Comparison of the susceptibilities at 1 T field for the crystal samples measured in this study and in Physical Review Materials 5, 064401 (2021).

Finally in Figure 4.2(b), a comparison is shown between our study and the previously reported single crystals in reference [Sun et al. 2021] regarding the magnetic susceptibility measurements. The comparison reveals a significant difference in the susceptibilities of the two crystal samples . Notably, a magnetic transition is observed around 11 K in the crystals studied in [Sun et al. 2021], while in our crystals, the transition occurs at much lower T $\sim$ 2.1 K. The observed Neel temperature in the previous work of [Sun et al. 2021] is in close proximity to the reported transition temperature of 12 K for the $x = 0$ compound, $YCu_3(OH)_6Cl_3$. The presence of a similar transition, reminiscent of the one observed in the $x = 0$ counterpart, supports the possibility of a phase mixture scenario also seen in specific heat.

4.2 Comparative study of specific heat measurement in Y-kapellasite

The specific heat was measured in P. Puphal's laboratory using the standard option of a Quantum Design Physical Properties Measurement System, employing a 5.94-mg inclusion-free single crystal. The temperature evolution of the specific heat is shown in Figure -4.3 and compared to the published results for $x = 0$ and $x = 1/3$ polycrystalline samples in [Barthélemy, Puphal, et al. 2019], as well to the $x = 1/3$ single crystal reported in [Sun et al. 2021]. Surprisingly, our $x = 1/3$ single crystal exhibits a distinct double peak at 33 K, which is absent in powder samples of the same compound. The underlying entropy change amounts to 0.1537 J/mol K, calculated using the powder sample as a baseline.

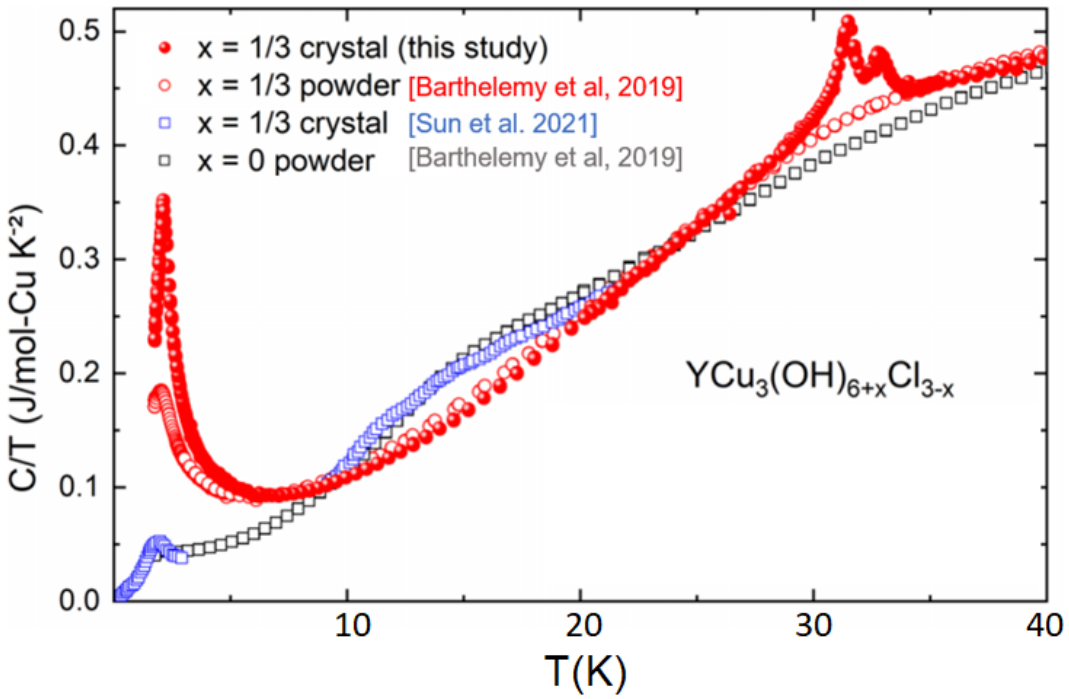

Figure 4.3: Comparison of the specific heat divided by temperature in the temperature range of 1.8 to 40 K for the $x = 1/3$ optimized large crystals with literature results for $x = 1/3$ and $x = 0$ powder samples [Barthélemy, Puphal, et al. 2019], as well as the reported inclusion-free $x = 1/3$ crystals from Ref. [Sun et al. 2021].

No sharp feature in the susceptibility is observed in this temperature range, suggesting that the double peak likely signifies a structural transition which is also confirmed by our neutron diffraction experiment discussed in this chapter. Importantly, this 33-K anomaly was not reported in the single crystals of reference [Sun et al. 2021].

The comprehension of the underlying reasons for the discrepancy between the presence of a specific transition in crystalline samples and its absence in powder samples remains limited. Powder samples, when synthesized below a specific threshold temperature, yield the formation of $YCu_3(OH)_6Cl_3$, while higher temperatures prompt the formation of $Cu_2(OH)_3Cl$. Previous research [Barthélemy, Puphal, et al. 2019] successfully achieved the synthesis of nearly phase-pure powder samples through very fine control of the synthesis temperature. However, despite these efforts, it is plausible that minute quantities of these parasitic phases, beyond the current detection capabilities of available

methods, may still persist within the samples. These trace impurities, even at exceedingly low concentrations, may have the potential to impede the observed structural (and magnetic) transition in the powder samples. Further scientific exploration is necessary to elucidate the precise influence of these subtle impurities on the overall behavior of the system. There is a significant hump observed around ~ 15 K in single crystals of Ref-[Sun et al. 2021] and the $x = 0$ powder sample, which are associated with magnetic transitions. The broad hump is absent in our phase-pure $x = 1/3$ single crystal, which is consistent with the macroscopic susceptibility data discussed in the previous section (Section 4.1). Thus it seems like that the sample used in reference [Sun et al. 2021] is a mixture of $x = 0$ and $x = 1/3$.

An anomaly at ~ 2.1 K, in the specific heat is observed in our study which has been also shown in previous reports for this compound in both powder and crystal form [Barthélemy, Puphal, et al. 2019], [Puphal, Bolte, et al. 2017]. Although for our single crystal the peak is sharper, a delta type cusp indicating a magnetic phase transition . However, the entropy gains in the above mentioned cases are comparable, approximately $0.1R\ln 2$, where $R\ln 2$ is the maximum magnetic entropy for this systems of $S = 1/2$ spins . This $\sim$ 2.1 K peak is attributed to a magnetic long-range ordering transition also investigated further with NMR, μSR and inelastic neutron scattering in next chapters.

4.3 Thermal expansion coefficient measurement for Y-kapellasite single crystal

To further investigate the anomalies at 33 K and 15 K, thermal expansion experiments were conducted by our collaborator Andrej Pustogow from TU Vienna. The experiments focused on measuring the thermal expansion coefficient α along the crystallographic c axis, which is perpendicular to the kagome layers. A capacitive dilatometer was used for these measurements. Figure 4.4 presents the thermal expansion coefficient $\alpha = \frac{1}{L}\frac{dL}{dT}$ (fractional increase in length per unit rise in temperature) in the temperature range where structural changes were observed in specific heat measurements.

We observe a similar anomaly below 33 K as in the C/T data, characterized by two slightly broadened peaks that overlap. The higher-temperature peak is larger than the lower-temperature peak, consistent with the trend observed in Figure 4.3. The relative length change associated with these sharp features is found to be $\Delta L/L = 10^{-4}$. Additionally, we identify another anomaly around 13 K, which is smaller in magnitude and can be examined in greater detail in inset (a). As the temperature drops below 5 K, a distinct anomaly in the thermal expansion coefficient α emerges, indicating the influence of magnetoelastic coupling as the system approaches the transition at 2.1 K, signifying the onset of antiferromagnetism.

In summary, the presence of distinct anomalies at both $\sim$ 13 and $\sim$ 33 K without any corresponding signature

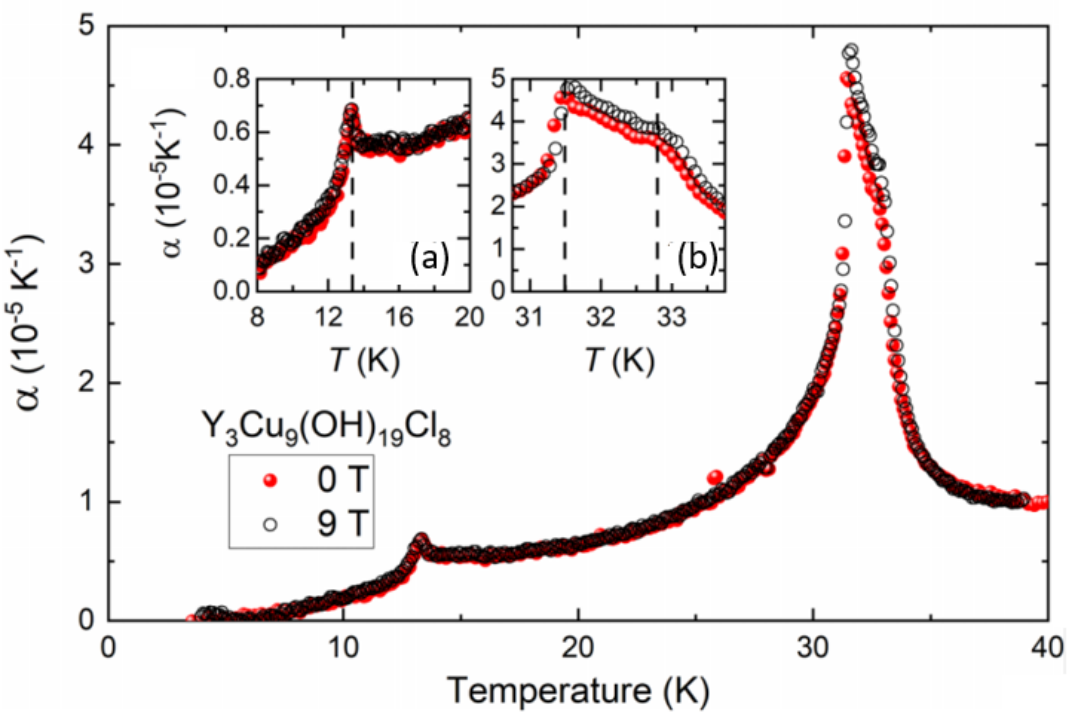

Figure 4.4: Evolution of the thermal expansion coefficient with temperature along the c-direction measured in one of the large single crystal of Y-kapellasite in two different magnetic field 0 and 9 Tesla . Insets (a) and (b) provide enlarged views of the peaks detected in the main panel around $\sim$ 15K and 33 K. It is worth noting that the two insets have different vertical scales.

in susceptibility provides strong evidence of significant structural effects within this compound featuring a distorted kagome lattice. Significantly, the application of a 9 T magnetic field along the c-axis does not induce any observable changes for the latter transition.

4.4 Neutron Diffraction measurements in Y-kapellasite

In collaboration with a team comprising Pascal Puphal, Edwin Kermarrec, Sylvain Petit (LLB), and Eric Ressouche (ILL), I participated in a neutron diffraction experiment using the D23 instrument, a two-axis thermal neutron diffractometer, at the Institut Laue-Langevin (ILL) in September 2021.

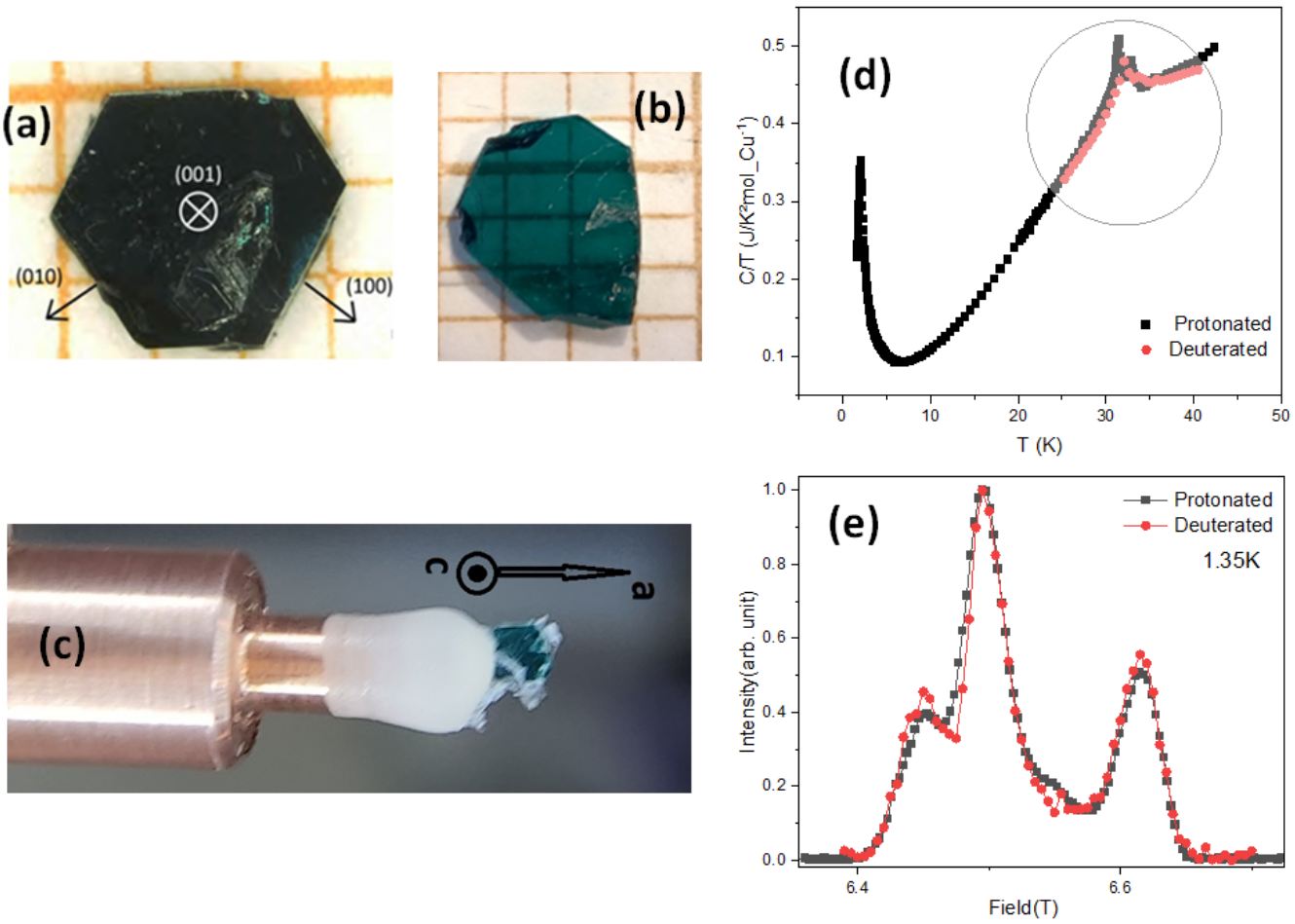

Figure 4.5: (a) Inclusion free deuterated crystal used for neutron diffraction experiment (b) where as protonated crystal used for NMR and μSR experiments (c) In the sample, the c-axis is aligned towards the viewer, and the a-axis is on the right. (d) characteristic peak at $\sim$ 33 K in specific heat in both deuterated and protonated crystal and (e) similar splitting of the ^{35}Cl NMR lines at 1.35 K (see chapter[6]).

The objective of this experiment was to investigate the crystal structure of a deuterated single crystal of $Y_3Cu_9(OD)_{19}Cl_8$ with a weight of 5.6 mg. Special care was taken during the preparation to ensure that the crystal was free from any inclusions and exhibited characterization consistent with the protonated sample, shown in figure-4.5. Indeed to further confirm the characterization of the deuterated crystal, I conducted specific heat measurements using the PPMS (Physical Property Measurement System) at LPS. This was done using the same crystal that was utilized in the neutron diffraction experiment, aiming to identify the unique $\sim$ 33 K peak, which serves as a distinctive characteristic for our samples. The comparison of the deuterated crystals' specific heat transition with

the protonated ones, as shown in Figure 4.5(d), revealed that both types of crystals exhibit the same transition behavior, validating the similarity of their structural models. To explicitly verify the magnetic transition and ground state similarities between the two types of crystals, I compared the 1.35 K ^{35}Cl NMR central line spectra (see figure-4.5 (e)). Remarkably, similar line splits were observed in both cases, providing strong evidence for the purity and consistency of the deuterated crystal used in the neutron study. To obtain accurate results, we meticulously aligned the crystal in the (HK0) plane using the Orient Express setup at ILL. The neutron diffraction measurements were conducted over a temperature range of 40–0.065 K, employing a fixed incident neutron wavelength of λ = 1.27 Å. Our primary focus was to investigate the impact of the structural transition occurring around $\sim$ 33 K on the crystal symmetry. Additionally, we aimed at examining the transitions at $\sim$ 15 K and $\sim$ 2.1 K by analyzing the atomic positions in the crystal structure. By comparing our findings with previously reported results from powder neutron diffraction in [Barthélemy, Puphal, et al. 2019] and x-ray data in [Sun et al. 2021], we aimed to gain a comprehensive understanding of the structural and magnetic properties of the $Y_3Cu_9(OD)_{19}Cl_8$ compound.

The refined crystal structure with R-3 space group closely matches the previously reported powder neutron diffraction data in Barthélemy, Puphal, et al. 2019. However, it is noteworthy to mention that in this reference [Barthélemy, Puphal, et al. 2019], there was a concern raised regarding the deuterium atom (D1) located next to O1 in the crystal structure. The refinement of its position indicated a distance of over 1 Å, which raised questions about its potential association with an O-H bond. As a result, the existence of the deuterium atom D1 was considered uncertain, leading to a revision in the chemical formula for the compound, as $Y_3Cu_9(OD)_{18}OCl_8$. To gain a deeper understanding of the crystal composition and address the uncertainties surrounding D1, P. Puphal and Samir Hammoud conducted further measurements using a combination of techniques. They utilized inductively coupled plasma mass spectroscopy (ICP-OES) with a SPECTRO CIROS CCD instrument and gas extraction with an Eltra ONH-2000 analyzer. These comprehensive measurements were essential in accurately determining the stoichiometry and hydrogen content of the compound. Additionally, vibrational O-H modes were observed, particularly associated with an electric field parallel to the kagome plane. Remarkably, these modes precisely matched the hydrogen/deuterium position (D1) in the crystal structure, providing further confirmation of its presence and role within the compound. Based on the compelling evidence obtained from these comprehensive measurements and observations, the ideal stoichiometry of $Y_3Cu_9(OH)_{19}Cl_8$ is confirmed and now adapted for our ongoing investigations and discussions.

Our $Y_3Cu_9(OH)_{19}Cl_8$ single crystal exhibits a crystalline structure that bears resemblance to kapellasite, shown in fig:4.6. This structural arrangement involves the stacking of kagome layers in an AA-type configuration, where yttrium ions occupy central positions within the hexagonal units (see Figure 4.7(c)). The separation distance between adjacent kagome layers is approximately 5.8 Å. The presence of chlorine ions plays a crucial role in effectively isolating the kagome layers from each other, leading to a strong decoupling similar to what is observed in kapellasite. Importantly, the diffraction data provide compelling evidence indicating the absence of any interchange or mixing

between yttrium and copper ions in these materials. Specifically, no copper ions are found between the layers or within the central regions of the hexagonal units. Considering the significant disparity in ionic radii between yttrium and copper, the likelihood of intermixing between these elements is indeed highly improbable.

From a chemical perspective, the substitution of one-ninth of the chlorine ions by oxygen ions in the $x = 0$ compound [Wei Sun et al. 2016] leads to the $x = \frac{1}{3}$ compound. This substitution occurs at the $O1$ sites, resulting in a superstructure with a unit cell size approximately nine times larger for $x = \frac{1}{3}$ compared to $x = 0$, while reducing the symmetry from $P3m1$ to $R\bar{3}$ space group, representing a rhombohedral crystal structure.

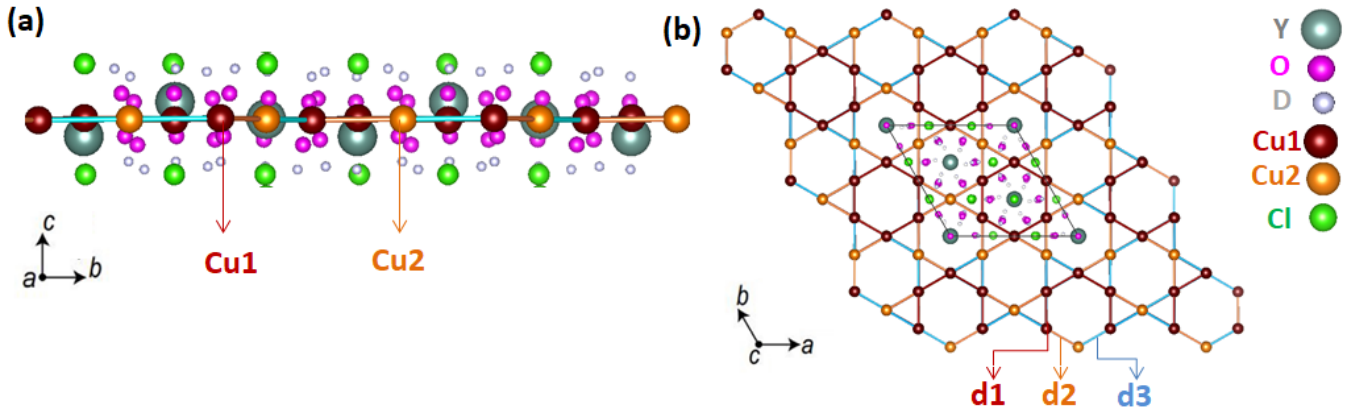

Figure 4.6: Kagome structure observed in our single crystal sample (which is not very different from previously reported [Barthélemy, Puphal, et al. 2019] already discussed in chapter [3]. (a) Along the a axis of a single kagome layer in the structure of the compound $Y_3Cu_9(OH)_{19}Cl_8$, there are displacements of both yttrium ions and copper ions with respect to the ideal geometry of the compound at $x = 0$. (b) View of the distorted magnetic lattice along c-axis, with two copper sites and three distances d1, d2 and d3, defining anisotropic interactions.

At the temperature of 40 K, the lattice parameters of the $Y_3Cu_9(OH)_{19}Cl_8$ crystal are found to be $a = b = 11.539(5)$ Å and $c = 17.1355(4)$ Å, with angles $\alpha = \beta = 90°$ and $\gamma = 120°$. It is worth mentioning the unique arrangement of D1, which occupies six equivalent sites with a partial occupancy of $1/6$ each. This information can be visualized in Figures 4.8(d) and (e). Also the kagome layers are not perfectly flat, they possess a thickness of 0.07(1) Å. The kagome network exhibits slight distortion, characterized by the presence of two types of copper sites, namely $Cu1$ and $Cu2$, which are located at the vertices of non-regular triangles. These triangles exhibit distinct side lengths, namely $d1 = 3.353(8)$ Å, $d2 = 3.328(11)$ Å, and $d3 = 3.314(8)$ Å. The distance between neighboring $Cu1$ sites is represented by $d1$, while the distances between $Cu1$ and $Cu2$ sites alternate between $d2$ and $d3$. This arrangement gives rise to two different types of hexagonal texture, as shown in Figure 4.6(b). Approximately one-third of the hexagonal patterns (highlighted in red in the figure) are regular, with a side length of $d1$, as they solely connect $Cu1$ sites. However, in the remaining two-thirds of the patterns, the hexagonal plates are irregular, with each side connecting a $Cu1$ site to a $Cu2$ site. This distinctive arrangement leads to an anisotropic magnetic network with three different anisotropic exchange energies, which plays a crucial role in shaping the magnetic properties and

behavior of the $Y_3Cu_9(OH)_{19}Cl_8$ compound.

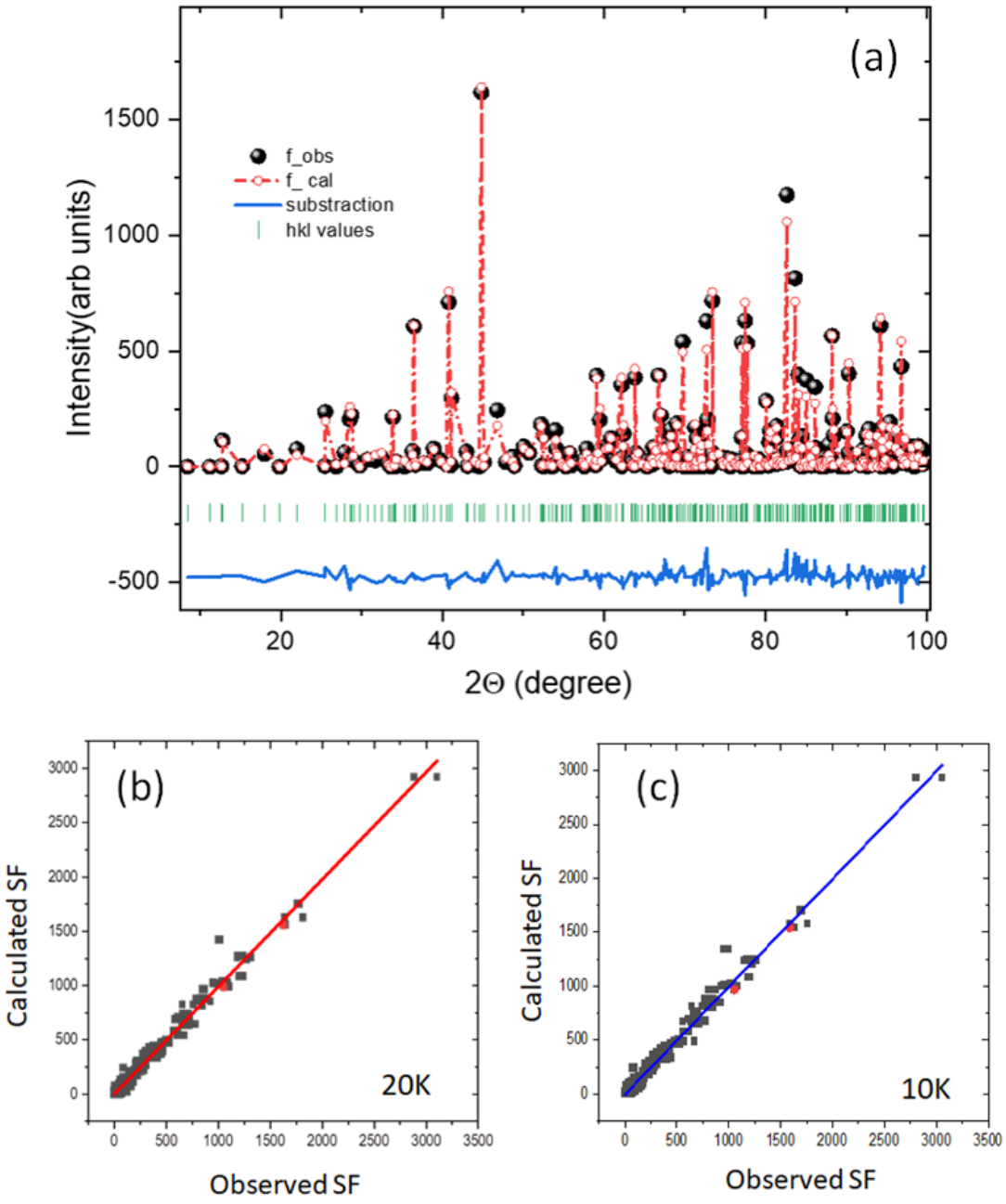

Figure 4.7: (a) Rietveld refinements at 40K with R$\bar{3}$ symmetry: the profile is calculated in red, peak positions are shown in green, and the difference between the calculated profile and the data is presented in blue. Green bars represent hkl positions. For temperatures of 10K and 20K, the observed and calculated structure factors are displayed with linear plots in (b) and (c) respectively. I have highlighted two points, (6,6,0) and (0,0,18), as red dots to emphasize that both of these Bragg peaks are in line with the R$\bar{3}$ structure and this bragg peaks will be studied with temperature scan, shown in figure-4.8 to investigate the $\sim$ 33 K transition.

Furthermore, it is observed that two-thirds of the yttrium ions, also referred to as $Y1$ sites in Table 4.1 (shown in Figure 4.6(a)), experience a shift from the center of the hexagonal kagome lattice. These displacements, projected

along the c-axis, correspond to a distance of $0.655(6)$ Å. These shifts lead to the formation of three distinct paths, each characterized by decreasing angles and corresponding to the distances between copper ions. The angle representing the superexchange path associated with distance d1 is $117.02°$(9), the angle $\angle$ Cu1-O4-Cu2 associated with distance d2 is $116.50°$(4), and the angle $\angle$ Cu2-O3-Cu1 associated with distance d3 is $113.0°$(5). These angles play a crucial role in determining the exchange interactions between the copper ions. Notably, the lower angle $\angle$ Cu2-O3-Cu1 leads to a lower value of J' compared to the other two exchange interactions [$J_{\hexagon} \approx J$], which are quite similar in magnitude.

As the temperature was gradually lowered, we observed a potential transition occurring around $\sim$ 33 K in both specific heat and thermal expansion measurements. To investigate this transition further, we conducted separate scans of the hh0 and 00l reflections as a function of temperature. Remarkably, both scans revealed a significant change in intensity at 33 K. This intensity change was observed across a wide range of Bragg reflections, displaying varying amplitudes between 40 K and 20 K. The temperature scans of the 660 and 0018 Bragg peaks, shown in Figures 4.8(a) and (b), clearly illustrate this abrupt intensity change of approximately 30% at the transition. Further examining the structure at 20 K, no noticeable alterations in lattice parameters or significant changes in the distance between Cu^{2+} ions have been observed. We emphasize that both of these Bragg peaks, (6,6,0) and (0,0,18), are consistent with the $R\bar{3}$ structure at 10 K and 20 K, shown in Figure 4.7 (b) and (c). Hence the kagome plane and super exchange angles still remain intact. However, the most observable changes occur at the D1 positions. The atomic positions are given in Table- 4.1. The initial publication, Puphal, Bolte, et al. 2017, first reported the crystal structure of Y-kapellasite [$Y_3Cu_9(OH)_{19}Cl_8$] with the R-3 space group. In that study, the positioning of hydrogen atoms was determined using symmetry-based arguments because the structure was evaluated with x-ray diffraction. Even below $\sim$ 33 K transitions we could reasonably refine all the data with R-3. However, in both cases, we did not observe any clear changes with temperature. The most plausible hypothesis suggests that the observed transition arises primarily from the D1 position within the crystal structure. At elevated temperatures, the D1 site exhibits a notable degree of mobility, allowing for dynamic rearrangements. However, as the temperature decreases, a progressive decrease in thermal energy causes the D1 site to undergo a freezing process. I received important suggestions and analytical help from Victor Baledent (Université Paris-Saclay, LPS) regarding D1 positions in the crystal structure: this freezing phenomenon culminates in an effective lowering of the crystal symmetry to the P1 space group. Within the P1 symmetry, the crystal system displays the manifestation of three distinct twin domains [shown in figure-4.9], indicating the existence of multiple crystallographic orientations. This complex interplay between temperature-dependent mobility and subsequent freezing of the D1 position contributes to the intriguing transition behavior observed in the system. Yet, given the potential existence of three different P1 configurations and hence domains, each dependent on the relative positioning of the three D1 sites within the unit cell, achieving a successful refinement with the P1 symmetry proves to be challenging with the available data. Consequently, we opted to refine our data using the currently known avarage R-3 structure, which demonstrated no significant

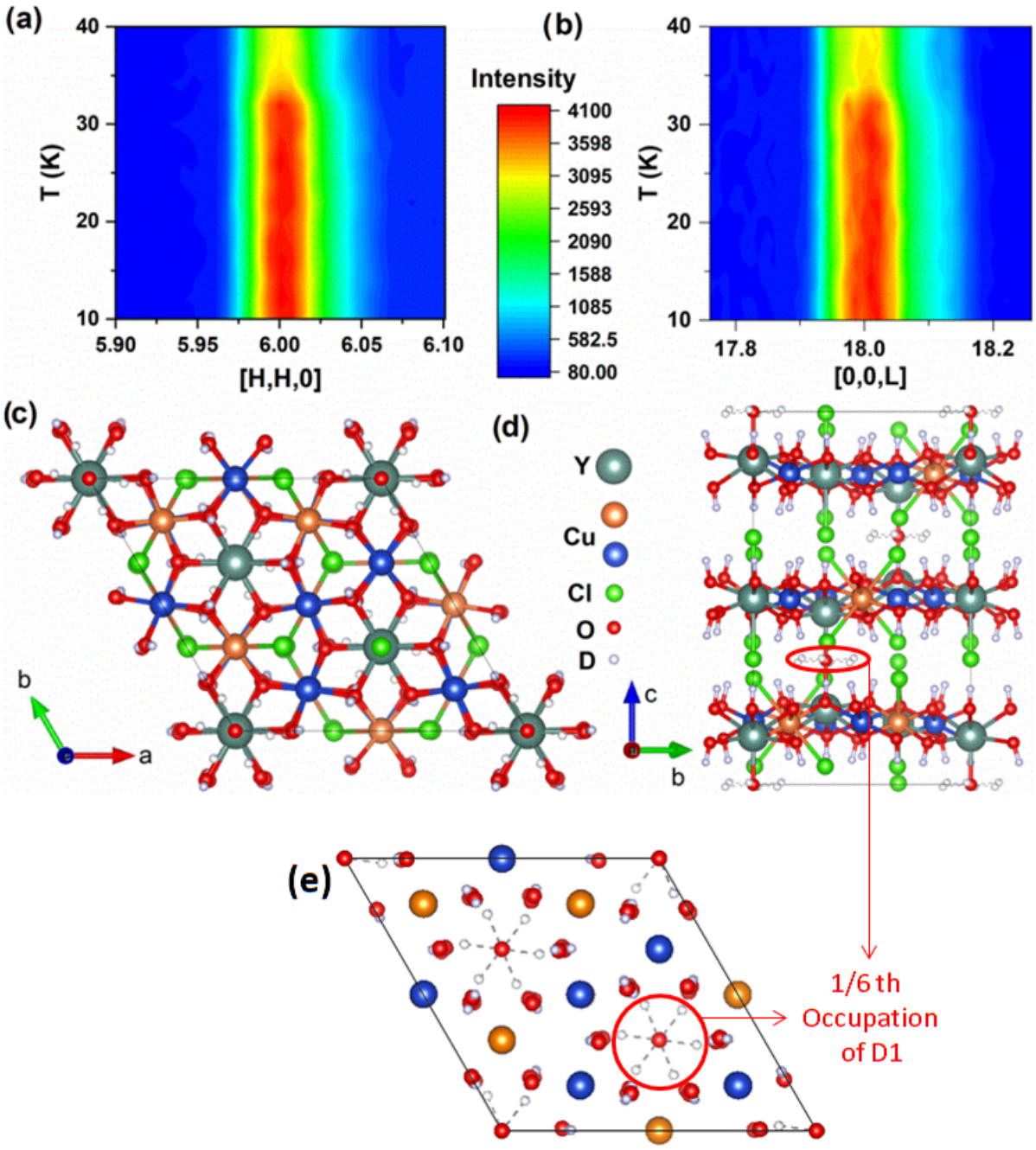

Figure 4.8: We conducted a temperature-dependent analysis by performing a scan with a step size of 2 K, focusing on the neutron diffraction intensity around the nuclear Bragg peaks, (a) (6,6,0) and (b) (0,0,18) peaks. To ensure consistency, the intensities in panel (b) were multiplied by 4/3 to match those in panel (a). The crystal structure was determined using neutron single crystal diffraction measurements at 40 K and was visualized along the (c) c-axis and (d) a-axis. Notably, within the structure, we observed a partial occupancy of 1/6 in the six interlayer D1 positions, (e) provides a c-axis view of the crystal structure of $Y_3Cu9(OH)19Cl_8$, excluding the yttrium and chlorine atoms to highlight the 1/6th occupation of D1.

alterations in the overall structure. Detailed results from the Rietveld refinement can be found in - Table 4.1.

During our systematic exploration of different temperatures, namely 40 K, 20 K, 8 K, and 65 mK, I carefully examined the behavior of the system. Notably, no significant changes were observed in the d1, d2, and d3 exchange

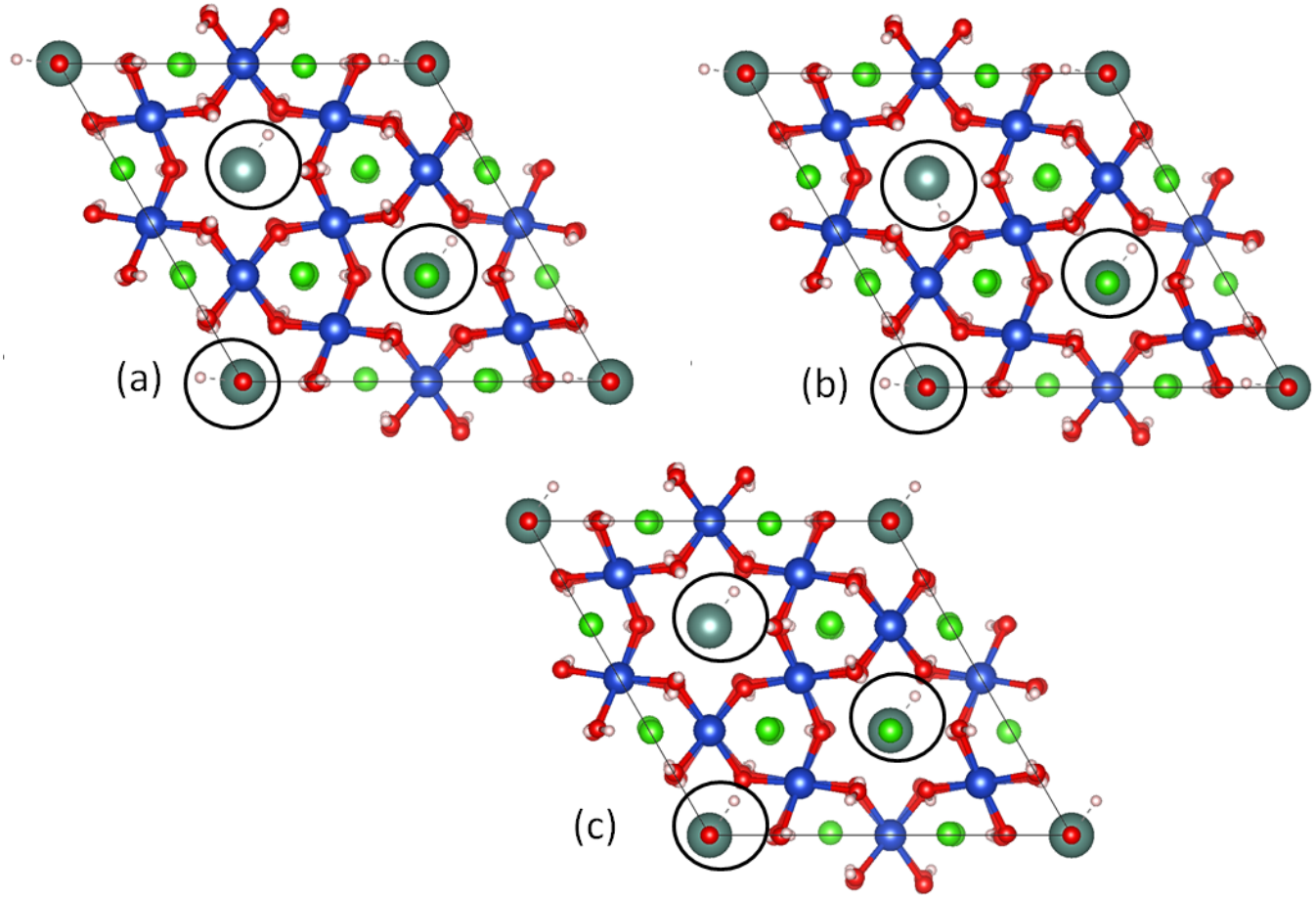

Figure 4.9: The crystal symmetry of $Y_3Cu_9(OD)_{19}Cl_8$ is thought to be reduced to lower symmetry, specifically P1 below 33K. In this reduced symmetry, the D1 site, where deuterons are located, exhibits distinctive freezing processes in three distinct ways, shown in (a), (b) and (c).

pathways.The superexchange pathways, represented by the Cu-O-Cu angle, are fundamental for comprehending the magnetic behavior of the system. Notably, these pathways remained unchanged throughout our investigation, indicating their stability and importance in mediating magnetic interactions. Additionally, our refined crystal structure, considering the R-3 symmetry, showed no major deviations in the lattice parameters. Interestingly, in the temperature range between 20 K and 8 K, there were no observable changes in the intensity of the system, as demonstrated in Figure 4.8 (a) and (b). This absence of intensity changes suggests that the observed transition at 15 K in the thermal expansion measurements may not correspond to a macroscopic symmetry breaking or a discrete jump in the order parameter, as typically observed in a second-order phase transition. Instead, it is plausible that this transition represents a crossover-like behavior, where there is a gradual release of entropy without a pronounced peak anomaly in the heat capacity.

The absence of magnetic Bragg peaks in the neutron diffraction q-scans at a temperature of 65 mK, despite a comprehensive exploration of reciprocal space, is a notable observation. The neutron diffraction scans were strategically designed to comprehensively explore a broad range of reciprocal space. In the h,h,0 plane, the scans

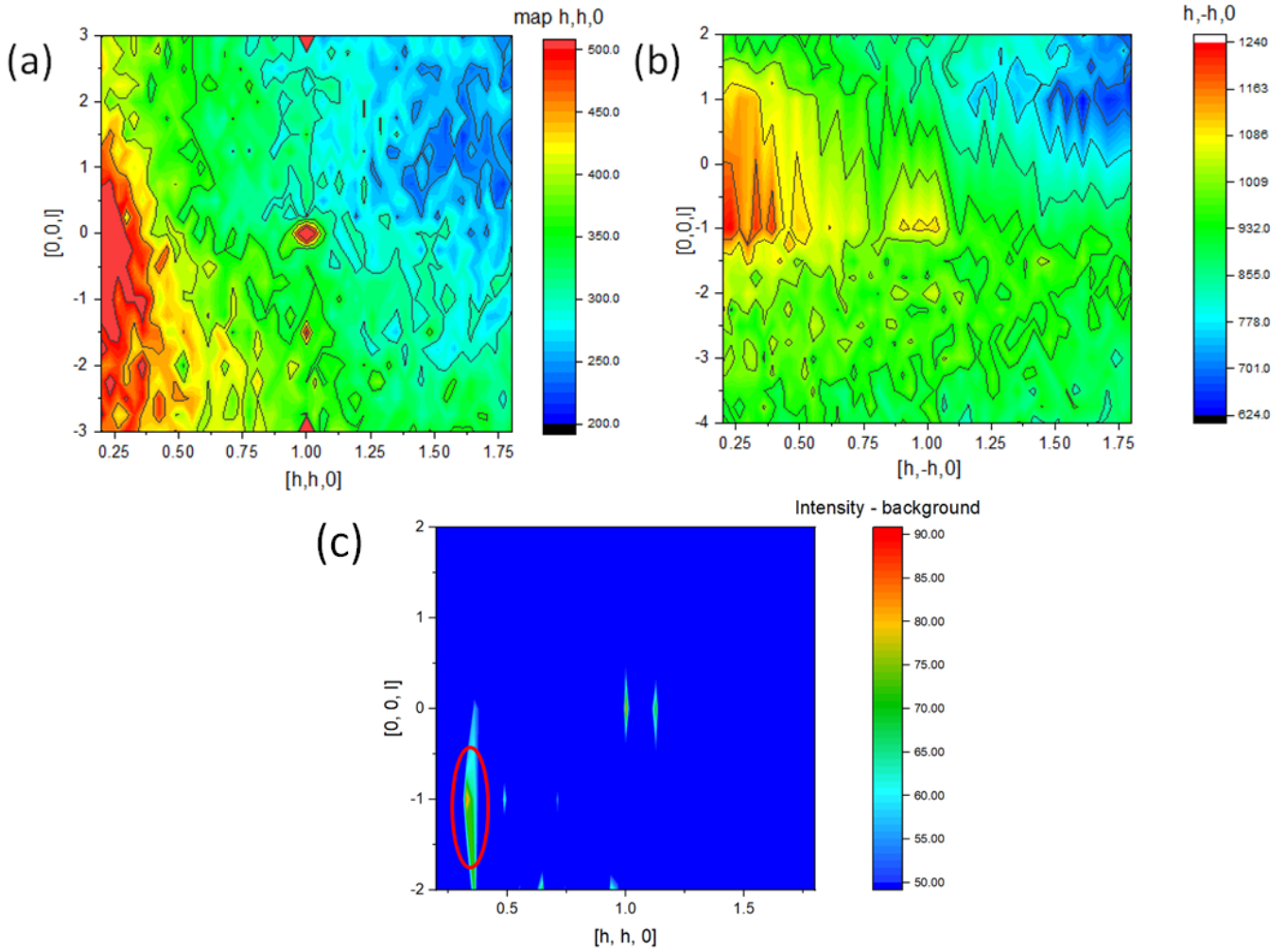

Figure 4.10: Map of Q-scans at 0.65 mK temperature. (a) Colour contour plot of Bragg intensities at hkl plane. (b) Similar plot for (h,-h,l) plane. (c) Substracted value of intensities of 40 K and 0.65 mK. The red circle is used to emphasize the positive subtracted intensity observed at (0.33, 0.33,-1) after subtraction.

covered a range from 0.20 to 1.8, while in the 0,0,l plane, the range extended from -3 to 3 with steps of 0.25 Additionally, to observe symmetric reflections in h,-h,0 plane, the same scan was performed with the same statistics (150000 cps). Certain intensity hikes were detected at the positions of nuclear Bragg peaks but no distinct magnetic Bragg peaks were evident. A particular area near (0.33,0.33,1) showed additional intensity upon subtraction of the 40K mapping data from the 0.65 mK data, as shown in Figure 4.10(c). However, it is important to note that measuring the magnetic wave vector (k) from a single Bragg peak can suggest multiple solutions, hence it is not conclusive in regarding magnetic order in the system. Also it is important to mention that this signal is weak, surpinsingly extended in the (0,0,l) direction and at low Q. Hence, it could be an artefact rather than a genuine magnetic intensity.

This observation is somewhat unexpected, especially considering the specific heat and susceptibility cusp observed around a temperature of approximately 2.1 K, which are indicative of a magnetic transition. The discrepancy between the absence of magnetic Bragg peaks and the other indications of magnetic ordering raises the possibility

of a scenario involving low magnetic moments of Cu^{2+} atoms in the kagome planes. To gain deeper insights and unravel the underlying mechanisms of magnetic ordering, it is essential to employ local sensitive techniques such as muon spin resonance (μSR) or nuclear magnetic resonance (NMR). These local probes can provide valuable information about the magnetic moments at the atomic level and shed light on the nature of magnetic interactions in the $Y_3Cu_9(OH)_{19}Cl_8$ compound.

Summary

In summary, our study of the x = 1/3 single crystal of Y-kapellasite revealed a distinctive double peak at 33 K in specific heat measurements. This double peak was absent in the powder samples and was not reported in previously studied single crystals. The absence of sharp changes in magnetic susceptibility (χ_{mag}) suggests that this peak at $\sim$ 33 K likely has a structural origin. Further thermal expansion experiments along the c-axis supported the presence of the 33 K and an additional 15 K anomalies.

Neutron diffraction experiments confirmed the $\sim$ 33 K peak, revealing a transition involving the freezing of the mobile D1 position and likely reducing symmetry to P1 with three different twin domains. Remarkably, despite the D1 position change, the average kagome lattice remained intact, with minimal changes in super exchange angles.

Additionally, a sharp peak at 2.1 K indicated a magnetic long-range ordering in specific heat data with divergence in FC/ZFC in magnetic susceptibility (χ). We also observed antiferromagnetic Curie-Weiss behavior with a Curie-Weiss temperature θ of around 100 K. No additional magnetic Bragg peaks could be detected at 65 mK with neutron diffraction measurement.

Table 4.1: Positions of atoms in the crystal structure at different temperatures.

T (K)	**0.065**			**8**			**20**			**40**		
	x/a	**y/b**	**z/c**	**x/a**	**y/b**	**z/c**	**x/a**	**y/b**	**z/c**	**x/a**	**y/b**	**z/c**
Y1	0	0	0.1318(7)	0	0	0.1314(6)	0	0	0.1324(7)	0	0	0.1302(5)
Y2	0	0	0.5	0	0	0.5	0	0	0.5	0	0	0.5
Cu1	0.6661(10)	0.8325(11)	0.5025(4)	0.6658(10)	0.8340(11)	0.5021(4)	0.6675(11)	0.8328(12)	0.5026(4)	0.6645(7)	0.8317(7)	0.5021(3)
Cu2	0.5	0	0.5	0.5	0	0.5	0.5	0	0.5	0.5	0	0.5
Cl1	0.6745(9)	0.0033(10)	0.2845(2)	0.6743(8)	0.0037(10)	0.28435(19)	0.6748(9)	0.0031(11)	0.2845(2)	0.6732(6)	0.0027(6)	0.28395(15)
Cl2	0	0	0.3368(5)	0	0	0.3368(5)	0	0	0.3365(6)	0	0	0.3373(4)
O1	0	0	0	0	0	0	0	0	0	0	0	0
D1	0.456(9)	0.776(10)	0.660(4)	0.455(9)	0.783(10)	0.664(4)	0.455(9)	0.776(10)	0.660(4)	0.462(7)	0.777(7)	0.661(3)
O2	0.8119(14)	0.8060(12)	0.5435(7)	0.8122(13)	0.8046(12)	0.5438(7)	0.8129(14)	0.8060(13)	0.5438(8)	0.8121(9)	0.8035(9)	0.5435(4)
D2	0.7769(19)	0.7778(17)	0.6011(9)	0.7874(18)	0.7858(17)	0.5991(9)	0.7723(17)	0.7722(16)	0.6030(8)	0.7866(13)	0.7827(13)	0.6005(6)
O3	0.5293(12)	0.6635(11)	0.5540(6)	0.5285(11)	0.6638(10)	0.5537(6)	0.5283(12)	0.6622(11)	0.5542(6)	0.5290(8)	0.6634(8)	0.5543(4)
D3	0.5494(17)	0.6731(18)	0.6065(8)	0.5575(16)	0.6709(17)	0.6082(8)	0.5452(15)	0.6740(18)	0.6051(8)	0.5548(12)	0.6692(13)	0.6069(5)
O4	0.5142(12)	0.8433(11)	0.4631(5)	0.5167(11)	0.8430(10)	0.4632(5)	0.5154(12)	0.8450(11)	0.4634(6)	0.5162(8)	0.8441(8)	0.4638(4)
D4	0.5008(16)	0.8310(17)	0.4096(8)	0.5013(16)	0.8328(16)	0.4097(8)	0.5018(17)	0.8320(17)	0.4099(8)	0.5029(12)	0.8337(12)	0.4099(6)

Chapter 5

Unveiling the Ground State of Y-Kapellasite: A μSR Investigation

In this chapter, we will focus on μSR studies conducted on single crystals of $Y_3Cu_9(OH)_{19}Cl_8$ (x = 1/3) and compare our results with those previously reported for powder samples in [Barthélemy, Puphal, et al. 2019]. In the previous studies involving bulk thermodynamics, neutron diffraction, and μSR experiments on powder samples, the authors did not observe any indications of magnetic freezing in $Y_3Cu_9(OH)_{19}Cl_8$ down to 20 mK, suggesting a possible a quantum spin liquid ground state. Motivated by the theoretical predictions of magnetic ordering at Q = $(1/3, 1/3)$ in $Y_3Cu_9(OH)_{19}Cl_8$ [Hering et al. 2022], along with compelling bulk thermodynamic properties and NMR results from single crystals discussed in the next chapter, we conducted a detailed μSR study to clarify the magnetic ground state of the material. Indeed, neutron diffraction did not give a compelling evidence for magnetic ordering.

As discussed in Chapter-[2], muons can detect small magnetic fields. Therefore, in order to investigate the magnetic properties of this distorted kagome compound at low temperatures, we aimed to determine whether the local fields experienced by the spins of the muons are static, indicating an ordered phase, or dynamic, suggestive of a spin liquid state. To achieve this, we conducted measurements at the Paul Scherrer Institute using the GPS and DOLLY beamlines, covering a temperature range from the high-temperature paramagnetic regime down to 0.28 K.

5.1 Experimental method

We started our experiment on the GPS beamline, where we measured muon signals in the temperature range $1.5\,\text{K} \leq T \leq 20\,\text{K}$. we packed a single crystal with dimensions $3 \times 3 \times 1\,\text{mm}^3$ and mass $\sim 15\,\text{mg}$ in an aluminum foil. We used a silver fork and a thin layer of aluminum tape to arrange the sample at the muon beam level. The veto mode was utilized to exclude muons that did not stop in the sample. We counted the number of muons stopping in

the sample, which was relatively low (17,000 muons stopped out of 100,000). Consequently, we mounted another single crystal with a similar shape and size, aligning them in a similar aluminum foil packaging that had been used previously. The number of muons stopping in the samples increased this time (27,000 muons stopped out of 100,000), providing a more prominent detector response to work with.

To measure at temperatures below 1.5 K, we utilized the DOLLY beamline, which is equipped with a ^{3}He cryostat (Oxford Heliox). This allowed us to investigate muon spin polarizations down to 0.28K. Similar to the GPS beamline, we used two co-aligned crystals in a copper foil with a thickness of 0.25 μm. The sample was arranged at the muon beam level using a copper fork, with a beam area of approximately $10 \times 10\,\text{mm}^2$. It was observed that around 30% of muons stopped in the sample with our setup. Hence we continued the experiment down to low temperatures (0.28K).

5.2 Muon sites determined at high temperature

In Figure 5.1, the spectrum obtained in the paramagnetic state at high temperature ($T = 20\,\text{K}$) and in zero field is shown where the incoming muon spins were parallel to c axis. In this regime, the electron spins fluctuate rapidly and inhomogeneously, hence the associated relaxation rate is negligible due to motional narrowing. The μSR signal is thus primarily influenced by the quasi-static magnetism of nuclear spins. Since muons are positively charged, they tend to stop at the most electronegative positions. Considering the structure of $Y_3Cu_9(OH)_{19}Cl_8$, muons can reside close to the OH^- groups and Cl^- ions in the crystal structure.

Although we have not obtained asymmetry data for longer times in our measurements, we have explored the possibility of the formation of μ-OH complexes with a typical slow oscillations, similar to those observed in herbertsmithite [Philippe Mendels et al. 2007], Mg-herbertsmithite [Kermarrec, Mendels, et al. 2011], or kapellasite [Fåk et al. 2012]. We considered these cases due to their similarities in origin and structure. These μ-OH complexes result from the dipolar coupling between the spins of the muons and the nuclear spins of the hydrogen ions, as introduced in Chapter 2. The spin of the muons probes the nearby largest nuclear spins. Therefore, at high temperature, the depolarization can be modeled by the equation:

$$a_0 P_{\text{para}}(t) = a_0 \left[f P_{\text{OH}}(t) + (1-f) K T_{\Delta_{\text{Cl}}}(t) \right] \tag{5.1}$$

The initial muon decay asymmetry $a_0 = 0.255$ has been obtained from the high-temperature fit under our experimental conditions. Here, f represents the fraction of muons forming μ-OH complexes. P_{OH} is the expected function for an μ-OH complex with Gaussian broadening Δ_{OH}. The remaining fraction, $1-f$, is attributed to muons that stop close to the Cl ions. KT is the Kubo-Toyabe relaxation, accounting for the Gaussian distribution of nuclear fields surrounding Cl^- atoms with a distribution width Δ_{Cl}.

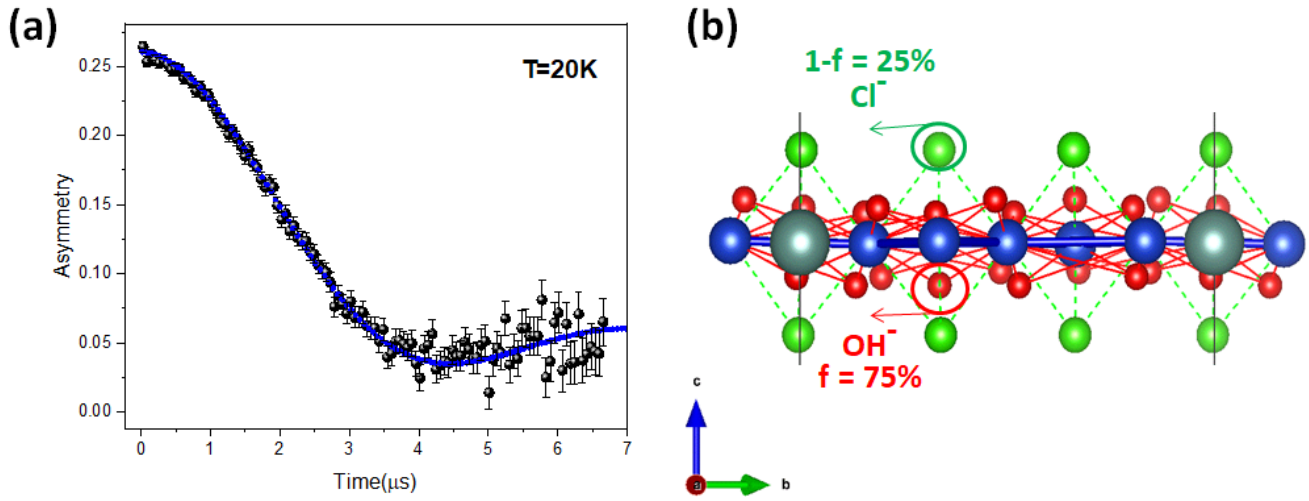

Figure 5.1: (a) Time evolution of zero field (ZF) μSR data at 20K , where the solid line indicates the fit with Equation 5.1. (b) A kagome layer of Cu^{2+} (blue balls) atoms, where OH^- (red balls) and Cl^- (green balls) represent electronegative sites where muons stop in the crystals. The parameter f from Equation 5.1 represents the percentage of muons stopping at the respective sites.

As explained in chapter 2, the calculated polarization used to describe the evolution at the OH^- site can be expressed as:

$$P_{\mathrm{OH}}(t) = e^{-\frac{\Delta_{OH}^2 t^2}{2}}\left[\frac{1}{6} + \frac{1}{3}\cos\left(\frac{\omega_{OH} t}{2}\right) + \frac{1}{3}\cos\left(\frac{3\,\omega_{OH} t}{2}\right) + \frac{1}{6}\cos\left(\omega_{OH} t\right)\right]. \tag{5.2}$$

where ω_{OH} is related to of the distance $d_{\mu-\mathrm{H}}$ between the muon and the nuclear moment of hydrogen, by the formula

$$\omega_{OH} = \frac{\hbar \mu_0 \gamma_\mu \gamma_H}{4\pi d_{\mu-H}^3} \tag{5.3}$$

$\gamma_\mu = 851.616$ Mrad/s/T and $\gamma_H = 267.513$ Mrad/s/T are the gyromagnetic ratios for muon and proton, respectively. The Gaussian prefactor is introduced to model the influence of random nuclear fields from further neighbors. The fitting has been done for zero field measurement at 20 K in GPS instrument using equations 5.1 and 5.2, and we obtained the fitting parameters at the paramagnetic region for static nuclear magnetization, which are presented in Table 5.1.

Static parameters	$Y_3Cu_9(OH)_{19}Cl_8$
$f\%$	75.00±1.00
ω_{OH} (Mrad.s^{-1})	0.55±0.02
$d_{\mu-H}$ (Å)	1.63±0.02
Δ_{Cl} (μs^{-1})	0.09±0.02
Δ_{OH} (μs^{-1})	0.208±0.02

Table 5.1: Static nuclear parameters derived from high temperature fit of the ZF asymmetry with Eq. 5.1.

The obtained fraction (f) in the fit agrees well with the molecular formula of the compound. Considering the 3:1

ratio of OH^- to Cl^- in the compound, the fraction of muons stopped near OH^- is three times higher than those probing Cl^- atoms. By employing the dipole pulsation ω_{OH}, we determined the distance $d_{\mu-H}$ to be approximately $\sim$ 1.6 Å between the position of the muon and the position of the hydrogen ion in an OH^- complex, as shown in Equation (5.3). Interestingly, this distance is quite similar to the distance between the two hydrogen ions of a water molecule ($\sim$ 1.5 Å), as observed in materials like herbertsmithite, Mg-herbertsmithite, or kapellasite [Philippe Mendels et al. 2007], [Fåk et al. 2012, [Kermarrec, Zorko, et al. 2014]. This observation further supports the formation μ-OH complexes in our system.

Thus, our analysis confirms the presence of at least two muon stopping sites based on the obtained spectra at high temperatures. While uncertainties persist regarding the exact distances of the muon stopping sites with respect to the neighboring magnetic Cu^{2+} atoms, a meaningful comparison can be made with a reference study [Tustain et al. 2020]. In this study, Zn-barlowite exhibits similar Cu-OH distances [approximately $1.5 - 1.9$ Å] to those observed in Y-Kapellasite, where muon positions could be computed and the long-range order is known.

5.3 Probing the magnetic ground state of $Y_3Cu_9(OH)_{19}Cl_8$

As discussed in Chapter 3, $Y_3Cu_9(OH)_{19}Cl_8$ exhibits a distorted kagome lattice and was proposed theoretically to host a long range order in magnetic ground state with a propagation vector of $Q = (\frac{1}{3}, \frac{1}{3})$ reported in Ref. [Hering et al. 2022]. Our μSR measurements at low temperatures indicate a distinct indication of the development of essentially static magnetism, associated with the freezing of the electronic spin degrees of freedom that decorate the kagome network.

As the temperature decreases, the relaxation rate of the μ^+ spins progressively increases, signifying the slowing down of fluctuations around a potential magnetic transition see in figure-5.2. Below $\sim$1.5 K, the shape of the asymmetry can be modeled by the following equation:

$$a_0 P_f(t) = a_0 \left[\frac{2}{3} \cos(\omega_f t + \phi) e^{-\frac{\sigma^2 t^2}{2}} + \frac{e^{-\lambda_f t}}{3} \right] \tag{5.4}$$

The above equation (Eq. 5.4) accounts for a magnetically ordered phase. In this equation, the coefficients $2/3$ and $1/3$ are used to represent the oscillatory and non-oscillatory components in our single crystal, respectively. The coefficients obtained indicate the presence of a randomly oriented local magnetic field with respect to the muon spin polarization, which is commonly observed in polycrystalline samples with randomly oriented grains. In single crystals, these coefficients can vary between zero and unity as the orientation between the local field and muon polarization can span from 0° to 90°. The exact direction of the local magnetic field in our system is currently unknown, even when considering the spin texture proposed in [Hering et al. 2022]. This is due to the contributions of finite dipolar fields from different kagome planes, leading to a random distribution of the local field at a certain

muon position. Additionally, the existence of multiple muon sites contributes to variations in obtaining the dipolar field values for each positions. Therefore, the system's behavior suggests that the local magnetic field is effectively averaged, resulting in an interpretation where approximately '1/3' of the field components are directed parallel to the initial spin direction of the muon, showing no precessions and slow relaxation (λ_f). Meanwhile, around '2/3' of the field components are perpendicular to the initial muon spin direction, inducing precession and time-dependent decay of the signal. The ordering function we mentioned as P_f in equation (5.4), shows a characteristic minima like a damped oscillation around '1/3'rd value of asymmetry depicting a development of a static local magnetic field in the system. In the frozen state, all muons precess with the frequency $\omega_f = \gamma_\mu B_{\text{int}}$. Hence, we observe the development of the internal magnetic field, B_{int}, as a function of ω_f. At the base temperature, we used this relation to determine the value of the internal magnetic field, which is $B_{\text{int}} = 8.6$ mT. An additional damping term has been introduced, where the damping parameter σ represents the width of the distribution of the internal magnetic field, as shown in Figure 5.3. In comparison with the internal magnetic field, we obtained a strong damping constant of $\sigma/\gamma_\mu = 3.2$ mT at the base temperature. The last term in Equation 5.4 represents the residual fluctuation in the frozen state.

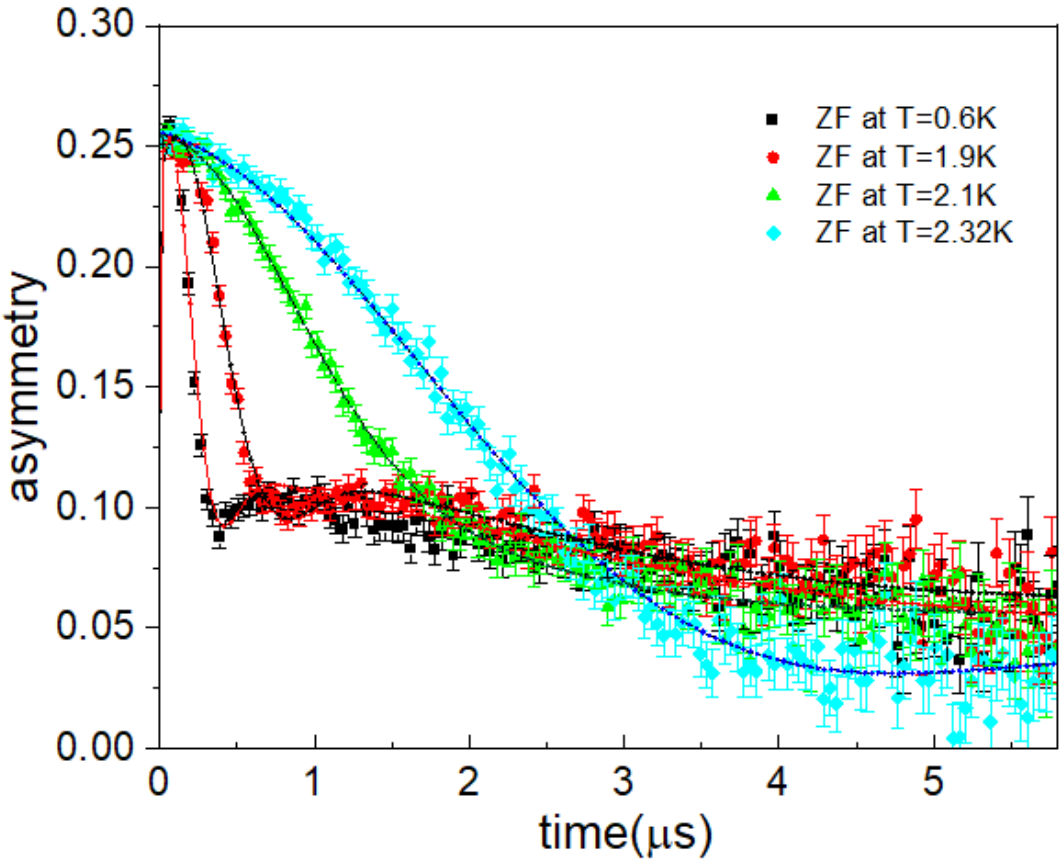

Figure 5.2: (a) Time evolution of zero field (ZF) muon decay asymmetry from 2.32 K to 0.6K. Solid lines are for the fits using the equation-5.5.

To fit the asymmetry across the entire temperature range, we combined equations 5.1 and 5.4 using a switching parameter f_f to track the frozen volume fraction in other words the portion of the sample where the electronic spin

degrees of freedom are frozen. The comprehensive equation used for fitting the complete set of μSR data is as follows:

$$a_0 P(t) = a_0 \left[f_f P_f(t) + (1 - f_f) P_{para}(t) e^{-\lambda_p t} \right] \tag{5.5}$$

By keeping all the static nuclear parameters constant (from Table 5.1), we were able to determine the frozen fraction (f_f), the oscillation frequency (ω_f), and its damping rate, as well as the relaxation rate λ_p or λ_f for the paramagnetic or frozen phase (as shown in Figure 5.3-(d)).

In the paramagnetic region, the frozen fraction (f_f) is zero, making the second part of the equation the only relevant component. Fluctuations are accounted for in the relaxation parameter λ_p. As the temperature decreases towards T_N, correlations between spins increase, the dynamics slows down leading to sharp changes in relaxation, which are clearly observed as a prominent peak at approximately 2.1 K. Concurrent with the relaxation rate, the frozen fraction begins to develop around 2.1 K taken as the transition temperature. The frozen fraction gradually approaches unity down to 1.8 K, indicating a fully ordered magnetic state. Additionally, it is worth mentioning that below 2.2 K, nuclear oscillations are completely overcome by a certain onset of damped oscillations, which causes the slow-relaxing '1/3' rd component of the frozen function P_f to cross over the high-temperature nuclear relaxation tail at longer times. This is an expected signature for static magnetism as shown in figure-5.2. These observations definitely point to a magnetic transition occurring around 2.1 K and completely ordered magnetic ground state.

However, even at the base temperature of 0.28 K, we can still observe residual fluctuations of the spins through the relaxation rates (λ_f). These fluctuations suggest the presence of residual dynamic processes within the magnetic lattice, indicating that the system retains some degree of dynamical behavior even in the ordered magnetic ground state. These findings provide valuable insights into the delicate balance between static and dynamic components in the magnetic behavior of $Y_3Cu_9(OH)_{19}Cl_8$ on this distorted kagome lattice.

In addition to the regular peak observed at around 2.1 K in the relaxation rate plot, another anomalous point has been identified at approximately 1.5 K. Interestingly, this anomalous behavior is distinct from the behavior of other variable parameters that remain unchanged at the same temperature unfortunately we could not try to reproduce it nor investigated in details. We note that a similar anomalous feature has been previously reported in the literature for Y-kapellasite [Biesner et al. 2022], and it has also been discussed in the context of Clinoatacamite [Zheng et al. 2005], as an indication of the re-entrance of spin dynamics in the system, suggesting the presence of additional complex magnetic phenomena beyond the regular ordering transition.

To further understand the static magnetic ground state, I will emphasize now the Longitudinal-Field (LF) measurements conducted at the base temperature of 0.28 K. Previous demonstrations have shown that below a temperature of 2.1 K, local static field can be observed in the system as a consequence of a magnetic transition. In this regard, I will present spectra obtained under two different applied longitudinal fields: one at 5 mT and the other around 50

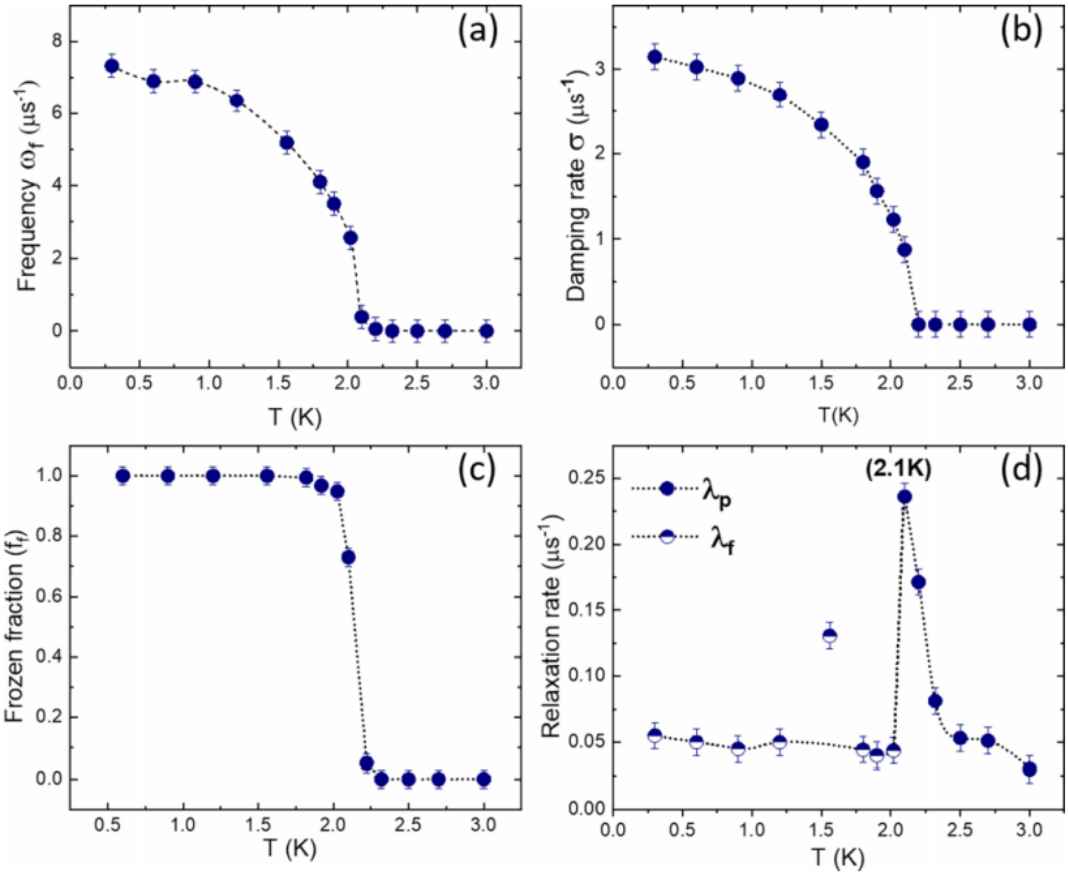

Figure 5.3: Temperature evolution of the parameters used in Eq. 5.5 to fit the ZF μSR data: a) frequency ω_f reflecting the internal field magnitude, b) the damping rate σ, c) the fraction f_f of the frozen phase and d) the relaxation rates in the paramagnetic (λ_p) and frozen (λ_f) phases.

mT. As explained in Chapter-[2], in case of static fields it is expected that an applied longitudinal field ≥ 5 times the internal field should nearly fully decouple the relaxation. The local internal field observed from the zero-field data is 8.6 mT. We utilized a simple model to illustrate the decoupling of the static magnetic field distribution as we applied a magnetic field higher than the local internal magnetic field, which serves as a prominent signature of static ordering.

$$P_{LF} = KT_{\Delta}(t)e^{-\lambda_{LF}t} \tag{5.6}$$

Although the fitting in figure-5.4 with this model is not optimum, we could still observe the decoupling of the magnetic field distribution at 50 mT. Using a 5 mT field, we can still observe characteristic dip due to the static magnetic ordering. However, it is interesting to note that even at low temperatures, there is a minute residual relaxation rate λ_{LF} of 0.02 μs^{-1} shown in '1/3' rd tail, indicating the possible presence of residual spin fluctuations.

To further discuss the development of the internal magnetic field below $\sim$ 2.1 K, it is worth highlighting that the observed magnetic field B_{int} = 8.6 mT is only half the value reported for $YCu_3(OH)_6Cl_3$ in [Zorko, Pregelj, Klanjšek, et al. 2019], which corresponds to the $x = 0$ variant of this compound. Based on high-temperature nuclear

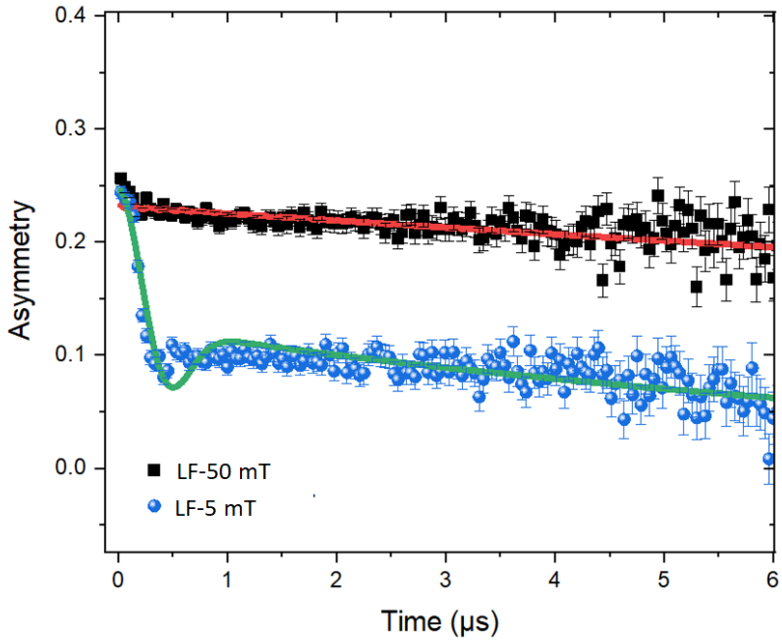

Figure 5.4: At the lowest attainable experimental temperature (0.28K), the spectrum was measured in under the application of longitudinal fields 5mT & 50 mT. The solid line curves on the graph represent the adjustments made according to Equation-5.6 to fit the data.

relaxation measurements, we know that the majority (75%) of the muons stop near OH^{-}, allowing us to estimate the dipolar magnetic field by considering the chemical structure of the μ-OH complex. By taking into account the dipolar coupling for a muon positioned at one of the three oxygen sites (O2, O3, O4) closest to the Cu and averaging the other various O and Cu distances [$r = 1.9(6)$ Å], we estimate a magnetic moment of approximately $\sim$0.065(5) μ_B. It is important to note that this estimation is rough and does not consider the actual (unknown) muon location but in any case the frozen moment is very small.

An insightful comparison can be drawn with barlowite, as discussed in [Tustain et al. 2020]. In barlowite, similar Cu-OH distances are observed, and the muon position can be precisely determined, allowing for a clear understanding of the long-range order. In barlowite, the internal magnetic field is approximately $\sim$101 mT, leading to a magnetic moment of approximately $\sim$0.4 μ_B [Tustain et al. 2020]. In contrast, the local magnetic field in Y-kapellasite is 10 times lower. Based on this comparison and estimation, we can safely conclude that the magnetic moment of Cu^{+2} is significantly reduced to approximately $\frac{1}{30}\mu_B$ for Y-kapellasite. This reduction indicates a fragile magnetic ordered phase.

5.4 Strong reduction of the ordered moments in the ground state

From the discussions above, it's evident that a clear indication of a magnetic transition has been observed at approximately 2.1 K in my study using single crystals [Chatterjee et al. 2023]. This transition is accompanied by the

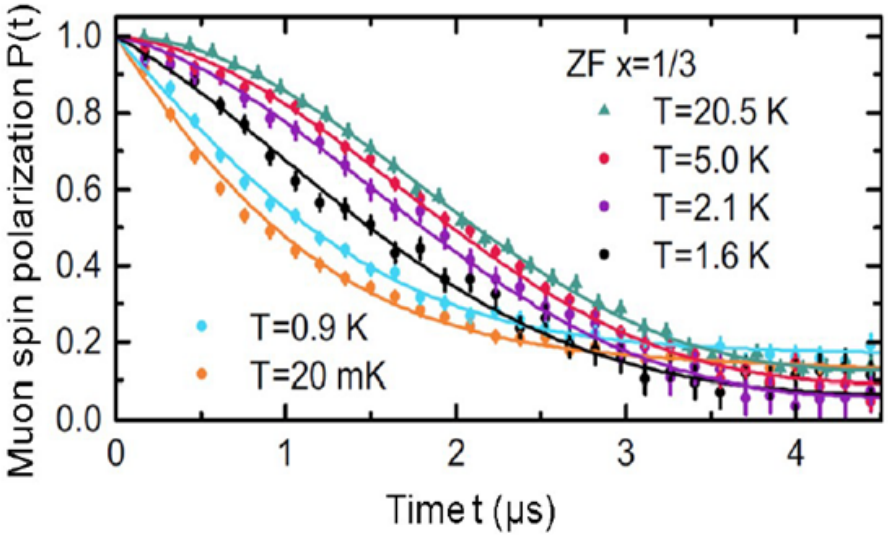

Figure 5.5: ZF μSR data for powder samples at different temperatures are presented in [Barthélemy, Puphal, et al. 2019] depicting no oredering down to 0.28 K.

observation of significantly reduced moments, suggesting the presence of large quantum fluctuations. These fluctuations imply that the system is in proximity to a phase boundary, potentially close to a spin liquid ground state. This behavior could be attributed to a model with multiple exchange constants, as described in reference [Hering et al. 2022], and indeed, as we will see in later chapters, Y-kapellasite appears to be situated close to such a phase boundary.

Furthermore, the possible presence of anti symmetric exchange interactions, the Dzyaloshinskii-Moriya interaction, should also be considered We have not conducted explicit measurements of the Dzyaloshinskii-Moriya interaction (DMI) on our $x = 1/3$ sample, which limits our ability to discuss the specific role of DMI in reducing magnetic moments. However Preliminary Electron Spin Resonance (ESR) measurements, conducted by Andrej Zorko, have also revealed an exceptionally broad spectrum, reminiscent of the $x = 0$ case. These measurements raise the possibility that the magnitude of the Dzyaloshinskii-Moriya vector may indeed be comparable to the estimated value for the compound with $x = 0$ [Arh et al. 2020], which is approximately $D/J \sim 0.25$. In the context of kagome antiferromagnetic systems, it has been observed that a decrease in the frozen moment occurs when the perpendicular component of the Dzyaloshinskii-Moriya vector approaches the critical threshold ($D_z/J > D_c/J \leq 0.1$) [Cepas et al. 2008] and [Ferrari et al. 2023]. According to the mean-field behavior, the magnetic moment close to critical point can be expressed as $m_{AF}^2 = (D_z - D_c)$. This implies a potential factor that might be responsible for the decrease in magnetic moments we observed.

In contrast to the single crystals, a previous study conducted on powder samples of this compound [Barthélemy, Puphal, et al. 2019] did not reveal any magnetic ordering. We have to consider the fact that we didn't observed any structural changes around $\sim$ 15K and $\sim$ 33K in case of powder sample (already discussed in chapter-[3]). We

can hypothesize that the presence of additional disorder (as discussed for the triangular lattice in the-[Murayama et al. 2020)] in the polycrystalline samples or slight variations in the interactions, possibly due to the absence of a structural transition, disrupt the delicate ordered state observed in large single crystals. It is noteworthy that the sensitivity to the crystallinity of the samples appears to be a common feature observed in anisotropic kagome compounds like vesigneite [Quilliam et al. 2011; Boldrin, Knight, and A. S. Wills 2016] and volborthite[H. Ishikawa et al. 2015, F. Bert et al. 2005] . The fragility of the ground state in all these compounds can be attributed to the subtle interplay between the structural properties and magnetic frustration. The specific arrangement of atoms in the crystal lattice, combined with the competing magnetic interactions, creates a delicate balance that determines the nature of the ground state.

Summary

In conclusion, our μSR investigation of Y-kapellasite ($Y_3Cu_9(OH)_{19}Cl_8$) has provided valuable insights into its magnetic ground state through μSR studies on single crystals. We identified a magnetic transition around 2.1 K, indicating the development of essentially static magnetism and a fully ordered magnetic ground state below 1.8 K. A rather broad distribution of local field with an averaged value of 8.6 mT has been observed. Our analysis further suggested a reduced magnetic moment of Cu^{2+}, approximately 1/30 μ_B, indicating a fragile magnetic ordered phase, likely influenced by quantum fluctuations at the frontier of a spin liquid phase. Comparing our results with previous studies on powder samples, we noted differences in the observed magnetic behavior. Single crystals displayed a distinct magnetic ordering, while powder samples exhibited dynamical ground states. This discrepancy may be attributed to the sensitivity of the crystallinity and structural properties, indicating the presence of additional disorder or variations in interactions in polycrystalline samples, which can disrupt the delicate ordered state observed in large single crystals.

Chapter 6

Chlorine (^{35}Cl) NMR studies in Y-Kapellasite, $Y_3Cu_9(OH)_{19}Cl_8$

As previously discussed, NMR serves as a valuable local probe for investigating magnetism in materials. It not only offers insights into the static magnetism but also provides valuable information about the local dynamics and structure of the system. In the case of Y-Kapellasite, four natural nuclei can serve as probes: Yttrium (^{89}Y), Hydrogen (^{1}H), Chlorine (^{35}Cl, and ^{37}Cl) . Initially, NMR measurements using ^{89}Y nuclei were considered and conducted by Quentin Barthelemy in powder sample. However, these measurements were eventually discarded due to the very long relaxation times of the ^{89}Y nuclei (over 20 seconds at 20 K) and the presence of fine NMR lines, which suggested a weak coupling of Yttrium to the magnetism of the compound. On the other hand, Chlorine, with its most abundant isotope ^{35}Cl (I = $3/2$, $\gamma = 4.17$ MHz/T), has already been used succesfully as a probe for studying the kagome planes in Kapellasite [Kermarrec, Zorko, et al. 2014]. Kapellasite shares an identical structure with $Y_3Cu_9(OH)_{19}Cl_8$, particularly considering the absence of interplanar Cu^{2+} ions between the kagome planes. We employ this local probe to extract information regarding the evolution of the electronic structure and intrinsic static and dynamic magnetism, with the aim of characterizing the ground state.

Therefore, I carried out ^{35}Cl NMR experiments on a single crystal of $Y_3Cu_9(OH)_{19}Cl_8$, weighing approximately $\sim$ 30 mg and the NMR measurements were conducted with an external magnetic field (H_{ext}) aligned parallel to the c-axis of the crystal, which is perpendicular to the large facet of the sample (see Figure 6.1).

6.1 Analysis of ^{35}Cl NMR spectra

6.1.1 Full spectrum of ^{35}Cl

Considering the structure of $Y_3Cu_9(OH)_{19}Cl_8$ already discussed in chapter-2, there are two distinct crystallographic chlorine sites (Figure 6.1) located between the planes at the center of the triangles and hexagons within the Cu^{2+} kagome structure. These chlorine sites, referred to as the triangular site (tri) and hexagonal site (hex) in the upcoming sections for convenience, can be distinguished by NMR.

In Figure 6.1, the complete ^{35}Cl spectrum is presented at a temperature of approximately 100 K, and a fixed magnetic field (H_0) of 7.553 Tesla, corresponding to a resonance frequency of ν = 31.510 MHz. This temperature is chosen to be well above any magnetic and structural transitions and ensures a good signal-to-noise ratio.

^{35}Cl possesses a nuclear spin of $I = 3/2$, resulting in three allowed transitions between the Zeeman-split nuclear levels. These transitions are modified by the quadrupolar interaction with neighboring electric charges. As a result, we observe three NMR lines per chlorine site: one central line corresponding to the $-1/2 \leftrightarrow 1/2$ transition, and two satellites associated with the $-3/2 \leftrightarrow -1/2$ and $1/2 \leftrightarrow 3/2$ transitions. We observe two distinct central lines for the triangular and hexagonal sites, with an intensity ratio of 3:1. This intensity ratio is proportional to the number of different chlorine sites (18 Cl_{tri} and 6 Cl_{hex}) per unit cell between the kagome planes at the center of the triangle or hexagon, respectively.

Summing up the entire spectrum, Figure 6.1 (c) displays a total of 6 lines: 2 central lines and 4 satellites originating from 2 different chlorine sites. I conducted an analysis of the temperature evolution of NMR lines to identify local structural distortions in the system, as well as the magnetic ordering at low temperatures.

6.1.2 Analysis of quadrupolar interactions

Due to the first-order perturbation, two satellites arise for a given chlorine site denoted by $\alpha = \text{hex}, \text{tri}$, resulting from quadrupolar interactions. The frequency difference between these satellites can be measured using equation 6.1 [Cohen and Reif 1957]:

$$\Delta\nu_{\alpha}^{(1)} = \nu_{Q}^{\alpha}\left(3\cos^2\theta_{\alpha} - 1 - \eta_{\alpha}\sin^2\theta_{\alpha}\cos 2\phi_{\alpha}\right) \tag{6.1}$$

In this equation, θ_α and ϕ_α represent the polar and azimuthal angles between the principal axes of the electric field gradient tensor (EFG) and the external magnetic field. The quadrupolar frequency shift ν_Q^α corresponds to the highest eigenvalue of the EFG tensor, which is proportional to the quadrupolar moment (Q) and represents the strength of quadrupolar interactions. The asymmetry parameter η_α reflects the deviation of the EFG tensor from cylindrical symmetry.

We positioned a single crystal (Figure 6.1) such that the magnetic field (H) is perpendicular to the plane facet

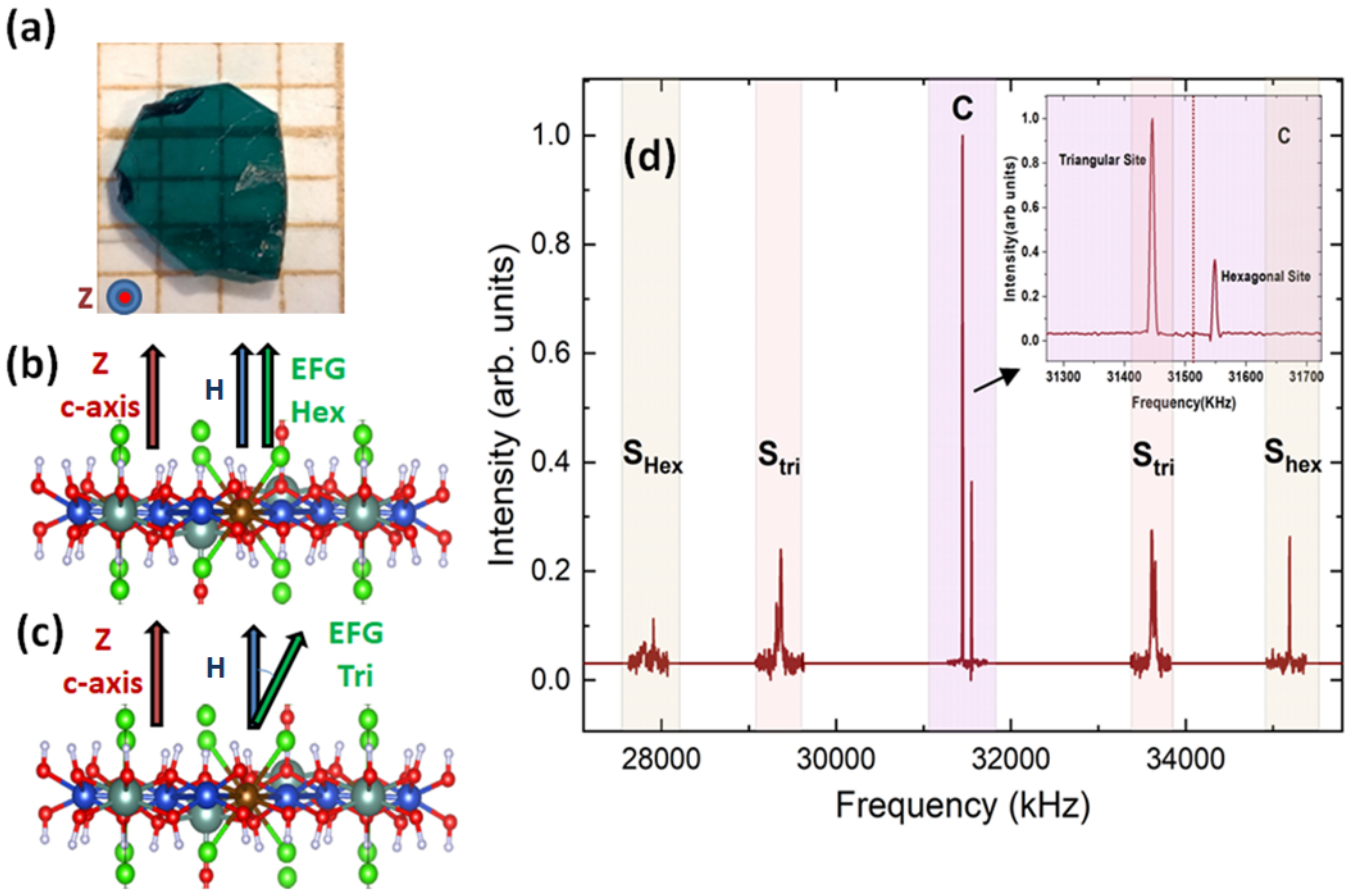

Figure 6.1: (a) Single crystal used for NMR (b) Orientation of the field (H), principle axis of EFG (Electric field gradient tensor), and c-axis of the crystal structure for the hexagonal site and for (c) the triangular site during NMR measurement.(d) Full NMR spectrum of ^{35}Cl at 100 K with the configuration $H_{\text{ext}} \parallel c$ of the single crystal, which shows 2 central lines (C) corresponding to Cl_{tri} (triangular site) and Cl_{hex} (hexagonal site), along with their corresponding pairs of satellites (S_{tri} and S_{Hex}). Inset: Enhanced view of the central lines (C). The dashed vertical line indicates the reference frequency $\nu_0 = 31.510$ MHz.

of the crystal. The hexagonal chlorine site is in a highly symmetric position, allowing the magnetic field (H), EFG tensor, and c-axis of the crystal to be parallel to each other. As a result, the asymmetry factor are $\eta_{\text{hex}} \approx 0$ and $\theta_{hex} \approx 0$ at high temperatures (> 33 K). Using Equation 6.1, it becomes evident that for the hexagonal site, the two satellites are at a maximum distance of $2\nu_Q^{\text{hex}}$. We directly estimated $\nu_Q^{\text{hex}} = 3640(5)$ kHz from Figure 6.1.

In contrast to the hexagonal site , the triangular site is much less symmetric, resulting in $\eta_{\text{tri}} \neq 0$. To determine the parameters θ_{tri} and ϕ_{tri}, we utilized the 40 K crystal structure obtained from single-crystal neutron diffraction to find the principal axes of the EFG tensor based on the point charge approximation.

From the EFG calculations, we obtained the parameters: $\theta_{\text{tri}} = 8.3°$, $\phi_{\text{tri}} = 123.0°$, and $\eta_{\text{tri}} = 0.33$. Hence using the measured distance between satellites in Equation 6.1, we determined $\nu_Q^{\text{tri}} = 2180(20)$ kHz. Due to H_{ext} not strictly aligning along the c-axis, the principal axis of the EFG tensor do not have exactly the same orientation θ_{tri} with respect to H_{ext} for the non-equivalent Cl triangular sites in the unit cell. This slight misalignment of $\pm 1.2°$ between the c-axis and H_{ext} causes the minute splitting of the triangular site satellites observed in Figure 6.1 and

discussed in the next section.

The central line quadrupolar shifts in the spectra (Figure 6.1 inset) are only influenced by second-order quadrupolar perturbations [Baugher et al. 1970] explained in detail in the chapter-2, described by the equation:

$$\nu_{\alpha}^{(2)} = -\frac{(\nu_Q^{\alpha})^2}{2\nu_0} f(\theta_\alpha, \phi_\alpha, \eta_\alpha), \tag{6.2}$$

Where ν_Q^{α} represents the quadrupolar frequency shift for the respective site. The value of the multiplicative factor, $\frac{(\nu_Q^{\alpha})^2}{2\nu_0}$, is 0.200 MHz for hexagonal Chlorine and 0.075 MHz for triangular Chlorine. In the case of axially symmetric EFG tensors, the function $f(\theta, \phi, 0)$ is given by:

$$f(\theta, \phi, 0) = \frac{3}{8}(1 - \cos^2\theta)(9\cos^2\theta - 1). \tag{6.3}$$

The second-order quadrupolar shifts cancels for the hexagonal site ($\nu_{\text{hex}}^{(2)} = 0$) due to $\theta_{\text{hex}} = 0$. For the triangular site, the second-order shift is $\nu_{\text{tri}}^{(2)} = -4(1)$ kHz, which is also relatively small.

Now, if we consider the positions of two central lines, from the equation

$$\nu_{\alpha}^{C} = \nu_0(1 + K_{\alpha}^{0} + K_{\alpha}^{s}) + \nu_{\alpha}^{(2)} \tag{6.4}$$

it will be very prominent that most of the contribution in the shift comes from the 1^{st} part where we are seeing a temperature-independent orbital term K_{α}^{0} and a spin shift K_{α}^{s} arising due to unpaired electrons of neighboring Cu^{2+}, which is proportional to susceptibility. Hence, this shift is mostly magnetic in nature.

6.1.3 Orientation of the single crystal with the external magnetic field (H_{ext})

When a single crystal is oriented along different axes relative to the external magnetic field, the NMR spectra experience significant changes in resonance position. These modifications occur due to variations in the orientation of the electric field gradient (EFG) with respect to the applied field direction. The quadrupolar interaction induces shifting and splitting of NMR lines. The number and arrangement of peaks in the NMR spectrum depend on the spin quantum number and the crystallographic symmetry of the single crystal (discussed in chapter-2). Hence the orientation becomes crucial to study structural and magnetic properties of this sample. I made an effort to position the flat surface of the single crystals perpendicular to H_{ext} to ensure an axially symmetric configuration. In this ideal configuration, one would expect $\theta_{\text{hex}} = 0$ and maximally separated hexagonal satellites. Additionally, all triangular sites should be equivalent with the same $\theta_{\text{tri}} = 8.3^{\circ}$. Our setup has a Goniometer connected with our probe to make slight adjustments by rotation of θ around an axis perpendicular to H_{ext} with a precision of 0.1 $^{\circ}$.Note that if the rotational axis is perfectly perpendicular to to c-axis then $\theta = \theta_{hex}$

We began our alignment process by focusing on the central line in the spectra. This is because, compared to the

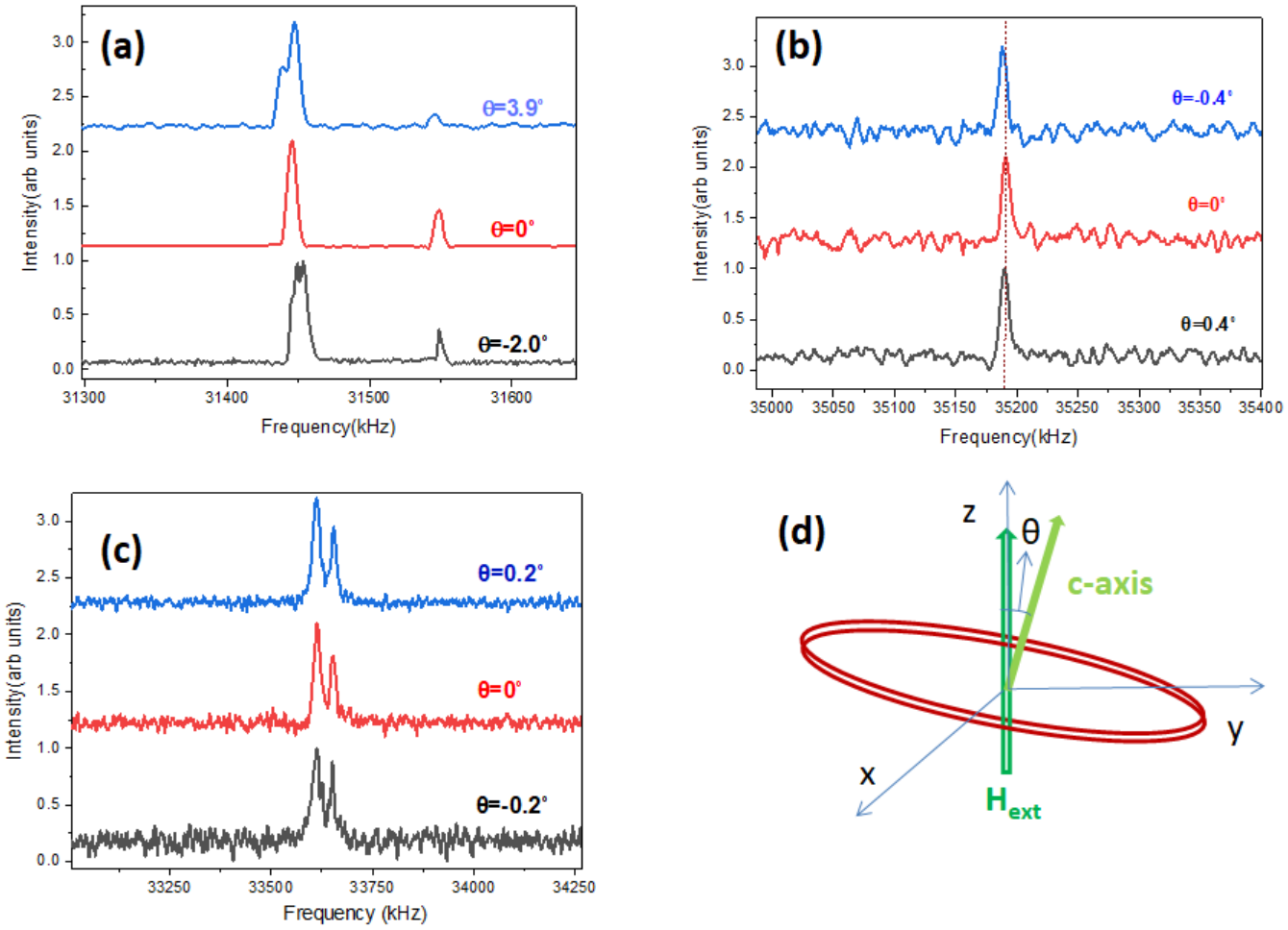

Figure 6.2: (a) Shape of the central line changes as the angle θ between the electric field gradient (EFG) and the external magnetic field (H_{ext}) varies. (b) The position of the maxima peaks in case of hexagonal satellite is adjusted by fine tuning θ_{hex} to maximize its shift according to-6.1 . (c) The best orientation, minimizing asymmetry, is determined for the position of the triangular satellite, taking into account θ_{tri} (d) Schematic diagram to show the misalignment between magnetic field and c axis of the crystal.

satellites, the central line is less susceptible to the effects of slight misalignment, thanks to the mitigating influence of 2nd order effects. In Figure 6.2(a), we can observe how even slight variations in θ result in the splitting of the central line corresponding to the triangular site. Once we achieved an optimal alignment by fine-tuning θ for the central line, we proceeded to examine the hexagonal satellites which are more susceptible to θ.

Referring to Equation 6.1, we know that for a polar angle $\theta_{hex} = 0$, the frequency shift caused by 1^{st} quadrupolar effects, denoted as $\Delta\nu^{(1)}_{hex}$, reaches its maximum value, which corresponds to the quadrupolar frequency shift ν_q. Consequently, we endeavored to track the peak of the hexagonal satellite and assigned the $\theta = \theta^{hex} = 0$ position to the most distant peak with respect to the reference frequency $\nu_0 = 31.50$ MHz, as illustrated in Figure 6.2-(b). We were unable to align the crystal further to achieve a single triangular satellite, we still observed a split in the triangular satellite in the spectra, indicating a non single value of $\theta_{\text{tri}} \sim \pm 1.2°$ for all triangular sites at high temperatures showed

in figure-6.2-(c). Several factors contribute to the alignment process, including the flatness of the crystal and sample holders, as well as the smallest angle adjustments achievable with reproducibility using the Goniometer. Therefore, there is always a small possibility of misalignment occurring due to mechanical errors.

6.1.4 Temperature evolution of the spectra and structural transitions

After best possible alignment of the sample and gaining a comprehensive understanding of the high-temperature spectra, we conducted a systematic study involving temperature variations. Drawing upon the insights gleaned from my extensive NMR study, I will focus on discussing both the central line and the satellites within the spectra. The NMR line shape and width are susceptible to local magnetic as well as electronic changes, allowing us to investigate the magnetic and structural transitions directly from the spectra. Investigating with a local probing technique like NMR gives an additional advantage of observing the effect of local electronic changes on two different sites altogether with temperature evolution. As we cool down the temperature below 40 K, significant changes in the spectra are observed both in the central line (Fig. 6.3) and satellites (Fig. 6.4). In the central line, the triangular site shows significant broadening, while the hexagonal site shows splitting (Fig. 6.3) of the central line. We have measured the line width of the triangular site and the evolution of the distance (d) between two peaks of the hexagonal site (in Fig. 6.3) to trace the changes with temperature.

The triangular site experiences a sudden broadening between 30 K and 40 K, and this broadening persists as the temperature continues to decrease, as illustrated in Figure 6.3(a). A notable change is observed at temperatures below 20 K, highlighted by an additional minor step around ($\sim$15 K).

On the other hand, the hexagonal site splits into two lines. We fitted the peaks with two Gaussian functions and plotted the distance (d) between the new peaks. This distance d follows a similar evolution as the triangular site. While our initial neutron diffraction data is not conclusive regarding the crystal structure change at the $\sim$33K transition, the hexagonal line splitting clearly demonstrates a reduction in symmetry, resulting in the presence of at least 2 non-equivalent hexagonal sites, shown in figure-6.4. Furthermore, as the temperature decreases below 30K, the hexagonal satellites evolve into a more complex line shape with additional peaks, as shown in Figure 6.4(b). This further indicates the effect of lowered symmetry constraints on the hexagonal sites of chlorine. The occurrence of another peak in the satellites and central line indicates the presence of at least two non-equivalent crystallographic hexagonal chlorine sites, confirming the change in the R-3 structure after the transition. The reduction in symmetry observed at this specific temperature can be linked to alterations in the Electric Field Gradient (EFG) tensor, as visually represented in Figure 6.4(c), and potentially attributed to variations in hyperfine coupling. Considering the possibility that the observed splitting arises only from alterations in the Electric Field Gradient (EFG) with respect to the external magnetic field (H_{ext}), we introduce a finite distribution of the polar angles among the new inequivalent hex sites at low temperature, $\Delta\theta_{\text{hex}}$. This introduced tilt can be precisely measured, thus providing an explanation

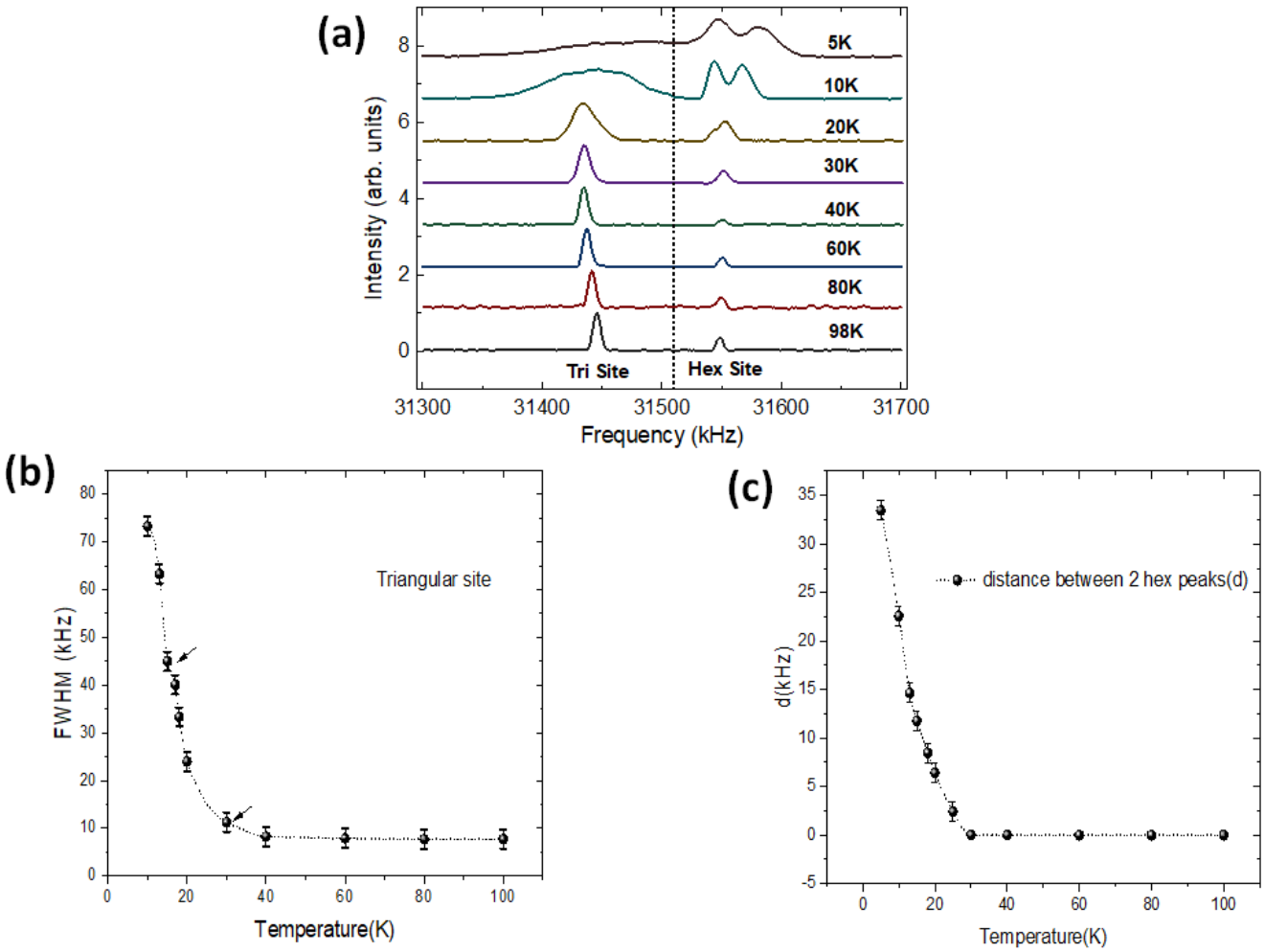

Figure 6.3: (a) Central line evolution with temperature. The change of the width and the splitting in the line below 40 K which become prominent below 20 K.(b) Change of central line width (Full Width Half Maximum) of the triangular site with temperaturesuggesting 2 anomalies one in between 30K and 40K and another small deviation at $\sim$ 15 K . (c) Distance between 2 peaks of hexagonal satellite arising due to structural change in between 30K & 40K although this splitting becomes much more prominent after 20K near the 2^{nd} transition.

for the NMR line shape variation through the presence of a non-zero $\Delta\nu_{\text{hex}}$. In contrast to the neutron structure where the calculated $\Delta\theta_{\text{hex}} = 0$, our analysis utilizing Equation 6.1 yields estimations of $\Delta\theta_{\text{hex}} \approx 6^{\circ}$ at 20 K and $\Delta\theta_{\text{hex}} \approx 11^{\circ}$ at 10 K temperature.

To determine the onset temperature for the structural transition with a better accuracy, we examined the satellites as indicated by the NMR line width anomalies. Indeed the quadrupolar effects are first-order perturbations in the satellites, the spectral changes are less pronounced at the transition temperature. Figure 6.4-(a) illustrates the abrupt change in the line shape and width of the hexagonal satellite, attributed to the structural transition around $\sim$ 33 K. Additionally, in Figure 6.4-(d), a sharp change in slope is observed below $\sim$ 13 K, indicating a secondary transition in the crystal structure, which is evident in thermal expansion and spin-lattice relaxation measurements. The anomaly at $\sim$ 13 K is found to be non-magnetic based on bulk susceptibility and μSR measurements. To further

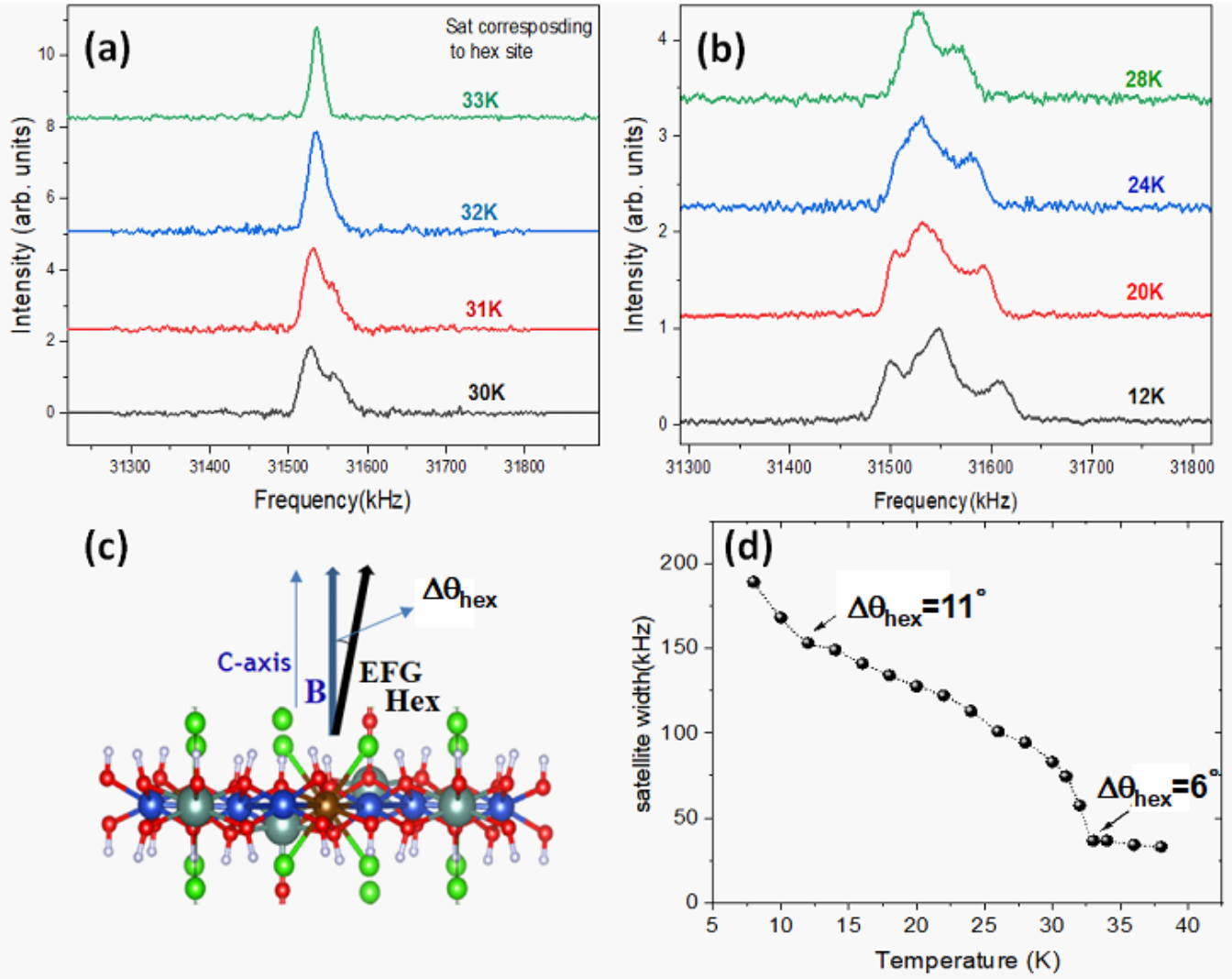

Figure 6.4: (a) Line shape change of hexagonal satellite at the structural transition, $\sim$ 33K. (b) As we go down in temperature the lineshape continuously changes in hexagonal satellite indicating lowering of symmetry from R-3 structure due to structural transition. (c) Development of finite tilt of EFG depicted by θ_{hex} in the crystal structure as a result of structural transition. (d) Plot of hexagonal satellite linewidth evolution with temperature which indicates two structural changes (black arrows) inducing change of polar angle (θ_{hex}) between the magnetic field and the electric field gradient (EFG).

investigate the nature of the kink around $\sim$ 13 K in the plot, a comparative experiment was conducted between ^{35}Cl and ^{37}Cl spectra.

Chlorine exhibits two natural isotopes, ^{35}Cl and ^{37}Cl, each with distinct gyromagnetic ratios ($\gamma_{^{35}Cl}/2\pi \sim 4.17$ MHz/T and $\gamma_{^{37}Cl}/2\pi \sim 3.48$ MHz/T) and quadrupolar moments ($Q_{^{35}Cl} \sim$ -7.9 x 10^{-30} rad m^2 A and $Q_{^{37}Cl} \sim$ -6.2 x 10^{-30} rad m^2 A). For comparison, we acquired a spectrum at 10 K, maintaining a reference frequency of 24.00 MHz, using two different magnetic field strengths: approximately 6.91 Tesla for ^{37}Cl and roughly 5.75 Tesla for ^{35}Cl. Figure 6.5 visually demonstrates the splitting of the hexagonal central line for both isotopes, indicative of the aforementioned transition.

To estimate the frequency difference $\Delta\nu^i$ between the two peak maxima for each isotope, we fitted two Gaussian functions to the split peaks in the hexagonal central line [6.5.(b)]. The ratio of the change in frequency between the two peaks is $\Delta\nu^{35}/\Delta\nu^{37} = 1.50(2)$. According to Equation 6.3, the frequency shift caused by second-order quadrupolar effects, $\nu_{hex}^{(2)}$, is proportional to the square of ν_Q, hence the square of the quadrupolar moment (^iQ) between the two nuclei. The ratio ($^{35}Q/^{37}Q)^2$=1.61(2), indicates that $\Delta\nu^i$ originates from quadrupolar effects for Cl^{35} and Cl^{37}.In contrast, gyromagnetic ratios (γ^i) are indicative of scaling static internal magnetic fields. The γ^{35}/γ^{37} ratio being 1.20, does not account for the observed change in $\Delta\nu^i$ between the two isotopes.

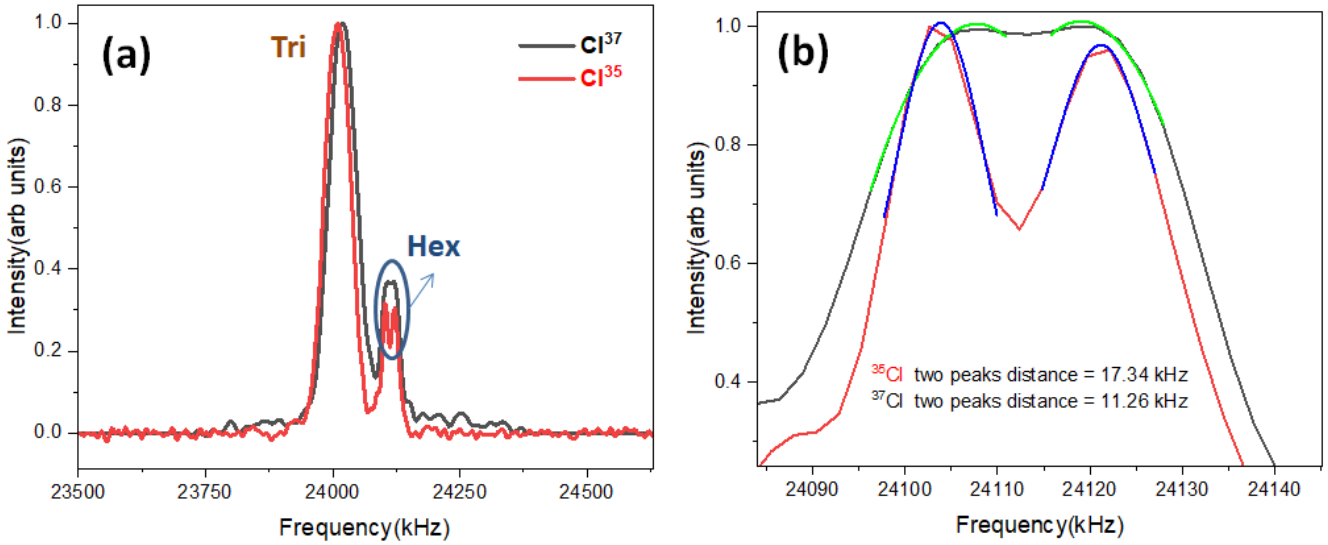

Figure 6.5: (a) Spectra (central line) obtained for 2 chlorine isotopes, ^{35}Cl and ^{37}Cl for a fixed reference frequency $\sim$ 24 MHz. The blue circle encompasses the hexagonal central line which is enlarged (b) to highlight the splitting of hexagonal central line around $\sim$ 10K for ^{35}Cl (red line) and ^{37}Cl (black line). These split peaks have been fitted with gaussian functions shown as blue line for ^{35}Cl and green lines for ^{37}Cl.

Consequently, we infer that the 13 K transition primarily holds an electrostatic character, signifying a structural transition. These findings are consistent with the conclusions drawn from the analysis of muon spin rotation (μSR) and susceptibility data, which did not show any signature of a magnetic transition around this temperature.

6.1.5 Low temperature spectra & magnetic transition

As we go below 6 K, we can observe from the bulk susceptibility data that the FC (Field Cooled) and ZFC (Zero Field Cooled) curves diverge (shown in figure-4.2), indicating the development of magnetic correlations down to the magnetic transition at $\sim$ 2.2 K. From Equation 6.4, we can observe that the positions of the two central lines depend on the spin susceptibility. The distribution of susceptibility (χ) and the increase in intrinsic magnetic correlations with decreasing temperature cause the NMR line to broaden, resulting in the blurring of the second-order quadrupolar contribution in the spectra. Consequently, the distinctive hexagonal and triangular lines partially overlap with each other, as shown in Figure 6.6(a).

Before delving into the quantitative discussion, it is important to clarify the approach we took for low-temperature measurements ($4.20\,\mathrm{K} \geq T \geq 1.30\,\mathrm{K}$), which involved field sweep techniques at a constant frequency ($\nu_0 = 31.510\,\mathrm{MHz}$) with an external magnetic field, $H_0 \parallel c$, instead of the more commonly used frequency sweep measurements at high temperatures. In the low-temperature region, as previously mentioned, the spectra become broadened. This poses a challenge even using a resonance cavity with a low-quality factor (Q) because it becomes difficult to probe the entire spectral range. In such cases, two possibilities arise. Either we can scan the entire spectrum by changing the frequency and recombine the results to obtain the complete spectrum. However, this approach would require adjustments to the RF cavity settings. Because of challenges in ensuring a constant quality factor for the probe across a wide frequency range, there is a possibility of encountering intensity loss and potential distortion of the line shape when sweeping the frequency. To address this concern, we opted to maintain a fixed frequency at 31.510 MHz and vary the magnetic field to acquire the spectra.

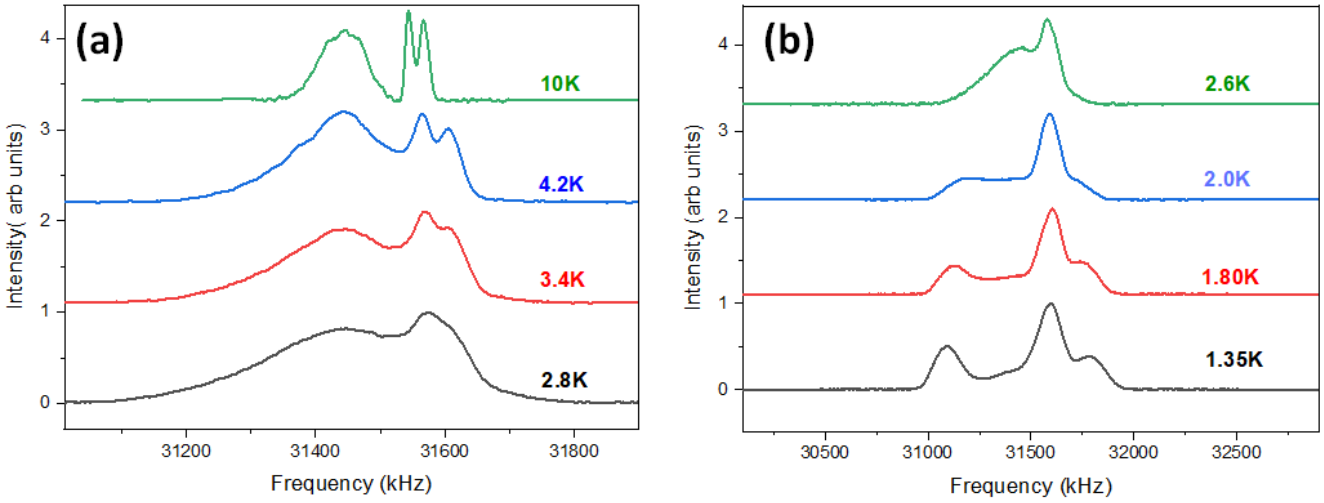

Figure 6.6: (a) Continuous development of the central line is highlighted with temperature evolution. Due to the increase of spin correlations at low temperature two sites broaden and merge which is further traced near (b) the magnetic transition region (on a extended scale in frequency).

To observe the continued spectral development from 10 K to 1.35 K and understand the overlapping of the two sites, we conducted field sweep measurements, incrementally increasing the magnetic field by 10 gauss at each step to ensure the capture of all the features in the ideal spectrum. Subsequently, we performed the recombination of Fourier transforms of the echoes taken at each step in the field, as illustrated in Figure 6.6. As shown in Figure 6.6 and 6.7, it becomes apparent that the triangular site merges with the hexagonal sites, causing the previously observed fine structures around 10 K to become less distinct. As the temperature decreases further, the magnetic broadening effect becomes more prominent compared to the quadrupolar features. To delve deeper into the interpretation of the spectra, we will analyze the field sweep data in conjunction with the spin texture model presented in reference [Hering et al. 2022].

To estimate the separate contributions from different sites in the central line, we fitted the hexagonal site with a

Gaussian function and subtracted it from the experimentally obtained spectra, shown in figure-6.7(a). The Gaussian line corresponding to the hexagonal site consistently displays a T_1 value approximately 10 times greater than that observed for the other segments of the central line, which primarily represents the triangular site. At $\sim$ 2.1 K, we observe an overall abrupt broadening of the central line. The broadening is primarily attributed to the triangular sites, although the hexagonal sites also exhibit a steep increase in line widths at this temperature. This anomaly in line widths serves as a spectral signature of the magnetic transition, which has also been observed in specific heat, thermal conductivity, μSR, and relaxation measurements. The emergence of two triangular sites with almost equal intensities that shift in opposite directions as the temperature decreases below 2.1 K, is also a landmark of spin ordering.

To quantify the broadening of the spectra, we calculated the fractional increase of line widths using the formula $\Delta W(T) = \frac{W(T)-W(3.6\text{K})}{W(3.6\text{K})}$. We applied this analysis to both sites in the central line, as shown in Figure 6.7(b), and to the satellites, as seen in Figure 6.8(b). In Figure 6.7(b), we observe the onset and effect of the magnetic transitions on each site individually within the central line. The hexagonal contribution extracted from the central line experiences a minute broadening below 2.0 K, slightly below the transition temperature of 2.1 K, and maintains a constant width after 1.8 K. This behavior aligns with our μSR data, where the frozen fraction of spins reaches 1 at 1.8 K, and where we also observed damped oscillations (indication of magnetic transition) at around 2.1 K. The unchanged lineshape also indicates the presence of a single hexagonal site in the magnetic lattice. For the triangular site, the broadening is more gradual below 4.2 K, but a sharp change in slope is observed around 2.1 K, which we attribute to the observed transition. Furthermore, the line splits into two broad lines, as shown at 1.35 K in Figure 6.7(a), indicating the presence of two or more triangular magnetic sites in the frozen structure. To eliminate speculation about two sites overlapping and potentially contaminating our quantitative analysis of low-temperature spectra, I replicated the same procedure with the satellites. Below 2.5 K, the hexagonal satellite appears more like a single broad line with minimal width increment. Although a slight kink is observed around $\sim$ 2.1 K [Figure 6.8(a)], the most conclusive results come from the analysis of the triangular satellite. The jump in line width at 2.1 K is more pronounced and definitive [Figure 6.8(b) and (c)].

To comprehensively model this spectrum, I would like to discuss this low temperature spectra as I have conducted a comparative study. In accordance with a recent theoretical investigation of the ground state in distorted kagome structures, such as Y-kapellasite (Hering et al. 2022), a (1/3,1/3) long-range order featuring a coplanar spin texture has been proposed, see chapter-[1] and [3]. Based on the predicted spin configuration [Figure 6.7(a)], the hyperfine fields at the hexagonal sites are either zero (for spins of different colors) or nearly zero (for spins of the same color). As a result, the line widths for the hexagonal sites show a moderate increase compared to the triangular site (Figure 6.7(b)). In contrast, the triangular sites exhibit finite hyperfine fields. Within the magnetic unit cell, each triangle consists of two nearly opposite spins and one uncompensated spin. This leads to three distinct magnetic sites labeled as **a, b,** and **c** in Figure 6.7, corresponding to the three different configurations of the uncompensated spin.

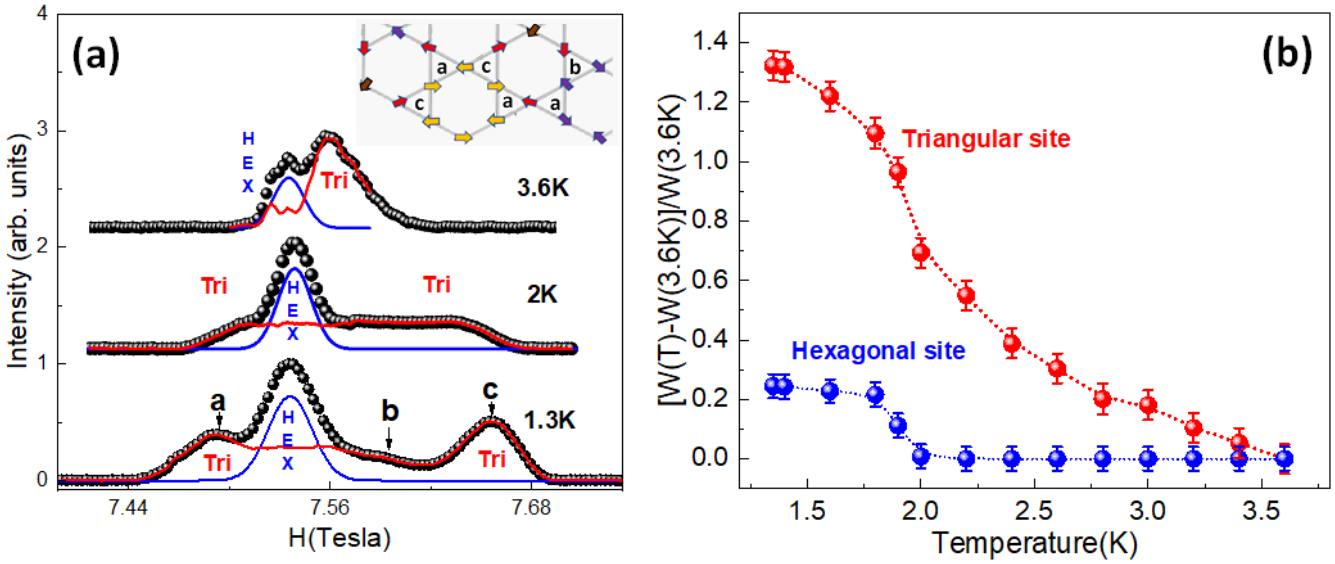

Figure 6.7: (a) Central line spectra at 1.3 K, 2 K, 3.6 K along with a segment of spin texture illustrating the Q=(1/3,1/3) ordering at the right corner of the figure. The hexagonal central line is fitted with a Gaussian function represented as a blue line and this hexagonal contribution is subtracted from the experimental spectrum to evaluate the triangular site contribution showed as red line. Taking dipolar fields into consideration, the spin texture depicts three distinct triangular sites: **a**, **b**, and **c**. Correspondingly, these sites can be associated with the observed spectra. Specifically, sites **a** and **c** exhibit nearly equal and opposite finite dipolar fields, while site **b** registers an almost negligible contribution in this context. (b) Temperature (T) evolution line widths W(T) for the triangular (red) and the hexagonal (blue) contributions.

It is thus anticipated that the low-temperature spectrum (below 2.1 K) manifests three separate lines corresponding to the triangular chlorine sites in the magnetically ordered phase. To be more quantitative we need to consider the hyperfine tensor. Regrettably, we don't know the relevant components of the hyperfine tensor; A^{yz}, A^{xz} which would demand an investigation of the spectra in H $\parallel$ ab configuration. In an initial approximation, we proceeded with the assumption that the coupling is exclusively dipolar in nature. Given the certain spin texture described above, we were able to calculate the dipolar fields at the positions of the chlorine atoms. The distances $(r = (x, y, z))$ from the copper spins to the chlorine atoms were determined using neutron diffraction data, and the dipolar field (H_{dip}) was calculated using the following equation:

$$\vec{H}_{dip} = \frac{\mu_0}{4\pi} \frac{3(\vec{\mu} \cdot \vec{r})\vec{r} - \vec{\mu} r^2}{r^5} \tag{6.5}$$

The distance, r, represents the distance between the copper spins and the chlorine atoms. The permeability in vacuum, μ_0, is defined as $4\pi \times 10^{-7}, \text{H} \cdot \text{m}^{-1}$. When an external magnetic field H_0 is applied, the magnetic moment aligns with the direction of this field, which, in our measurements, is oriented along the z-direction. The dipole field (H^z_{dip}) along the c-axis is generated by the Cu^{2+}magnetic moment of $0.1\mu_B$, arranged in accordance with the theoretically predicted spin texture.

Given this configuration, we have observed a minor dipolar field (B^z_{dip}(tri) $\sim$ 1.3 Gauss) at the triangular site **b**, and two identical and opposing dipolar fields (around 52.5 G each) at the highlighted triangles **a** and **c** in Figure

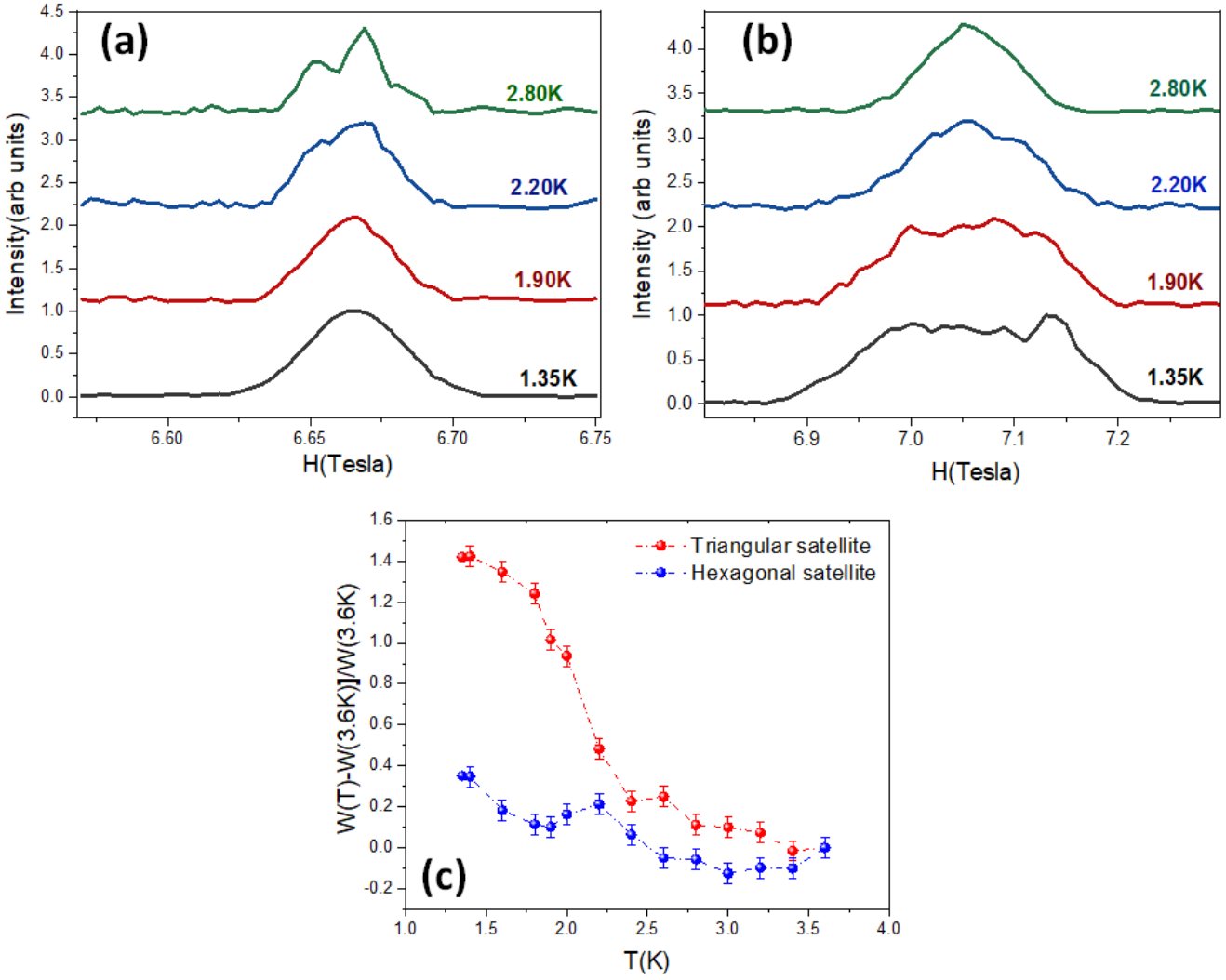

Figure 6.8: (a) Hexagonal satellite (b) triangular satellite development at low temperature near the magnetic transition region, down to $\sim$ 1.35K. (c) Temperature(T) evolution of the line widths W(T) at half maximum for the triangular (red) and the hexagonal (blue) satellites.

6.5. In the NMR spectra at 1.4 K (Figure 6.7), two broad split peaks are discernible from the triangular sites **a** and **c** with nearly equal intensity. As previously discussed, these peaks shift in opposite directions below the magnetic transition temperature of approximately 2.1 K, attributed to the uncompensated triangles **a** and **c**. At the center of the central line, there is an almost negligible contribution to the dipolar field intensity from the triangular site **b**, which aligns with the nearly absent dipolar field in the proposed spin configuration. Consequently, the theoretically proposed spin texture at the ground state seems to align with the experimentally observed spectrum in the ordered phase (below 2.1 K) for both sites. Although we can not make a quantitative comparison, it's crucial to acknowledge certain limitations that emerged during the comparative and experimental analysis. While our dipolar considerations of the interactions do provide a qualitative explanation for the observed spectra at 1.35 K, . Owing to our current lack of knowledge concerning the stacking arrangement along the c-axis, we find ourselves unable to compute the

local fields at the Cl site in the 3D ordered magnetic structure calculations along the z direction.

6.1.6 Probing local susceptibility by ^{35}Cl NMR

The use of local techniques such as NMR offers distinct advantages due to it's ability to measure the histogram of differently probed susceptibilities, rather than just an average. This characteristic enables the separation of different contributions within the sample. As we have discussed previously in Chapter 3, the magnetic Hamiltonian comprises terms such as dipolar, orbital, and contact interactions, all of which contribute to the local magnetic field H_{loc}. Consequently, triangular sites and hexagonal sites experience different electronic couplings, leading to variations in their respective H_{loc} values. To track the local susceptibility, we track the NMR lines shift with respect to the reference frequency ν_0 as a function of temperature under an external magnetic field H_0. By analyzing the changes in NMR line positions as temperature is varied, we can gain insights into the behavior of the local susceptibility.

We have already discussed the extremely small second-order quadrupolar contributions in subsection 6.1.2. Therefore, from equation 6.4, we can calculate the shifts and subsequently determine the local susceptibility (χ_{local}) from the experimentally obtained spectra.

$$K^{\alpha}_{shift} = \frac{\nu^{C}_{\alpha} - \nu_0}{\nu_0} = K^{s}_{\alpha}(T) + K^{0}_{\alpha} \tag{6.6}$$

As discussed in Chapter 3, the spin shifts K^{α}_{s} from the NMR spectrum for a $H_0 \parallel c$ configuration provide a direct measure of the local susceptibility (χ_{local}) along the c axis. Making the simplifying assumption of a scalar coupling, the relationship can be expressed as follows:

$$K^{\alpha}_{s} = A_{\text{hf}} \cdot \chi_{local} \tag{6.7}$$

and at high temperatures $\chi_{local} = \chi_{\text{SQUID}}$ (χ_{SQUID} represents macroscopic susceptibility) due to low magnetic correlations (paramagnetic state), so we obtain the linear equation between K^{α}_{shift} and χ_{SQUID} by combining equations 6.6 & 6.7,

$$K^{\alpha}_{shift} = A_{\text{hf}} \cdot \chi_{\text{SQUID}} + K^{\alpha}_{0} \tag{6.8}$$

hence we can obtain hyperfine constant A_{hf} from the plot between K^{α}_{shift} and macroscopic susceptibility(χ_{SQUID}) measured along c direction at a field 1 Tesla in the range 150-300K. We obtained K^{α}_{shift} by fitting a Gaussian function around the peak maxima in individual spectra and comparing the shift relative to the reference frequency. In the case of triangular and hexagonal sites, the central line spectra indicate that they move in opposite directions. Specifically, the triangular site shifts towards lower frequencies, while the hexagonal site shifts towards higher frequencies compared to the reference line (ν_0). Therefore, $K^{\text{tri}}_{\text{shift}}$ and $K^{\text{hex}}_{\text{shift}}$ have opposite signs, suggesting that the triangular site is coupled to its magnetic environment via a negative hyperfine coupling constant, while the hexagonal site has

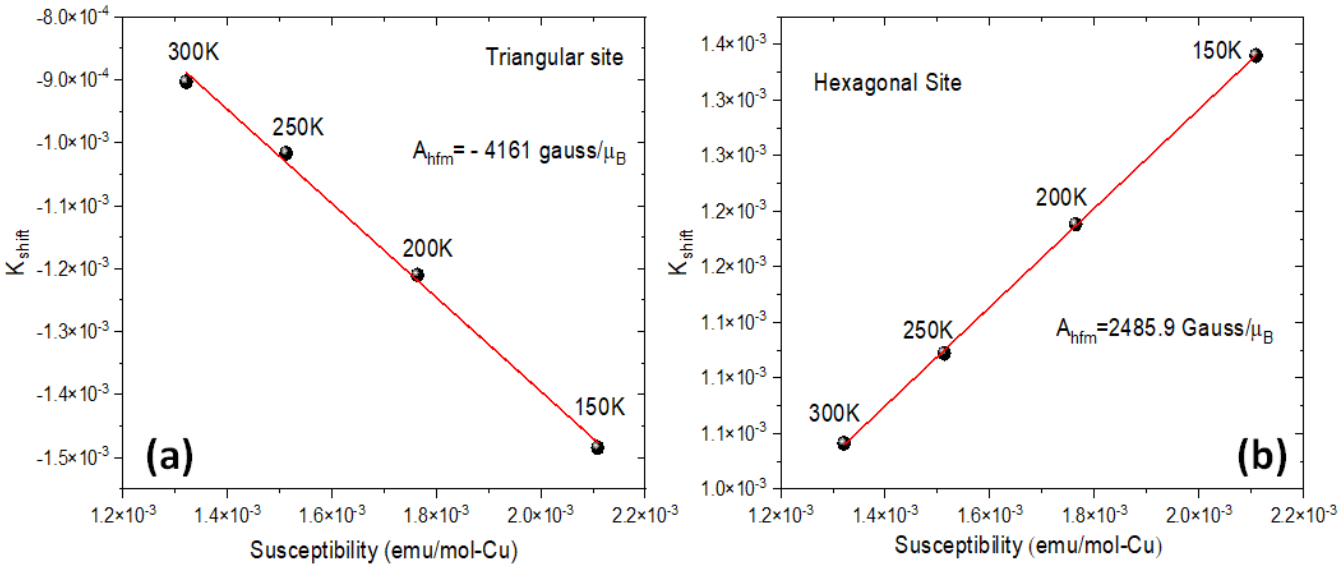

Figure 6.9: (a) Shifts vs macroscopic susceptibility (SQUID data obtained at 1 Tesla) has been plotted at high temperatures for the triangular site and (b) the hexagonal site.The red line is a linear fit following equation 6.8 to obtain A_{hf} for both sites.

a positive hyperfine constant [showed in figure- 6.9]. For the $H_0 \parallel c$ configuration, we report the following hyperfine constant values: $A_{\text{hf}}^{\text{tri}} = -0.426\,T/\mu_B$ and $A_{\text{hf}}^{\text{hex}} = 0.245(3)\,T/\mu_B$, along with temperature-independent chemical shift values: $K_0^{\text{tri}} = 52(10)$ ppm and $K_0^{\text{hex}} = 120(10)$ ppm for the triangular and hexagonal sites, respectively. Upon reducing the temperature (below 100 K), a notable enhancement in spin correlations becomes evident. This phenomenon arises due to the distinct magnetic environments and the different experiences of hyperfine coupling for both triangular and hexagonal sites. Around 100 K, a surprising divergence between the local susceptibilities of the triangular and hexagonal sites becomes noticeable [as shown in Figure 6.10.(a)]. The bulk susceptibility appears to resemble an average of the local responses from these two sites. This divergence likely relates to distinct couplings for these distinct sites. It's important to highlight that our hyperfine constant (A_{hf}) calculations have focused solely on the z direction, and other components of A_{hf}, such as A_{hf}^{xz} and A_{hf}^{yz}, contribute differently to each of the sites. This asymmetry enhances the likelihood of diverse in-plane correlation developments, although the bulk susceptibility does not show a clear sign of change in magnetic anisotropy (χ_{ab}/χ_c) in this temperature range.

As the temperature decreases, the error bars of the local susceptibility increase due to the broadening of the line widths at low temperatures. This broadening leads to a higher error in determining K_{shift}. Consequently, the triangular site exhibits larger error bars compared to the hexagonal site, as the triangular site experiences significantly more broadening than the hexagonal site at lower temperatures. Although we attempted to calculate K_{shift} below 10 K, the line shapes also undergo changes (splitting) along with the line widths due to structural alterations around 33 K and 15 K. As a result, we are unable to track the shifts below 10 K.

The local susceptibility has been determined using equation 6.7, employing the form $\chi_{\text{local}} = \frac{K_{\text{shift}}}{A_{\text{hf}}}$ at different

temperatures. Figure 6.10 displays the local susceptibility for both triangular and hexagonal sites, as well as the macroscopic susceptibility, within the temperature range of $10\,\mathrm{K} \leq T \leq 300\,\mathrm{K}$.

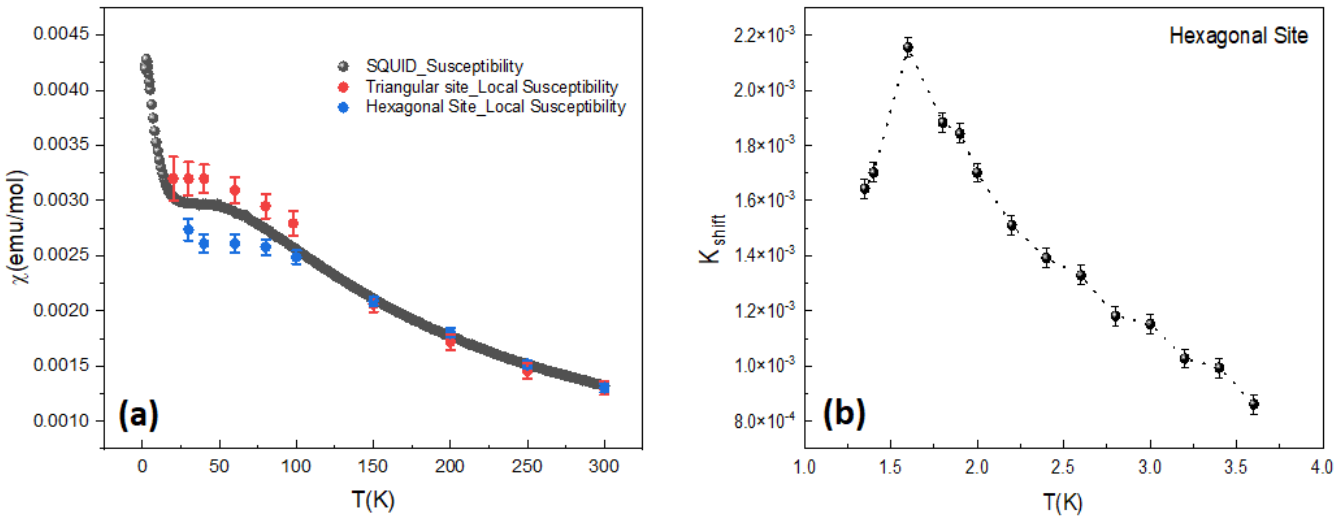

Figure 6.10: (a) Susceptibility (χ) versus temperature (T) plot. Black dots indicates macroscopic susceptibility (M/H) obtained from SQUID measurements with 1 Tesla field along c where as red dots and blue dots represents local susceptibilities for triangular and hexagonal sites. (b) Shifts were plotted for hexagonal site at low temperature($1.30K \leq T \leq 3.6K$).

However at lower temperatures (below 5 K), as discussed previously in the context of field sweep (H_0) measurements at a fixed frequency (31.510 MHz), even though there is an overlap between the two sites, we can effectively trace the shifts of the hexagonal site. This traceability owes itself to the comparatively minimal alterations in line widths and shapes for the hexagonal site when juxtaposed with the triangular site within the temperature range of $1.30, \mathrm{K} \leq T \leq 3.6, \mathrm{K}$. Interestingly, the shifts observed in the hexagonal line (K^{hex}_{shift}) display a distinctive peak at approximately 1.6 K [Figure 6.10.(b)], quite lower than the transition temperature 2.1 K. One possible reason for this discrepancy is that the shift in the ordered phase may have additional contributions from the in-plane internal field through non diagonal hyperfine coupling terms. These hypothetical contributions should increase gradually as the order parameter develops.

6.1.7 Summary of the static NMR study

The investigation involving ^{35}Cl NMR on oriented $Y_3Cu_9(OH)_{19}Cl_8$ crystals of the two distinct chlorine sites: hexagonal and triangular, aimed at uncovering intricate structural and magnetic insights by utilizing a temperature-dependent approach. The acquired spectra, which portray the evolution across different temperatures, have revealed intriguing structural deformations occurring at 33 K and 15 K. These deformations have not only illuminated symmetry-breaking phenomena, which were not apparent in the neutron diffraction data, but also confirmed the structural nature of the observed transitions. A deeper understanding of the modified spectra at lower temperatures, following the aforementioned structural deformations, has been achieved. The identification of a magnetic transition

around $\sim$ 2.1 K, represents an important development. While the impact of hyperfine couplings is evident within the system, challenges related to the comprehensive evaluation of all tensor components have led us to tentatively propose a purely dipolar magnetic interaction model. This assumption aligns remarkably well with theoretical predictions of a spin texture with the (1/3,1/3) propagation vector. Despite successfully deducing the local susceptibilities of distinct sites, the precise determination of magnetic moments values in the ordered phase remains intricate, given uncertainties regarding the stacking of the kagome plane along the c-axis. Additionally, the contribution of the external magnetic field to the overall magnetization in the ordered phase could play a role.

6.2 Relaxation time (T_1) measurements of different ^{35}Cl sites

6.2.1 Probing dynamics with T_1 measurements

In addition to our static NMR measurements, we have conducted spin-lattice relaxation (T_1) measurements, which provide valuable insights into relaxation processes involving both quadrupolar and magnetic effects. In the upcoming section, we will present a comprehensive analysis of the longitudinal relaxation time (T_1) for both the triangular (Cl_{tri}) and hexagonal (Cl_{hex}) sites. From a magnetic perspective, the relaxation time T_1 is intimately connected to the imaginary component of the transverse magnetic susceptibility ($\chi_\perp$), incorporating magnetic correlations. This relationship is described by the following equation:

$$\frac{1}{T_1^M} = \frac{k_B T}{\hbar} \sum_q |A(q)|^2 \frac{\chi_\perp^{''}(q, 2\pi\nu)}{2\pi\nu} \tag{6.9}$$

In this case, the excitation of the system occurs at frequency ν, and $A(q)$ represents the spatial Fourier transform of the hyperfine coupling (A). Fluctuations in the quadrupole interaction energy experienced by the nuclear spin arise due to the presence of an electric field gradient. These fluctuations play a role in the relaxation process and can enhance the rate of spin-lattice relaxation, depending on the specific characteristics of the system and the experimental conditions [Suter et al. 1998] . For systems like chlorine, where the nuclear spin quantum number is $I = \frac{3}{2}$, considering the quadrupolar Hamiltonian is relevant by accounting for quadrupolar effects, we can accurately capture the influence of relaxation on structural transitions. The resulting effective T_1 value can be expressed as follows:

$$\frac{1}{T_1} = \frac{1}{T_1^M} + \frac{1}{T_1^Q} \tag{6.10}$$

Consequently, when employing an appropriate irradiation frequency, dynamic measurements in NMR enable to probe of the complete excitation spectrum of the systems.

6.2.2 Site specific T_1 values: methods and results

To determine the longitudinal relaxation time, we employed the standard pulse sequence $\frac{\pi}{2} - t - \frac{\pi}{2} - \tau - \pi$, where t represents the time interval between the initial $\frac{\pi}{2}$ pulse and the Hahn echo sequence $\frac{\pi}{2} - \tau - \pi$. In our experimental setup, we conducted a Fourier transform of the spin echo and analyzed the relevant section of the spectrum as a function of time delays (t). For temperatures above 5 K, the separation between the central lines corresponding to the Hex and Tri sites remains distinct. Capitalizing on this separation, we successfully measured the T_1 values for both sites with precision. These measurements were carried out while maintaining a constant magnetic field of $H_0 = 7.553$ T.

Delving into further technical specifics, the width of the RF cavity governs the spectral region we can examine, and this width is inversely proportional to the duration of the π pulse in Hahn's sequence. In our particular case, the π pulse duration amounts to 4 μs, which corresponds to probing an area of around 250 KHz in the frequency domain. While this area might be relatively small compared to the entirety of the spectrum displayed in Figure 6.1.(c) at a temperature of 100 K, it is adequately expansive to encompass the central lines of the two chlorine sites, which are separated by approximately 120 KHz. Consequently, we are able to capture the complete central line by performing a single Fourier transform of the corresponding echo. Our approach for spin lattice relaxation measurements is thus discerning, as depicted in Figure 6.11(a). We achieve this selectivity by integrating either the hexagonal or the triangular line.

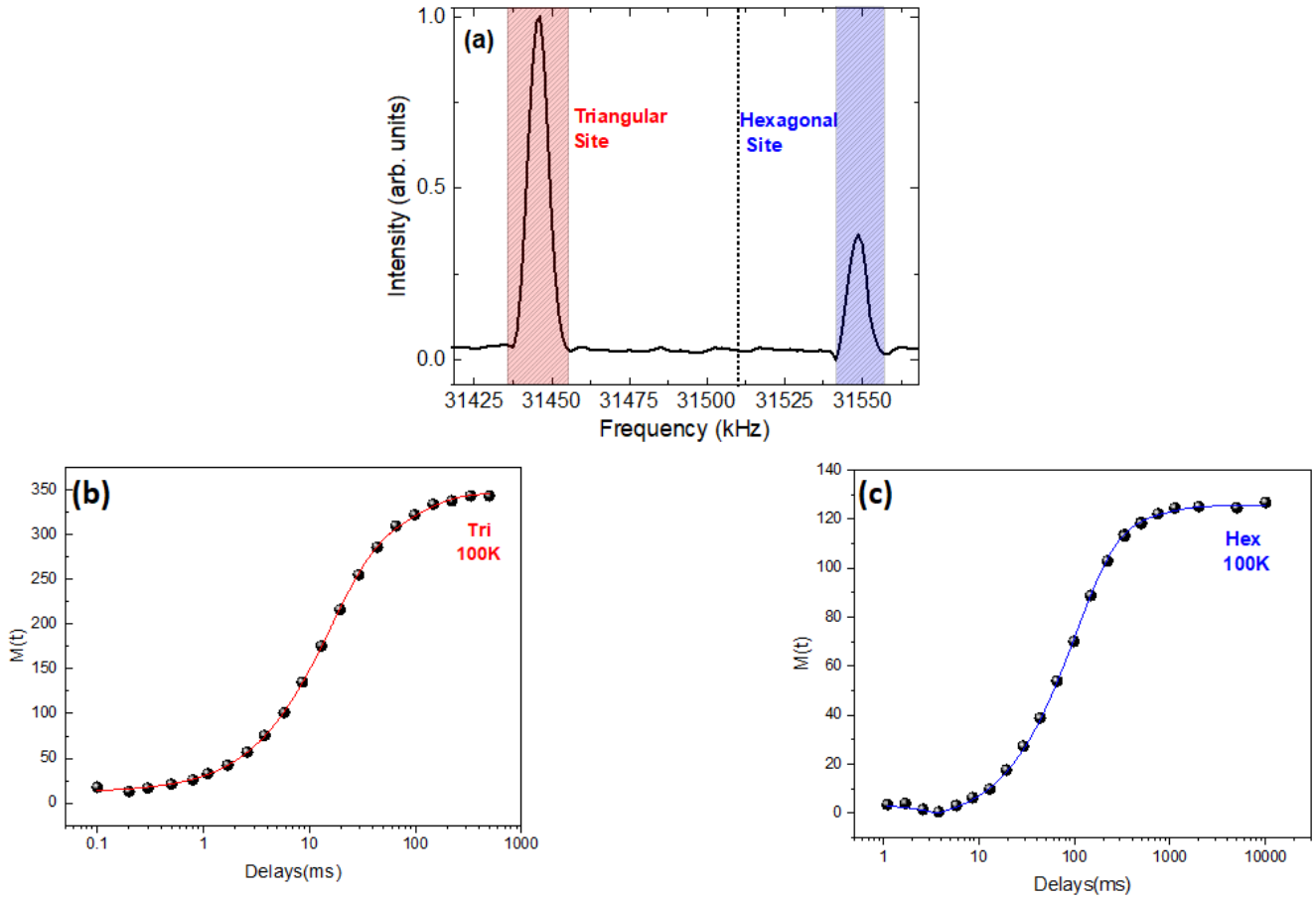

Figure 6.11: (a) Area of integration showed for triangular site and hexagonal site on frequency domain at a fixed field ($H_0 = 7.553$ Tesla) for the spectrum at T = 100K to measure magnetisation M(t) recovery with induced delays (a)relaxation data for triangular site & (b) hexagonal site where the red and blue lines lines are fit with equation-6.11.

The relaxation curves depicted in Figure 6.11(b) and (c) illustrate the behavior of the nuclear magnetization, M(t), as it returns to its maximum intensity, M_{sat}, for a specific site. By analyzing these curves, we can extract the longitudinal relaxation time T_1 for both the triangular and hexagonal sites.

The nucleus ^{35}Cl has a spin of $I = \frac{3}{2}$, resulting in the existence of three distinct nuclear transitions due to the

quadrupolar contribution. As a result, to extract T_1 values from the recovery curves of nuclear magnetization $M(t)$ at different temperatures, the dataset must be fitted with a multi-exponential equation, as detailed in prior research [Suter et al. 1998]. Concerning the central line,

$$M(t) = M_{sat}\left(1 - ae^{-\left(\frac{t}{T_1}\right)^{\beta}} - be^{-\left(\frac{6t}{T_1}\right)^{\beta}}\right) \tag{6.11}$$

where the parameters a and b adhere to the general relationship $a + b = 1$, and for a pureely magnetic relaxation $a = 0.1$. We used this fixed value for all our analysis. At 100K temperature, the two chlorine sites are distinctly separated in the spectrum [Figure 6.10(a)], thereby avoiding any cross-relaxation effects between the sites. The observed T_1 value at 100 K for the triangular site is approximately 102 ms, while for the hexagonal site, it's around 700 ms. These values clearly indicate substantial differences in the relaxation times between the two sites, which is a distinctive feature that we utilized to differentiate between the different sites when they overlap at low temperatures.

The parameter β is a phenomenological stretching parameter that reflects the potential distribution of T_1 values [Choi and W Gilbert Clark 1961]. The behavior of $\beta(T)$ is depicted in Figure 6.13(b) and 6.14(b). At elevated temperatures, the stretching parameter β remains constant ($\beta = 1$), indicating that satisfactory fits are achieved with a purely exponential relaxation model. However, as the temperature decreases a broader distribution of T_1 is observed close to 33 K transition, resulting in a change in β ($\beta \leq 1$), which is in line with the abrupt broadening of NMR lines as a result of structural (33 K & 15 K) and magnetic transitions (2.1 K) discussed earlier. It's important to emphasize that to accurately extract T_1 values from the relaxation curve, considering different values of β is crucial. Neglecting to incorporate $\beta < 1$ would result in inadequate quality of fits, as illustrated in Figure 6.12(d).

At temperatures below 5 K, the merging of the triangular and hexagonal sites occurs, as discussed in Subsection 6.1.5. This merging can potentially lead to the mixing of T_1 values between these different sites. However, despite this merging, the distinctiveness of the maximum intensity of the hexagonal site remains preserved, accompanied by a moderate change in the width of the central line (Figure 6.7) across the low temperature range ($1.4 \geq T \geq 4.2$ K). This situation enables us to fix the external magnetic field at the point corresponding to the maximum intensity of the hexagonal site in the spectra and acquire the magnetization recovery curve at that specific field value. As an illustration, in Figure 6.12(a), we set an external magnetic field $H_0 = 7.535$ T at 1.35 K, with a fixed frequency of 31.510 MHz, which corresponds to the maximum intensity of the hexagonal central line. By integrating the echoes with respect to time delays (t), we obtained the relaxation curve depicted in Figure 6.12(c).

In contrast, the behavior of the triangular site is different. It broadens and splits around the magnetic transition point (approximately 2.1 K), but the peaks' maxima remain distinct from the peak of the hexagonal site. Therefore, for a temperature of 1.35 K, we adjusted the external magnetic field to $H_0 = 7.655$ T [Figure 6.12(a)], corresponding to the peak of one of the triangular sites. This allowed us to specifically probe the relaxation at this site and obtain the relaxation curve [Figure 6.12(b)]. Similarly, on the other side of the spectrum, we conducted identical experiments

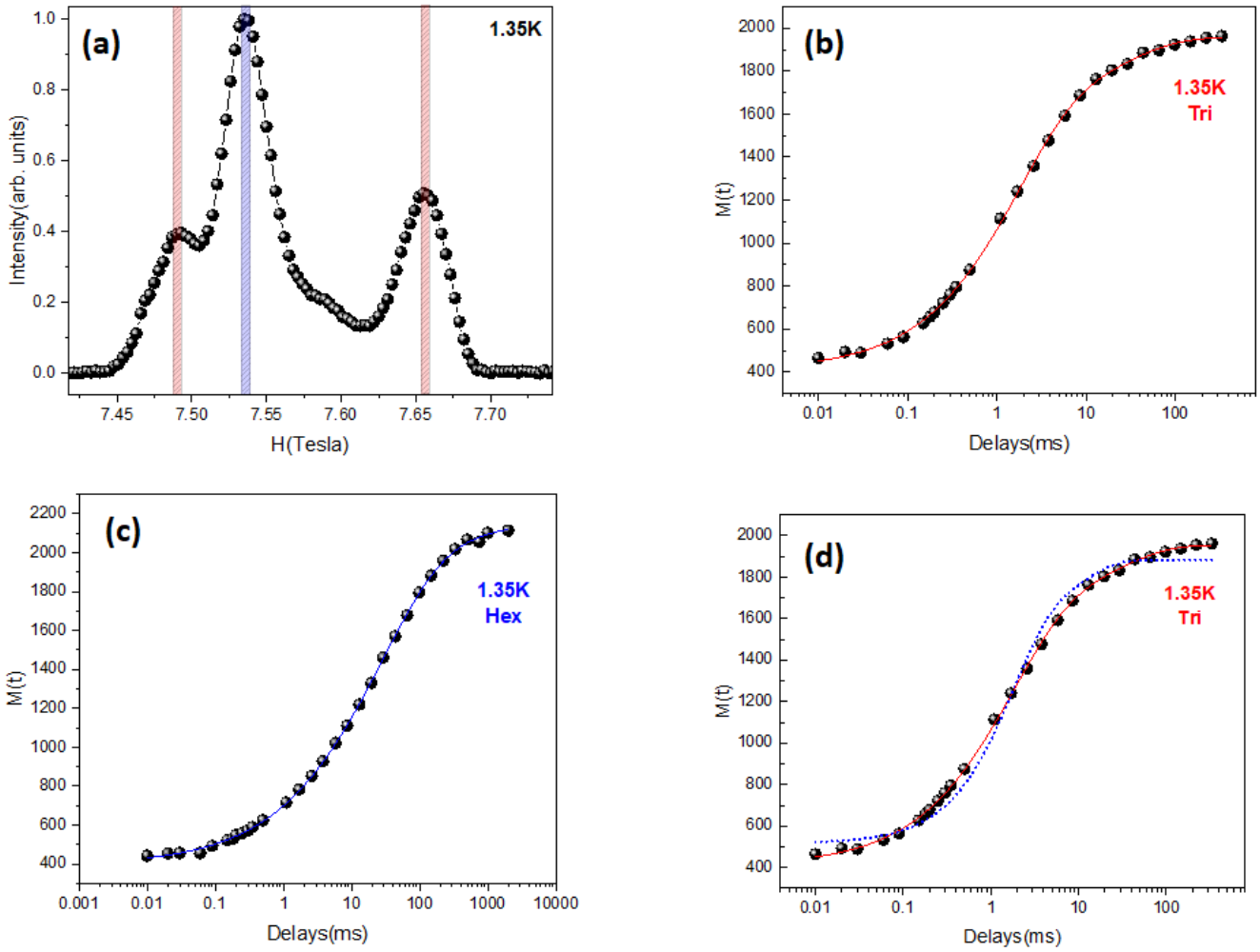

Figure 6.12: (a) Area of integration showed for triangular sites (red area) and hexagonal site (blue area) on time domain at a fixed frequency for the spectrum at T = 1.35K to measure magnetisation M(t) recovery with induced delays (b) relaxation curve for triangular site and (c) hexagonal site where the red and blue lines lines are fit with equation-6.11 with a finite β. (d) For 1.35 K at triangular site relaxation data, with variable parameter $\beta < 1$(red line) and also with fixed parameter $\beta = 1$ (blue dots).

at a fixed field of approximately 7.655 T. Remarkably, both of these contributions have nearly the same strength and relaxation time ($T_1 = 23.5 \pm 3.10$ ms), confirming their common origin from the triangular site. In contrast relaxation times for the hexagonal sites are approximately 10 times longer than those for the triangular sites.

Having described our experimental setup and the analytical approach to obtain spin-lattice relaxation data (T_1) along with its distribution parameter (β), we proceeded with the experiments. We performed the mentioned experiments and then fitted the magnetization recovery with the multi-exponential equation (6.11) in the temperature range from 1.35 K to 300 K, focusing on the central line. The resulting insights into the local dynamics of the system are illustrated in figures 6.13 and 6.14. The temperature-dependent evolution of T_1^{-1} for the triangular site is depicted in Figure 6.13(a).

The obtained relaxation data unveils three distinct transitions. A sharp peak at around $\sim$ 33 K and a relatively

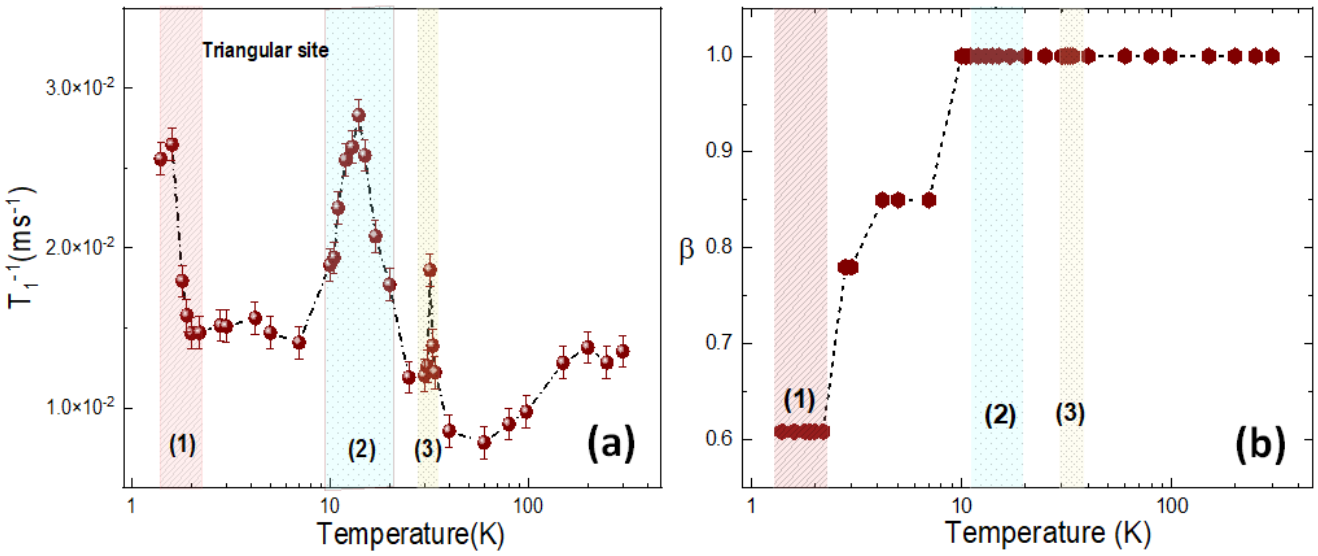

Figure 6.13: (a) Plot of inverse spin lattice relaxation(T_1^{-1}) rate with temperature for the triangular site where 3 different peaks are highlighted depicting 3 different transitions. Region (2) & (3) are highlighting structural transitions and region (1) depicts magnetic transition. (b) Plot of T_1 distribution parameter β derived from equation-6.11 with temperature for the triangular site.

broader peak at approximately $\sim$ 15 K signify structural transitions. The peak observed at lower temperatures corresponds to the magnetic transition point at $\sim$ 2.1 K. Notably this 2.1 K transition is also mentioned in reference-[Jierong Wang et al. 2022] where proton NMR has been implemented specifically at low temperature. These transition points align seamlessly with the evolution of NMR line shapes and widths, as well as with thermal conductivity and specific heat measurements conducted on this single crystal.

While fitting the relaxation curve for the triangular site, we observe that the distribution parameter β undergoes changes ($\beta < 1$), indicating a broader distribution of T_1 values from high to low temperatures possibly due to an increase in spatial correlation as the temperature decreases. However, during the transition regions [(1), (2), and (3)] illustrated in Figure 6.13, β can be held constant without any significant reduction in fitting quality. This observation assures that the peaks in T_1^{-1} accurately capture the anomalies in local dynamics resulting from temperature variations and are not influenced by correlated fitting parameters in the magnetization recovery equation, thus avoiding possible artifacts.

To investigate the hexagonal sites, a similar approach was employed, as depicted in Figure 6.14. As discussed earlier, the intermixing of two distinct sites along the central line raises the possibility of detecting contributions from other sites during site-specific relaxation studies. Specifically, Figure 6.12(a) illustrates how the hexagonal central line peak was probed, ensuring that the influence from the triangular site was eliminated as much as possible. To further confirm this behavior, we also conducted T_1 measurements on the hexagonal satellite in the low-temperature regime where the different sites overlapped in the central line. Hence we could attribute any observed effects particular to the hexagonal sites. To fit the magnetization recovery curve on the hexagonal satellites, we have used

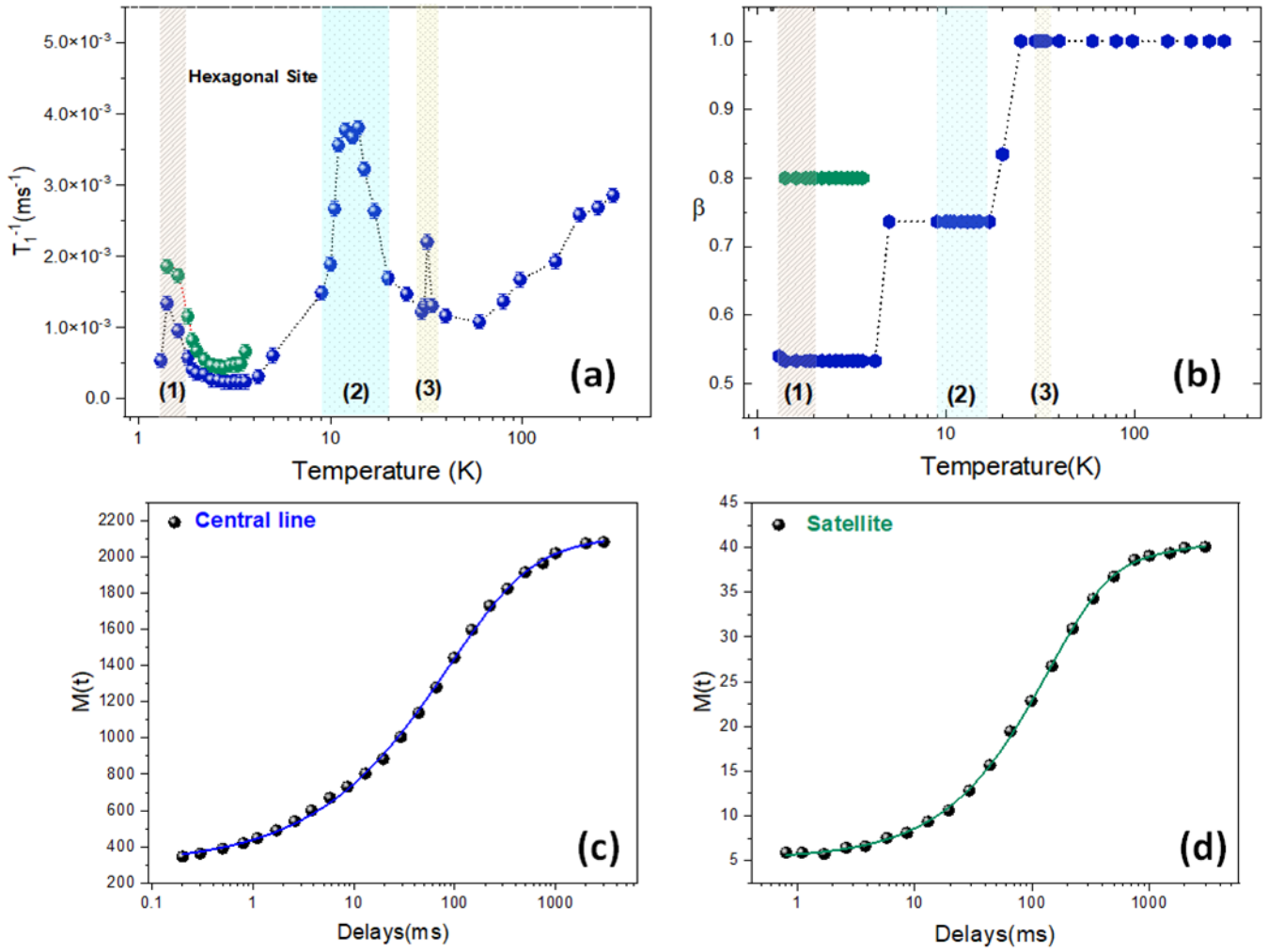

Figure 6.14: (a) T_1^{-1} versus temperature plot for hexagonal site depicting 3 different transitions (1),(2) & (3) where blue dots are for central line and green dots are relaxations shown by hexagonal satellites. (b) Plot of T_1 distribution parameter β derived from equation-6.11 with temperature for the Hexagonal site. Blue and green dots are representing β for hexagonal central line and satellites.

the formula :

$$M(t) = M_{sat}[1 - ae^{-(\frac{t}{T_1})^{\beta}} - be^{-(\frac{3t}{T_1})^{\beta}} - ce^{-(\frac{6t}{T_1})^{\beta}}] \tag{6.12}$$

where a+b+c=1; with values a = 0.1, b= 0.5 and c= 0.4. Although there were slight changes observed in the T_1 values and β parameter (shown in Figure 6.14(a) and (b), respectively), the overall pattern of their development remained consistent. This suggests that the hexagonal satellites exhibit dynamics similar to those observed along the central line, including a magnetic transition occurring at approximately 2.1 K.

6.2.3 Discussion

Based on our experimental data and analysis, we have observed three transitions in the excitation spectra of the single crystals in Y-kapellasite for both the triangular and hexagonal sites. These transitions consist of two structural transitions (around 33 K and 15 K) and a magnetic transition at 2.1 K. The transition at around 33 K exhibits a sharp nature, indicating a breaking of symmetry in the crystal structure at this temperature.

When dealing with an insulator in a paramagnetic state, the paramagnetic fluctuations are influenced by the value of the exchange interaction J. We calculated this paramagnetic Moriya limit of T_1 for both hexagonal and triangular sites using the following equation:

$$\frac{1}{T_1} = \frac{\sqrt{2\pi}\gamma^2 g^2 A_{hf}^2 S(S+1)}{3 z_1 \omega_e}; \tag{6.13}$$

where

$$\omega_e = \frac{J}{\hbar}\sqrt{\frac{2zS(S+1)}{3}} \tag{6.14}$$

In the equation, ω_e represents the exchange frequency defined by Moriya, and z is the number of magnetic neighbors for the probed spins, which is 4 for kagome systems. For the hexagonal site, with $z_1 = 6$, assuming that each Cl probes 6 nearest neighbor Cu atoms, the expected theoretical value for the magnetic fluctuations in the paramagnetic limit of T_1 is approximately 1120 ms. This calculation considers $J_{\text{kago}}^{hex} \approx 120K$ (averaging over different J values in the two different types of hexagons in the magnetic lattice) and the hyperfine constant $A_{\text{hf}}^{\text{hex}} = 0.245$ T/μ_B. Similarly, for the triangular site ($z_1 = 3$), the calculated T_1 is approximately 170 ms. This takes into account $J_{\text{kago}}^{tri} \approx 114$ (averaging out 3 J values constituting the triangular site) and the hyperfine constant $A_{\text{hf}}^{\text{tri}} = -0.426$ T/μB. These theoretical values do not match the experimentally obtained values of T_1 for the triangular site (~ 72 ms) and the hexagonal site (~ 360 ms) around a temperature of 300 K. Moreover the experimental relaxation rate $1/T_1$ is not clearly temperature independent even around 300K at least for the hexagonal site. The experimental findings indicate a noteworthy discrepancy: the measured T_1 values are notably shorter than the theoretically calculated values hence Moriya paramagnetic limit doesn't work. This intriguing observation implies that at higher temperatures, our systems are impacted not only by temperature-independent paramagnetic fluctuations but also by quadrupolar fluctuations, as elucidated in equation 6.10. This relaxation mechanism arises due to the quadrupolar coupling between the nucleus's electrostatic quadrupolar moment eQ and the electric field gradient (EFG) at the nucleus's site, leading to distinct effects on the triangular and hexagonal sites due to their differing local environments.

Based on our previous observations of hydrogen atoms in the system, it is evident that the H1 proton undergoes

movement at high temperatures, which significantly contributes to the relaxation measurement (T_1). We have noted that T_1 is influenced by quadrupolar fluctuations, as evidenced by the observed peaks at temperatures of 33 K and 15 K due to structural transitions.

Summary

Our study of the ^{35}Cl NMR systems clearly shows two contributions from two different chlorine sites. This investigation aims to provide a comprehensive understanding of the structural and magnetic characteristics of the $Y_3Cu_9(OH)_{19}Cl_8$ system within the temperature range of 1.35 K to 300 K. Through a combination of static and dynamic investigations. The observed sharp transition at 33 K signifies a structural rearrangement, while the broader crossover at 15 K indicates more complex modifications in the system. Moreover, the identification of a magnetic transition occurring at approximately 2.1 K has further enriched our understanding of the ground state corroborating our μSR results. Notably, our comparative analysis supports the presence of the Q=(1/3,1/3) ordering in this crystal as proposed theoretically [Hering et al. 2022]. The two distinct chlorine sites, hexagonal and triangular, are each characterized by unique hyperfine constants. This distinction leads to the manifestation of two distinct spin-lattice relaxation times for these sites. Importantly, even when these sites overlap in the spectra, the differing T_1, enable their identification.

Chapter 7

Concluding Insights: Exploring Inelastic Neutron Scattering and the Phase Diagram of Y-Kapellasite

To conclude this study, in this chapter, I will present the inelastic data and interaction exchange values to discuss the phase diagram that has been explored for this yttrium kapellasite. Edwin Kermarrec along with Jannis Willwater, Jacques Ollivier conducted inelastic neutron scattering experiments on large deuterated single crystals of $Y_3Cu_9(OD)19Cl_8$ to investigate the magnetic excitations and determine the magnetic order within this anisotropic kagome antiferromagnet (data can be found at-[E. Kermarrec et al. 2020]). These experiments were performed using the IN5 disk chopper time-of-flight spectrometer [Jacques Ollivier and Mutka 2011] at the Institut Laue-Langevin in 2020. To ensure precise alignment, a collection of single crystals with a combined mass of 0.3 g was carefully arranged in the (H, H, L) horizontal plane and securely attached to a thin aluminum plate using the hydrogen-free CYTOP solution (CTL-809M).

An incident neutron wavelength of $\lambda = 2.6$ Å has been used, corresponding to an incident energy of $E_i = 12.1$ meV, to search for excitations across a broad range. Subsequently, a neutron wavelength of $\lambda = 4.8$ Å, corresponding to $E_i = 3.55$ meV, was utilized to probe the spectrum in more detail. The resulting full width at half maximum (FWHM) energy resolution was 0.08 meV. By systematically rotating the sample stage perpendicular to the neutron beam direction, the reciprocal space could be mapped out comprehensively. To ensure accuracy, the efficiency of the detectors was carefully calibrated using preliminary measurements conducted on a vanadium can. These inelastic neutron scattering experiments provided us with invaluable insights into the magnetic excitations, allowing us to identify the magnetic interactions and orders present within the $Y_3Cu_9(OD)_{19}Cl_8$ system.

7.1 Evolution of the dynamical structure factor with temperature

The identification of magnetic scattering was limited to energies below 3 meV, which was an unexpected observation considering the significant antiferromagnetic Curie-Weiss temperature of $\theta_{CW} = -102$ K . Therefore, our focus was directed towards conducting measurements using a low incident energy of 3.55 meV. We examined the temperature-dependent changes in the dynamical neutron structure factor $S(q, E)$. Figure- 7.1 illustrates intensity contour color plots of $S(q, E)$ along the $[H, H, 0]$ direction. The phenomenon observed at a temperature of 60 K is a significant contribution from phonons, which refers to vibrations in the crystal lattice. As the temperature decreases to 20 K and below, the contribution from phonons diminishes considerably. This temperature-dependent behavior leads to the appearance of distinct and nearly vertical columns of intensity in close proximity to two specific wave vectors: $K_1 = (2/3, 2/3, 0)$ and $K_2 = (4/3, 4/3, 0)$. In addition to the columns of intensity, a broad region of intensity is observed around 2 meV, aligned with the $[1, 1, 0]$ direction. As the temperature is further lowered to the base temperature

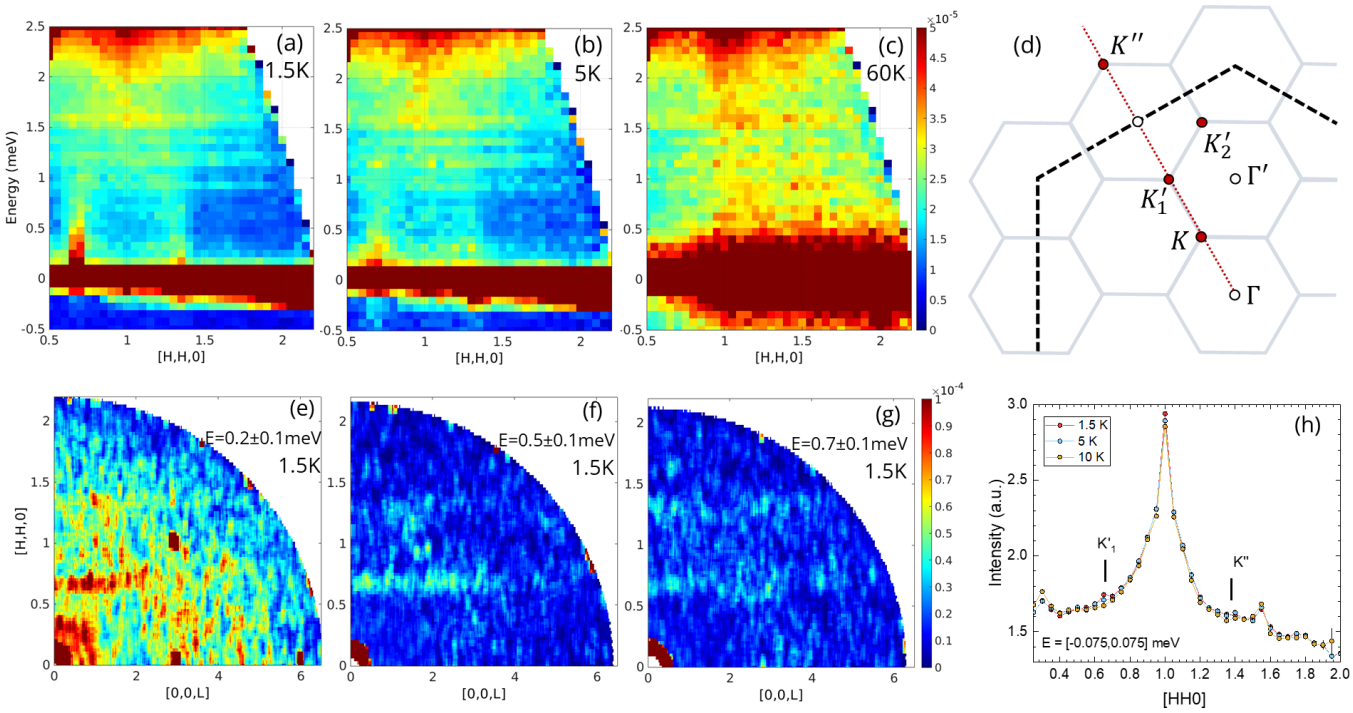

Figure 7.1: (a)–(c) The dynamical structure factor $S(q, E)$ along the $[H, H, 0]$ direction (integrated over $L = [-6, 6]$) was examined at temperatures of 1.55 K, 5 K, and 60 K .(d) The Brillouin zone boundaries (gray lines) are depicted, including the K and Γ points, along with the extended Brillouin zone (black dashed line) in reciprocal space. The red dotted line indicates the $[H, H, 0]$ direction. (e)–(g) The energy evolution of $S(q, E)$ was analyzed in the (H, H, L) plane at a temperature of 1.55 K. (h) An inelastic neutron scattering (INS) measurement was performed, integrating the energy over the elastic resolution and considering the range of $-6 < L < 6$. This measurement exhibited a weak increase at 1.5 K at the K_1 position and possibly also at K_2, which is characteristic of the (1/3, 1/3) magnetic order. Other discernible peaks were found to be unrelated to magnetic origins from the absence of T dependence.

of 1.5 K, a remarkable phenomenon occurs. Well-defined dispersive features emerge from the aforementioned wave vectors (K_1 and K_2). These dispersive features are attributed to the excitations of spin waves. The observed

scattering patterns in the study exhibit a distinct two-dimensional nature, as evidenced by the presence of scattering intensity rods along the [0, 0, L] direction. This characteristic validates the use of the two-dimensional Heisenberg kagome antiferromagnet model for the subsequent analysis. As discussed in Chapter-[4], neutron diffraction did not yield conclusive results for magnetic Bragg peak determination likely due to the low magnetic moment of Cu^{+2} ions within the kagome lattice. During the conducted experiment utilizing time-of-flight measurements, the elastic contribution was isolated by integrating over twice the energy resolution, which was estimated to be around 0.15 meV. At the base temperature of 1.5 K, Figure 7.1(h) reveals the emergence of minute magnetic Bragg peaks at the limit of resolution. It is important to acknowledge that the precision in pinpointing the exact positions of these peaks is constrained by the measurement's resolution. Specifically, these small magnetic Bragg peaks are visible at the K_1 position, corresponding to a concentration of magnetic scattering intensity at this particular wave vector. The K_1 position, characterized by the coordinates $(2/3, 2/3, 0)$, represents a distinctive point within reciprocal lattice space. Additionally, there are less distinct peaks observed at the K_2 position $(4/3, 4/3, 0)$. The detection of elastic scattering lends support to the presence of a magnetic noncollinear coplanar phase within the material. Nonetheless, it is important to acknowledge that the observed peaks do not significantly exceed the noise level in terms of intensity.

7.2 Evaluation of anisotropic exhange interactions and phase diagram

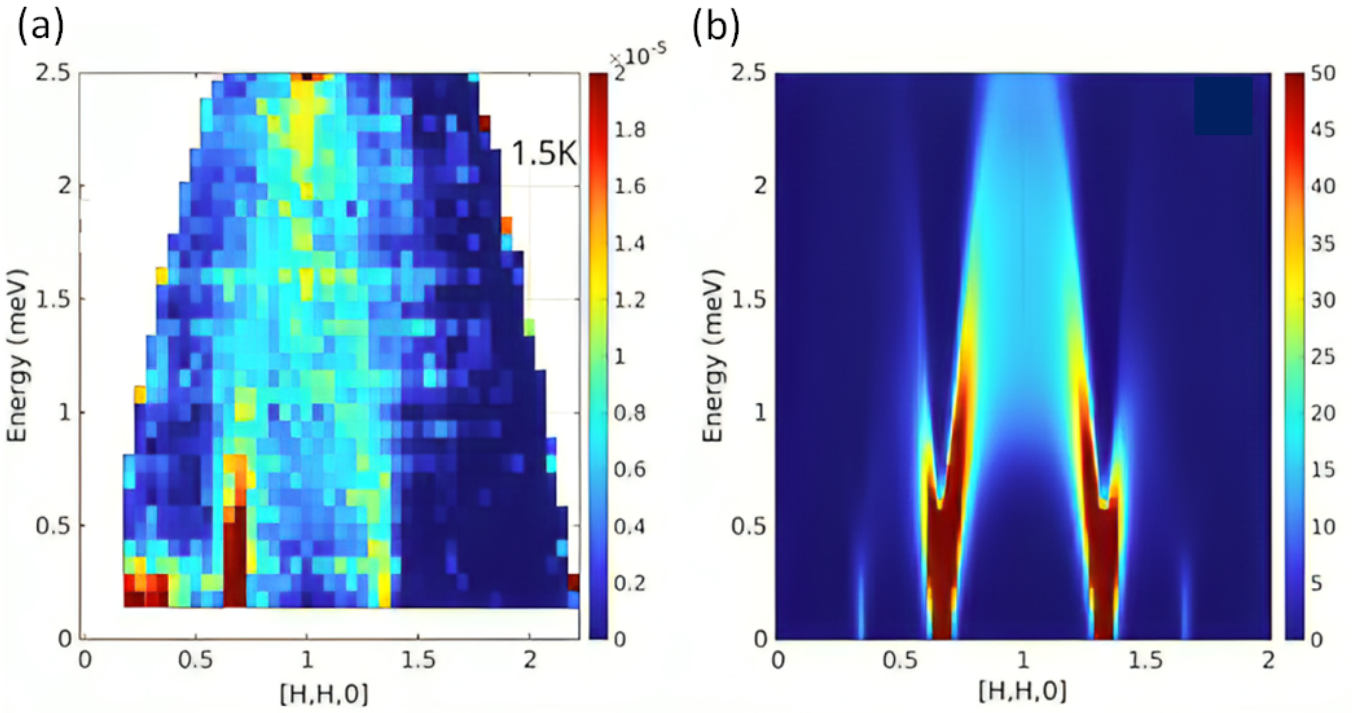

Figure 7.2: (a) A comparison is made between experimental data and (b) and spin-wave simulations at a temperature of 1.5 K. In order to emphasize the magnetic contribution, the INS data in (a) was subtracted by a 5 K dataset.

To enhance the isolation of the inelastic magnetic contribution at 1.5 K, a background subtraction technique was employed. The background signal was generated by replicating the dataset obtained at 5 K. To determine the background signal accurately, an integration was performed along the [H, H, 0] direction within the range H = [1.6, 2]. This specific range was selected based on the observation that it exhibited minimal contributions from both phonons and magnetic effects. By integrating within this range, a representative background signal was obtained. By subtracting this background signal from the original dataset, the resulting subtracted data specifically isolates the inelastic magnetic contribution at 1.5 K. Figure- 7.2 showcases this subtracted data, showing clearly spinwave excitation. The plot clearly illustrates the presence of dispersive excitations originating from the wave vectors K_1 and K_2. These excitations exhibit a characteristic dispersion pattern, merging into a broad arch shape that spans the energy range from 1 to 2.5 meV.

Taking into account the observed in-plane distortion of the kagome lattice and recent ab initio density functional theory (DFT) results from [Hering et al. 2022], Edwin Kermarrec performed linear spin-wave calculations using the SPINW package [Toth and Lake 2015]. These calculations were based on the Heisenberg model, incorporating nearest-neighbor interactions described in details in chapter [1]. The aim was to simulate the excitations within the anisotropic kagome lattice.

The corresponding Hamiltonian for the system is given by:

$$H = \sum_{\langle i,j \rangle} J_{ij} \mathbf{S}_i \cdot \mathbf{S}_j,$$

where the sum is taken over first nearest-neighbor pairs (i, j). In this equation, J_{ij} represents the exchange interaction strength between the spins at sites i and j, while $\mathbf{S}_i$ and $\mathbf{S}_j$ represent the spin operators at those respective sites.

The exchange interaction strengths J_{ij} in the Hamiltonian can take three different values: $J_{\hexagon}$, J, and J', which depend on the bonds d_1, d_2, and d_3, as depicted in Figure 5.5. Based on their density functional theory (DFT) calculations conducted in the study of Y-kapellasite, [Hering et al. 2022] confirmed the relevance of such spin models, see chapter [3]. The DFT calculations yielded the values of the antiferromagnetic couplings: $J_{\hexagon} = J = 140\,\text{K}$ and $J' = 10\,\text{K}$. In order to perform spin-wave simulations, an enlarged unit cell with nine sites was employed due to the presence of two distinct copper sublattices. The simulations were carried out assuming a coplanar order characterized by a propagation vector $Q = \left(\frac{1}{3}, \frac{1}{3}\right)$, In the case where $J_{\hexagon} = J = J'$, the model corresponds to the well-known $\sqrt{3} \times \sqrt{3}$ phase of the classical kagome antiferromagnetic model. However, this model fails to reproduce the experimental data when J exceeds 15 K, primarily due to the observed maximum in the energy band around 2.5 meV. Considering the Curie-Weiss temperature of $\theta_{CW} = 102\,\text{K}$, which implies a higher exchange value, the isotropic case is not applicable. Instead, the excitations are studied by varying the parameters J and J'. By examining the evolution of the spin-wave spectrum with different values of J and J', the best model is determined to be $J_{\hexagon} = J = 140\,\text{K}$ and $J' = 63\,\text{K}$. These parameter values exhibit the closest agreement with the experimental data and provide the most accurate representation of the system's excitation.

Moreover To adequately explain the broad distribution of intensity observed at [1,1,0] across the energy range from 1 to 2.5 meV, it has been found that a single set of interactions is insufficient. Instead, considering a tentative assumption of approximately 10% distribution of J', attributed to local disorder, yields a satisfactory fit to the inelastic data. By incorporating this assumption, the analysis depicted in Figures 7.2 indicates the presence of exchange interaction strengths $J_{\hexagon} = J = 140(10)\,\text{K}$ and $J' = [56, 70]\,\text{K}$, where J and J' represent the respective exchange interaction strengths within the system. The inclusion of a distribution of J' values addresses the observed broad distribution of intensity and provides a better agreement with the experimental inelastic data. This suggests that local disorder, characterized by the range of J' values, plays a significant role in shaping the intensity pattern and energy dependence of the excitation in the system.

7.3 Phase diagram and overall discussion on ground state of Y-kapellasite

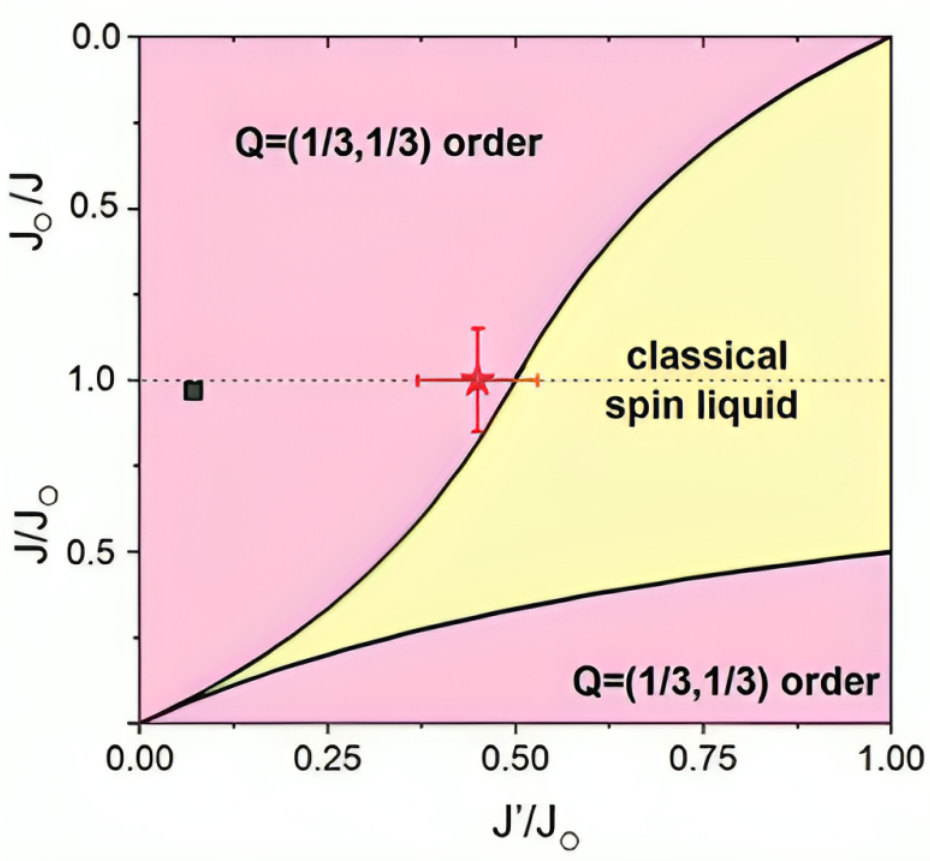

Figure 7.3: The classical phase diagram, originally published in [Hering et al. 2022], was reproduced. The black square represents the position obtained from DFT calculations [Hering et al. 2022], while the red star indicates the location of Y-kapellasite using the exchange couplings determined in our study. This comparison provides valuable insights into the agreement between experimental observations and theoretical predictions, further supporting our understanding of the magnetic behavior in this system.

I have reproduced the classical phase diagram from [Hering et al. 2022], which can be examined through our experimental findings to better understand the underlying ground state of this distorted kagome lattice. The inelastic neutron scattering (INS) data reveals the presence of elastic scattering at 1.35 K, which is consistent with the static magnetism observed by muon spin relaxation (μSR) and nuclear magnetic resonance (NMR) line broadening and shifting. These collective findings provide strong support for the existence of a magnetic ground state with the wave vector $Q = (1/3, 1/3)$. Our investigation of Y-kapellasite has led to the identification of a set of magnetic interactions that align qualitatively with the predictions from density functional theory (DFT) and variational Monte Carlo studies. However, a notable discrepancy arises between our experimental determination of $J' = 63(7)$ K and the theoretical calculation of $J' = 10.3(7)$ K. This leads to the identification of Y-kapellasite's position in the phase diagram still in the Q = (1/3, 1/3) magnetic order but in close proximity to the classical spin-liquid phase, see figure-7.3.

We note that a non-negligible J interaction is in line with the geometric arrangement of Cu-OH-Cu bond angles

in Y-kapellasite. These bond angles exhibit only a slight variation of 4.6° among the three different bonds, indicating a nearly uniform structural environment for the Cu atoms involved in the magnetic interactions. Notably, the smallest bond angle, measuring 113.1° and corresponding to the interaction strength J', remains considerably larger than 105°, a value known to result in a small ferromagnetic interaction of approximately -15 K in Zn-kapellasite [Fåk et al. 2012].

Furthermore, in an effort to reproduce the broad magnetic excitations observed in inelastic neutron scattering (INS), a distribution of approximately 10% for the J' interaction was introduced, suggesting the presence of some form of disorder in the system. However, unlike Zn-kapellasite and other materials with Zn- and Cu-based kagome structures, the significant difference in ionic radii between Y^{3+} and Cu^{2+} indicates that there should be no substantial intersite mixing. Interestingly, no evidence of such disorder in the magnetic lattice was detected above 33 K, as evidenced by neutron diffraction and nuclear magnetic resonance (NMR) spectroscopy, which exhibited well-resolved narrow lines. This suggests that any potential distribution of J' interaction becomes noticeable only at lower temperatures, possibly due to the structural instabilities observed at 33 and 13 K. The slight variations in the local environment, as detected below 33 K by NMR involving chlorine nuclei, may account for the moderate distribution of the interaction while preserving the overall high-temperature magnetic model. This hypothesis gains support from the observation that both the lattice parameters and the magnetic lattice remain unchanged within our measurement accuracy in neutron diffraction across the entire temperature range, even down to 65 mK.

As discussed earlier, the experimentally determined interactions position Y-kapellasite in the classical phase diagram, situated near the boundary between the (1/3, 1/3) long-range ordered phase and the classical spin liquid phase, as illustrated in Figure 7.3. Although the specific influence of quantum fluctuations in this proximity to the phase boundary has not been thoroughly investigated, it is plausible to anticipate their significant role in the system.

One notable consequence of the proximity to the phase boundary is the strongly reduced value of the Cu^{2+} moments, measuring less than 0.1 μ_B. These reduced moments might not be readily detected through standard neutron diffraction techniques. However, they give rise to static internal fields that are observable in both NMR and μSR experiments. While the proposed anisotropic nearest-neighbor model has shown success in elucidating the physics of $Y_3Cu_9(OH)_{19}Cl_8$, refining the model should enhance our comprehension of this material. This entails quantifying and addressing the significance of the Dzyaloshinskii-Moriya interaction, which has been identified as a critical factor driving long-range order in the sister compound $YCu_3(OH)_6Cl_3$ [Arh et al. 2020], exhibiting a perfect kagome lattice . Additionally, a key research perspective involves investigating quantum fluctuations, especially their impact at the phase boundaries. I have started to investigate a variant of this material with Br instead of chlorine to explore more this magnetic rich phase diagram as shown in the next part of the manuscript.

Summary

In the inelastic neutron scattering data at 1.5 K, a magnetic contribution was present and identified as spin waves. Linear spin-wave calculations, were performed using the SPINW package and were based on the nearest neighbour Heisenberg model, considering only nearest-neighbor interactions. This approach resulted in the determination of three different exchange interaction values: $J_{\hexagon} = J = 140(10)$, K and $J' = [56, 70]$, K. The value of J' is observed to be significantly larger than the theoretically calculated value, which was approximately $J' \sim 10$ K based on first principles calculations. Moreover the inclusion of a distribution of J' values was necessary to account for the observed broad distribution of intensity, which suggests local disorder in the system.

The experimentally determined interactions place Y-kapellasite in the classical phase diagram, near the boundary that separates the (1/3, 1/3) long-range ordered phase from the classical spin liquid phase. While the impact of quantum fluctuations in such close proximity to the phase boundary has not been extensively explored, it is conceivable that these fluctuations play a significant role in reducing the Cu^{2+} moments to less than 0.1 μB.

Chapter 8

Bridging the Gap: Exploring the Bromine Variant of Y-Kapellasite - $Y_3Cu_9(OH)_{19}Br_8$

As previously highlighted, recent years have witnessed significant endeavors focused on the doping of Herbertsmithite, $ZnCu_3(OH)_6Cl_2$. In this thesis, I have discussed the strategic approach aiming at substituting Zn^{2+} ions with Y^{3+} ions. Notably, systems such as $YCu_3(OH)_{6+x}Cl_{3-x}$ have undergone extensive investigation [Barthélemy, Puphal, et al. 2019], [Puphal, Bolte, et al. 2017], [Wei Sun et al. 2016], [Arh et al. 2020], [Zorko, Pregelj, Gomilšek, et al. 2019], [Sun et al. 2021], and [Chatterjee et al. 2023], which have shed light on the structural and dynamic implications arising from these doping variations. Another intriguing outcome of these endeavors is the emergence of the compound $Y_3Cu_9(OH)_{19}Br_8$. This bromine variant, which exhibits some degree of structural disorder as $YCu_3(OH)_6Br_2[Br_x(OH)_{1-x}]$ with $x \approx 0.51$ or 0.33, has been recognized for its promising potential in hosting a dynamic ground state [X.-H. Chen et al. 2020], [F. Lu et al. 2022], and [Zeng et al. 2022]. As in the chlorine part within $Y_3Cu_9(OH)_{19}Br_8$, the copper ions adopt a kagome lattice arrangement with antiferromagnetic in-plane interactions, and the inherent structural design effectively minimizes the occurrence of interlayer magnetic defects. To follow up my study with chlorine variant, this distinctive variant highlights the probable existence of unique magnetic and electronic properties, thereby emphasizing the demand for thorough and comprehensive exploration and understanding.

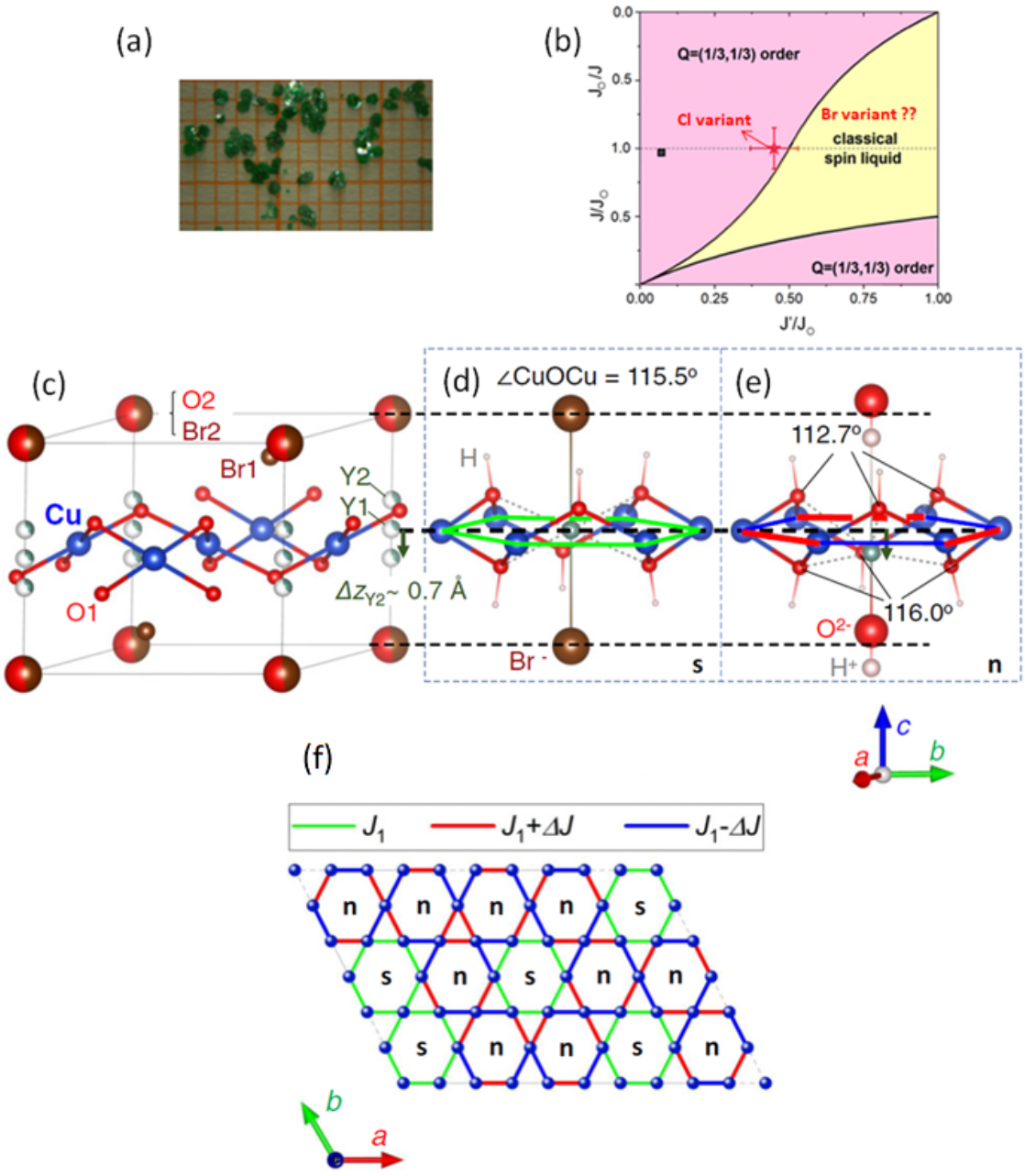

Figure 8.1: (a) $Y_3Cu_9(OH)_{19}Br_8$ single crystals were synthesized by P. Puphal and used for our investigations. (b) The previously explored phase diagram for the chlorine variant is depicted in Hering et al. 2022, where the black square represents the position determined through DFT calculations, and the red star indicates the location of $Y_3Cu_9(OH)_{19}Cl_8$ based on exchange couplings from [Chatterjee et al. 2023]. This signifies that the presence of Br^- ions, with their distinct ionic radius, can potentially fine-tune the exchange coupling in $Y_3Cu_9(OH)_{19}Br_8$, potentially shifting its ground state toward a spin liquid regime. (c-f) The figures (c) to (f) are adapted from [J. Liu et al. 2022]. (c) Depicts the lattice structure of $YCu_3(OH)_{6.5}$ $Br_{2.5}$ as obtained from X-ray diffraction measurements. (d) and (e) Illustrate the optimized crystal structures for supercells containing symmetric (s) and nonsymmetric (n) environments, respectively. The nonsymmetric environments (with a probability of approximately 70%) stem form deviations of Y^{3+} ions from their ideal positions (indicated by green arrows) and the presence of alternate superexchange pathways along the hexagons of the kagome lattice of Cu^{2+}. (f) Provides a schematic representation of the their model, highlighting the presence of approximately 30% uniform hexagons (in green) and around 70% randomly distributed hexagons with alternating bonds (in blue and red)

8.1 State of the art: The New Frontier of Kagome Lattice, $Y_3Cu_9(OH)_{19}Br_8$

In an effort to explore the proposed phase diagram outlined in the study by [Hering et al. 2022] pertaining to the distorted kagome lattice, we have utilized the $Y_3Cu_9(OH)_{19}Cl_8$ variant [Chatterjee et al. 2023]. This allowed us to investigate the impact of the proximity to the spin liquid ground state on its magnetically ordered ground state shown in figure-8.1(b), manifested as a reduction in experimentally observed magnetic moment, where Cu^{+2} moment reduced to 1/30 μ_B. In our pursuit of deeper insights into the ground state characteristics of these distorted kagome compounds, we opted to introduce a form of chemical pressure. This involved the incorporation of larger ions into the system as compared to chlorine. The purpose of adopting this approach was to investigate its influence on the bond lengths and angles within the kagome lattice structure. Hence we aimed to explore potential alterations in the exchange interactions that govern the system's magnetic behavior [$J_{\hexagon}$, J, J' shown in figure-8.1(b)]. This avenue of investigation holds the promise of potentially inducing conditions conducive to the realization of a spin liquid ground state. Motivated by the idea and collaborating with Pascal Puphal from Max Planck Institute in Stuttgart, we obtained small single crystals of the $Y_3Cu_9(OH)_{19}Br_8$ compound, as depicted in Figure-8.1(a). These single crystals served as the basis for a series of comprehensive investigations. I have conducted a comprehensive array of experimental techniques to gain a thorough understanding of the ground state properties. These included thermodynamic measurements such as specific heat and susceptibility analyses, as well as detailed Nuclear Magnetic Resonance (NMR) and Muon Spin Relaxation (μSR) studies.

Before delving into my own measurements, it's essential to recapitulate the existing findings and reported information concerning the bromine variant of the compound. The first bromine-substituted variant, characterized by an almost perfectly structured kagome layer, was detailed in [X.-H. Chen et al. 2020]. This variant, denoted as $YCu_3(OH)_6Br_2[Br_x(OH)_{1-x}]$, was synthesized through a hydrothermal method, with x approximating 0.51. This particular compound has been suggested as a potential candidate for a quantum spin liquid state. Similar to the chlorine case, bromine-substituted variant also showcases a layer structure reminiscent of kapellasite, featuring well-isolated kagome lattice decorated by magnetic ions (Cu^{2+}) with a spin quantum number of $S = 1/2$. The compound also exhibits two distinct positions for yttrium ions (Y^{+3}), mirroring the observations made in its chlorine analogue [Wei Sun et al. 2016]. Furthermore the refinement of x-ray diffraction data has revealed that the Br atoms exhibit partial substitution by (OH) groups, leading to the structural formula of $YCu_3(OH)_{6.5}$ $Br_{2.5}$. In a subsequent publication by [J. Liu et al. 2022], this intriguing phenomenon of site mixing between polar OH^- and nonpolar Br^- ions was further emphasized. The interplay of these ions leads to the introduction of local distortions within the Cu-O-Cu exchange pathways [shown in figure-8.1 (c)-(e)]. Consequently, it was observed that approximately $70(2)\%$ of the hexagons within the kagome lattice displayed alternating bonds and hence interactions ($\sim$ J1 - Δ J and J1 + Δ J), as shown in Figure 8.1(d), while the remaining hexagons maintained almost uniform bonding ($\sim$ J1). The $YCu_3(OH)_{6.5}$ $Br_{2.5}$ compound also continues to serve as an illustration of a spin-$\frac{1}{2}$ kagome Heisenberg antiferromagnet (KHA),

characterized by a notably robust coupling strength of $\langle J1 \rangle \approx 51$ K.

This intricate arrangement of bonds resulted in significant structural heterogeneity across the kagome lattice, and was proposed to favor disorder-induced gapless spin liquid state. Subsequent investigations [Zeng et al. 2022], [F. Lu et al. 2022] further emphasize the pivotal role of this structural disorder in influencing the behavior of $YCu_3(OH)_6Br_2[Br_x(OH)_{1-x}]$. Notably, in the work of [Zeng et al. 2022] where a similar crystal growth process as in reference [X.-H. Chen et al. 2020] was employed, a new variant, $YCu_3(OH)_6Br_2[Br_{0.33}(OH)_{0.67}]$, was reported. Heat capacity measurements have shown that this new variant lacks any ordering down to temperatures as low as 50 mK, which aligns with the characterization of a Dirac quantum-spin liquid state.

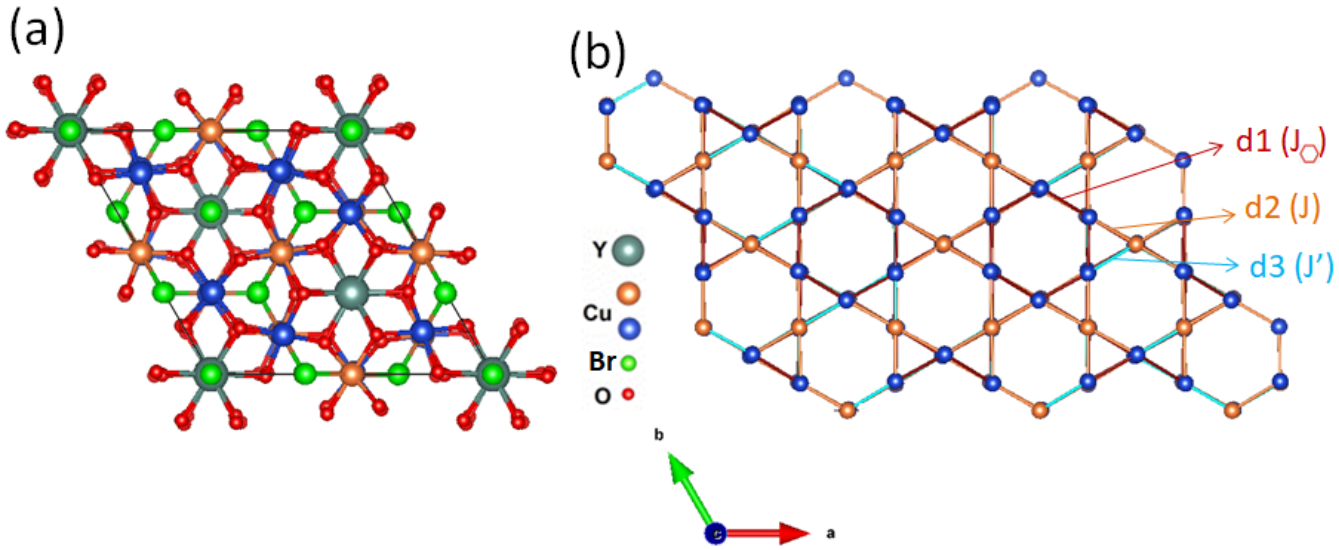

Figure 8.2: (a) The crystal structure obtained from xray diffraction measurements at 296 K, viewed along the c-axis. (b) A view of the distorted kagome along the c-axis, featuring two copper sites and three distances: d1, d2, and d3, which correspond to anisotropic interactions $J_{\hexagon}$, J, and J'.

However, our systematic investigation of single crystals of $Y_3Cu_9(OH)_{19}Br_8$ has revealed a distinct narrative concerning the structural and magnetic models for this compound. Contrary to previous studies, the single crystals we employed for our study do not confirm the presence of structural disorder between Br^- and OH^- ions. Instead, the structure closely resembles that of the Cl (x=1/3) variant. These contrasting findings will be thoroughly explored and discussed in the forthcoming sections.

The crystal structure analysis was conducted using x-ray measurements by Pascal Puphal. The refinement was performed at a temperature of 296 K with the $R\bar{3}$ space group. The lattice parameters are mentioned in the table-8.1 in comparison to the Cl case. In this arrangement, kagome layers are stacked in an AA-type configuration, with yttrium ions occupying central positions within the hexagonal units (refer to Figure 8.2(c)). The separation between adjacent kagome layers is approximately 5.9850(6) Å.

The presence of bromine ions effectively isolates the kagome layers from each other, resulting in strong decoupling, similar to what is observed in the chlorine variant of Y-kapellasite ($Y_3Cu_9OH_{19}Cl_8$). The angle associated with

Parameters	$Y_3Cu_9OH_{19}Cl_8$	$Y_3Cu_9OH_{19}Br_8$
Unit Cell Parameters		
a=b	11.539(5) Å	11.94(5) Å
c	17.1355 Å	18.35(4)
Bond Lengths and Angles		
$d1$	3.353(8) Å	3.3964(5) Å
$\angle d1(J_{\hexagon})$	117.02° (9)	118.08(11)°
$d2$	3.328(11) Å	3.3899(4) Å
$\angle d2(J)$	116.50° (4)	115.95(3)°
$d3$	3.314(8) Å	3.2640(4) Å
$\angle d3(J')$	113.0° (5)	110.7(9)°

Table 8.1: Comparing the lattice parameters and bond lengths of the kagome planes with the associated bond angles.

the distorted hexagons, denoted as $\angle d2$ = Cu2-O3-Cu1 and related to distance d2 = 3.3899(4) Å, is reported to be approximately 115.95° (3). This angle is comparable to the value of 115.5° reported in reference [J. Liu et al. 2022], and it is similar to the corresponding angle in the chlorine variant (see table- 8.1).

These angles play a significant role in determining the exchange interactions between the copper ions. Notably, the $\angle d3$ = 110.7°(9) Å likely leads to a lower value of J' compared to the other two exchange interactions [$J_{\hexagon} \approx J$], which are quite similar in magnitude. This signifies a distorted kagome structure, although considering the values of $\angle$ d1, $\angle$d2, and $\angle$ d3, the observed distortion is more pronounced than in the Cl variant. Therefore, in the phase diagram, the ground state should move away from the isotropic case.

Besides, it's important to note that due to x-ray measurements, we cannot comment on the hydrogen disorder in the sample at higher temperature in the paramagnetic regime. Since the structural information we obtained is quite similar to that of the chlorine variant, we will initially assume the same magnetic model. As we proceed, we will utilize additional bulk and local techniques to thoroughly investigate into the magnetic properties and discuss them in detail.

8.2 Thermodynamic characterization of the $Y_3Cu_9OH_{19}Br_8$ single crystals

8.2.1 Specific heat measurements

I performed specific heat measurements down to 1.8 K temperature, utilizing a standard Quantum Design PPMS (Physical Property Measurement System) at the Laboratoire de Physique des Solids (LPS). This experimental arrangement allowed for the manipulation of magnetic fields spanning from 0 to 9 Tesla. For the measurements, we crushed the crystals into a powdered sample weighing approximately 2.2 mg. It's important to note that a typical error of around 5% on the mass could occur due to the loss of small grains during the mounting process on the platform. We utilized Apiezon N Grease, a heat transfer medium well-suited for low-temperature and high-vacuum conditions.

In the figure- 8.3, we compare the specific heat data acquired for both $Y_3Cu_9OH_{19}Br_8$ and its chlorine counterpart $Y_3Cu_9OH_{19}Cl_8$. An intriguing revelation in the case of the bromine variant is the conspicuous absence of the 33 K peak, which was notably pronounced in the single crystals of the chlorine variant. This absence suggests that either the significant structural modification extensively discussed in [Chatterjee et al. 2023] is not present in $Y_3Cu_9OH_{19}Br_8$ or shifted in the temperature range. Instead, we have detected a distinct peak at approximately 15.5 K in this system, an observation that was lacking in the chlorine variant. although, it's worth noting that in $Y_3Cu_9OH_{19}Cl_8$, there was nonetheless a crossover-like transition in this temperature range detected through thermal expansion data and NMR relaxation measurements.

Furthermore, our specific heat measurements conducted at zero magnetic field have revealed two additional peaks, one at 9 K and another at 2.3 K, as depicted in figure-8.3(a). To delve into the nature of these peaks and the associated transitions, we systematically varied the applied magnetic field to observe their field-dependent behavior. Remarkably, the 15 K peak exhibited minimal changes in its position or shape as the magnetic field was increased. In contrast, the 9 K peak displayed a gradual suppression as the magnetic field strength increased. Given the magnetic nature and relatively small amplitude of this transition, we postulate the possibility of an impurity phase, possibly $Cu_2(OH)_3Br$, which itself has a transition temperature of approximately 9.3 K as reported in reference-Zhao et al. 2019. We further investigate this aspect in more detail using susceptibility measurements and localized techniques in subsequent stages confirming this hypothesis.

Regarding the $\sim$2.3 K peak, it exhibits a dependency on the applied magnetic field, signifying its magnetic nature. However, unlike its presence in the Cl variant as a sharp delta-like feature, in this sample, it manifests as a bump. As we examine Figure 8.3, it becomes clear that this $\sim$ 2.3 K bump diminishes gradually with increasing magnetic field, yet it does not shift towards higher temperatures. This distinctive behavior diverges from observations in other kagome compounds like herbertsmithite where weakly correlated impurity spins lead to Schottky anomalies, resulting in such shifts [Vries et al. 2008],[Barthélemy, Demuer, et al. 2022]. We can conclude that we do not observe a signature of free spins, and instead, we attribute this bump to a magnetic transition.

8.2.2 Susceptibility measurements

I have conducted magnetization measurements using a Quantum Design MPMS-XL SQUID (Superconducting Quantum Interference Device) magnetometer at LPS (Laboratoire de Physique des Solides). The measurements were performed on a pile of single crystals with a total weight of 41.8 mg with their c-axis oriented along the field. The bulk magnetization data we obtained in the temperature range 1.8 K till 300 K is shown in figure-8.4. For comparison with the chlorine variant, we have presented the 3 T data for $Y_3Cu_9OH_{19}Cl_8$, shown in figure-8.4(a). In the case of $Y_3Cu_9OH_{19}Br_8$, a pronounced hump is observed around 9 K in the susceptibility curve, as depicted in Figure- 8.4 (a) and (c). This transition around $\sim$ 9.3 K is also evident in the specific heat measurements. Its

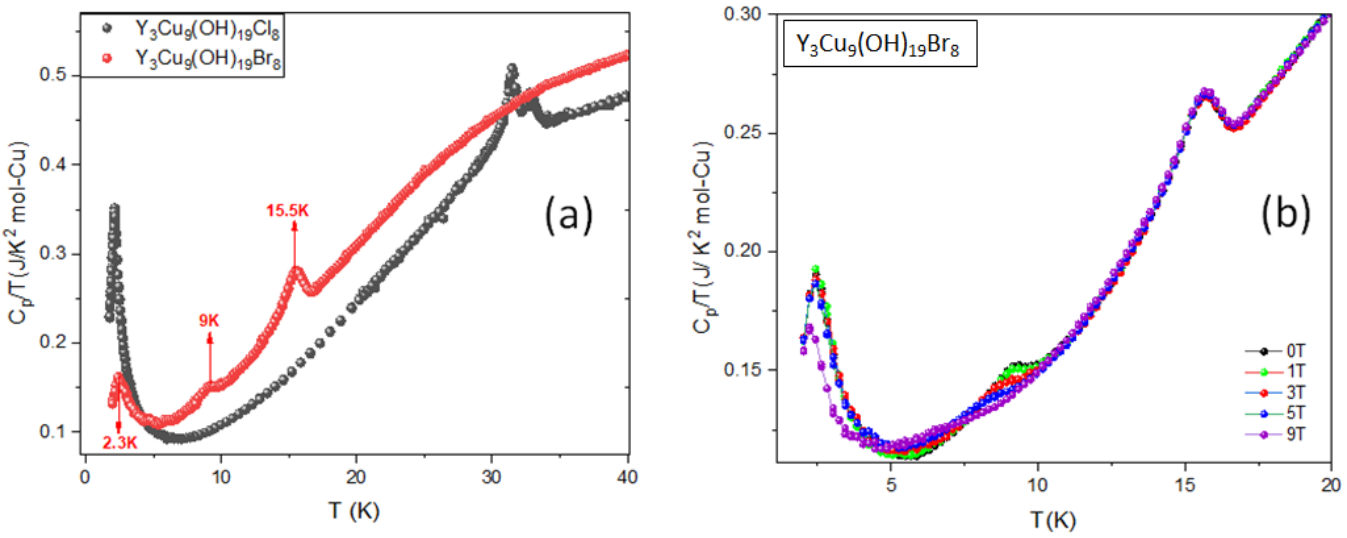

Figure 8.3: (a) Specific heat comparison between $Y_3Cu_9OH_{19}Cl_8$ and $Y_3Cu_9OH_{19}Br_8$ at zero field with in the temperature range 1.8K-40K. (b) Variation of specific heat with 5 different magnetic field 0 T, 1 T, 3 T, 5 T and 9 T has been shown to depict the origin of transitions at low temperature.

presence in susceptibility also hints at a probable contribution from a magnetic impurity phase within the sample, as demonstrated later with local techniques. In figure-8.4 I also compare our susceptibility data with published results [X.-H. Chen et al. 2020] and [J. Liu et al. 2022] in other bromine compounds in order to better understand the differences in bulk magnetic properties. While, a similar trend is observed at high temperatures, significant deviations become apparent below 50 K may be due to difference in impurity and free spins percentage in various sample. The temperature-dependent magnetic susceptibility is presented in Figure 8.4(c) for different applied magnetic field strengths: H = 7 T, 5 T, 3 T, 1 T, and 0.1 T. Notably, at lower temperatures ($T < 50$ K), the magnetic susceptibility demonstrates a clear dependence on the applied magnetic field. It is worth mentioning that the parasitic magnetic phase transition at 9 Tesla gets suppressed beyond 5 T, and no corresponding peaks similar to the one observed at $\sim$ 2.3 K in the specific heat measurements were detected.

At temperatures roughly above 60 K, the magnetic susceptibility $\chi_{\text{macro}}(T)$ follows a Curie-Weiss type trend. The antiferromagnetic Curie-Weiss curve indicates a Curie-Weiss temperature (θ_c) of 74 (2) K taken from a fit of the 1 T data within the temperature range of 100-300 K [Figure 8.4(d)]. The calculated Curie constant (C_c) is $0.450(2)$ cm^3.K/mol Cu, and by utilizing this value of C, we deduced the Landé g-factor as $g = 2.17(2)$ corresponding to an effective moment calculated along the c-axis $\mu_{eff} = 2.07\mu_B$/Cu. However, below 60 K, the increase in χ_{macro} deviates from the Curie-Weiss behavior, indicating the emergence of correlation effects. The magnetization exhibits a linear evolution as a function of the field at low temperature ($T = 1.8$ K) [as shown in Figure 8.4(e)]. It is important to mention that, in comparison to other reported samples in [J. Liu et al. 2022], [X.-H. Chen et al. 2020], [Zeng et al. 2022], the M-H curve shows a lesser contribution of free spins, as it appears more linear, and no spin saturation of magnetization is observed with the increasing magnetic field.

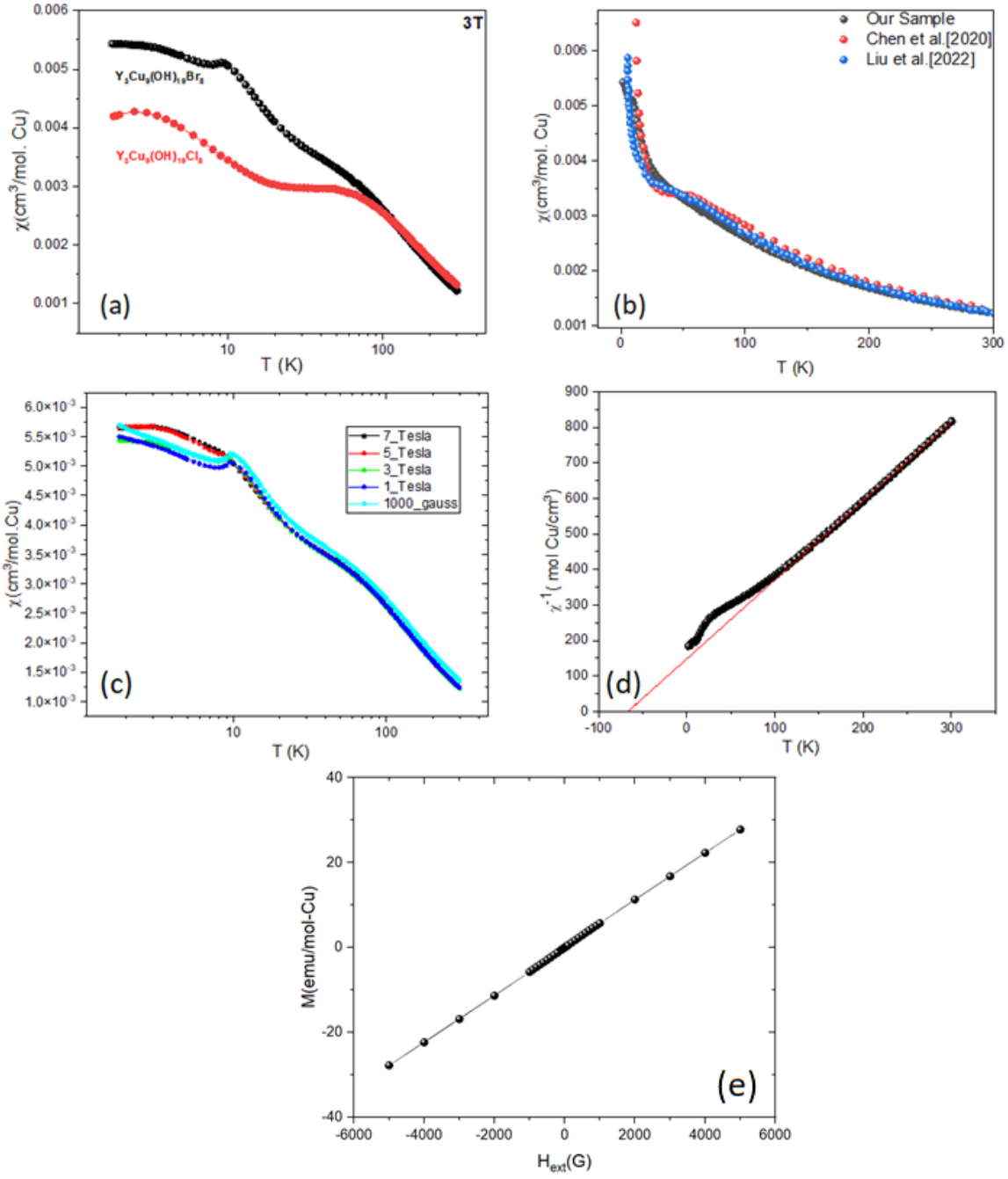

Figure 8.4: (a) Comparison between the susceptibility of $Y_3Cu_9OH_{19}Cl_8$ and $Y_3Cu_9OH_{19}Br_8$ at a magnetic field of 3 T, encompassing the temperature range from 1.8 K to 300 K. (b) A comparative analysis of susceptibilities across different samples, including [X.-H. Chen et al. 2020], [J. Liu et al. 2022] and our findings. (c) Thermal evolution of susceptibility under various external fields ($7T$, $5T$, $3T$, $1T$, $1000G$) is demonstrated. (d) Linear Curie-Weiss fitting within the high-temperature regime ($150 \leq T \leq 300$ K) is presented in the χ^{-1} vs T plot. (e) The linear variation of magnetisation (M) with magnetic field (H) at a low temperature (T=1.8K) has been depicted.

Summary

(1) With the aim of further exploring the phase diagram of the anisotropic kagome model, we investigate the bromide version of Y kapellasite. The substitution of Cl by the larger Br ions preserves the R$\bar{3}$ space group and increases the lattice parameters. Consequently, the lengths of the edges of the Cu triangles and the corresponding superexchange angles are modified, seemingly toward a more anisotropic model. In contrast to recent reports in the literature, our small single crystals do not exhibit sizeable Br/OH mixing and show a quite different low-temperature behavior with several transitions not reported so far.

(2) Specific heat measurements were conducted down to 1.8 K, with magnetic fields up to 9 Tesla. A comparison between $Y_3Cu_9OH_{19}Br_8$ and $Y_3Cu_9OH_{19}Cl_8$ revealed the absence of the 33 K peak but the emergence of a new non-magnetic peak at around $\sim$ 15.5 K in the former, suggesting structural differences. Furthermore, field-dependent specific heat measurements provide evidence for magnetic peaks at 9 K and 2.3 K in $Y_3Cu_9OH_{19}Br_8$. SQUID magnetization measurements were conducted on co-aligned single crystals. Above 60 K, a Curie-Weiss behavior is observed, yielding a sizable AF interaction but weaker than in the Cl counterpart, with θc of 74 (2) K. A small 9 K hump in susceptibility correlates with specific heat, suggesting the presence of magnetic impurity. In contrast to $Y_3Cu_9OH_{19}Cl_8$, we do not observe a peak or hysteresis that could signal a magnetic transition around 2 K.

Chapter 9

Exploring the Microscopic Realm: μSR and NMR Investigations of $Y_3Cu_9(OH)_{19}Br_8$

As highlighted in the preceding chapter, all previous studies [J. Liu et al. 2022, X.-H. Chen et al. 2020, Zeng et al. 2022] pertaining to the Br variant have consistently reported the absence of any ordering in the system, even at extremely low temperatures. However, our prior investigations, which involved bulk thermodynamics experiments conducted on small single crystal samples, have unveiled evidence of magnetic freezing in $Y_3Cu_9(OH)_{19}Br_8$ at a temperature of approximately 2.3 K. It's worth noting that the specific heat peak observed does not exhibit the characteristics of a sharp delta-type transition but rather manifests as a broad hump. Additionally, no distinct transition has been observed in the susceptibility data. Given these circumstances, the utilization of local techniques becomes imperative. These methods will not only enable us to discern the ground state of our samples but also assist in comprehending the underlying distinctions that we have observed in comparison to bulk thermodynamic measurements and other similar reported samples.

9.1 Experimental details

We conducted measurements at the Paul Scherrer Institute using the DOLLY spectrometer, enabling us to investigate muon spin polarizations in the temperature range of 0.27 K $\leq T \leq 40$ K. Approximately 300 mg of the sample, in the form of small crystals, was enclosed within a 0.25 μm thick copper foil.

9.2 Muon sites and impurity phase

Similar to the arguments made for $Y_3Cu_9(OH)_{19}Cl_8$, in our study, we have identified two major μ^+ stopping sites. These stopping sites are characterized by different fractions for μ^+ ions, which tend to stop at the most electronegative positions within the crystal. Given the crystal structure of $Y_3Cu_9(OH)_{19}Br_8$, it is likely that muons can reside in proximity to the OH^- groups and Br^- ions within the structure. The spectrum obtained in the paramagnetic state at high temperature ($T = 40$, K) and in zero field is shown in Figure 9.1. At this temperature the electron spins experience rapid and inhomogeneous fluctuations. The relaxation rate associated with these fluctuations is negligible due to motional narrowing. Consequently, the μSR signal is primarily influenced by the magnetism of nuclear spins.

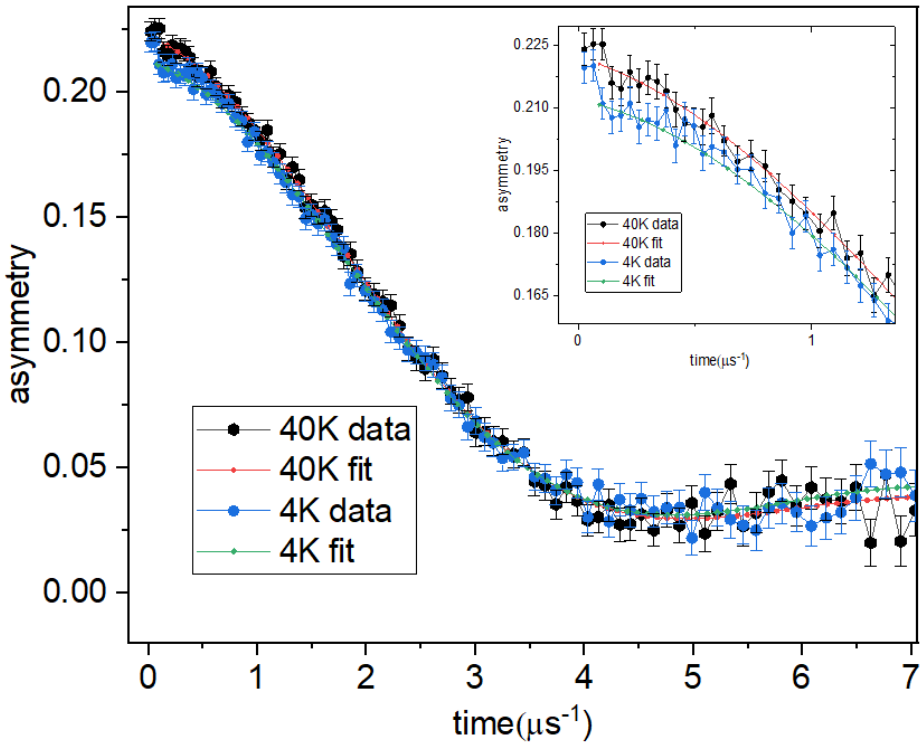

Figure 9.1: The zero-field asymmetry at 40 K and 4 K is shown in the figure, along with the fit using the same equation that was used for the chlorine variant at high temperatures, considering , P_{OH} as the expected function for a μ-OH complexe, ref-9.1. The inset provides a zoomed view of the plot at a smaller time scale, which clearly depicts the change in asymmetry.

We did not obtain asymmetry data for longer times in our measurements as we have performed experiments similar to Cl variant in PSI with a short time window. However, we have explored the possibility of the formation of μ-OH complexes that exhibit slow oscillations. These oscillations arise due to the dipolar coupling between the spins of the muons and the nuclear spins of the hydrogen ions. At high temperatures, the depolarization can be modeled by an equation similar to the one used for the chlorine variant:

$$a_0 P_{\mathrm{para}}(t) = a_0 \left[f P_{\mathrm{OH}}(t) + (1-f) K\, T_{\Delta_{\mathrm{Br}}}(t) \right] \tag{9.1}$$

The muon decay asymmetry a_0 was determined to be 0.225 through the 40 K temperature fit performed under our specific experimental conditions. Within the equation, the parameter f accounts for approximately 73% of the muons engaged in the formation of μ-OH complexes. The term P_{OH} describes the anticipated behavior of a μ-OH complex, incorporating Gaussian broadening denoted as Δ_{OH} with a value of 0.189$\pm$0.02 $\mu\mathrm{s}^{-1}$. Conversely, the remaining fraction of 27% corresponds to muons that stop in close proximity to Br ions. The term KT includes the Kubo-Toyabe relaxation function, which accounts for the Gaussian distribution of nuclear fields around Br^- ions. This distribution is characterized by a width denoted as Δ_{Br} with a value of approximately $\sim$ 0.42 $\pm$ 0.02 $\mu\mathrm{s}^{-1}$. Between 40 K and 4 K, an impurity phase has been observed, demonstrating a change in initial asymmetry a_0 by 5% as shown in Fig-9.1 (a). The observed change in asymmetry is certainly linked to the anomaly observed around 9 K in susceptibility measurements. The rapid initial decrease in asymmetry is likely a result of the internal fields emerging below approximately 9 K, which corresponds to the transition temperature of the impurity phase, comprising about 5% of the sample volume.

9.3 Probing the ground state

As the temperature decreases, the relaxation rate undergoes a gradual increase, indicating the gradual slowing down of electronic spin fluctuations in anticipation of a potential magnetic transition. This phenomenon can be effectively described using the following equation:

$$a_0 P(t) = a_0 \left[f_f P_f(t) + (1 - f_f) P_{para}(t) \right] e^{-\lambda t} \tag{9.2}$$

where for the frozen fraction,

$$a_0 P_f(t) = a_0 \left[\frac{2}{3} \cos\left(\omega_f t + \phi\right) e^{-\frac{\sigma^2 t^2}{2}} + \frac{1}{3} \right] \tag{9.3}$$

Equation-9.3 corresponds to the relaxation expected for a long-range ordered magnetic phase in a randomly oriented powder sample. It is used to model the rapid initial relaxation observed below 2.20 K.

Unlike the chlorine variant, our observations indicate a degree of inhomogeneity within the system, as the frozen fraction (f_f) notably deviates from unity even at the lowest temperature, as shown in Fig. 9.2(d). This observation suggests that approximately 40% of the spins in the system contribute to the emergence of static internal fields. The absence of oscillation in the fast-relaxing signal demands a significant damping parameter in equation-9.3, related to a substantial distribution of the internal field. Fluctuations are taken into account through the relaxation parameter λ in the paramagnetic phase and in the frozen state. Importantly, the relaxation rates effectively demarcate the transition point at 2.2 K, as illustrated in figure- 9.2(b). The absence of complete freezing, and the persistent relaxation observed well below 2.2 K, suggests a certain level of dynamic behavior in the system's ground state. This behavior clearly differs from the Cl analogue with its fully frozen ground state.

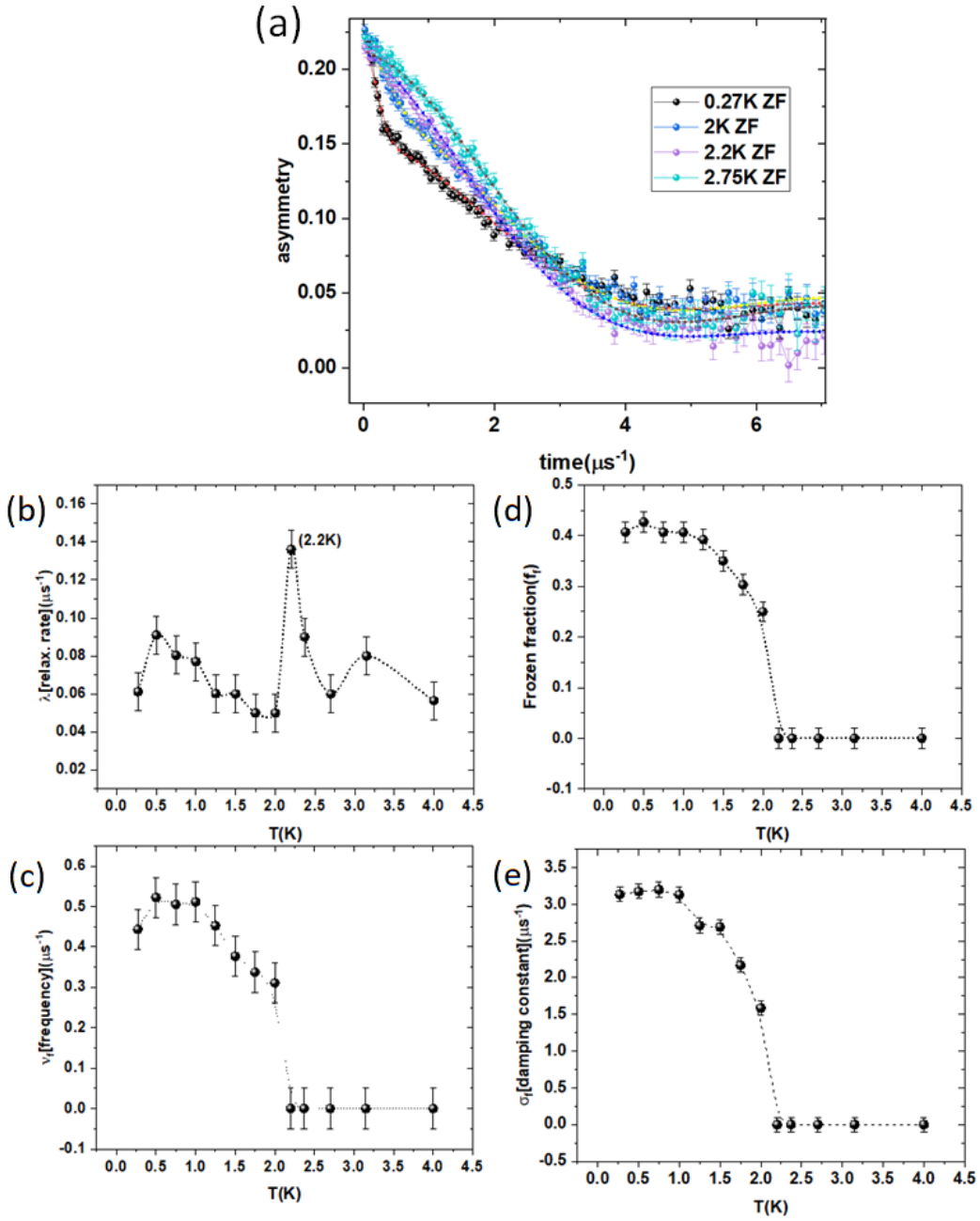

Figure 9.2: (a)Time evolution of the ZF asymmetry at some selected temperatures. (b)- (e)Temperature evolution of the parameters used in Eq. 9.3 to fit the ZF μSR data: (b) the relaxation rate (λ) (c) the frequency ν_f reflecting the internal field magnitude, (d) the fraction f_f of the frozen phase, and (e) the damping rate (σ).

9.4 NMR as a local probe to understand the structural and magnetic transitions in Br variant

Similar to our study with the chlorine variant, we chose to investigate the behavior of the bromine compound using NMR techniques. Our initial attempts involved aligning small crystals in close proximity, but the non-planar surfaces and low mass posed challenges in detecting clear signals. Hence, we proceeded to produce a powder from these miniature crystals and then alligned the resulting powder along the c-axis using an external magnetic field. To ensure the desired orientation and compactness even after the field was withdrawn, we employed a slow hardening epoxy glue.

The bromine (Br) nuclei in the system have a spin of 3/2 and are characterized by a gyromagnetic ratio of $\gamma/2\pi \sim 11.5$ MHz/Tesla for ^{79}Br and 10.48 MHz/Tesla for ^{81}Br. While both isotopes were investigated due to their nearly equal natural abundance, the presence of the ^{63}Cu signal from the NMR coil in proximity to ^{81}Br led to certain complexities. Consequently, at lower temperatures, the central line for ^{81}Br tends to broaden and merge with the ^{63}Cu line. As a result, to examine structural and magnetic transitions, the data primarily focused on ^{79}Br measurements.

9.4.1 Full Spectra with two different Br isotope

Our alignment process using NMR focused on the central line in the NMR spectra. This choice was made because, in contrast to the satellites, the central line is affected, at 2nd order only by slight misalignments. Once we attained an optimal alignment by fine-tuning for the central line the angle 'θ' between c-axis and the external magnetic field, we proceeded to investigate the hexagonal satellites, which are more sensitive to variations in θ. This stepwise approach ensured an easier alignment process. In the crystal structure of $Y_3Cu_9(OH)_{19}Br_8$, as discussed previously for the chlorine variant, there exists two distinct bromine sites (depicted in Figure 9.3). These bromine sites, denoted as the triangular site (tri) and hexagonal site (hex), are situated between the planes at the center of the triangles and hexagons within the Cu^{2+} kagome structure, analogous to the chlorine variant. We have observed two different sites for each isotope, as expected, thus no obvious signs of large Br/OH exchange. Nonetheless, we note that the lines are broader in our sample compared to the chlorine variant (at 100 K, the hexagonal and triangular lines in the Br variant are twice as broad as those in the chlorine variant). This may be attributed to several factors. It's possible that our sample has more disorder within the system compared to the chlorine variant. Additionally, the fact that our sample is not a single crystal could also contribute to this broadening, as there might be a distribution of orientations of the grains in the powder sample.

The complete bromine spectrum is showcased in Figure 9.3, recorded at a temperature of approximately 45 K, with a fixed frequency of 82.72 MHz and a full field sweep encompassing all the satellite peaks for both Br isotopes.

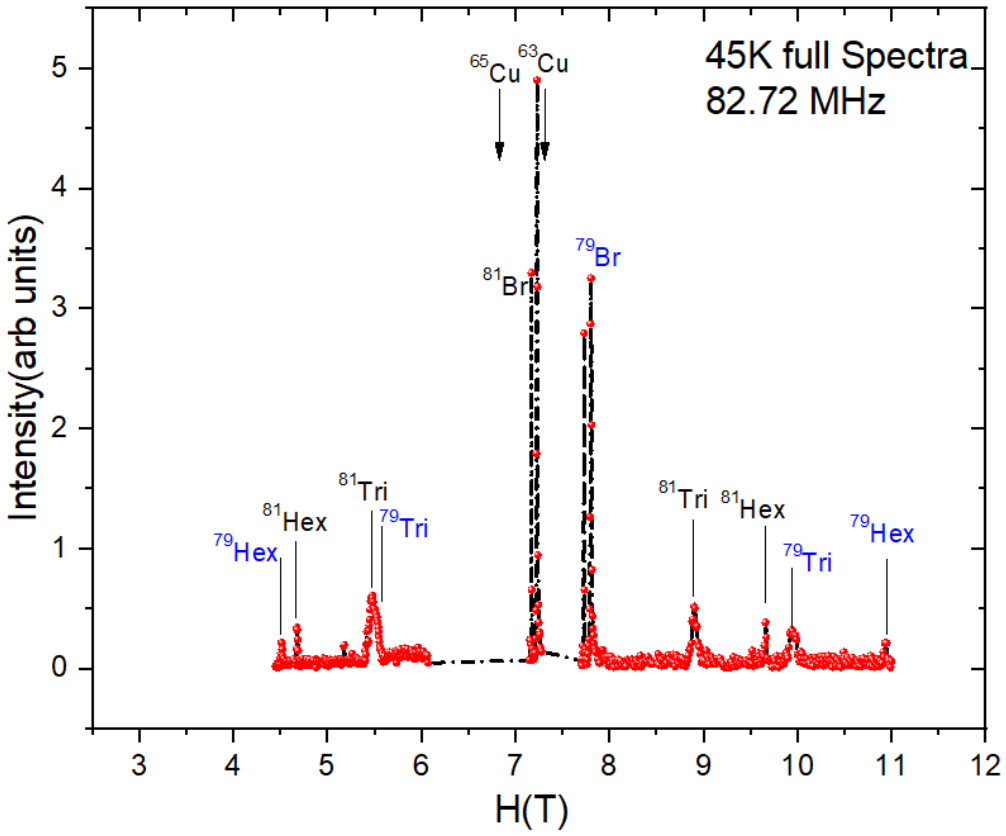

Figure 9.3: The complete NMR spectrum of both ^{81}Br and ^{79}Br at 45 K at a resonance frequency 82.72 MHz, obtained with the $B_{\text{ext}} \parallel c$ configuration of the oriented powder, reveals two central lines for each Br isotope, corresponding to Br_{tri} (triangular site) and Br_{hex} (hexagonal site), accompanied by their respective pairs of satellites. This spectrum provides a comprehensive view of the NMR behavior of the Br nuclei in the crystal lattice.

This temperature selection ensures that the measurements are conducted well above any potential magnetic or structural phase transitions, guaranteeing the accuracy and reliability of the data. At this temperature, it exhibits approximately $\nu_Q^{hex} \sim 33.3$ MHz and $\nu_Q^{tri} \sim 23.5$ MHz (note that in case of the triangular site this value is not corrected for the tilt on the EFG with respect to c-axis). Next, our focus will be on investigating the structural transitions in our systems, which have attracted attention in bulk thermodynamic measurements. The shape and width of NMR lines are sensitive to both local magnetic and electronic changes, making them valuable tools for directly investigating structural and magnetic transitions from the spectra. Employing a local probing technique like NMR offers the added advantage of separately observing the effects of local electronic changes on two distinct sites as the temperature evolves.

9.4.2 Evaluating hyperfine coupling from High temperature spectra

The variations in electronic couplings experienced by the triangular and hexagonal sites lead to distinct values for their respective local hyperfine fields (H_{loc}). These differences are clearly manifested in the observed NMR shifts for these two types of sites. Our approach to investigating the local susceptibility involves analyzing the deviation of NMR lines from the reference frequency ν_0 under the influence of an external magnetic field H_0, a methodology similar to that employed for the chlorine variant. To quantify the shift K_α (α=hex, tri), we conducted Gaussian fitting around the peak maxima in individual spectra, enabling us to determine the shift relative to the reference frequency, which is $\nu_0 = 87.770$ MHz, corresponding to a magnetic field of 8.23 Tesla for the Br^{79} nucleus.

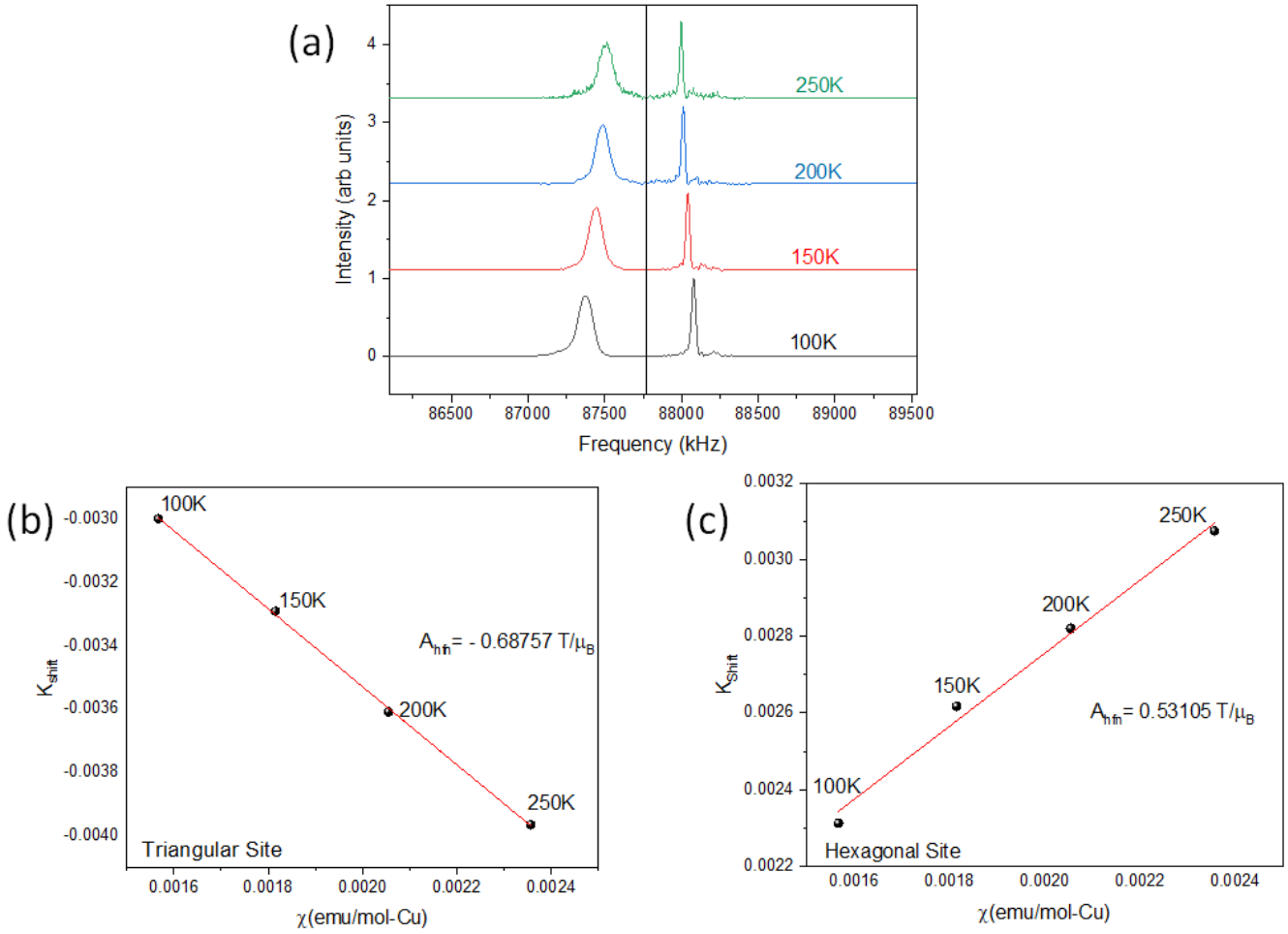

Figure 9.4: (a) The shift evolution with temperature is illustrated, showcasing the central line of Br_{81} with a reference frequency of 87.770 MHz. (b) Shifts versus macroscopic susceptibility, obtained from SQUID data at 3 Tesla, have been plotted for the triangular site, while (c) a similar plot is presented for the hexagonal site. Notably, the red line signifies a linear fit used to determine the hyperfine coupling constant (A_{hf}) for both of these sites.

In the case of the triangular and hexagonal sites, the central line spectra display shifts in opposite directions. Precisely, the triangular site exhibits a shift towards lower frequencies, whereas the hexagonal site shifts towards higher frequencies in comparison to the reference line. Consequently, K_{tri} and K_{hex} possess opposite signs, signi-

fying that the triangular site interacts with its magnetic surroundings through a negative hyperfine coupling constant, while the hexagonal site possesses a positive hyperfine constant (as illustrated in Figure 9.4).

The hyperfine constant values we determined for the configuration where $H_0 \parallel c$ are $A_{\text{hf}}^{\text{tri}} = -0.68757, T/\mu B$ for the triangular site and $A_{\text{hf}}^{\text{hex}} = 0.53105, T/\mu B$ for the hexagonal site. When comparing these values to those reported in the reference Zeng et al. 2022 along the z-axis, which are $A_{\text{hf}}^{\text{tri}} = -0.68, T/\mu B$ and $A_{\text{hf}}^{\text{hex}} = 0.55, T/\mu B$, we observe that similar hyperfine coupling constants exist for different samples, despite some minor differences in the numerical values. This consistency suggests that certain magnetic properties are preserved across various samples of the same compound, at least above 100 K.

9.4.3 Structural Transition

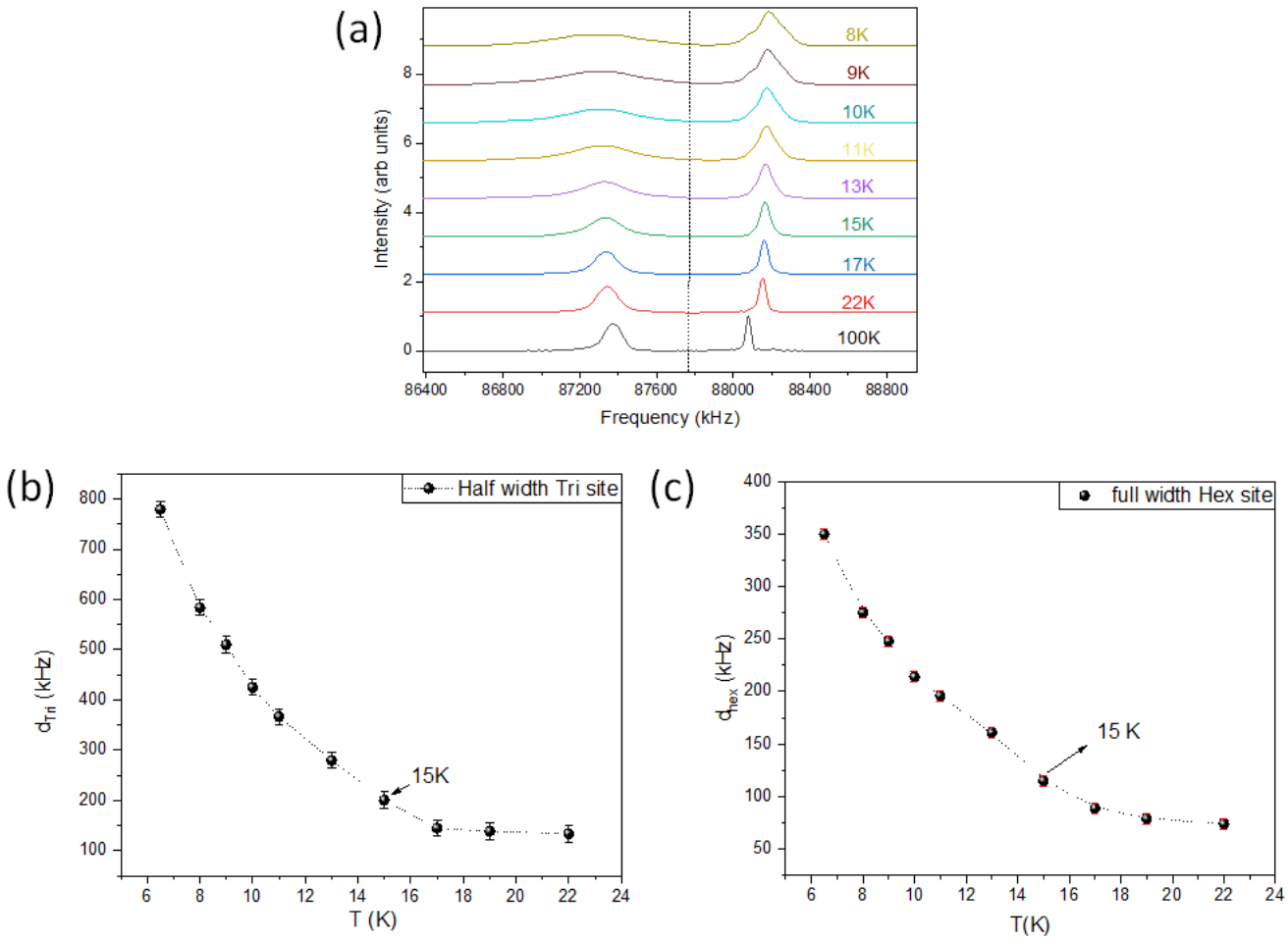

Figure 9.5: (a) The temperature evolution of the central line for ^{79}Br with respect to the reference frequency $\nu_0 = 87.770$ MHz. (b) Change in the full width at half maximum (FWHM) of the central line for the triangular site as a function of temperature, indicating anomalies at around $\sim$ 15 K. (c) The full width of the central line for the hexagonal site as a function of temperature also demonstrates clear anomalies occurring at around 15 K. This observation is consistent with the structural transition we identified in specific heat.

To investigate the central line of ^{79}Br, field sweep measurements were conducted at a fixed frequency of $\nu_0 = 87.770$ MHz, spanning from 8.10 Tesla to 8.30 Tesla with 100 gauss increments. Subsequently, Fourier transforms were applied to the collected echoes, and these Fourier transforms were recombined to obtain the complete signal.

In the central line for ^{79}Br, a significant broadening was observed, particularly at the triangular site, as the temperature decreased to below 15K. This broadening effect was also evident at the hexagonal site. The broadening aligns with the specific heat with a sharp transition occurring around $\sim$15 K identified as a structural transition from it's magnetic field independence. To quantify this broadening phenomenon, a plot of the full width at half maximum (FWHM) for the triangular site line against temperature variation was generated, as shown in Figure 9.5(b), along with the full width measurements for the hexagonal site shown in Figure 9.5(c).

Beyond the broadening, both sites exhibit a splitting, most prominently for the triangular site, although an additional shoulder is also clearly visible below 10K for the hexagonal site. This reminds the changes observed in the chlorine counter part at it's 33 K structural transition suggesting a similar distortion.

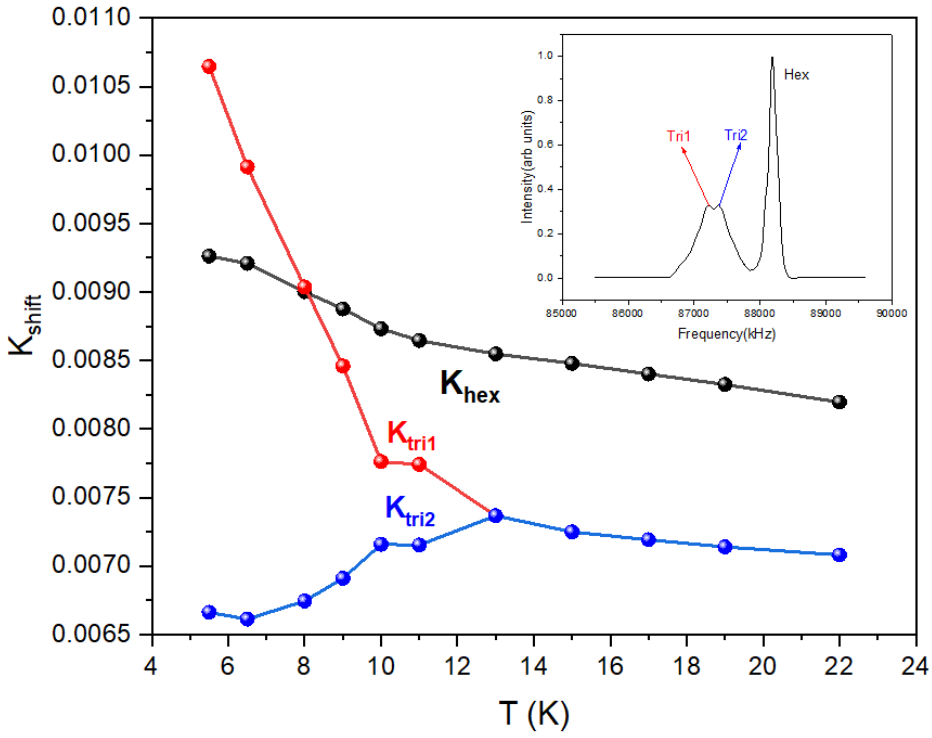

Figure 9.6: Shifts (K_{shift}) has been shown for different local Br sites, derived from the spectra in the temperature range of 6 K to 22 K. They provide insights into the 15 K structural transition. The inset shows the 9 K spectra for the central line of Br_{79}.

In more details, Figure 9.6 displays the shift for both triangular and hexagonal sites within the temperature range of $5\,\text{K} \leq T \leq 22\,\text{K}$. The observed broadening and splitting of the triangular site below the 15 K transition, as well as the opposite shifts of the split sites, are indicative of structural transitions and changes in the local magnetic environment. The shift of the hexagonal site also changes slope below $\sim$ 12 K, showing a faster increase

at low temperature. This is also probably related to the structural transition occurring around 15 K, although the effect is less pronounced compared to the triangular site, a pattern similar to what was observed for the Cl site. This discrepancy in sensitivity to the structural transition can be explained by the fact that the principal axis of the hexagonal electric field gradient (EFG) is in close alignment with the external magnetic field. Consequently, the second-order quadrupolar interactions in the hexagonal site are smaller, leading to less significant shifts.
To study further the observed structural distortion, we complemented our static NMR measurements with spin-lattice relaxation (T_1) measurements. These T_1 measurements provide valuable insights into relaxation processes related to the electronic distribution surrounding the probed atom. The nucleus ^{81}Br has a spin of $I = \frac{3}{2}$ like Cl, leading to the presence of three distinct nuclear transitions due to the quadrupolar contribution. Consequently, to extract T_1 values from the recovery curves of nuclear magnetization $M(t)$ at different temperatures, the dataset must be fitted with a multi-exponential equation, as detailed in chapter-2.

Regarding the central line, the equation for relaxation (T_1) is as follows:

$$M(t) = M_{sat}\left(1 - ae^{-\left(\frac{t}{T_1}\right)^{\beta}} - be^{-\left(\frac{6t}{T_1}\right)^{\beta}}\right) \tag{9.4}$$

The parameters a and b are constrained by the relationship $a + b = 1$, with a specific value assigned to $a = 0.1$, for the analysis of the relaxation (T_1) data of the central line. These parameters, checked from the fitting procedure conducted at a temperature of 100 K, are held constant for other temperatures within the range of $1.3, \text{K} \leq T \leq 300, \text{K}$, as we focus on investigating the central lines of different sites with comparable energy excitations. Indeed, the clear separation of the two bromine sites in the spectrum at 100 K [Figure 9.5(a)] is significant as it eliminates any cross-relaxation effects between the sites. Importantly, this separation persists until 6 K, allowing us to effectively examine the 15 K transition that has been observed in the width measurements in the spectra.

As for the Cl variant, at 100 K, the relaxation times (T_1) reveal a significant contrast between the triangular and hexagonal sites. Specifically, the triangular sites exhibit an approximate value of 4 ms, while the hexagonal sites display a considerably longer relaxation time, approximately 37 ms. This notable disparity of a nearly 10 fold disparity in relaxation times proves to be a distinctive feature that we have harnessed for distinguishing between these sites, particularly when the hexagonal and triangular sites undergo a split around approximately 12 K. Moreover, this substantial distinction in relaxation times implies that the hexagonal sites are less strongly coupled to the kagome structure in comparison to the triangular sites.

The distribution parameter β serves as the stretching parameter in the context of the relaxation (T_1) measurements. The behavior of $\beta(T)$ is illustrated in the inset of Figure 9.7(c) and 9.7(d). For the hexagonal site at high temperatures, β remains almost constant and we could fix it to β=1, indicating that satisfactory fits are achieved with a purely exponential relaxation model. However, as the temperature decreases, a broader distribution of T_1 values emerges likely due to the increased spin correlation below 30 K. Consequently, the parameter β is reduced and

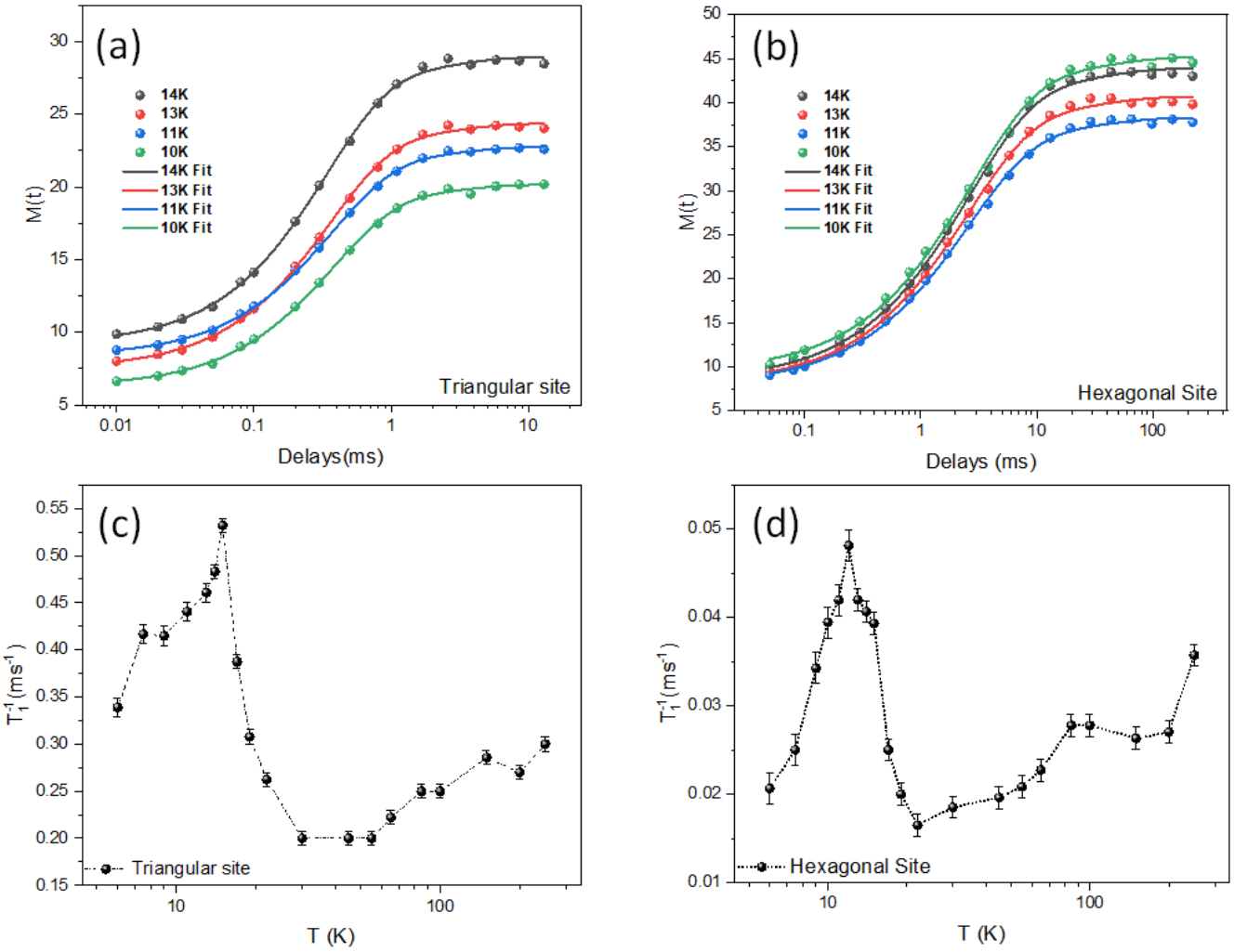

Figure 9.7: (a) Demonstration of the fits with Equation (9.4) for the triangular site and also for (b) the hexagonal site. (c) and (d) Plots of $1/T_1$ versus temperature for the triangular site and hexagonal sites, respectively, with the exponential stretching parameter β shown in the inset.

remains relatively constant down to around 1.3 K. There we fix β to 0.8 below 30. For the triangular site β could be fixed to 1 for the whole temperature range.

The utilization of the parameter β remaining relatively constant within the transition temperature range, avoids fitting artefacts in identifying the structural transition occurring around 15 K. The acquired relaxation data sheds light on this transition, which resembles what was observed in the chlorine variant. Importantly, the transition revealed by T_1 measurements does not exhibit a sharp character but instead appears as a broad transition for both the triangular and hexagonal sites. Moreover, the disparities in the order of T_1 values between the triangular and hexagonal sites persist consistently across the transition.

It's worth noting that the published data on $1/T_1$ in F. Lu et al. 2022 did not observe a transition around 15 K, which contrasts with our findings. However, at 100 K, the triangular site in their data exhibited a T_1 value of around 3 ms, which is quite comparable to our samples. This consistency in results in the paramagnetic phase (T$>\theta$)

is particularly evident, especially regarding the hyperfine coupling, which we observed to be quite similar in both samples.

9.4.4 Ordering of the Impurity phase at 9 K

As mentioned in the previous section and in our μSR analysis, it's worth noting that our sample contains a 5 percent impurity likely of $Cu_2(OH)_3Br$. This impurity material exhibits long-range antiferromagnetic (AFM) order at T_N = 9.3 K, as reported in Zhao et al. 2019. Notably, as the temperature decreases, there is an interesting transition observed in the magnetic behavior of this impurity. Below 7.5 K, the magnetic anisotropy changes from Heisenberg to *XY*, as indicated by changes in the anisotropic magnetic susceptibility of this compound [Zhao et al. 2019]. This impurity's magnetic properties introduce an additional layer of complexity to our study, and it's important to consider its effects when analyzing our NMR shift data for the impurity peak. In our sample, we have indeed observed a distinct peak in the NMR spectra at a magnetic field strength of $\sim$ 8.4 Tesla, slightly outside the ^{79}Br spectra from the intrinsic phase (see figure-9.9), while maintaining a fixed frequency of 87.770 MHz. Intriguingly, as we lower the temperature, we have noted a gradual shift in the position of this peak, specifically towards the right, away from the reference line. This shift becomes particularly prominent at around 7.5 K, which aligns with the transition we previously mentioned, shown in figure-9.8. Importantly, at temperatures above 1.4 K, this shifted peak does not interfere with the central line in our NMR spectra. This lack of interference assures us that our understanding of the spectra is accurate and that the observed transitions are indeed genuine, without any contamination (if well crystallized, it probably has satellites).

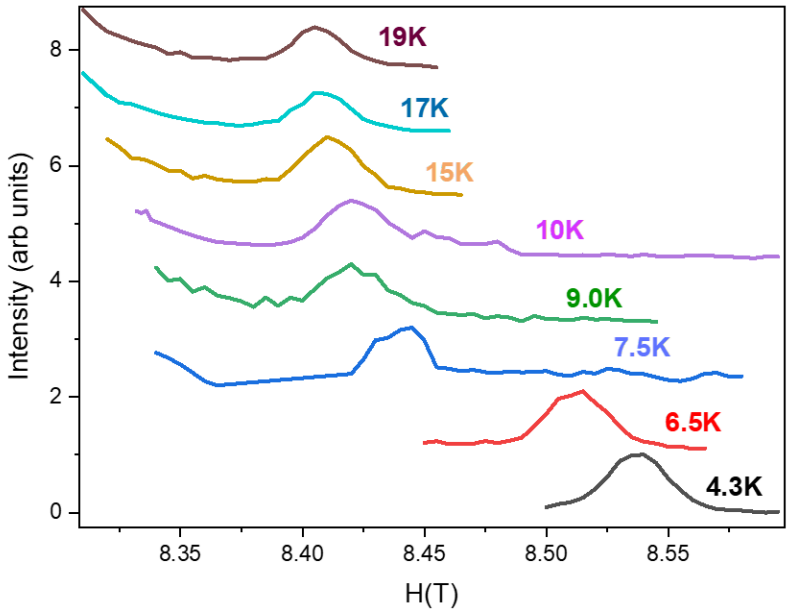

Figure 9.8: The temperature evolution of the impurity peak is clearly observable in the NMR spectra, particularly below 20 K. A significant shift in the peak's position is evident, occurring at approximately 7.5 K. This distinctive shift serves as a signature of the presence of $Cu_2(OH)_3Br$, the impurity in the sample.

9.4.5 Magnetic ordering at 2.2 K

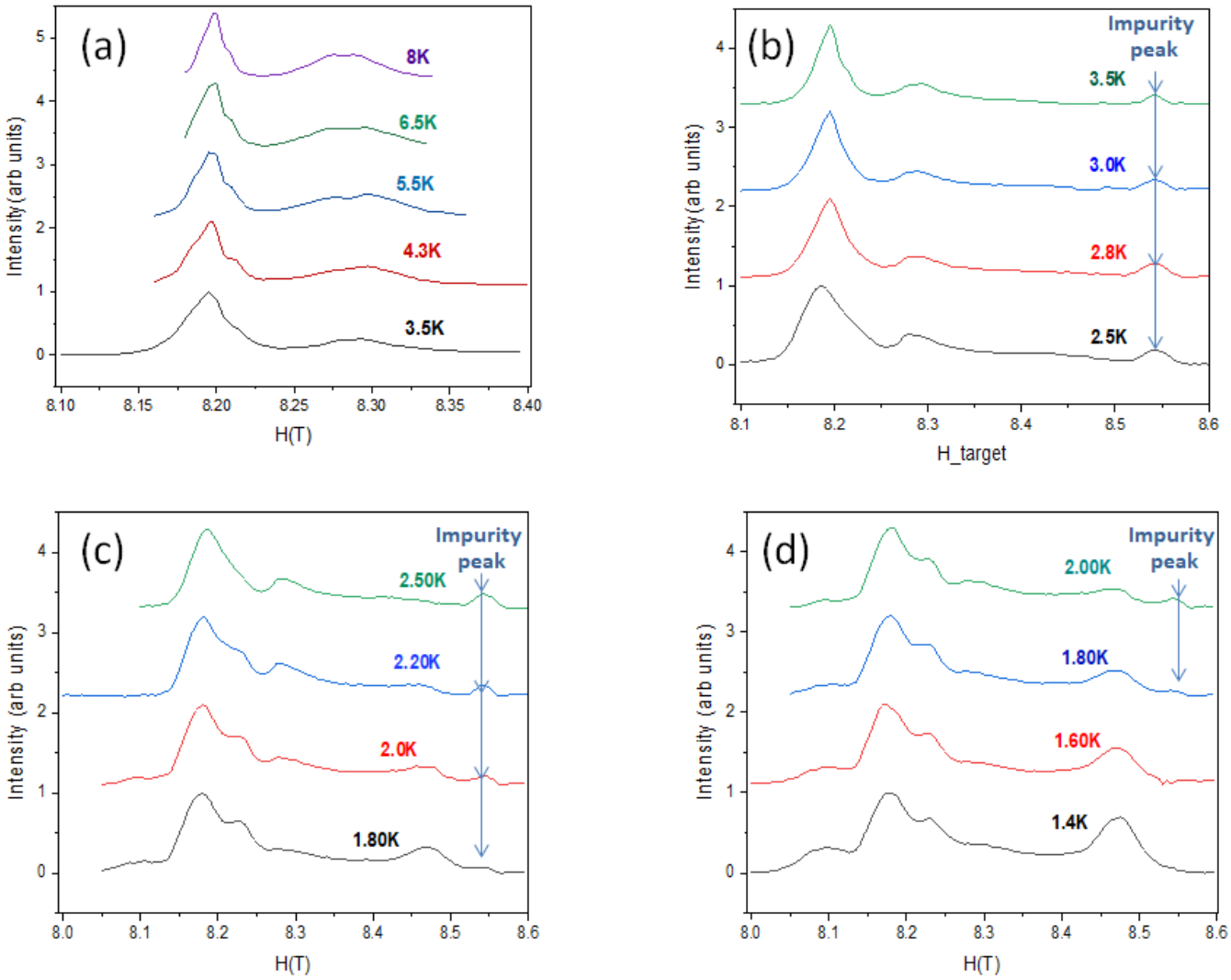

Figure 9.9: Field sweep spectra at various temperatures were obtained while maintaining a fixed frequency of $\nu_0 = 87.770$ MHz.

As indicated by the μSR study, we have indeed detected clear evidence of partial spin freezing taking place at approximately 2.2 K in our sample. It's worth highlighting that the NMR spectra obtained below 2.1 K display significant broadening, which is also consistent with a magnetic transition, similar to what was observed in the chlorine variant. However, the spectra in the bromine sample appear different, indicating distinct magnetic behavior in comparison to the chlorine variant.

At all low temperatures, from 8 K down to 1.30 K, NMR spectra were recorded using field sweep measurements, as illustrated in Figure-9.9. These measurements were consistently performed at a constant frequency of $\nu_0 = 87.770$ MHz, with the external magnetic field aligned along the c-axis. The distribution of susceptibility (χ) and the increase in intrinsic magnetic correlations with decreasing temperature lead to the broadening of the NMR line. As a result,

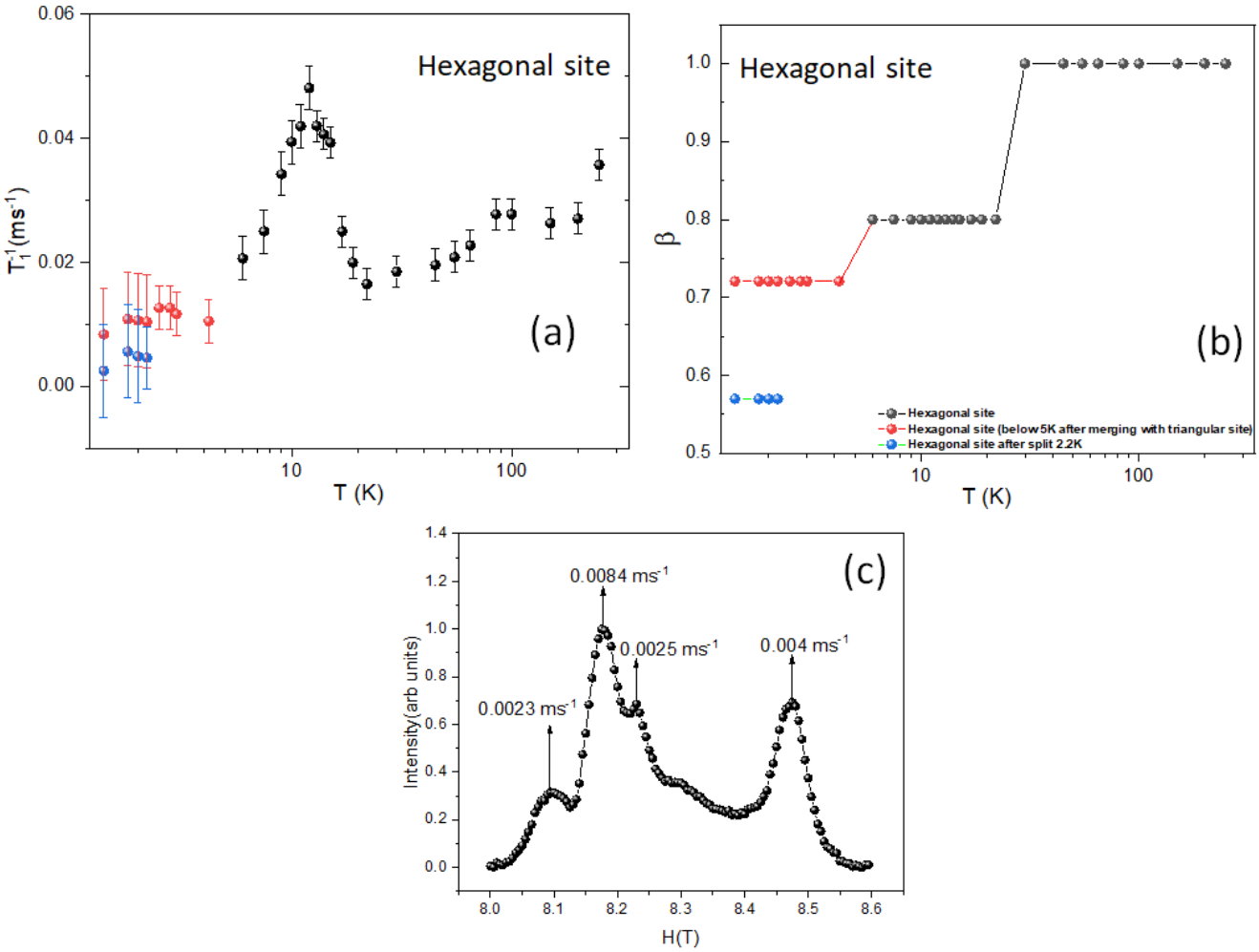

Figure 9.10: (a) The plot of $1/T_1$ vs. temperature for the hexagonal site is presented here, covering a temperature range from 1.4 K to 300 K. In the plot, the red dots represent the hexagonal sites below 5 K, where there is an overlap with the triangular site. Below 2.5 K, as indicated by the blue dots, the hexagonal sites split, and these dots represent the inverse relaxation times for the emerging line at 8.235 T.(b) The evolution of the distribution parameter β with temperature is depicted. Although no specific peak has been observed for any site in the $1/T_1$ vs. T plot, figure-(c) demonstrates the $1/T_1$ values at various position in the 1.4 K spectrum in the frozen phase.

the characteristic hexagonal and triangular lines partially overlap with each other, below 5 K. The spectra below 2.5 K exhibit a complex form, with the emergence of several additional peaks. While the central lines merge with each other, the peak corresponding to the hexagonal site maintains almost constant intensity at around $\sim$ 8.20 Tesla. However, another peak occurs at 2.2 K around 8.23 T at variance with the Cl case. If this additional peak arise from a splitting of the hexagonal site it could indicate a possible frozen fraction coexisting with the presence of a non frozen paramagnetic phase. In Figure-9.10 (a) and (b), we focus on these split hexagonal sites during our spin-lattice relaxation measurements. Interestingly, we did not observe any distinct peaks in the $1/T_1$ vs. temperature plots for both of these sites at 8.19 Tesla and 8.23 Tesla. This observation may be critical to confirm the partial transition, in contrast to the clear critical behavior observed in the Cl case.

To gain a clearer understanding, we focus on the 1.4 K spectra. The frozen part, constituting 40% of the sample,

doesn't evolve further below this temperature, as observed in μSR experiments. The 1.4 K spectrum displays multiple peaks, as shown in Figure-9.10(c), quite similar to the chlorine variant except for the 8.23 T peak. However, upon comparing the relaxation times (T_1) between various positions, we realized that they have all increased, and the overall differences in T_1 between the two sites had vanished. No site-specific distinctive peaks in relaxation were observed in the system, which makes the identification of the sites difficult. To gain further insights into the inhomogeneous spin freezing observed in the NMR spectra, one should probably investigate the satellite peaks as well, especially in regions where the two sites do not overlap with each other.

9.5 Discussion

In a comparative analysis between our sample and the one studied in [F. Lu et al. 2022], we examined the full width half maximum (FWHM) to gain insights into the amount of disorder of our sample. Both triangular and hexagonal lines in our sample are less broad compared to the published data, spanning from 300 K to 100 K. This observation is noteworthy because it implies that our sample is less disordered compared to the reported single crystals in [F. Lu et al. 2022], as depicted in figure-9.11. As our sample exhibits less disorder and our X-ray measurements suggest

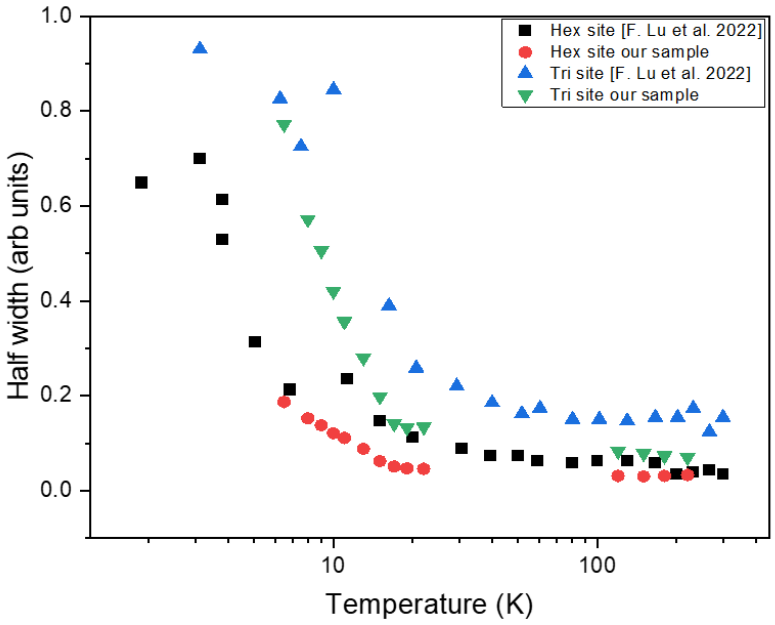

Figure 9.11: We compared the half widths of both the hexagonal and triangular sites in our sample to those reported in [F. Lu et al. 2022]. Our data displayed narrower half widths across the temperature range from 300 K to 100 K, indicating that our NMR lines exhibit less disorder than the ones reported in [F. Lu et al. 2022].

similarity between the Cl and Br variants, we still rely on the disorder free model reported in [Hering et al. 2022]. As already reported in our sample we observe a sharp broadening below 15 K of the NMR lines signaling a well defined structural transition. Interestingly the NMR lines in [F. Lu et al. 2022] also broadens in the same T range but more progressively. This suggests that the same kind of structural instabilities also exist in their single crystals but

is somewhat smeared out by the Br/OH disorder.

Since relaxation measurements did not detect any transition at 2.1 K, and the overall system exhibits a more dynamic ground state compared to the chlorine variant, our idea of implementing chemical pressure by using bromine atoms appears to be a step in the right direction for exploring the spin liquid part of the phase diagram of this anisotropic distorted kagome compound. In future development neutron scattering experiment could prove to be crucial in determining the ground state of this compound if spin wave can be detected.

Summary

(1) In this last experimental chapter, we investigated the small $Y_3Cu_9(OH)_{19}Br_8$ single crystal with μSR and NMR local techniques.

(2) μSR results give evidence for a partial magnetic freezing of 40% of the sample below 2.2 K. This partial freezing was unnoticed in susceptibility measurements but corresponds to a bump in heat capacity.

(3) NMR measurements were performed on an oriented powder sample with the magnetic field applied along the c-axis, as for the previous chlorine variant investigation. We observe two well-resolved Br sites as expected. The NMR lines are substantially narrower than the published results in [F. Lu et al. 2022] on samples with Br/OH disorder but broader than the chlorine case.

(4) The 15.5 K transition manifests as a sharp broadening of the lines and their splitting in agreement with the structural origin and a reduction of the crystal symmetry, as in the chlorine case at $\sim$ 33 K.

(5) The magnetic transition at 2.2 K is also clearly observed through a characteristic change in the spectra. Although we could not interpret it unambiguously because of the merging of the lines and absence of clear T1 contrast.

(6) At variance with the Cl case, we observed no critical slowing down in relaxation measurements likely as a result of the only partial freezing and the mostly dynamical character of the ground state.

Chapter 10

Conclusion and Future Perspective

Our investigation primarily focused on large, phase-pure single crystals of $Y_3Cu_9(OH)_{19}Cl_8$. We employed a range of experimental techniques, including local μSR and NMR measurements, as well as complementary thermodynamic and neutron scattering experiments. Unlike prior research conducted on powder samples, our examination of single crystals unveiled subtle structural instabilities occurring at temperatures around 33 K and 13 K. Remarkably, these instabilities did not disrupt the overall symmetry of the magnetic system or the underlying magnetic model. Instead, they were attributed to the localization of one of the hydrogen atoms. Additionally, our findings provided compelling evidence for a bulk magnetic phase transition occurring at approximately 2.1 K, as corroborated by multiple experimental approaches. This transition aligns with theoretical predictions of a $(1/3, 1/3)$ long-range ordering. However, our analysis of spin wave excitations suggested that the compound lies close to the boundary of the classical liquid phase. This proximity likely introduces significant quantum fluctuations, resulting in a notably reduced ordered moment for Cu^{2+}. This reduced moment remained elusive in neutron diffraction measurements but was successfully detected through μSR and NMR techniques.

With the aim of probing other regions of the phase diagram, our focus shifted towards investigating the bromine (Br) version of the system. Utilizing similar thermodynamic and localized methods on a set of small individual crystals that were aligned along their c-axis, we detected a structural transition occurring at approximately 15 K. Additionally, a magnetic transition was observed around 9 K, which was attributed to the presence of an impurity phase. Remarkably, the system displayed inhomogeneous spin freezing, resulting in a partially ordered ground state below 2.5 K. This partial freezing resembles the lack of magnetic order observed in powdered samples of the chlorine (Cl) variant, in contrast to the single crystals, underscoring the susceptibility of the ground state to disorder.

These observations naturally prompt further investigation, aimed at perturbing the system and exploring the phase diagram. Various perturbations, such as strain, disorder, and high magnetic fields, can be introduced to the system, potentially influencing the exchange couplings within the anisotropic kagome network. Some of these tracks have already been explored, while others are ongoing projects, including our own. In the following, I will discuss

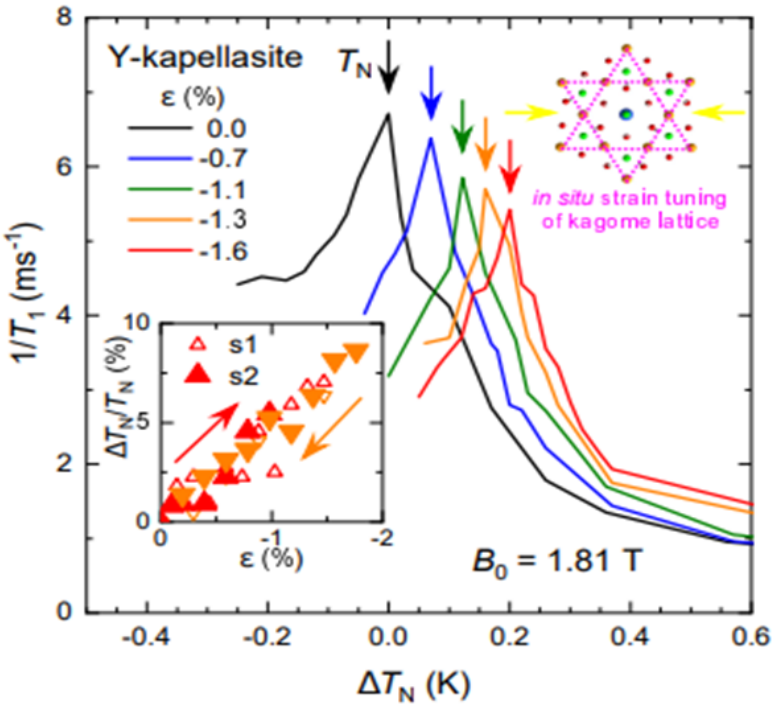

Figure 10.1: The spin-lattice relaxation rate, denoted as T_1^{-1}, was measured with an applied magnetic field aligned parallel to the crystallographic direction a while subjecting the kagome lattice to uniaxial compression within the kagome plane, as illustrated in the top-right sketch. Inset: The application of an in-plane strain of $\sim$ 2% resulted in a significant enhancement of the transition temperature, quantified as $\Delta T_N/T_N \approx 10\%$.

these perturbations in some detail.

One notable approach that I will discuss is the impact of strain on modifying the superexchange interactions and potentially altering the nature of the ground state. This is a relatively recent topic covered in the arxiv article [Jierong Wang et al. 2022]. The authors conducted proton Nuclear Magnetic Resonance (NMR) measurements in the temperature range of 1.5 K to 200 K, revealing a distinct signature of a magnetic transition occurring at approximately 2.2 K under zero strain. This transition is depicted with line width and spin-lattice measurements, similar to our chlorine NMR results. The spin-lattice relaxation rate results under different applied strains are reproduced in Figure (10.1). This large shift in T_N is ascribed by the authors to a change in the ratio of the interactions. Hence, uniaxial strain appears to release the frustration and stabilize the ordered ground state. In line with these ideas, another intriguing avenue is to explore the impact of hydrostatic pressure. Due to its extreme sensitivity to even small magnetic moments, μSR is a particularly well-suited technique for monitoring the system's evolution under pressure. We have scheduled beamtime for September 27th at the GPD beamline at PSI, where hydrostatic pressures of up to 20-25 kbar can be achieved, offering the possibility to fine-tune the kagome network. This pressure adjustment holds the potential to drive the system towards a spin liquid ground state or enhance the ordered phase, as indicated in the magnetic phase diagram [Hering et al. 2022]. As mentioned previously, an alternative method to apply pressure is through the introduction of larger atoms, such as bromine. This approach has led to the creation of $Y_3Cu_9(OH)_{19}Br_8$,

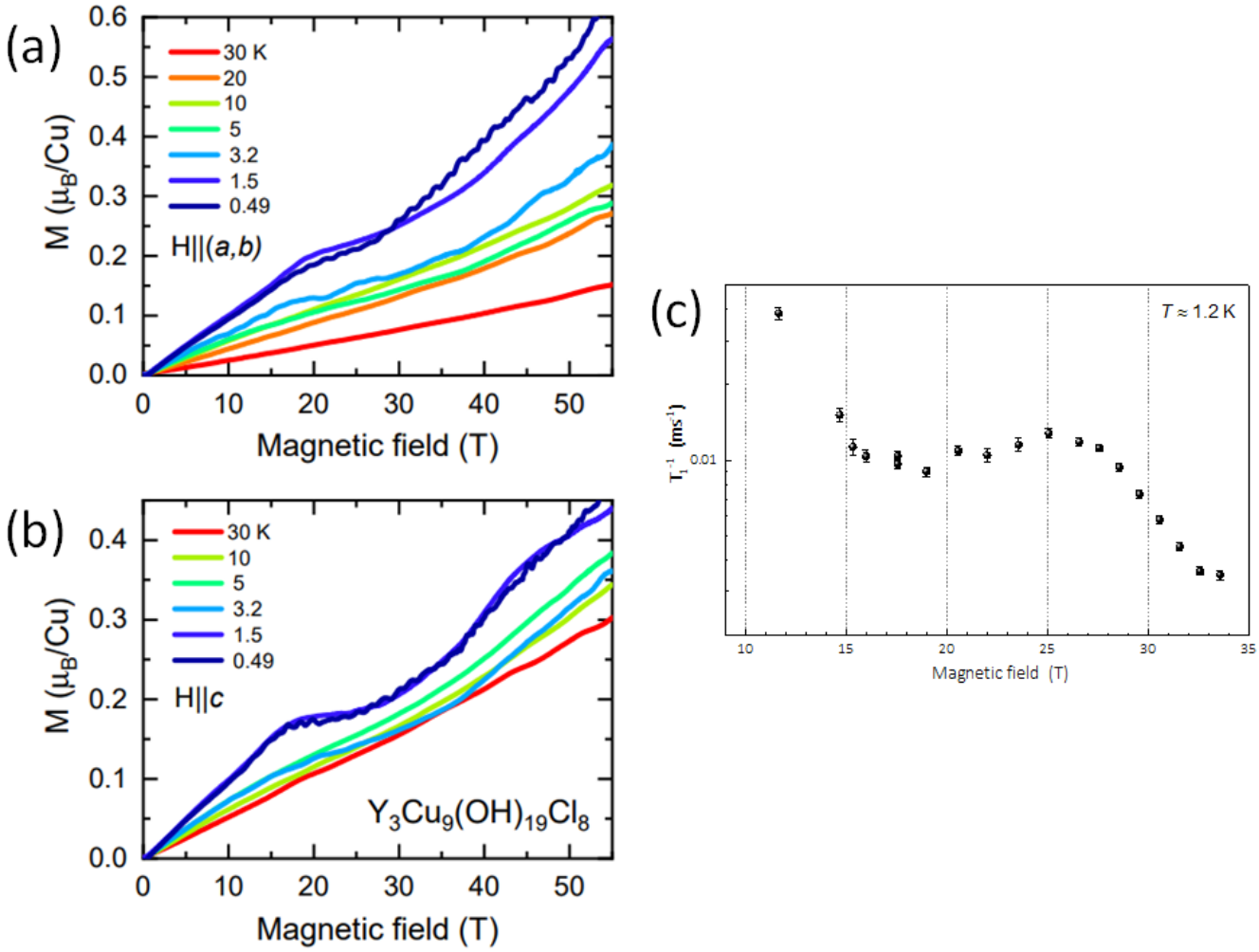

Figure 10.2: Magnetization of Y-kapellasite in pulsed magnetic fields up to 55 T. a) Magnetization M in the a, b-plane, $H \parallel (a, b)$. b) Results for the c-axis, $H \parallel c$. c) this magnetic plateau has been depicted with spin lattice relaxation measurements, T_1^{-1} vs field plot upto 33 T.

which is extensively discussed in Part-B of this thesis. In addition to the chemical pressure effect, some prior studies [F. Lu et al. 2022, Zeng et al. 2022, J. Liu et al. 2022] have attributed the observed spin liquid state in $Y_3Cu_9(OH)_{19}Br_8$ to disorder effects. The disorder stemming from the presence of Br-OH sites intermixing in the crystal structure can significantly disrupt magnetic ordering in such systems. This raises intriguing questions regarding the absence of ordering in the powder sample of the chlorine variant [Barthélemy, Puphal, et al. 2019], possibly due to prominent disorder effects associated in powder .

Finally, I will discuss the effect of an external magnetic field, as initially reported in [Biesner et al. 2022]. Above approximately 5 K, the magnetization exhibits a nearly linear dependence on the external magnetic field, up to 50 T. However, at lower temperatures, notably below T_N=2.2 K, a distinct magnetization plateau emerges, typically observed at magnetic fields slightly above 15 T. This plateau phenomenon is observed in both in-plane and out-of-plane magnetization measurements shown in figure-10.2, with plateau values of approximately $0.21\mu_B$ for the a-b

plane and approximately $0.18\mu_B$ for the c-axis at a temperature of 1.5 K. As the magnetic field is increased beyond this plateau region, the magnetization starts to rise again, deviating from the plateau response. An analysis of the differential magnetization reveals a subtle change in the slope of the magnetization curve in the magnetic field range of 40 to 45 T. This may suggest the presence of another magnetization plateau, with values of approximately $0.37\mu_B$ for the a-b plane and approximately $0.33\mu_B$ for the c-axis. In pursuit of a deeper understanding of this magnetic plateau, I conducted high-field NMR measurements at the LNCMI-Grenoble during the writing of this thesis. The magnetization plateau is clearly reflected in the spin-lattice relaxation data within the field range of 16 T to 26 T. While additional investigations are required to comprehend the evolution of the NMR spectra with respect to changes in magnetic field strength and temperature, these studies hold the potential to provide crucial insights into the behavior of local magnetic sites and the evolution of the magnetic structure and excitations within the plateau region.

Thus, it becomes evident that not only external perturbations such as high magnetic fields and high pressures but also the introduction of various disorders in the samples have yielded diverse effects on the ground state of Y-kapellasite. The rich family of Y-kapellasite compounds that we have started to investigate in this thesis, presents a multitude of possibilities and continues to be a subject of great scientific interest.

Bibliography

Abragam, Anatole (1961). *The principles of nuclear magnetism*. 32. Oxford university press.

Anderson, Philip W (1973). “Resonating valence bonds: A new kind of insulator?” In: *Materials Research Bulletin* 8.2, pp. 153–160.

— (1987). “The resonating valence bond state in La2CuO4 and superconductivity”. In: *science* 235.4793, pp. 1196–1198.

Andrew, ER and DP Tunstall (1961). “Spin-lattice relaxation in imperfect cubic crystals and in non-cubic crystals”. In: *Proceedings of the Physical Society* 78.1, p. 1.

Arh, T et al. (2020). “Origin of magnetic ordering in a structurally perfect quantum kagome antiferromagnet”. In: *Physical Review Letters* 125.2, p. 027203.

Ashcroft, Neil W and N David Mermin (1976). “Solid State Physics, College edn”. In: *Thomson Learning Inc*.

Barthélemy, Quentin, Albin Demuer, et al. (2022). “Specific heat of the kagome antiferromagnet herbertsmithite in high magnetic fields”. In: *Physical Review X* 12.1, p. 011014.

Barthélemy, Quentin, Pascal Puphal, et al. (2019). “Local study of the insulating quantum kagome antiferromagnets YCu 3 (OH) 6 O x Cl 3- x (x= 0, 1/3)”. In: *Physical Review Materials* 3.7, p. 074401.

Baugher, JF et al. (1970). “A study of dipole-broadened NMR powder lineshapes in the presence of second-order quadrupole effects with applications to polycrystalline borates”. In: *Journal of Magnetic Resonance (1969)* 3.3, pp. 415–426.

Bednorz, J George and K Alex Müller (1986). “Possible high T c superconductivity in the Ba- La- Cu- O system”. In: *Zeitschrift für Physik B Condensed Matter* 64.2, pp. 189–193.

Bert, F. et al. (Aug. 2005). “Ground State of the Kagomé-Like $S = 1/2$ Antiferromagnet Volborthite $\mathrm{Cu_3V_2O_7(OH)_2 \cdot 2H_2O}$”. In: *Phys. Rev. Lett.* 95 (8), p. 087203. DOI: 10.1103/PhysRevLett.95.087203. URL: https://link.aps.org/doi/10.1103/PhysRevLett.95.087203.

Bert, Fabrice (2014). “Local probes of magnetism, NMR and μSR: A short introduction”. In: *École thématique de la Société Française de la Neutronique* 13, p. 03001.

Bethe, Hans (1931). “Zur theorie der metalle: I. Eigenwerte und eigenfunktionen der linearen atomkette”. In: *Zeitschrift für Physik* 71.3-4, pp. 205–226.

Biesner, Tobias et al. (2022). “Multi-Center Magnon Excitations Open the Entire Brillouin Zone to Terahertz Magnetometry of Quantum Magnets”. In: *Advanced Quantum Technologies* 5.6, p. 2200023.

Bilitewski, Thomas, Mike E Zhitomirsky, and Roderich Moessner (2017). “Jammed spin liquid in the bond-disordered kagome antiferromagnet”. In: *Physical Review Letters* 119.24, p. 247201.

Bloch, Felix (1946). “Nuclear induction”. In: *Physical review* 70.7-8, p. 460.

Blundell, SJ (1999). “Spin-polarized muons in condensed matter physics”. In: *Contemporary Physics* 40.3, pp. 175–192.

Blundell, SJ and T Lancaster (2023). “DFT+ μ: Density functional theory for muon site determination”. In: *Applied Physics Reviews* 10.2.

Blundell, Stephen J et al. (2022). *Muon Spectroscopy: An Introduction*. Oxford University Press.

Boldrin, D., K. Knight, and A. S. Wills (Oct. 2016). “Orbital frustration in the S = 1/2 kagome magnet vesignieite, BaCu3V2O8(OD)2”. In: arXiv: 1610.01436 [cond-mat.mtrl-sci].

Bramwell, Steven T and Michel JP Gingras (2001). “Spin ice state in frustrated magnetic pyrochlore materials”. In: *Science* 294.5546, pp. 1495–1501.

Castelnovo, Claudio, Roderich Moessner, and Shivaji L Sondhi (2008). “Magnetic monopoles in spin ice”. In: *Nature* 451.7174, pp. 42–45.

Cepas, Olivier et al. (2008). “Quantum phase transition induced by Dzyaloshinskii-Moriya interactions in the kagome antiferromagnet”. In: *Physical Review B* 78.14, p. 140405.

Chatterjee, Dipranjan et al. (2023). “From spin liquid to magnetic ordering in the anisotropic kagome Y-kapellasite Y 3 Cu 9 (OH) 19 Cl 8: A single-crystal study”. In: *Physical Review B* 107.12, p. 125156.

Chen, Xiao-Hui et al. (2020). “Quantum spin liquid candidate YCu3 (OH) 6Br2 [Brx (OH) 1- x](x 0.51): With an almost perfect kagomé layer”. In: *Journal of Magnetism and Magnetic Materials* 512, p. 167066.

Choi, Q Won and W Gilbert Clark (1961). “Spin-Lattice Relaxation Time of F19 Nuclei in Ag2F”. In: *The Journal of Chemical Physics* 34.5, pp. 1584–1584.

Clark, WG et al. (1995). “Magnetic resonance spectral reconstruction using frequency-shifted and summed Fourier transform processing”. In: *Review of scientific instruments* 66.3, pp. 2453–2464.

Cohen, MH and F Reif (1957). “Quadrupole effects in nuclear magnetic resonance studies of solids”. In: *Solid state physics*. Vol. 5. Elsevier, pp. 321–438.

Colman, RH, C Ritter, and AS Wills (2008). “Toward perfection: kapellasite, Cu3Zn (OH) 6Cl2, a new model s= 1/2 kagome antiferromagnet”. In: *Chemistry of Materials* 20.22, pp. 6897–6899.

Cox, SFJ (1987). “Implanted muon studies in condensed matter science”. In: *Journal of Physics C: Solid State Physics* 20.22, p. 3187.

Depenbrock, Stefan, Ian P McCulloch, and Ulrich Schollwöck (2012). “Nature of the spin-liquid ground state of the S= 1/2 Heisenberg model on the kagome lattice”. In: *Physical review letters* 109.6, p. 067201.

Downie, Lewis J et al. (2015). “Novel s= 1/2 kagome lattice materials: Cs2ticu3f12 and rb2ticu3f12”. In: *Crystals* 5.2, pp. 226–243.

Elhajal, Maged et al. (2005). “Ordering in the pyrochlore antiferromagnet due to Dzyaloshinsky-Moriya interactions”. In: *Physical Review B* 71.9, p. 094420.

Enderle, M et al. (2010). “Two-spinon and four-spinon continuum in a frustrated ferromagnetic spin-1/2 chain”. In: *Physical review letters* 104.23, p. 237207.

Fåk, B et al. (2012). “Kapellasite: A kagome quantum spin liquid with competing interactions”. In: *Physical review letters* 109.3, p. 037208.

Ferrari, Francesco et al. (2023). “Static and dynamical signatures of Dzyaloshinskii-Moriya interactions in the Heisenberg model on the kagome lattice”. In: *SciPost Physics* 14.6, p. 139.

Fu, Mingxuan et al. (2015). “Evidence for a gapped spin-liquid ground state in a kagome Heisenberg antiferromagnet”. In: *Science* 350.6261, pp. 655–658.

Fu, Ying et al. (2021). “Dynamic fingerprint of fractionalized excitations in single-crystalline Cu3Zn (OH) 6FBr”. In: *Nature Communications* 12.1, p. 3048.

Garwin, Richard L, Leon M Lederman, and Marcel Weinrich (1957). “Observations of the failure of conservation of parity and charge conjugation in meson decays: the magnetic moment of the free muon”. In: *Physical Review* 105.4, p. 1415.

Godoy, PF, M Schmidt, and FM Zimmer (2020). “The Ising model on the layered J1-J2 square lattice”. In: *Physics Letters A* 384.27, p. 126687.

Grbić, Mihael Sran et al. (2013). “Microscopic Properties of the Pinwheel Kagome Compound Rb 2 Cu 3 SnF 12”. In: *Physical Review Letters* 110.24, p. 247203.

Guterding, Daniel, Roser Valenti, and Harald O Jeschke (2016). “Reduction of magnetic interlayer coupling in barlowite through isoelectronic substitution”. In: *Physical Review B* 94.12, p. 125136.

Han, TH et al. (2011). “Synthesis and characterization of single crystals of the spin-1 2 kagome-lattice antiferromagnets Zn x Cu 4- x (OH) 6 Cl 2”. In: *Physical Review B* 83.10, p. 100402.

Han, Tian-Heng et al. (2012). “Fractionalized excitations in the spin-liquid state of a kagome-lattice antiferromagnet”. In: *Nature* 492.7429, pp. 406–410.

Harris, Mark J et al. (1997). “Geometrical frustration in the ferromagnetic pyrochlore Ho 2 Ti 2 O 7”. In: *Physical Review Letters* 79.13, p. 2554.

Hayano, RS et al. (1979). “Zero-and low-field spin relaxation studied by positive muons”. In: *Physical Review B* 20.3, p. 850.

Henley, Christopher L (2009). “Long-range order in the classical kagome antiferromagnet: Effective Hamiltonian approach”. In: *Physical Review B* 80.18, p. 180401.

Hering, Max et al. (Jan. 2022). “Phase diagram of a distorted kagome antiferromagnet and application to Y-kapellasite”. In: *npj Computational Materials* 8.1, pp. 1–10. DOI: 10.1038/s41524-021-00689-0.

Huse, David A and Andrew D Rutenberg (1992). “Classical antiferromagnets on the Kagomé lattice”. In: *Physical Review B* 45.13, p. 7536.

Ishikawa, H et al. (2015). “One-third magnetization plateau with a preceding novel phase in volborthite”. In: *Physical review letters* 114.22, p. 227202.

Ishikawa, H. et al. (June 2015). “One-Third Magnetization Plateau with a Preceding Novel Phase in Volborthite”. In: *Physical Review Letters* 114.22, p. 227202. DOI: 10.1103/physrevlett.114.227202.

Janson, O et al. (2016). “Magnetic Behavior of Volborthite Cu 3 V 2 O 7 (OH) 2· 2 H 2 O Determined by Coupled Trimers Rather than Frustrated Chains”. In: *Physical review letters* 117.3, p. 037206.

Kelly, ZA, MJ Gallagher, and TM McQueen (2016). “Electron doping a kagome spin liquid”. In: *Physical Review X* 6.4, p. 041007.

Keren, Amit (1994). “Dynamical simulation of spins on kagomé and square lattices”. In: *Physical review letters* 72.20, p. 3254.

— (1995). “Simulation of spin dynamics on kagomé and square lattices”. In: *Journal of magnetism and magnetic materials* 140, pp. 1493–1494.

Kermarrec, E, P Mendels, et al. (2011). “Spin-liquid ground state in the frustrated kagome antiferromagnet MgCu 3 (OH) 6 Cl 2”. In: *Physical Review B* 84.10, p. 100401.

Kermarrec, E, A Zorko, et al. (2014). “Spin dynamics and disorder effects in the S= 1 2 kagome Heisenberg spin-liquid phase of kapellasite”. In: *Physical Review B* 90.20, p. 205103.

Kermarrec, E. et al. (2020). “Spin excitation spectra in the kagome candidate material $Y_3Cu_9(OH)_{19}Cl_8$”. In: *Institut Laue-Langevin (ILL)*. DOI: 10.5291/ILL-DATA.4-05-774. URL: https://doi.ill.fr/10.5291/ILL-DATA.4-05-774.

Khuntia, P et al. (2020). “Gapless ground state in the archetypal quantum kagome antiferromagnet ZnCu3 (OH) 6Cl2”. In: *Nature Physics* 16.4, pp. 469–474.

Kubo, Ryogo (1981). “A stochastic theory of spin relaxation”. In: *Hyperfine Interactions* 8.4-6, pp. 731–738.

Lacroix, Claudine, Philippe Mendels, and Frédéric Mila (2011). *Introduction to frustrated magnetism: materials, experiments, theory*. Vol. 164. Springer Science & Business Media.

Lake, B, DA Tennant, and SE Nagler (2000). “Novel longitudinal mode in the coupled quantum chain compound KCuF 3”. In: *Physical Review Letters* 85.4, p. 832.

Lancaster, T et al. (2007). “Muon-fluorine entangled states in molecular magnets”. In: *Physical review letters* 99.26, p. 267601.

Läuchli, Andreas M, Julien Sudan, and Erik S Sørensen (2011). “Ground-state energy and spin gap of spin-1 2 Kagomé-Heisenberg antiferromagnetic clusters: Large-scale exact diagonalization results”. In: *Physical Review B* 83.21, p. 212401.

Lecheminant, P et al. (1995). “Spin stiffnesses of the quantum Heisenberg antiferromagnet on a triangular lattice”. In: *Physical Review B* 52.13, p. 9162.

Lee, Patrick A, Naoto Nagaosa, and Xiao-Gang Wen (2006). “Doping a Mott insulator: Physics of high-temperature superconductivity”. In: *Reviews of modern physics* 78.1, p. 17.

Lee, Stephen L, Ray Cywinski, and SH Kilcoyne (1999). *Muon science: Muons in physics, chemistry and materials*. Vol. 51. CRC press.

Lee, Tsung-Dao and Chen-Ning Yang (1956). “Question of parity conservation in weak interactions”. In: *Physical Review* 104.1, p. 254.

Liu, Jiabin et al. (2022). “Gapless spin liquid behavior in a kagome Heisenberg antiferromagnet with randomly distributed hexagons of alternate bonds”. In: *Physical Review B* 105.2, p. 024418.

Liu, Qihang et al. (2018). “Electron doping of proposed kagome quantum spin liquid produces localized states in the band gap”. In: *Physical Review Letters* 121.18, p. 186402.

Lord, JS, SP Cottrell, and WG Williams (2000). “Muon spin relaxation in strongly coupled systems”. In: *Physica B: Condensed Matter* 289, pp. 495–498.

Lu, Fangjun et al. (2022). “The observation of quantum fluctuations in a kagome Heisenberg antiferromagnet”. In: *Communications Physics* 5.1, p. 272.

Matan, K et al. (2010). “Pinwheel valence-bond solid and triplet excitations in the two-dimensional deformed kagome lattice”. In: *Nature Physics* 6.11, pp. 865–869.

Mazin, II et al. (2014). “Theoretical prediction of a strongly correlated Dirac metal”. In: *Nature communications* 5.1, p. 4261.

McDowell, AF (1995). “Magnetization-recovery curves for quadrupolar spins”. In: *Journal of Magnetic Resonance, Series A* 113.2, pp. 242–246.

Mendels, P et al. (2005). “Cascade of bulk magnetic phase transitions in Na x CoO 2 as studied by muon spin rotation”. In: *Physical review letters* 94.13, p. 136403.

Mendels, Philippe et al. (2007). “Quantum magnetism in the paratacamite family: towards an ideal kagomé lattice”. In: *Physical review letters* 98.7, p. 077204.

Mermin, N David and Herbert Wagner (1966). “Absence of ferromagnetism or antiferromagnetism in one-or two-dimensional isotropic Heisenberg models”. In: *Physical Review Letters* 17.22, p. 1133.

Michal, VP, A Yaouanc, and P Dalmas de Réotier (2010). “Muon Spin Rotation in Pauli Limited Superconductors”. In: *arXiv preprint arXiv:1012.4392*.

Moessner, Roderich and John T Chalker (1998). “Low-temperature properties of classical geometrically frustrated antiferromagnets”. In: *Physical Review B* 58.18, p. 12049.

Morenzoni, E et al. (2001). “Muon spin rotation and relaxation experiments on thin films”. In: *Hyperfine interactions* 133, pp. 179–195.

Mourigal, Martin et al. (2013). “Fractional spinon excitations in the quantum Heisenberg antiferromagnetic chain”. In: *Nature Physics* 9.7, pp. 435–441.

Müller, Markus and Bernd G Müller (1995). “Cs2Cu3MIVF12 (MIV= Zr, Hf)–Kristallstruktur und magnetische Eigenschaften”. In: *Zeitschrift für anorganische und allgemeine Chemie* 621.6, pp. 993–1000.

Murayama, H et al. (2020). “Effect of quenched disorder on the quantum spin liquid state of the triangular-lattice antiferromagnet 1 T- TaS 2”. In: *Physical Review Research* 2.1, p. 013099.

Nakano, Hiroki and Toru Sakai (2011). “Numerical-diagonalization study of spin gap issue of the Kagome lattice Heisenberg antiferromagnet”. In: *Journal of the Physical Society of Japan* 80.5, p. 053704.

Narita, Koziro, Jun-ichi Umeda, and Hazime Kusumoto (1966). “Nuclear Magnetic Resonance Powder Patterns of the Second-Order Nuclear Quadrupole Interaction in Solids with Asymmetric Field Gradient”. In: *The Journal of Chemical Physics* 44.7, pp. 2719–2723.

Nishimoto, Satoshi, Naokazu Shibata, and Chisa Hotta (2013). “Controlling frustrated liquids and solids with an applied field in a kagome Heisenberg antiferromagnet”. In: *Nature communications* 4.1, p. 2287.

Norman, MR (2016). “Colloquium: Herbertsmithite and the search for the quantum spin liquid”. In: *Reviews of Modern Physics* 88.4, p. 041002.

Ollivier, Jacques and Hannu Mutka (2011). “IN5 cold neutron time-of-flight spectrometer, prepared to tackle single crystal spectroscopy”. In: *Journal of the Physical Society of Japan* 80.Suppl. B, SB003.

Počanić, D et al. (2004). “Precise Measurement of the $\pi+\rightarrow \pi$ 0 e+ ν Branching Ratio”. In: *Physical Review Letters* 93.18, p. 181803.

Puphal, Pascal, Michael Bolte, et al. (2017). “Strong magnetic frustration in Y 3 Cu 9 (OH) 19 Cl 8: a distorted kagome antiferromagnet”. In: *Journal of Materials Chemistry C* 5.10, pp. 2629–2635.

Puphal, Pascal, Kizhake Malayil Ranjith, et al. (2019). “Tuning of a Kagome Magnet: Insulating Ground State in Ga-Substituted Cu4 (OH) 6Cl2”. In: *physica status solidi (b)* 256.9, p. 1800663.

Purcell, Edward M, Henry Cutler Torrey, and Robert V Pound (1946). “Resonance absorption by nuclear magnetic moments in a solid”. In: *Physical review* 69.1-2, p. 37.

Quilliam, J. A. et al. (Nov. 2011). “Ground state and intrinsic susceptibility of the kagome antiferromagnet vesignieite as seen by ^{51}V NMR”. In: *Phys. Rev. B* 84 (18), p. 180401. DOI: 10.1103/PhysRevB.84.180401. URL: https://link.aps.org/doi/10.1103/PhysRevB.84.180401.

Radebaugh, Ray (2009). “Cryocoolers: the state of the art and recent developments”. In: *Journal of Physics: Condensed Matter* 21.16, p. 164219.

Richter, J et al. (2010). “The frustrated spin-1/2 J1-J2 Heisenberg ferromagnet on the square lattice: Exact diagonalization and Coupled-Cluster study”. In: *arXiv preprint arXiv:1002.2299*.

Ritchey, I, Premala Chandra, and Piers Coleman (1993). “Spin folding in the two-dimensional Heisenberg kagomé antiferromagnet”. In: *Physical Review B* 47.22, p. 15342.

Schenck, Alex (2017). “Static magnetic properties of metallic systems explored by μSR-Spectroscopy”. In: *Muon Science*. Routledge, pp. 39–83.

Schenck, Alexander and Kenneth M Crowe (1971). “” Slow” Muon Depolarization in a Single Crystal of Gypsum (CaS O 4· 2 H 2 O)”. In: *Physical Review Letters* 26.2, p. 57.

Shores, Matthew P et al. (2005). “A structurally perfect S= 1/2 kagome antiferromagnet”. In: *Journal of the american chemical society* 127.39, pp. 13462–13463.

Slichter, Charles P (2013). *Principles of magnetic resonance*. Vol. 1. Springer Science & Business Media.

Smith, JH, EM Purcell, and NF Ramsey (1957). “Experimental limit to the electric dipole moment of the neutron”. In: *Physical Review* 108.1, p. 120.

Sonier, JE (2002). *Muon Spin Rotation/Relaxation/Resonance (μSR) Brochure*.

Sun, W et al. (2021). “Magnetic ordering of the distorted kagome antiferromagnet Y 3 Cu 9 (OH) 18 [Cl 8 (OH)] prepared via optimal synthesis”. In: *Physical Review Materials* 5.6, p. 064401.

Sun, Wei et al. (2016). “Perfect Kagomé lattices in YCu 3 (OH) 6 Cl 3: a new candidate for the quantum spin liquid state”. In: *Journal of Materials Chemistry C* 4.37, pp. 8772–8777.

Suter, A et al. (1998). “Mixed magnetic and quadrupolar relaxation in the presence of a dominant static Zeeman Hamiltonian”. In: *Journal of Physics: Condensed Matter* 10.26, p. 5977.

Toth, S and B Lake (2015). “Linear spin wave theory for single-Q incommensurate magnetic structures”. In: *Journal of Physics: Condensed Matter* 27.16, p. 166002.

Toulouse, G, J Vannimenus, and JM Maillard (1977). “Spin glasses and roughening transition”. In: *Journal de Physique Lettres* 38.22, pp. 459–461.

Tustain, Katherine et al. (2020). “From magnetic order to quantum disorder in the Zn-barlowite series of S= 1/2 kagomé antiferromagnets”. In: *npj Quantum Materials* 5.1, p. 74.

Vries, Mark A de et al. (2008). “Magnetic ground state of an experimental S= 1/2 kagome antiferromagnet”. In: *Physical review letters* 100.15, p. 157205.

Wang, Jiaming et al. (2021). “Emergence of spin singlets with inhomogeneous gaps in the kagome lattice Heisenberg antiferromagnets Zn-barlowite and herbertsmithite”. In: *Nature Physics* 17.10, pp. 1109–1113.

— (2022). “Freezing of the Lattice in the Kagome Lattice Heisenberg Antiferromagnet Zn-Barlowite ZnCu 3 (OD) 6 FBr”. In: *Physical Review Letters* 128.15, p. 157202.

Wang, Jierong et al. (2022). “Controlling frustrated magnetism on the kagome lattice by uniaxial-strain tuning”. In: *arXiv preprint arXiv:2209.08613*.

Wannier, GH0038 (1950). “Antiferromagnetism. the triangular ising net”. In: *Physical Review* 79.2, p. 357.

Watanabe, Daiki et al. (2016). “Emergence of nontrivial magnetic excitations in a spin-liquid state of kagomé volborthite”. In: *Proceedings of the National Academy of Sciences* 113.31, pp. 8653–8657.

Wilkinson, JM and SJ Blundell (2020). “Information and decoherence in a muon-fluorine coupled system”. In: *Physical Review Letters* 125.8, p. 087201.

Yoshida, Hiroyuki et al. (2012). “Orbital switching in a frustrated magnet”. In: *Nature communications* 3.1, p. 860.

Zeng, Zhenyuan et al. (2022). “Possible Dirac quantum spin liquid in the kagome quantum antiferromagnet YCu 3 (OH) 6 Br 2 [Br x (OH) 1- x]”. In: *Physical Review B* 105.12, p. L121109.

Zhao, ZY et al. (2019). “Magnetism study on a triangular lattice antiferromagnet Cu2 (OH) 3Br”. In: *Journal of Physics: Condensed Matter* 31.27, p. 275801.

Zheng, XG et al. (2005). “Coexistence of long-range order and spin fluctuation in geometrically frustrated clinoatacamite Cu 2 Cl (OH) 3”. In: *Physical review letters* 95.5, p. 057201.

Zorko, A, M Pregelj, M Gomilšek, et al. (2019). “Negative-vector-chirality 120 spin structure in the defect-and distortion-free quantum kagome antiferromagnet YCu 3 (OH) 6 Cl 3”. In: *Physical Review B* 100.14, p. 144420.

Zorko, A, M Pregelj, M Klanjšek, et al. (2019). “Coexistence of magnetic order and persistent spin dynamics in a quantum kagome antiferromagnet with no intersite mixing”. In: *Physical Review B* 99.21, p. 214441.